ISOSPIN IN (p,n) REACTIONS BETWEEN MIRROR NUCLEI: THE LANE MODEL AND COMPARISONS BETWEEN POLARIZATIONS AND ANALYZING POWERS

ROGER C. BYRD

Triangle Universities Nuclear Laboratory
Department of Physics
Duke University

1978

ISOSPIN IN (p,n) REACTIONS BETWEEN MIRROR NUCLEI: THE LANE MODEL AND COMPARISONS BETWEEN POLARIZATIONS AND ANALYZING POWERS

by

Roger C. Byrd

Department of Physics
Duke University

Date: _____

Approved:

_____
Richard L. Walter, Supervisor

_____

_____

_____

_____

Dissertation submitted in partial fulfillment of the requirements for the degree of Doctor of Philosophy in the Department of Physics in the Graduate School of Duke University

1978

ABSTRACT

(Physics)

ISOSPIN IN (p,n) REACTIONS BETWEEN MIRROR NUCLEI: THE LANE MODEL AND COMPARISONS BETWEEN POLARIZATIONS AND ANALYZING POWERS

by

Roger C. Byrd

Department of Physics
Duke University

Date: _____

Approved:

_____
Richard L. Walter, Supervisor

_____

_____

_____

_____

An abstract of a dissertation submitted in partial fulfillment of the requirements for the degree of Doctor of Philosophy in the Department of Physics in the Graduate School of Duke University

1978

ABSTRACT

ISOSPIN IN (p,n) REACTIONS BETWEEN MIRROR NUCLEI:

THE LANE MODEL

AND

COMPARISONS BETWEEN POLARIZATIONS AND ANALYZING POWERS

by

Roger C. Byrd

In order to supplement polarization studies of (p,n) reactions between mirror nuclei, absolute (p,n) cross sections for ^{9}Be and ^{15}N have been obtained in energy regions where it was felt that direct reaction calculations would be helpful in interpreting the observed polarization phenomena. The $^{9}Be(p,n_0)^{9}B$ data were measured every 10° from 0° to 100° (c.m.) at 11.0, 12.0, 13.5, and 15.0 MeV and are intended to extend the lower energy results of Walker et al. (1965b). A 0° excitation function from 8 to 15 MeV suggests a broad resonance below about 11 MeV. Relative errors of about 3% and absolute normalization errors of 5-10% were assigned. For $^{15}N(p,n_0)^{15}O$, the data also allowed evaluation of the usefulness of the TUNL (n,n) time-of-flight cross-section facility for (p,n) measurements. Supplementary data to that of Wong et al. (1961) were obtained in the form of 0° to 170° (c.m.) angular distributions at 9.05, 10.3, 11.0, and 11.3 MeV in 10° increments, with a 0° excitation function in 200 keV steps from 8.45 to 11.65 MeV. Relative errors were about 3%, and absolute normalization should be good to

5%. The excitation function results are in good agreement with the coarser data of Wong et al., but we now have evidence for much narrower structure than was previously indicated. Although this result precludes the use of a direct reaction model for $^{15}N(p,n_0)^{15}O$ below at least 12 MeV, the ^{9}Be data appeared to be suitable for analysis using an optical model.

A computer program TWAVE3 was written which is capable of simultaneously fitting cross-section and polarization data for (p,p) and (n,n) elastic and (p,n) quasielastic scattering. The calculation solves exactly the coupled equations resulting from application of isospin conservation to the systems of proton-target, neutron-target, and neutron-analog optical model potentials. An important feature is the ability to use any of the various different potential representations, e.g., (U_0,U_1) or (U_p,U_n), and combinations of volume or surface-peaked form factors, all without compromising Lane model consistency. Particular attention has been paid to the inclusion of the isospin symmetry-breaking coulomb effects for target-analog coulomb displacement energies Δ_c and the proton coulomb correction energy, nominally the $\Delta V_c = 0.4Z/A^{1/3}$ term. Finally, a non-linear least-squares search can be carried out for up to twenty-two parameters to simultaneously fit angular distributions of the cross section and polarization for both elastic and quasielastic scattering.

As an application of this program, we have attempted to describe ^{9}Be data from 11 to 15 MeV for the elastic scattering cross section and polarization and the quasielastic (p,n) cross section--all using a single Lane potential. The predictions for this data were excellent, but no simultaneous fit to the charge-exchange analyzing power could be obtained. This

work yields four conclusions. First, a careful application of the Lane model formalism is capable of impressive correlation of results for the three related elastic and charge-exchange reactions. Second, careful attention is needed to transformations of potential representations and form factors, e.g., surface versus volume potentials, and all potentials are not equivalent. Third, inclusion of significant isospin symmetry-breaking coulomb corrections must be handled in a reasonable and self-consistent manner--in other analyses this may have been a serious error. Finally, the failure to describe the charge-exchange analyzing power provides strong evidence for the need for the inclusion of an $(\ell \cdot s)(t \cdot T)$ isospin-dependent spin-orbit term to provide a direct spin and isospin flip, e.g., spin-up proton to spin-down neutron.

Comparisons of the polarization observables P^y and A_y for (p,n) reactions between mirror nuclei are expected to provide information about isospin symmetry breaking effects (Conzett, 1974) and spin-flip mechanisms (Arnold, 1977) in nuclear reactions. We have therefore obtained a considerable amount of P^y and A_y data on (p,n_0) reactions between the light mirror nuclei ^3H - ^3He, ^9Be - ^9B, and ^{15}N - ^{15}O. Specifically, P^y data were obtained for ^3H as an excitation function from 2.0 to 3.75 MeV and angular distributions at 2.26 and 2.46 MeV. The data set for ^9Be includes angular distributions of A_y and P^y from 10°-100° (c.m.) for 8.1, 9.1, and 10.0 MeV, forward angle A_y angular distributions at 2.7 MeV (25° to 60°,c.m.) and 2.9 MeV (25° to 90°, c.m.) for comparison to the P^y data of Rohrer and Brown (1976), and A_y data from 0° to 100° (c.m.) at 11.0,12.0, 13.5, and 15.0 MeV. Three-angle (30°, 50°, and 70°; lab) excitation functions of P^y and A_y have been obtained in at most 0.5 MeV steps

through the energy region from 2.9 to 10.0 MeV. Uncertainties of most data are in the range of 2-5%. As with the previous $T(p,n_0)^3He$ data, all results indicate good to excellent agreement between the two quantities. In particular, there is impressive agreement between A_y data of Rohrer and Brown and the present P^y and A_y data at very low energies, where coulomb symmetry-breaking was initially expected to be most important. For ^{15}N, angular distributions of P^y and A_y from 10° to 110° (c.m.) also indicate good agreement between the two quantities. This comparison was further checked by angular distributions of P^y and A_y at 5.65 and 6.28 MeV, and of A_y at 5.17, 7.9, 8.5, and 9.2 MeV. Excitation functions at 20°, 50° and 100° (lab) for both P^y and A_y were obtained from 4.5 to 9.2 MeV. In strong contrast to the earlier 10.3 and 11.3 results, below about 9 MeV there are widespread differences in the magnitudes and even the signs of the two quantities.

We have attempted to understand the appearance of $P \neq A$ results for the $^{15}N(p,n_0)^{15}O$ reaction only in terms of the symmetry arguments of Conzett's Theorem (Conzett, 1974) and the constraints relating polarization observables (Arnold, 1977). Our results indicate that there is good evidence for the existence of isospin and configuration mixing effects in the ^{16}O intermediate state which could lead to $P \neq A$. Further, these mechanisms seem less likely in the case of the lighter targets ^9Be and ^3H.

ACKNOWLEDGEMENTS

A very large amount of encouragement and assistance in this work has been provided by my advisor, Dr. Richard Walter, and two recent senior members of my research group, Paul Lisowski and Werner Tornow. Tom Clegg has been literally instrumental in obtaining a major portion of this data. Much of the earlier results also required contributions from Gunter Mack and Stan Skubic. The theoretical analysis has benefited greatly from discussions with Steve Cotanch, Henry Hogue, Ron Cusson, and Sven Maripuu.

Several friends have provided essential support - my thanks to Mike, Kate, Brenda, Avie, Steve, Keith, Chris, Priscilla, and Denny. I especially thank my parents, whose support through the years has been crucial.

For everything that has come out right, production credit is due to Mike Bailey (graphics), Bob Hilko and David Turner (photography), Kate Bell (editing), and Bonnie Ferrell (typing).

This work was supported in part by the Department of Energy.

CONTENTS

LIST OF FIGURES

LIST OF TABLES

ISOSPIN IN (p,n) REACTIONS BETWEEN MIRROR NUCLEI: THE LANE MODEL AND COMPARISONS BETWEEN POLARIZATIONS AND ANALYZING POWERS

PREFACE

Quasielastic (p,n) Reactions and the Lane Model

One of the basic problems of nuclear physics has been nucleon-nucleus scattering, where the nucleon may be either a neutron or proton. An obvious approach, suggested by the isospin formalism of particle physics, is to regard neutron scattering as simply "uncharged proton" scattering. In examining this analogy one immediately finds that, because of the difficulties in detecting uncharged particles, data for neutron-nucleus scattering is generally much less precise and plentiful than the corresponding proton data; furthermore, it often appears in the literature long after the corresponding proton measurements have been reported. These differences have often resulted in an tortuous path for comparisons of neutron and proton scattering.

In the late 1950's sufficient neutron cross-section results became available to provide the first real insights. Attempts to understand the proton potential anomaly, i.e., the difference between nuclear scattering potential depths for incident neutrons and protons, led to the understanding (Green and Sood, 1958) that at least part of the difference was non-coulomb with a systematic proportionality to (N-Z)/A, the nuclear symmetry parameter. Another important development was the "discovery" of the (p,n) isobaric analog reaction by Anderson and Wong (1961). These two effects

were brought together in a theory by Lane (1962), which may be outlined as follows.

The symmetry term of the optical model for nucleon-nucleus elastic scattering varies as either plus or minus (N-Z)/A for protons versus neutrons and thus suggests a general dependence on projectile isospin $\vec{t}$ to provide the sign and target isospin $\vec{T}$ to scale the magnitude. Lane suggested the scalar product $4(\vec{t} \cdot \vec{T})/A$, which has two important features. First, it is an explicitly charge-independent isoscalar. Second, when rewritten with raising and lowering operators, it implies not only the term $4t_3T_3/A = \pm (N-Z)/A$ but a t_+T_- operator, which can generate a (p,n) charge-exchange reaction, the t_+ changing proton to neutron and the T_- changing target nucleus to analog.

A severe test of the Lane model was seeing if this $\vec{t} \cdot \vec{T}$ term could indeed relate (p,p), (p,n), and (n,n) scattering data. The results were promising, and the late 1960's and early 1970's saw several analyses testing this viewpoint. The first section of this work is largely concerned with implications and extensions of these analysis.

Comparisons of Polarization and Analyzing Power

The results presented in the first section, however, are not the end of the story. Just as with elastic scattering, where polarization data were necessary to completely define potentials (Rosen et al., 1965), it was important to improve sensitivity to spin effects by including (p,n) polarization data in such analyses. Again, since neutron work is intrinsically difficult, the appearance of the first extensive results for any target, those of Smith and Thornton, was not until 1972. Originally, the only results available were measurements of P, the outgoing neutron polarization, since these were considerably easier than the corresponding measurements for the (p,n) analyzing power A. This situation changed with the advent of relatively intense polarized ion sources, and the first measurements of (p,n) analyzing powers, for $T(p,n_0)^3He$, were published by a Los Alamos group in 1972 (Haight et al.). Immediately a new problem arose, since the observables P and A, which must be identical in elastic scattering, were apparently different for quasielastic (p,n) reactions. The interpretation of this result and its incorporation into charge-exchange reaction theory then became a topic of some interest.

It was at about this time that our laboratory's involvement in these studies began. Some work was begun on (p,n) polarization transfer studies, and the installation of a new beam-pulsing facility made cross-section measurements inviting. While we were setting up to take data, the Los Alamos A results for $T(p,n_0)^3He$ were remeasured (Jarmer et al., 1974)

and the difference between A and P was confirmed. Further studies were underway on the next heavier (p,n) mirror reaction, $^{7}Li(p,n_0)^{7}Be$ (Rohrer and Brown, 1973), so we began taking data on the next heavier case, $^{9}Be(p,n_0)^{9}B$, seeking cross-section and analyzing power data to extend and compare to the existing $\sigma(\theta)$ and $P(\theta)$ data of Walker et al. (1965b). Initially, the relative cross-section data were intended only to support the A data, but a further experiment allowed us to calibrate our detector and obtain absolute results. As with $T(p,n_0)^{3}He$, these first A data for ^{9}Be were in marked disagreement with existing P data, as were the results of a very careful second experiment. Approaching the Fourth Polarization Symposium at Zurich in 1975, we were extending the A measurements to $^{15}N(p,n_0)^{15}O$ and simultaneously measuring new polarization data for both ^{9}Be and ^{15}N under the most carefully controlled conditions possible. The results of this series of measurements were presented at the Zurich meeting (Byrd et al., 1976a, and Lisowski et al., 1976). At that time the available theoretical guidance was provided by Conzett's Theorem (Conzett, 1974); by using isospin symmetry arguments, Conzett showed that for (p,n) reactions P = A in the absence of coulomb effects. Significantly, our new polarization and analyzing power data were in close agreement with each other for both reactions $^{9}Be(p,n_0)^{9}B$ and $^{15}N(p,n_0)^{15}O$.

The next development came at the Washington APS meeting in 1976 from discussions of the existing results on $T(p,n_0)^{3}He$ and $^{7}Li(p,n_0)^{7}Be$ (Doyle et al., 1976) and $^{9}Be(p,n_0)^{9}B$ and $^{15}N(p,n_0)^{15}O$ (Byrd et al., 1976b). The comparisons for ^{3}H and ^{7}Li still showed differences of

the order of 10-20%, but our difficulties in reproducing older P data for ^{9}Be and ^{15}N indicated that the disagreements were not necessarily evidence of charge symmetry breaking near the coulomb barrier. We therefore remeasured the P data for $T(p,n_0)^{3}He$ and extended both P and A measurements for ^{9}Be and ^{15}N to lower energies.

In this final round of results, we found that: (1) the new $^{3}H(p,n_0)^{3}He$ P data were in excellent agreement with the A data and (2) the equality for $^{9}Be(p,n_0)^{9}B$ extended to lower energies, while (3) the $^{15}N(p,n_0)^{15}O$ data showed strong differences between P and A for energies between 4.5 and 9.2 MeV. These results were presented at the 1977 APS Washington meeting (Byrd et al., 1977). All of the TUNL data for P and A that is mentioned above will be presented in this thesis.

Lane Optical Model Studies

In an attempt to better understand the reaction mechanism, we have extended the abundant $\sigma(\theta)$ data that exist for $^{15}N(p,n_0)^{15}O$ below 9 MeV to the highest energies of our P and A results, giving fairly complete charge-exchange data sets for both ^{9}Be and ^{15}N over a wide energy region. In Table 1 we summarize the various sets of $\sigma(\theta)$, $P(\theta)$, and $A(\theta)$ data for $T(p,n_0)^{3}He$, $^{9}Be(p,n_0)^{9}B$, and $^{15}N(p,n_0)^{15}O$ obtained in connection with this work.

The recent thrust of this research has been to attempt calculations of the most straightforward of the observed results, i.e., the distributions for $\sigma(\theta)$ and $A(\theta)$ in the $^{9}Be(p,n_0)^{9}B$ reaction at direct reaction energies. We used an ambitious approach which has tested the Lane model to its limits. The insights from this study are helpful in organizing an investigation of the P and A comparison, but the present model is simply not powerful enough to explain charge-exchange polarization effects.

The organization of the following presentation follows the logical historical development of isospin effects in (p,n) mirror reactions and not the chronological order in which the various experiments were performed. We begin with (p,n) cross-section measurements and discuss the results of the Lane model calculations. In the second section we then give a detailed comparison of P and A experiments in general and attempt to interpret the results obtained in this work.

TABLE 1

SUMMARY OF THESIS DATA

Cross Sections $\sigma(\theta,E)$

$^{9}Be(p,n_0)^{9}B$

$\sigma(\theta)$: 11.0, 12.0, 13.5, 15.0 MeV

$\sigma(E)$: 0°; 10-15 MeV

$^{15}N(p,n_0)^{15}O$

$\sigma(\theta)$: 9.05, 10.3, 11.0, 11.3 MeV

$\sigma(E)$: 0°; 8.45-11.65 MeV

Polarizations $P^{y}(\theta,E)$

$^{9}Be(p,\vec{n}_0)^{9}B$

$P^{y}(\theta)$: 2.7, 2.9, 8.1, 9.1, 10.0 MeV

$P^{y}(E)$: 50°; 7.9-10.0 MeV

30°,50°,70°; 2.7-10.0 MeV

$^{15}N(p,\vec{n}_0)^{15}O$

$P^{y}(\theta)$: 5.65, 6.28, 10.3, 11.3 MeV

$P^{y}(E)$: 40°; 10.3-11.4 MeV

20°,50°,100°; 4.5-11.3 MeV

Analyzing Powers $A_y(\theta,E)$

$^{3}H(\vec{p},n_0)^{3}He$

$A_y(\theta)$: 2.26, 2.46 MeV

$A_y(E)$: 45° (c.m.); 2.0-3.75 MeV

$^{9}Be(\vec{p},n_0)^{9}B$

$A_y(\theta)$: 8.1, 9.1, 10.0, 11.1, 12.0, 13.5, 15.0 MeV

$A_y(E)$: 30°,50°,70°; 2.9-15.0 MeV

$^{15}N(\vec{p},n_0)^{15}O$

$A_y(\theta)$: 5.17,5.65,6.28,7.9,8.5,9.2,10.3,11.3 MeV

$A_y(E)$: 40°; 10.3-11.4 MeV

20°,50°,100°; 4.5-11.3 MeV

PART ONE

THE LANE POTENTIAL OPTICAL MODEL AND (p,n) REACTIONS BETWEEN LIGHT MIRROR NUCLEI

I. MEASUREMENTS OF (p,n) CROSS SECTIONS

Introduction

It will be clear in the sections to follow that acquisition of cross-section results has been an substantial part of this work. This importance is basically three-fold. First, we need the $\sigma(\theta)$ measurements corresponding to our $A(\theta)$ and $P(\theta)$ data in order to make associated Legendre polynomial fits to the products σA or σP. Second, reaction mechanisms, i.e., the contributions of direct or resonant channels, are usually more easily recognized in cross-section results than in polarization results. For example, the direct nature of the $^{9}Be(p,n_0)^{9}B$ reaction mechanism and the resonance structure of $^{15}N(p,n_0)^{15}O$ were investigated to determine valid energy regions for optical model approaches. Finally, many cross-section measurements are of interest primarily to the neutron polarization program and therefore must be obtained by members of this group in cooperation with the TUNL neutron scattering group. The collection, analysis, and interpretation of these results require us to develop techniques and expertise often specialized to our goals. For instance, the $\sigma(\theta)$ measurement for ^{9}Be investigated the usefulness of the new TUNL beam-pulsing facility for measurements using the beam line in our own target area and determined the

efficiency calibration of our own neutron detectors. The ^{15}N experiment allowed evaluation of the specialized TUNL (n,n) time-of-flight system as a tool for (p,n) cross-section studies, projecting the use of the target systems for future polarization and cross-section studies.

The purpose of a cross-section measurement is to express the yield of particles $dN(\theta)$ at a particular angle θ obtained with an incident beam intensity I; $dN(\theta) = I\sigma(\theta)$. In order to extract a cross-section value, it is necessary to normalize the result by removing dependences on the amount of target material and the size and efficiency of the detector. The resulting expression can be written as

$$dN(\theta) = N_0 n \eta \sigma(\theta) d\Omega$$

where N_0 is number of incident particles, n is the number of target nuclei per cm^2, η is the detector efficiency, and $d\Omega$ is the solid angle subtended by the detector. It will be helpful to remember that much of our discussion is devoted to extraction of the values of $dN(\theta)$ from the data collected and the calibration of the detector efficiency η.

In the next sections we will examine in some detail how these quantities were measured in the $^{9}Be(p,n_0)^{9}B$ and $^{15}N(p,n)^{15}O$ experiment, starting with ^{9}Be.

A. The $^{9}Be(p,n_0)^{9}B$ Experiment

Data Collection and Reduction

The $^{9}Be(p,n_0)^{9}B$ cross-section data were obtained using the pre-acceleration pulsed-beam facility of the TUNL accelerator. For this study the beam was brought into the neutron polarization target area. It was necessary to insert a capacitive beam pickoff inside the beam pipe in the target area to generate a timing pulse. Target shielding was provided by adapting the massive neutron spin-precession solenoid for use as a detector shield by inserting a specially-designed double-truncated conical brass collimator. The ^{9}Be target was a 4.7 $\mu g/cm^2$ thick foil ($\Delta E \approx 125$ keV at 13.5 MeV) mounted onto a 51 mm thick tantalum beam stop. The neutrons were detected at a flight path of 103 cm by a cylindrical NE213 scintillator whose active volume had a diameter of 3.65 cm and a depth of 2.86 cm.

Detector biases were set to exclude proton recoil energies below either 1.8 or 3.3 MeV, while neutron energies in the experiment ranged from approximately 7.1 to 13.1 MeV. The electronics set-up was based on a standard neutron time-of-flight arrangement (Glasgow et al., 1975), which included pulse-shape discrimination to suppress gamma ray events in the detector. To reduce counting rates in the electronics, timing was started by a pulse from the neutron detector and stopped by a delayed pulse from the capacitive beam pickoff.

Several representative time-of-flight spectra are shown in Figure 1 for different incident proton energies. Note that the start-stop arrangement gives neutron flight time, measured from the target to the detector, as increasing (energy decreasing) to the left. The large peak is the n_0 group (ground state in ^9B) and the next peak is the n_1 group (2.36 MeV state in ^9B). The continuum is due primarily to the four-body breakup reaction (Bauer, Anderson, and Wong, 1964) and secondarily to neutrons from Ta(p,n). The Q-value for the breakup process $^9Be + p \rightarrow p + n + 2\alpha$ is -1.573 MeV, below the -1.854 MeV value for the ground state group. The breakup continuum will therefore seriously contaminate the n_0 group as its yield increases at higher energies and forward angles (Walker et al., 1965b).

At 0°, the underlying target-plus-breakup background correction ranged from about 10% at 10.0 MeV to 20% at 15.0 MeV; in the worst case, the back-angle minimum at 15.0MeV, the correction reached 36%. These estimates were obtained from an off-line computer analysis which represented backgrounds as polynomial shapes extrapolated to zero near the center of the n_0 peak, consistent with kinematics for the breakup reaction. Uncertainties in background line shapes are likely to be limiting factor in the precision of the extracted counts for the n_0 peak.

The analysis at this point has obtained the unnormalized yields $dN(\theta)$ required above. The factors for incident intensity N_0, areal density of target nuclei n, and solid angle $d\Omega$ were all easily obtained in the standard manner. The efficiency $\eta(E_n)$, however, must either be calculated from nuclear cross sections or measured directly.

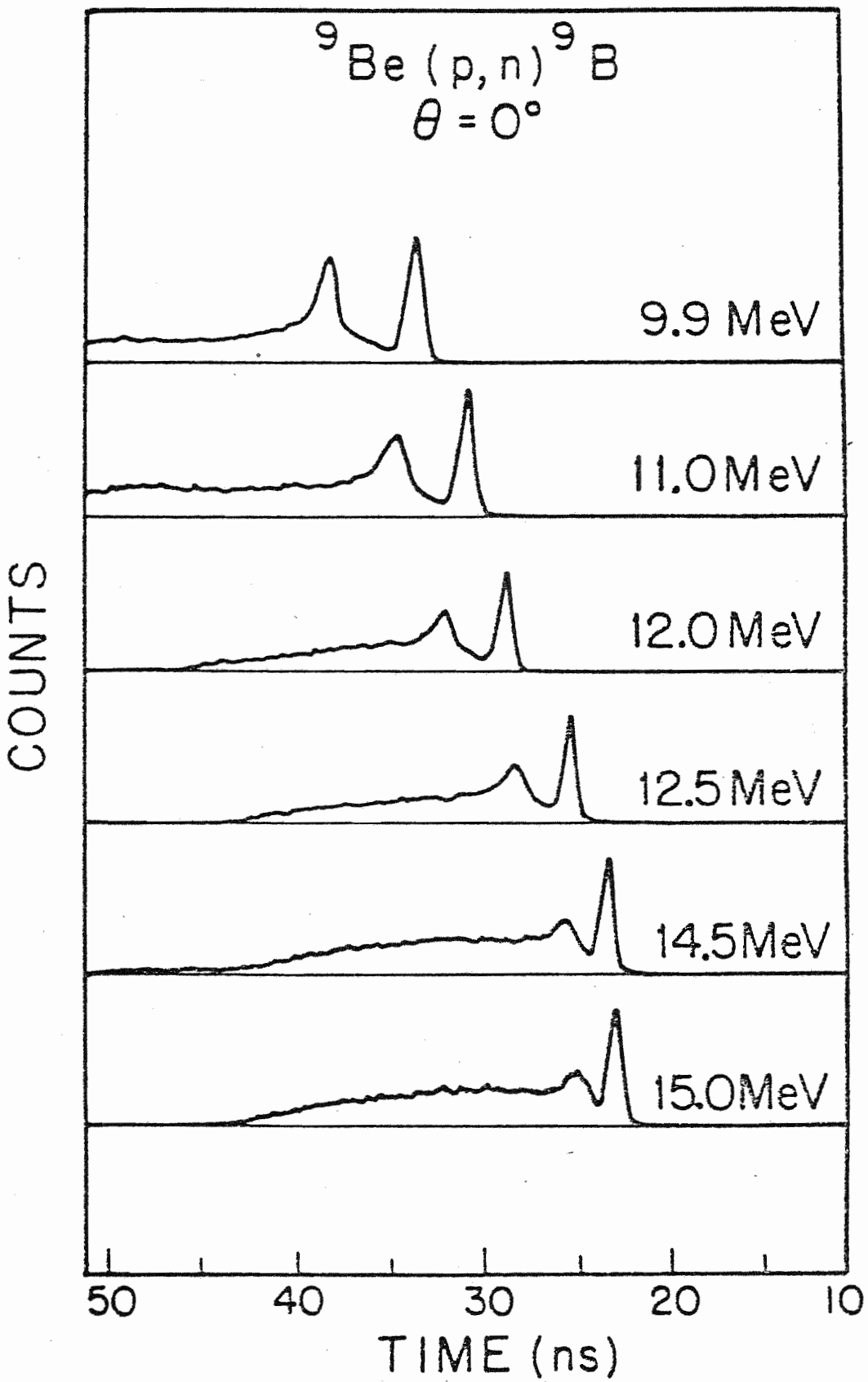

Figure 1. $^{9}Be(p,n)$ Time-of-Flight Spectra

Efficiency Function

The detector used in the $^{9}Be(p,n_0)^{9}B$ $\sigma(\theta)$ experiment was a Nuclear Enterprises NE213 (type BA1) organic liquid scintillator encased in a glass cylinder having external dimensions of 5.08 cm in diameter and 3.175 cm in depth. The efficiency calibration was based on measurements of the neutron yield from the $D(d,n_0)^{3}He$ reaction. The yield was measured at three bias settings (expressed in multiples of ^{137}Cs bias as 0.25 × Cs, 0.50 × Cs, and 1.0 × Cs) for neutron energies E_n ranging between 2 and 17 MeV. The three yield curves were converted to efficiency curves using the known $D(d,n_0)^{3}He$ cross section. These efficiency curves were parameterized by a least-squares fitting function ETA which provided the basis of a general polynomial interpolation for any desired value of energy and bias. Results for the bias values given above are shown in Figure 2 along with the corresponding data.

In an attempt to support this calibration and to allow more reliable extrapolation to other energies and biases, a comparison was made to results of an absolute efficiency calibration provided by George Morgan (1975) for a similar scintillator (same material but of active volume 3.81 cm diameter × 3.81 cm depth). The comparisons desired between our function ETA above and the calculation of Morgan were: (1) a volume correction, and (2) conversion from Morgan's bias in Light Output Units (L.O.U.) (Verbinski et al., 1968), to our values in Cs bias units.

For the first conversion, it was decided to renormalize the 0.5 × Cs and 1.0 × Cs data to the curves of Morgan. The factor determined was $\eta(\text{TUNL}) = 0.83 \times \eta(\text{Morgan})$. The interior dimension of the

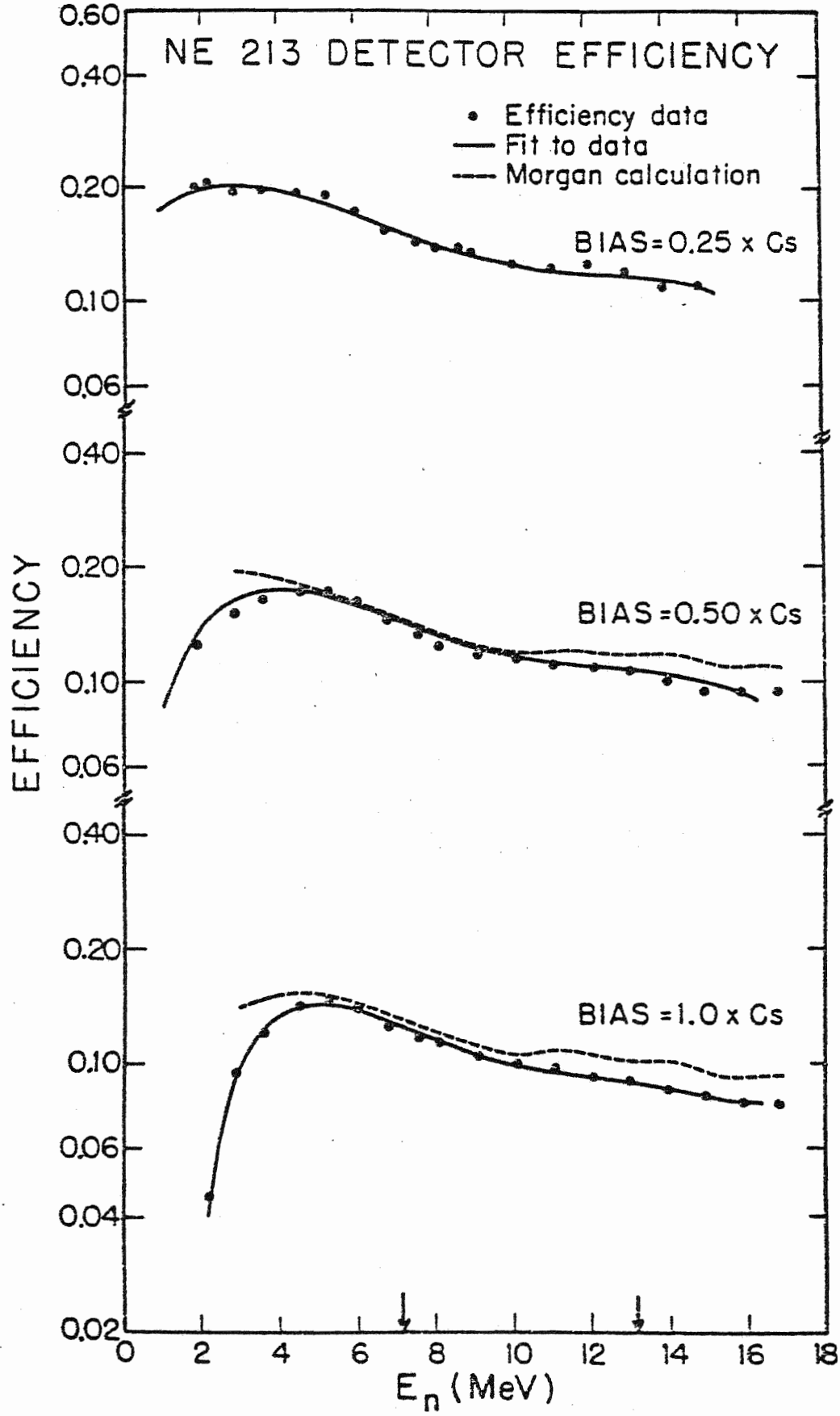

Figure 2. Neutron Detection Efficiencies for NE 213 Scintillator

container for the NE213 liquid scintillator used in the measurements were unavailable, and the best estimates from visual inspection placed the active volume at 3.65 cm diameter by 2.86 cm height, giving a volume roughly 0.69 times that used in Morgan's calculation.

As for the conversion of bias measurements, the low-energy portion of the efficiency function, i.e. the "cut-off region," was found to yield a conversion of 1.0 L.O.U. = 0.96 × Cs bias, with an uncertainty of $\pm$ 0.04. Some comments are in order. First, the low energy behavior of the data may be influenced by resolution effects, which do not appear to be included in Morgan's calculation. On the other hand, errors in this conversion are critical mainly for neutron energies near the cut-off, since the dependence is weak elsewhere. In the region employed for the analysis of our data, which is indicated by arrows in Figure 2, a shift in bias from 1.0 to 2.0 × Cs results in a change of only about 10% in the efficiency. Despite the difficulty in converting the L.O.U. units to multiples of Cs bias, the observed proton energy cut-off point obtained with our assumption agrees well with the conversion of Drosg et al. (1972) between Cs bias units and proton recoil energies.

Taking the above factors into consideration, we felt that the shape and normalization of our own efficiency calibration were consistent with the calculation provided by Morgan, as shown in Figure 2. The final cross-section results were obtained using our own curves. In view of the comparisons above, we believe that the efficiency for the energy region of the present experiment was known to 5%. It is hoped to verify this using a new absolute efficiency calibration based on a Los Alamos calculation provided by Dr. Paul Lisowski.

Presentation of Results

Our measurements were intended to extend those of Walker et al. (1965b), whose highest energy was 10.9 MeV. Our results consist of angular distributions at 11.0, 12.0, 13.5, and 15.0 MeV and an overlapping 0° excitation function from 10.0 to 15.0 MeV. The data are presented in Figures 3 and 4 and tabulated in the Appendix. The errors shown are total absolute errors, and the $\sigma(\theta)$ curves in the angular distributions are based on Legendre polynomial fits to the data. The TUNL values at 11.0 MeV may be compared with the Livermore data of Walker et al. (1965b) at 10.9 MeV. The shapes are quite similar, but the Livermore values are approximately 1.25 to 1.35 times those of TUNL, although a difference of no more than 3% is expected because of the apparent dependence of $\sigma(\theta)$ on energy. Similarly, the Livermore 0° values are about 1.1 mb/sr (18%) greater than the corresponding values from the TUNL excitation function. Since Walker et al. claim less than 10% absolute error and our similar estimate is 5%, the measurements do not quite agree in magnitude.

In attempting to evaluate the contribution of non-direct processes, particularly compound or resonance effects, we are struck by two features in the region below 12 MeV. The 0° cross section decreases from about 6.2 mb/sr at 10 MeV to 4.9 mb/sr at 12 MeV. Also, the first minimum in the differential cross section becomes shallower with decreasing energy, seems to disappear completely at 9.7 MeV (according to the data of Walker et al.), and is again clearly in evidence at several lower energies. These observations lead us to suggest that a direct reaction

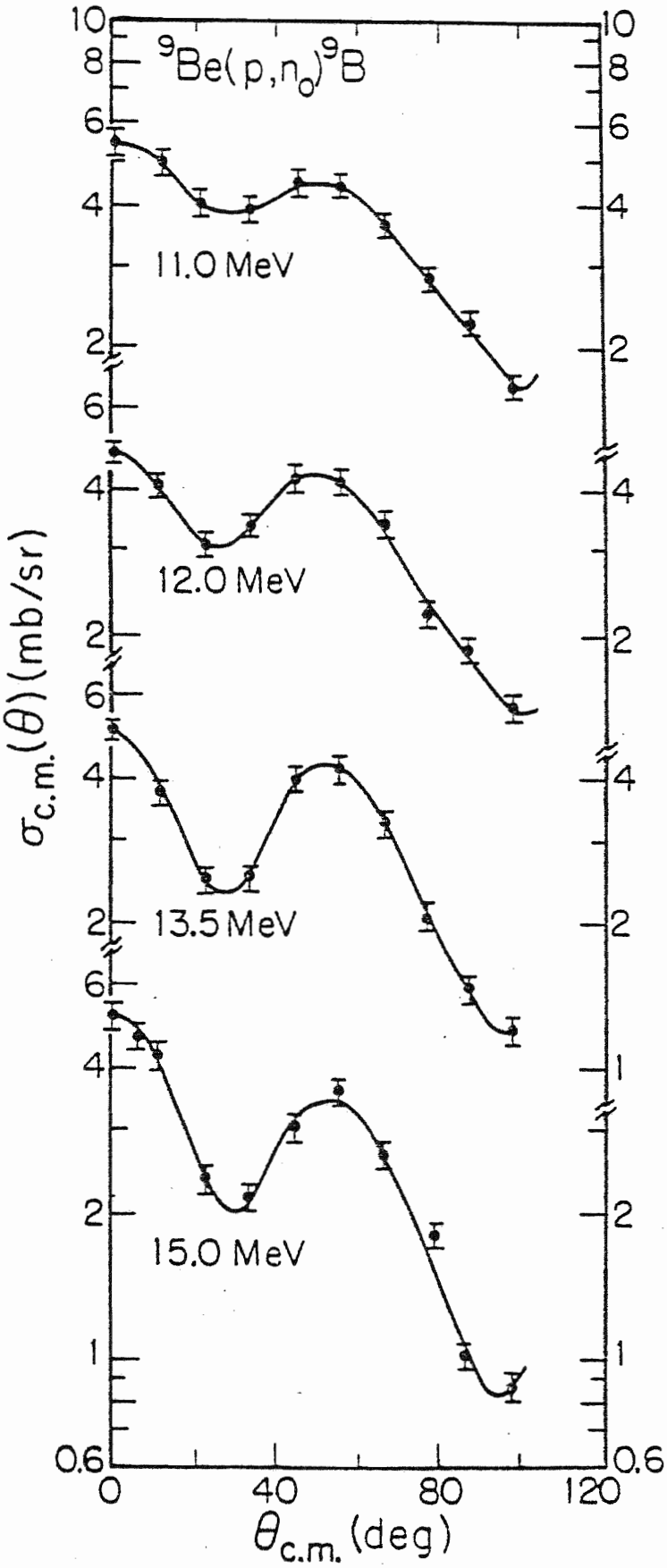

Figure 3. Angular Distributions of the $^9Be(p,n_0)^9B$ Cross Section

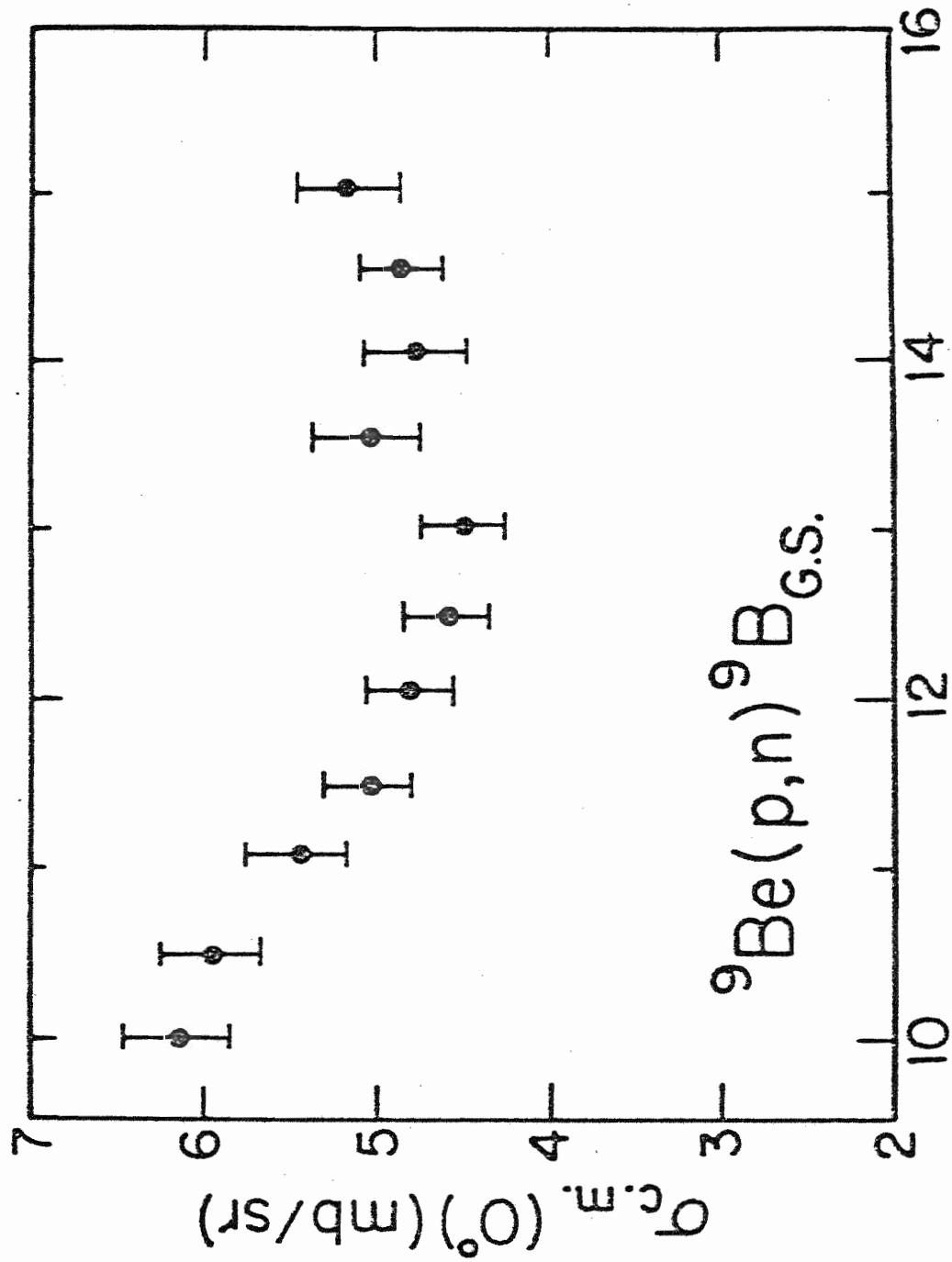

Figure 4. Excitation Function of the ^{9}Be(p,n$_0$)^{9}B Cross Section

approach may have considerably more difficulty in describing the region below 11 MeV than the data in the region above 12 MeV.

B. The $^{15}N(p,n_0)^{15}O$ Experiment

Purpose

The measurements of the $^{15}N(p,n_0)^{15}O$ cross section in the region of 8-12 MeV were made for three reasons. First, we felt that the existing data, those of Wong et al. (1961), were too coarse in energy to allow us to evaluate the contribution of resonance effects to the reaction at the higher energies of our P and A comparison. Second, we needed the functional form of $\sigma(\theta)$ at 10.3 and 11.3 to supplement the $P(\theta)$ and $A(\theta)$ distributions at those energies. Finally, it was inviting to investigate a (p,n) reaction using the well-established (n,n) cross-section facility developed at this laboratory over the past few years (Glasgow et al., 1975).

Experimental Arrangement

The important advantages of this system will be outlined here, as they will be useful in interpreting the discussion of the (p,n) experiment and its results. First, background reduction has been one of the primary design goals of the system. Careful attention was paid to minimizing both the production of background and its subsequent detection. For example, collimators, slits, and gas target assemblies were specially designed and a high vacuum maintained to reduce contamination of the gas target foils. A massive, optimized shield and associated collimator were designed to reduce source and room-scattered neutrons.

Another important feature of the system is the relatively good inherent time resolution (1.5-2.0 ns) obtained by the chopping-bunching facility and the detector and its electronics. Finally, in using this extensively refined system, we were able to take advantage of existing data acquisition software and procedures developed using the expertise of the neutron time-of-flight staff. This was particularly valuable in two respects: (1) the entire setting up and data collection required only 28 hours of accelerator time, and (2) the absolute neutron detection efficiency of the system had been previously calibrated.

Several minor modifications, some of which can be seen in Figure 5, were made to the system to change over from (n,n) to (p,n) measurements. First, a beam-line extension was inserted to bring the target over the goniometer pivot point. Second, a special $^{15}N_2$ low-volume filling system was built and installed. Third, the large tungsten shadow bar which normally shields the main detector and its large shield from the primary neutron flux was removed. Finally, the 90° vertical monitor was realigned to point at the extended gas target position.

Experimental parameters were influenced by the anticipation of excellent counting rates in comparison to the double-scattering approach needed for (n,n) work. The $^{15}N_2$ gas purity was 98.9 mole-% $^{15}N_2$, 1.1 mole-% $^{14}N_2$ (Mound Laboratory). The gas cell was 2.93 cm long with a 3.5 mg/cm^2 molybdenum entrance foil. The target thickness for the 9.05 MeV angular distribution was approximately 170 keV; for all other measurements it was about 140 keV thick (to 9 MeV protons). The flight path was set at maximum, 4.0 m, and the detector bias was calibrated to 1.0 × Cs, which corresponds to 1.9 MeV for proton recoils in NE218.

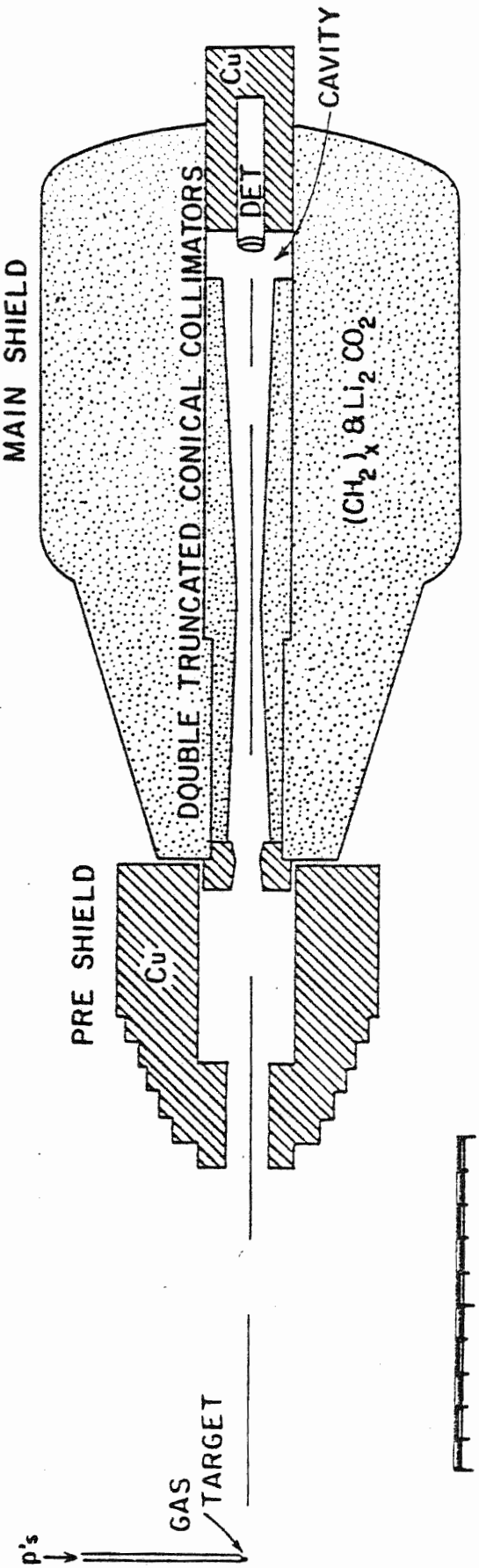

Figure 5. Target and Detector Arrangement for the $^{15}N(p,n_0)^{15}O$ Cross-Section Experiment

Neutron energies in the experiment ranged from 3.9 MeV (9.05 MeV, 160° lab) to 8.1 MeV (11.65 MeV, 0°). Data were obtained at 9.05, 10.3, 11.0, and 11.3 MeV, usually at every 10° between 0° and 160° (lab). A 0° excitation function was also measured from 8.45 to 11.65 MeV. The determination of the reaction angle θ was made to within $\pm$ 0.2° (lab). To help detect systematic drifts, data were taken in 20° steps, increasing from 0° to 160° and then decreasing from 150° to 10°, with a repeat measurement at 0°. Various points were repeated for consistency checks; in all cases reasonable agreement was obtained.

Background Contributions

Much of the discussion to follow concerns the extraction of the background effects in this experiment. Our goal is not simply to correct the present data, but to understand background behavior in regard to future experiments. We are therefore interested in such relationships as time correlation and energy or angle dependence of both neutron and gamma-ray sources. The signatures of these events are usually recorded and discussed in the form of spectra of various types, as was done here.

We first examine the time-correlated aspects of the measurement in terms of Figure 6, a logarithmic plot of yield versus the detection time measured from the arrival of the beam burst at the target. Note the incomplete removal of the target gamma-ray peak by subtraction of the spectrum obtained with no ^{15}N target gas, which implies that at least part of the gamma yield is prompt gammas from the gas. The n_0 peak again rides on a continuum of background events, despite the approximately

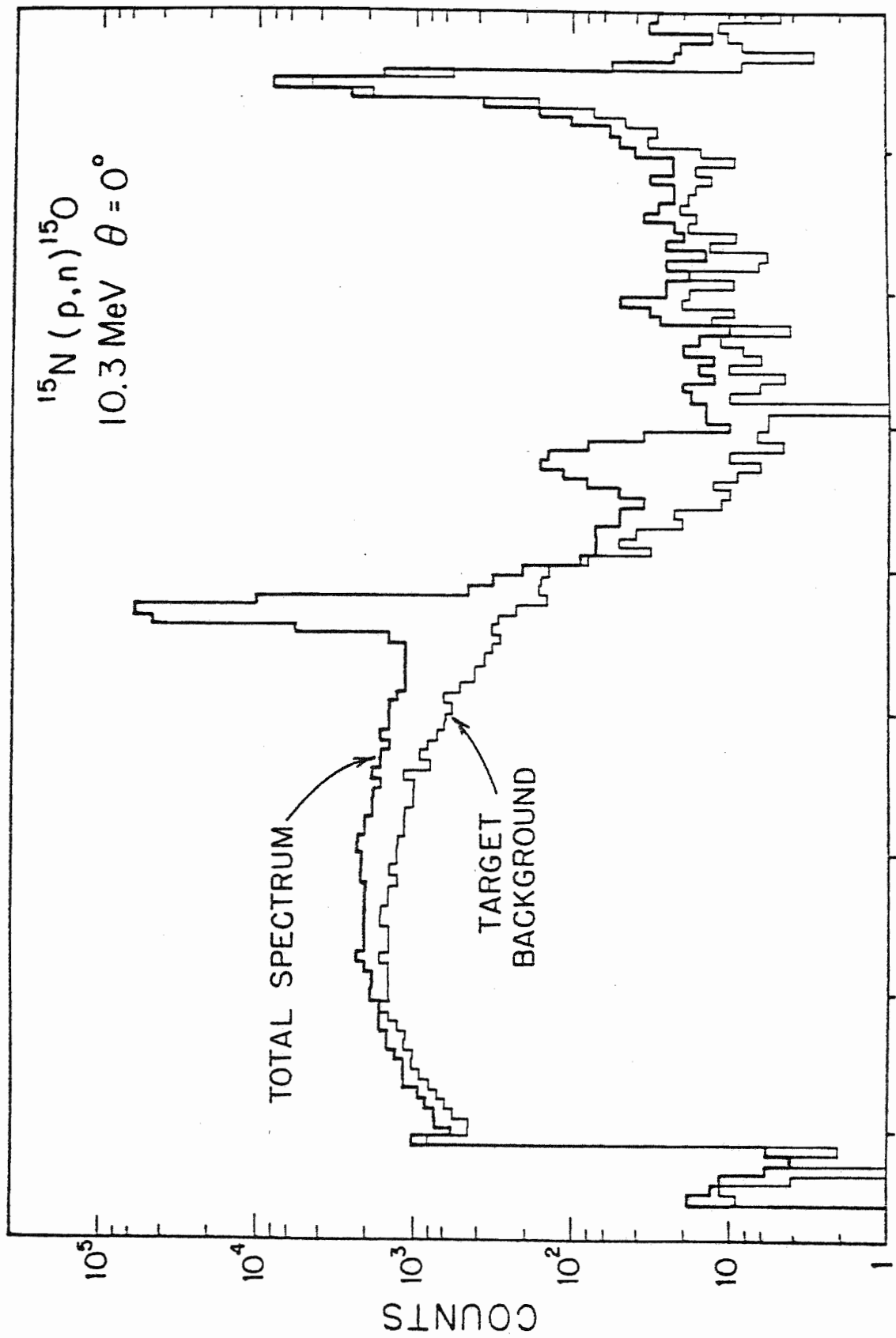

Figure 6. Logarithmic Time-of-Flight Spectrum for the $^{15}N+p$ Reaction

5 MeV separation of the n_1 group (not present in this particular spectrum).

Before speculating further on the source of this background, we examine some more of its characteristics in Figure 7. On the left are shown the time spectra from the zero-degree measurements of each of our angular distributions. Note that the target gamma ray becomes more prominent at higher energies, as does the continuum background, implying that at least part of the continuum may be due to problems with the n-γ pulse-shape discrimination circuit, either because of high gamma energy (dynamic range problems), count rate (pile-up problems), or simply an increased ratio of gamma-ray to neutron-producing yields. Further, the connection of at least part of this background to the target gas, as seen previously in Figure 5, suggests that (n,γ) reactions or neutron inscattering from the detector shield may be a problem. This is especially likely since the normal (n,n) experimental configuration relies on a tantalum shadow bar to reduce the neutron flux striking the detector shield. Further discussion of background behavior will be given later, after explaining the data reduction used to quantitatively extract its contribution from a particular spectrum.

Normalization

In approaching the problem of determining the ground state contribution, one should keep in mind that the goal is to extract the area of the n_0 peak from the main detector and normalize this area to some quantity which reflects the number of incident particles striking the the target. We start by explaining the basis of our normalization. In

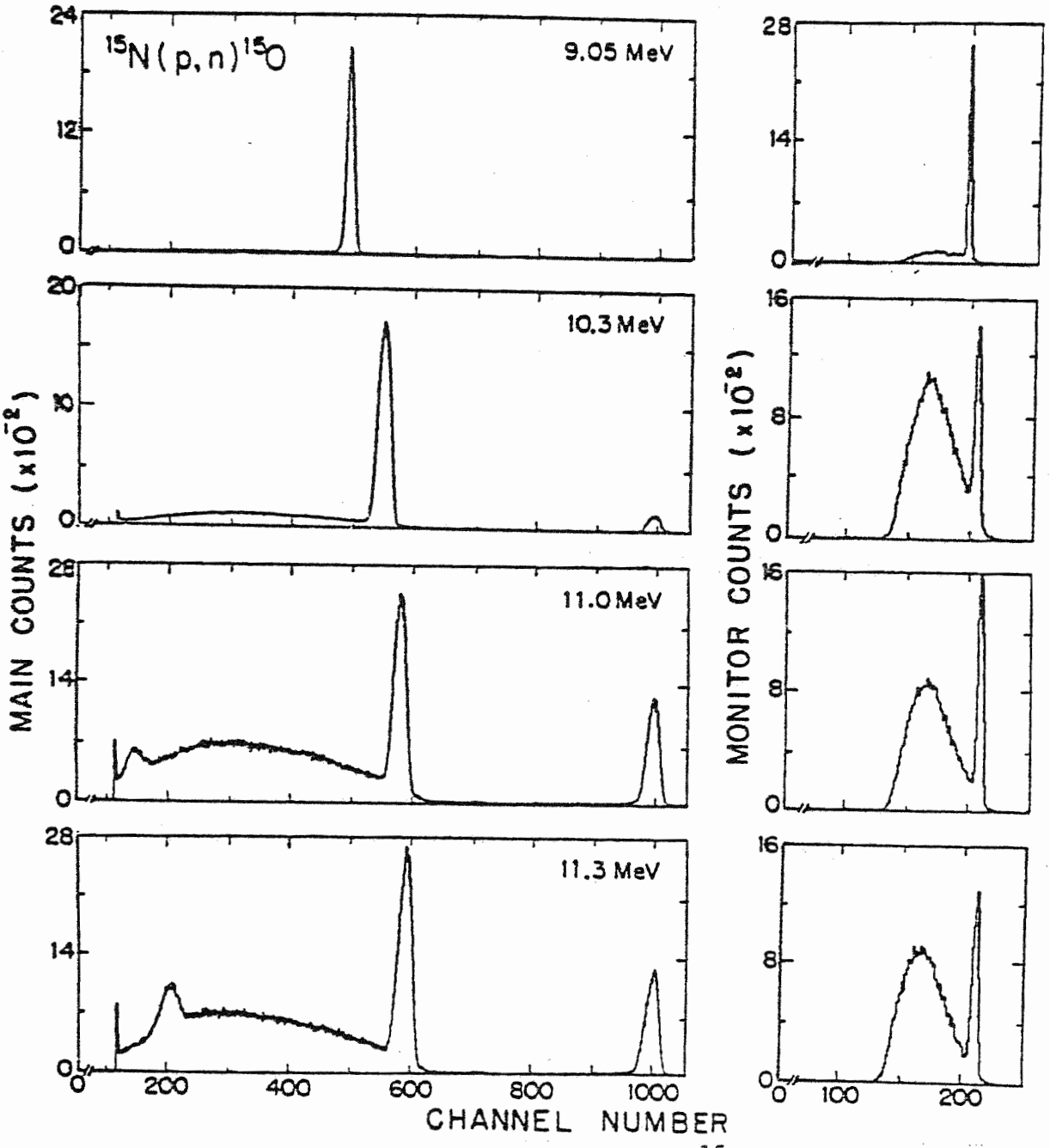

Figure 7. Time-of-Flight Spectra for the $^{15}N+p$ Reaction at 0°

principle, a simple charge integration is quite suitable, but in practice this approach can have difficulties. For example, drifts in the beam position may cause particles to strike collimators, allowing collection of charge which results in no neutron yield from the target gas. More subtly, marginal triggering of the electronics which process the signal from the capacitive beam pick-off may prevent identification of valid detector events. Both of these problems require careful beam handling and monitoring of pick-off signals if normalization is made directly to charge integration.

An alternate approach which is sometimes useful is normalization to a monitor neutron detector which remains stationary directly above the target as the main detector is moved through the angular distribution. Its advantage is illustrated by the elimination of the two previously-mentioned problems. First, beam wander affects both the monitor and main detector equally, since both record only yield-producing events. Second, pick-off triggering produces timing signals required for storage in both spectra, so effects are proportional. All that is required for normalization to monitor counts is that: (1) the monitor counting rate be constant, i.e., independent of the main detector position as it is moved through the angular range, and (2) some means is provided to obtain the relative monitor normalization to absolute values.

In these experiments we have obtained both angular distribution and excitation function data. Note that monitor normalization is meaningless in the excitation function, since the monitor counting rate clearly changes with proton energy. We therefore were careful to check collimator

currents and the pick-off signal detection efficiency during the excitation function measurements, and these results are directly normalized to the integrated proton beam current, i.e., the collected charge. In the angular distributions, monitor normalization is possible to the extent that the monitor counting rate is independent of the main detector position or angle. Within each angular distribution we have normalized all yields to monitor counts, providing four separate relative normalizations. We have then used the ratio of collected charge to monitor counts averaged over each entire distribution to normalize the $\sigma(\theta)$ zero-degree yield to the $\sigma(E)$ excitation function value. In the presentation of results we will outline an approach to normalizing all data simultaneously.

Yield Extraction

We now focus on determining the areas of the peaks of interest in the spectra for the main and monitor detectors. In determining the area of the n_0 peak in the main time-of-flight (TOF) spectrum, preliminary use of the TOF group's spectrum stripping program convinced us that a linear background was acceptable within our desired uncertainties. This conclusion allowed use of a simpler charged-particle cross-section program CSEC9, which was specifically altered for this experiment to generate linear backgrounds and the total counts for the n_0 peak.

The background corrections obtained for the n_0 data are seen in Figure 8 to vary smoothly with angle. Note that the shapes are somewhat the same for all energies. This behavior is due at least partly to the

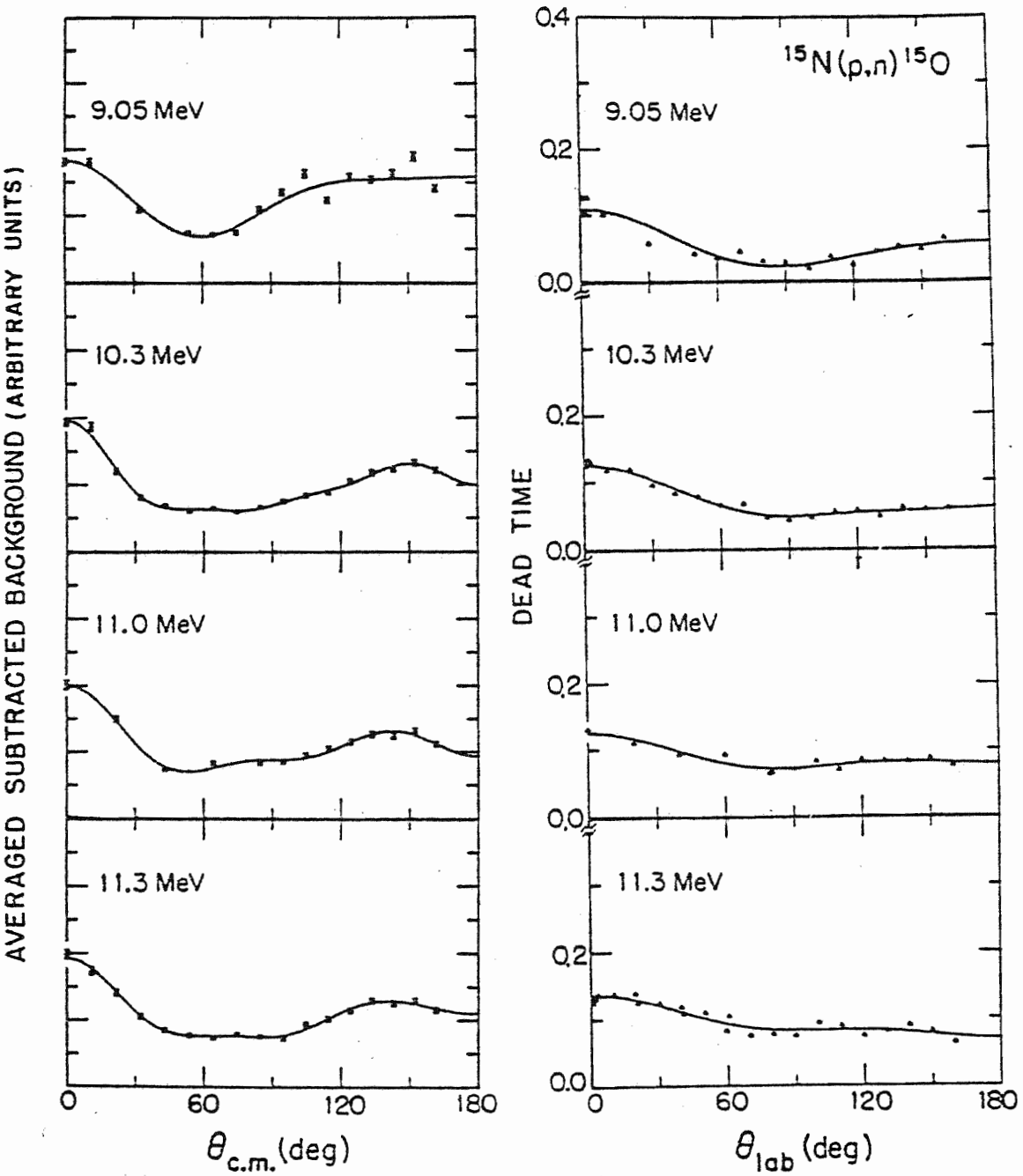

Figure 8. Corrections to Main Detector Time-of-Flight Spectra

fact that the n_0 peak will walk back to lower energies with increasing angle, thus riding farther up on the background shoulder. However, the magnitude of the continuum increases at forward and backward angles, in agreement with the suggestion that it results partly from (n,n) and (n,γ) contributions from the detector shield and therefore is roughly proportional to the forward and backward-peaked cross section. There may even be additional effects at angles between 0° and 20° and near 160°, which are regions where the various target room walls are quite close to the detector.

Correction was also made for the main detector dead time, which was determined from the ratio of gated to ungated clock pulses at each angle. These results are shown in the right side of Figure 8 and have shapes similar to the background distributions, as expected from the above argument.

Special care was taken in examining the monitor spectrum. The narrowness of the peak suggested that a linear background might fluctuate erratically from spectrum to spectrum because of sensitivity to small time shifts, so we have included the background in the region near and underneath the n_0 peak in the monitor normalization. It was therefore essential to verify that this background contribution was not correlated to the main detector position. In the process of extracting the total area, we also estimated monitor n_0 peak-to-background ratio, which is shown on the left of Figure 9. Two conclusions can be made: the angle-independence is confirmed, and the subtraction is indeed erractic and verifies the need for inclusion of the full area.

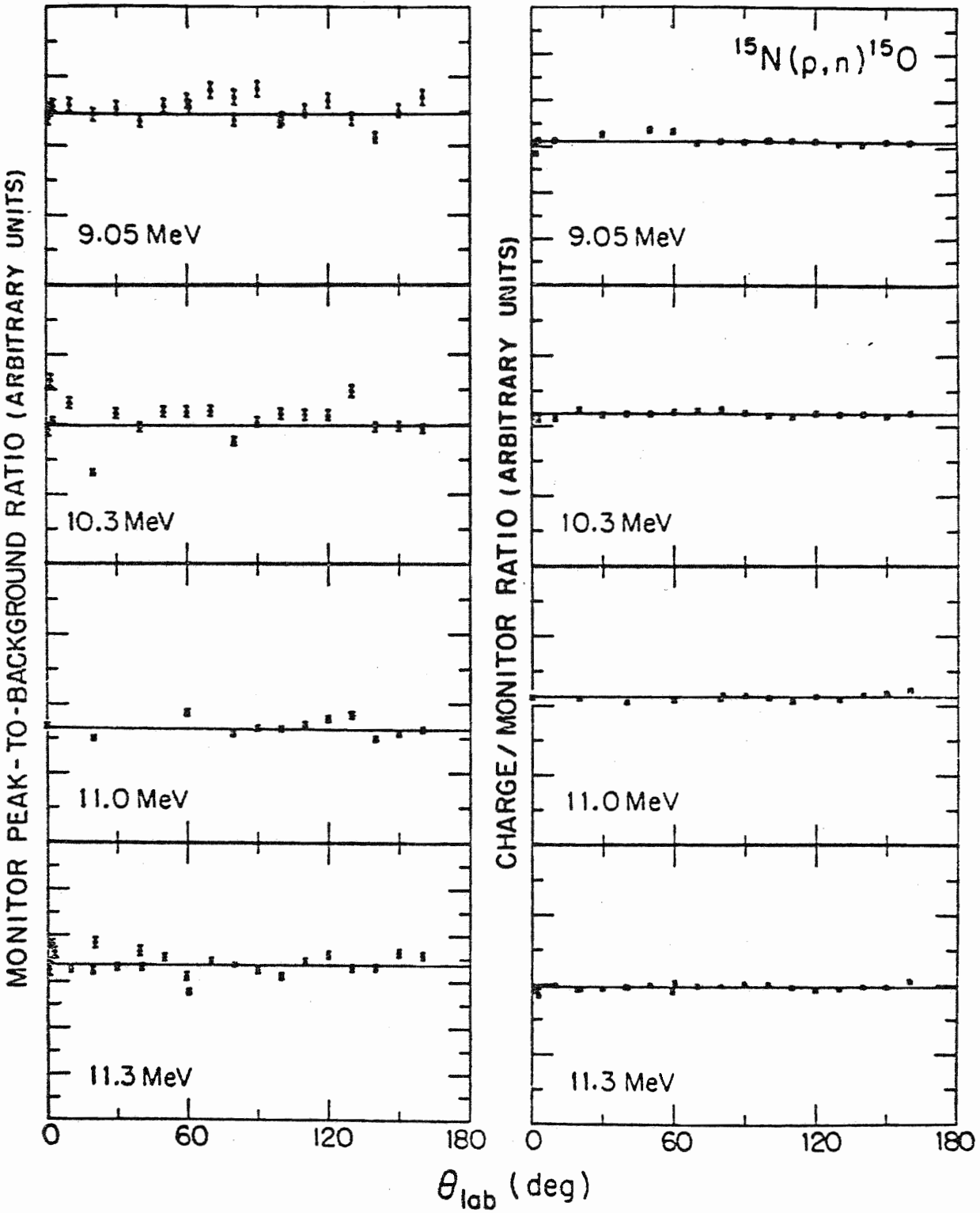

Figure 9. Corrections to Monitor Detector Time-of-Flight Spectra

As a further check on the stability of the monitor, we have computed the ratios of collected charge to monitor counts. It is apparent from the right side of Figure 9 that either method of normalization is acceptable, since there is no evidence for a linear correction to the angle dependence at the 10% significance level by an f-test (Bevington, 1969). This check is important, since the excitation function must be normalized to collected charge, as the monitor counting rate is energy-dependent in this case.

Efficiency Correction

We have now obtained values of the ground state neutron yield normalizable to incident charge. The major remaining parameter in a cross-section measurement is the detector efficiency, which is obtainable from previous system calibrations by the TOF staff and is shown in Figure 10. The efficiency function is normally measured by that group relative to the $^{1}H(n,n)^{1}H$ cross section, so its proper use requires that one or more comparison measurements of n-p scattering be made during the $^{15}N(p,n)^{15}O$ experiment. With our geometry, however, such a measurement is impossible since there is no scattering sample. Nevertheless, the unnormalized efficiency function provides a relative calibration and corrects the shape of our $\sigma(\theta)$ distributions for the shape of the $\eta(E_n)$ function. In fitting the resulting relative cross sections, we found that chi-square values could be reduced to about 1.0 per point by assignment of an additional shape error of 1.0%, which has been included in all results here.

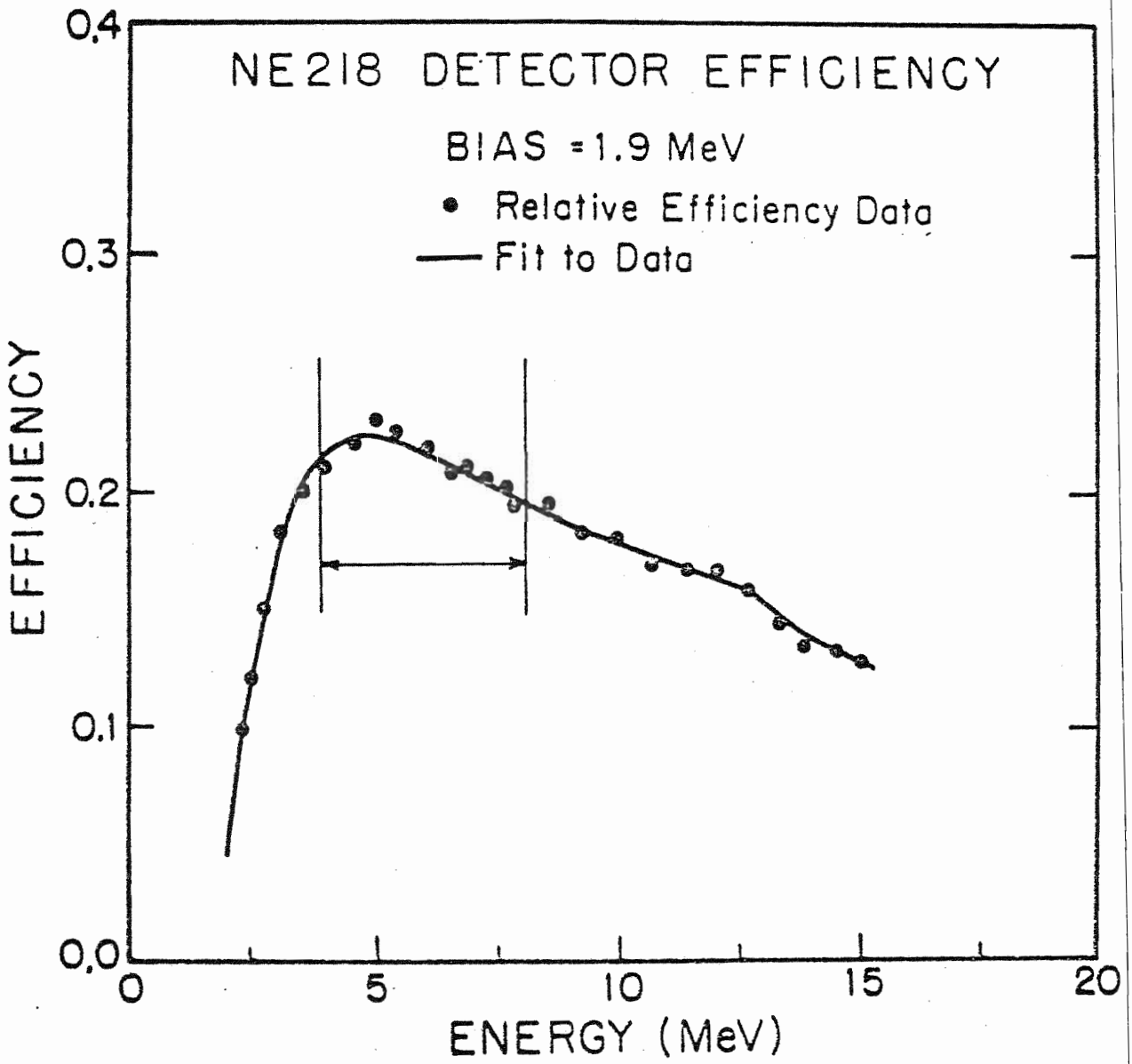

Figure 10. Neutron Detection Efficiency for NE 218 Scintillator

A possible source of this additional uncertainty is errors in the shape of $\eta(E_n)$ as interpolated between measured values. To estimate this effect, we examine the efficiency for the range of neutron energies involved in this experiment, which is indicated by the arrows in Figure 10. The near-linearity in this region suggests that the contribution to the relative error from this source should be small; discussions with NTOF staff indicated an upper limit of 2.0%. This value is consistent with our 1.0% assignment, since a portion of the shape error would not affect a chi-square test. Our relative error is thus viewed as a minimum case.

Unfortunately, it is difficult to assign an absolute uncertainty, since the only absolute calibration attempted by the neutron group at TUNL has been normalization to a calculation by G. Morgan similar to that discussed for our $^{9}Be(p,n_0)^{9}B$ experiment. In the present case correct volumes were known and the only comparison between relative measurements and calculation was in converting Light Output Units to Cs bias units. Again, we optimistically assign an error of 5-10%, and all errors shown here are relative and do not include this contribution.

Presentation of Results

As before, the formula for the cross section may be written

$$\sigma(\theta) = \frac{1}{\eta(E_n)} \frac{dN(\theta)}{N_0 n d\Omega}$$

where

$\eta(E_n)$ is the absolute detection efficiency at the energy E_n

$dN(\theta)$ is the yield

N_0 is the number of incident protons

n is the number of target scatterers per cm^2

$d\Omega$ is the solid angle subtended by the detector.

Numerous variables may be re-expressed in terms of the quantities directly obtained at our laboratory:

$$N_0 = bs \times 6.25 \times 10^{10}$$

$$n = t/A \times 6.02 \times 10^{20}$$

$$d = d^2/r^2 \times 7.85 \times 10^{-5}$$

where

b is number of beam current integrator counts

s is beam current integration scale in μA

t is target thickness in mg/cm^2

A is atomic number

d is detector diameter in cm

r is flight path in meters .

We thus obtain for $\sigma(\theta)$ in mb/sr:

$$\sigma(\theta) = \frac{dN(\theta)r^2A}{\eta(E_n)bstd^2} \times 3.38 \times 10^{-1}$$

For example, nominal values for 11.3 MeV, 0° were

$dN = 4.78 \times 10^4$ counts

r = 4.0 meters

A = 15

η = 0.2 at 7.1 MeV

b = 5481 counts

s = 2.0

$t = 3.5\ mg/cm^2$

$d = 8.9\ cm$

Substitution into the equation above gives $\sigma(0°) = 6.4$ mb/sr.

The final angular distribution results are shown in Figure 11 and listed in the Appendix. The shapes are in fair agreement with those of Hansen and Stelts (1963) and Wong et al. (1961) at comparable energies, although the different target thicknesses for the two experiments make an exact comparison impossible. The change in shape over the energy range from 8 to 12 MeV can now be seen clearly by combining the data from Wong et al. with that of the present work, particularly with the inclusion of the 11.0 MeV distribution.

Finally, to better see the resonance structure in this energy region, we have used the same target (ΔE = 170 keV) to measure a 0° cross section from 8.45 to 11.65 MeV. The previous data of this nature consisted mainly of the $^{15}N(p,n)^{15}O$ total cross section data of Barnett (1968) shown in Figure 40 and the excitation functions at 5° and 40° (lab) of Wong et al., both of which indicate width of about 0.5 MeV. In contrast, our results, shown in Figure 12 and listed in the Appendix, support widths on the order of our target thickness, i.e., 100 to 200 keV.

The curve through the excitation function points is merely a guide to the eye, and is repeated in the lower part of the figure for comparison to the Livermore data and their predicted structure. Note that the 0° cross sections obtained from the TUNL angular distributions are in good agreement with our excitation function values. Also, all TUNL points are consistent with the 5° excitation function results from

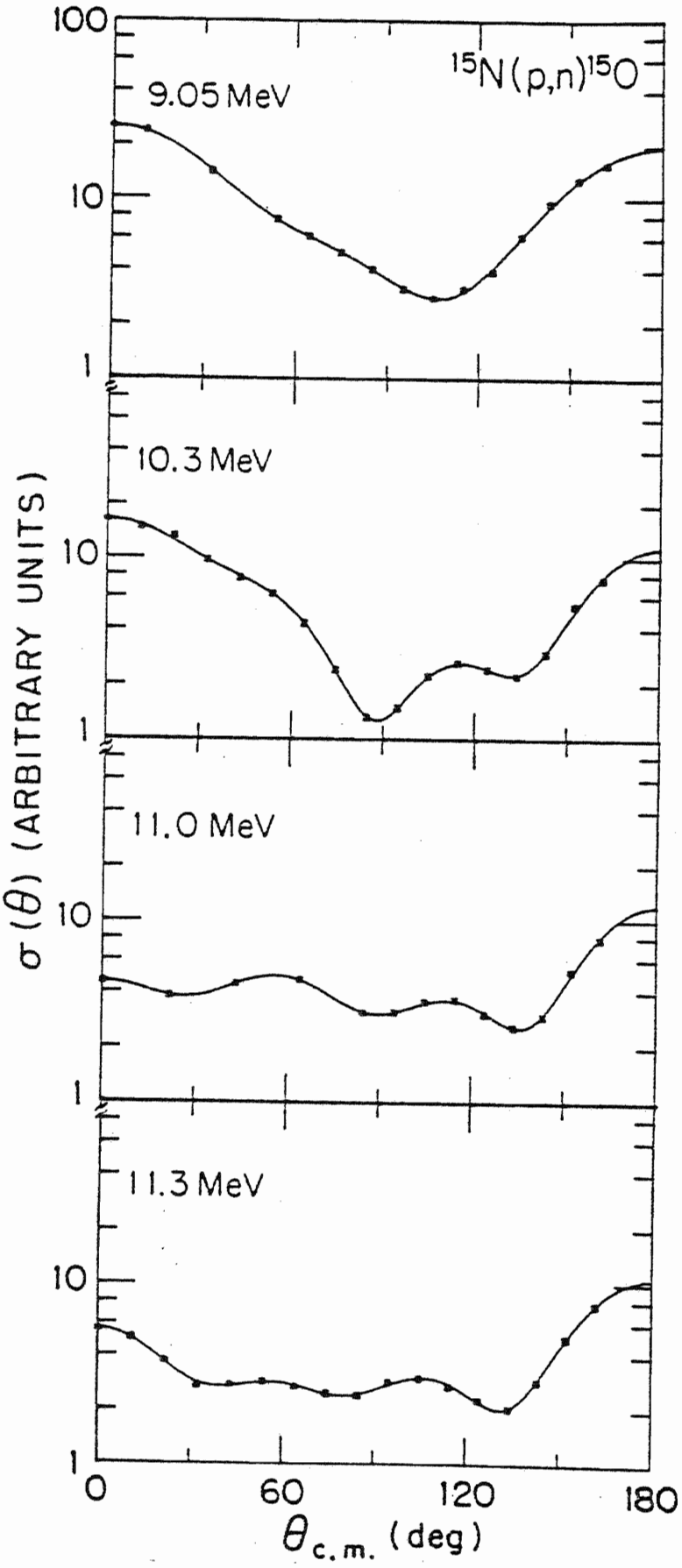

Figure 11. Angular Distributions of the $^{15}N(p,n_0)^{15}O$ Cross Section

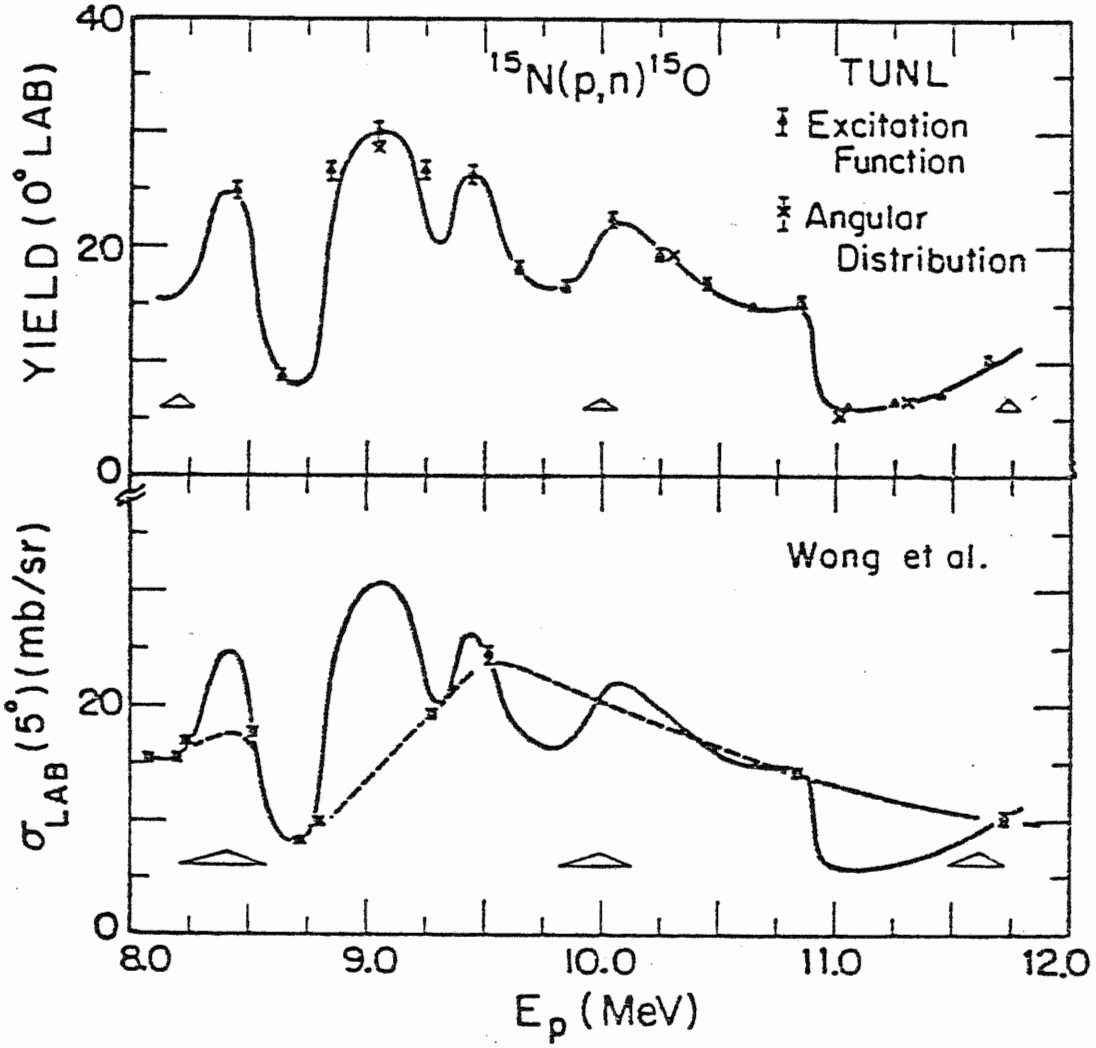

Figure 12. Excitation Function of the $^{15}N(p,n_0)^{15}O$ Cross Section

Wong et al., which verifies the absolute normalization of these results.

In conclusion, we see that the advantages of the NTOF system as far as precision and convenience are certainly impressive. In comparison to the previous $^{9}Be(p,n_0)^{9}B$ experiment, the relative and absolute accuracies here are much higher, yet the results required relatively minor modification of the systems designed for (n,n) work. With a modest amount of further development, primarily in the areas of (1) pulse-shape discrimination to give better gamma-ray suppression, and (2) efficiency function calibration, a program of several (p,n) reaction studies could be easily undertaken with the facilities at TUNL.

II. The Lane Potential Optical Model

Introduction

The second half of our study of (p,n) reactions presents the theory used to interpret the preceding experimental results. Two factors led to our final approach. First, a survey of the literature quickly revealed that such reactions have usually been handled using Lane potential optical models to be described below. Second, the author of a computer code to perform just such a calculation, Prof. S. Cotanch, had recently joined the TUNL staff.

We subdivide the entire discussion of our theory into Part A, the Lane optical model motivation, derivation, and development, and Part B, the application of the resulting model. Starting with Part A, in Section 1 we explain our view of the basis of the Lane model and develop the optical model potentials resulting from our assumptions. In Section 2 this approach is compared to those in the literature and expanded accordingly. Particular attention is paid to the assumptions made and the difficulties encountered in other analyses. Turning to application in Part B, we first describe a computer program which was written to perform the calculations needed to test our assumptions. Finally, our last section reports the results of a comprehensive attempt to use this program in describing elastic and quasielastic scattering from ^{9}Be.

A. DEVELOPMENT OF THE LANE OPTICAL MODEL

1. FORMAL DERIVATION OF EQUATIONS

Basis of Approach

The basis of the Lane model will be dealt with here, but only briefly since comprehensive discussions are found elsewhere (Lane, 1962, and Satchler, 1969). We simply point out that the phenomenological optical potential for the nucleon-nucleus interaction appears to require a symmetry term on the order of $V_{sym} = \mp 27(N-Z)/A$, where the minus refers to incident protons, the plus to incident neutrons. Since $(N-Z)/A$ can be written as $2T_3/A$, where T_3 is the target isospin projection, a parameterization of $V_{sym} = 4t_3T_3/A$ is suggested, with t_3 the projectile isospin projection ($-\frac{1}{2}$ for protons, $+\frac{1}{2}$ for neutrons). This form in turn suggests the charge-independent scalar product $\vec{t} \cdot \vec{T}$, which further leads to (p,n) quasielastic reactions induced by the t_+T_- off-diagonal term, as shown below. These formal considerations were justified by Lane, who derived the $\vec{t} \cdot \vec{T}$ form of the interaction as the sum of two-body Heisenberg forces and the exchange effects of other forces averaged over a Fermi gas.

There is another approach to the Lane model, however, which has seen little exposure in nuclear physics. Consider a division of the nuclear force into strong and electromagnetic interaction parts. We

immediately observe that the dominant effects in the interaction should be due to the characteristics of the strong force. The electromagnetic effects may be treated as perturbations since the coulomb potential between nucleons is approximately 5% of the strong interaction (McCarthy, 1968). The principal features of the strong interaction are expressed by the related concepts of charge independence and isospin conservation. In fact, our division of the nuclear force into strong and electromagnetic parts becomes even more revealing since the strong interaction conserves isospin, while the electromagnetic does not. We may therefore attempt to approach the problem in terms of isospin conservation and then introduce the isospin-violating coulomb effects separately. As will be seen both in the development of the equations for the Lane model and the discussion of differences between P and A, the insight provided by this approach is quite valuable.

Returning to the formulation of the Lane potential, we begin by explicitly writing the nuclear force as a two-component interaction with isospin-dependent and independent parts, indentifying our $\vec{t} \cdot \vec{T}$ term as the dependent one. The starting point for the development of an optical model potential consistent with the Lane formalism thus becomes $U = U_0 + 4(\vec{t} \cdot \vec{T})U_1/A$.

At this point we should establish a notation for optical model potentials. As a start, we write a general potential as a complex function $U = V + iW$. We may also divide potentials into isospin dependent and independent parts with $U = U_0 + 4(\vec{t} \cdot \vec{T})U_1/A$, as shown in the previous section. In this notation, two sets of equations are implied:

$V = V_0 + 4(\vec{t} \cdot \vec{T})V_1/A$ and $W = W_0 + 4(\vec{t} \cdot \vec{T})W_1/A$. Further, each V or W may be a superposition of volume and surface (derivative) Woods-Saxon form factors, although this generality may not always be needed. To illustrate, the complete expression for a volume V_0 would be

$$V_0(r) = -V_0(1 + \exp(X_0))^{-1};\ X_0 = (r - r_0A^{1/3})/a_0,$$

and for a surface W_0:

$$W_0(r) = -4a_{os}W_0(d/dr)(1 + \exp(X_{os}))^{-1};\ X_{os} = (r - r_{os}A^{1/3})/a_{os}.$$

The spin-orbit potential is usually assumed to be real and isospin-independent, hence

$$V_{so}(r) = -V_{so}(\frac{r}{m_\pi c})^2(1/r)(d/dr)(1 + \exp(X_{so}))^{-1};\ X_{so} = (r - r_{so}A^{1/3})/a_{so}.$$

Finally, the coulomb potential is that for a uniformly-charged sphere of radius $R_c = r_cA^{1/3}$ and target charge Z:

$$V_c(r) = Ze^2(2R_c)(3 - r^2/R_c^2);\quad r \leq R_c$$
$$= Ze^2/r \qquad\qquad ;\quad r \geq R_c$$

For a complete discussion of the potential used one should consult the technical report by S. Cotanch on the basic code SUMIT (Cotanch, 1973).

Derivation of Optical Model Potentials

We now proceed to derive the basic equations of the Lane potential optical model in some detail, since the validity and success of the analysis to follow depends crucially on the nature of the assumptions involved. In the sections to follow we (1) describe nucleon-nucleus

states in isospin notation; (2) derive the strict charge-independent Lane potential; (3) develop the Schrödinger equations for the processes of interest; and (4) explain our assumptions for inclusion of the charge symmetry-violating coulomb effects.

In order to apply the Lane model to the nucleon-nucleus optical model, it is first necessary to develop a formalism to handle states in terms of isospin quantum numbers and then derive potentials as matrix elements in this formalism. We first write defining expressions for nucleon states, nucleus states, and then nucleon-nucleus states. The isospin states of nucleon projectiles are denoted by $|t,t_3>$, taking $|n> = |\frac{1}{2},\frac{1}{2}>$ and $|p> = |\frac{1}{2},-\frac{1}{2}>$, so that $t_-|n> = |p>$. We write nuclear states as $|T,T_3>$, with

$$T_\pm|T,T_3> = [(T \pm T_3 + 1)(T \pm T_3)]^{1/2}|T,T_3 \pm 1>. \qquad (1)$$

Our target ground state is $|C> = |T,T>$; its isobaric analog is $|A> = |T,T-1>$. These states are thus related by $|A> = (2T)^{-1/2}T_-|C>$.

We now want to combine the nucleon and nucleus states using angular momentum coupling, i.e.,

$$|T,T_3> \times |\tfrac{1}{2},t_3> = \sum_{T_t} <T\ \tfrac{1}{2},T_t t_3|T\ \tfrac{1}{2},T_t,T_{t_3}>|T_t,T_{t_3}> .$$

The states we shall need are given by:

$$|pC> \equiv |p> \times |C> = |\tfrac{1}{2},-\tfrac{1}{2}> \times |T,T> \qquad (2a)$$

$$|nA> \equiv |n> \times |A> = |\tfrac{1}{2},\tfrac{1}{2}> \times |T,T-1> \qquad (2b)$$

$$|nC> \equiv |n> \times |C> = |\tfrac{1}{2},\tfrac{1}{2}> \times |T,T> \qquad (2c)$$

To evaluate the required angular momentum coupling coeffficents, we will need:

$$\langle T\,\tfrac{1}{2},T_3,\tfrac{1}{2}|\,T\,\tfrac{1}{2},T \pm \tfrac{1}{2},T_{t_3}\rangle = \left(\frac{t \pm T_{t_3} + \frac{1}{2}}{2T+1}\right)^{1/2} \tag{3a}$$

$$\langle T\,\tfrac{1}{2},T_3,-\tfrac{1}{2}|\,T\,\tfrac{1}{2},T\ \ \tfrac{1}{2},T_{t_3}\rangle = \left(\frac{T \pm T_{t_3} + \frac{1}{2}}{2T+1}\right)^{1/2} \tag{3b}$$

At this point it is convenient to introduce the notation $|T_>\rangle \equiv |T + \frac{1}{2},T_3\rangle$, $|T_<\rangle \equiv |T - \frac{1}{2},T_3\rangle$. Then, using equations (1-3), we obtain:

$$|pC\rangle = (2T+1)^{-1/2}(|T_>\rangle + (2T)^{1/2}|T_<\rangle) \tag{4a}$$

$$|nA\rangle = (2T+1)^{-1/2}((2T)^{1/2}|T_>\rangle - |T_<\rangle) \tag{4b}$$

$$|nC\rangle = |T_>\rangle \tag{4c}$$

In addition, it will be necessary to have the inverse equations which express the states $|T_>\rangle$ and $|T_<\rangle$ as:

$$|T_>\rangle = (2T+1)^{-1/2}(|pC\rangle + (2T)^{1/2}|nA\rangle) \tag{5a}$$

$$|T_<\rangle = (2T+1)^{-1/2}((2T)^{1/2}|pC\rangle - |nA\rangle) \tag{5b}$$

We must now derive the Lane potential expressions as matrix elements of $U = U_0 + 4(\vec{t} \cdot \vec{T})U_1/A$ in the above nucleon-nucleus isospin representation. It is necessary to introduce the following reaction notations:

$$C(p,p)C : \langle pC|U|pC\rangle = U_{pC} \tag{6a}$$

$$C(n,n)C : \langle nC|U|nC\rangle = U_{nC} \tag{6b}$$

$$A(n,n)A : \langle nA|U|nA\rangle = U_{nA} \tag{6c}$$

$$C(p,n)A : \langle nA|U|pC\rangle = U_{pn} \tag{6d}$$

The primary problem is in evaluating the matrix elements for the $\vec{t} \cdot \vec{T}$ term. Two useful methods are discussed below, the first appropriate for uncoupled nucleon and nucleus isospins $\vec{t}$ and $\vec{T}$, the other evaluated in the coupled $\vec{T}_t$ representation. The uncoupled approach is based ón the relation

$$\vec{t} \cdot \vec{T} = (T_+t_- + T_-t_+ + 2T_3t_3)/2 \ . \tag{7}$$

Recall from equation (1) that the raising and lowering operators are given by:

$$T_\pm|T,T_3\rangle = [\,(T \pm T_3 + 1)(T \mp T_3)\,]^{1/2}|T,T_3 \pm 1\rangle .$$

Using equation (7), the $\vec{t} \cdot \vec{T}$ part of equations (6) is evaluated as follows:

$$\langle pC|\vec{t} \cdot \vec{T}|pC\rangle = \langle T,T|T_3|T,T\rangle\langle \tfrac{1}{2}, -\tfrac{1}{2}|t_3|\tfrac{1}{2}, -\tfrac{1}{2}\rangle \tag{8a}$$

$$= -T/2$$

$$\langle nC|\vec{t} \cdot \vec{T}|nC\rangle = \langle T,T|T_3|T,T\rangle\langle \tfrac{1}{2},\tfrac{1}{2}|t_3|\tfrac{1}{2},\tfrac{1}{2}\rangle \tag{8b}$$

$$= T/2$$

$$\langle nA|\vec{t} \cdot \vec{T}|nA\rangle = \langle T,T-1|T_3|T,T-1\rangle\langle \tfrac{1}{2},\tfrac{1}{2}|t_3|\tfrac{1}{2},\tfrac{1}{2}\rangle \tag{8c}$$

$$= (T - 1)/2$$

$$\langle nA|\vec{t}\cdot\vec{T}|pC\rangle = \frac{1}{2}\langle nA|T_+t_- + T_-t_+|pC\rangle$$

$$= \frac{1}{2}\langle A|T_-|C\rangle\langle n|t_+|p\rangle$$

$$= \frac{1}{2}\langle T,T-1|T_-|T,T\rangle\langle\tfrac{1}{2},\tfrac{1}{2}|t_+|\tfrac{1}{2},-\tfrac{1}{2}\rangle$$

$$= (T/2)^{1/2} \qquad (8d)$$

In the derivation of equation (8d), note that the (p,n) transition is generated specifically by the (T_-t_+) operator.

We now use the coupled representation, evaluating the $(\vec{t}\cdot\vec{T})$ part of equations (6) using

$$\vec{t}\cdot\vec{T} = (T_t^2 - T^2 - t^2)/2. \qquad (9)$$

Clearly, with this approach we must use expressions (5) to evaluate the matrix elements for $\langle T_t^2\rangle$. This is done as follows:

$$\langle pC|\vec{t}\cdot\vec{T}|pC\rangle = (\tfrac{1}{2})(2T+1)^{-1}(\langle T_>| + (2T)^{1/2}\langle T_>|)T_t^2$$

$$(|T_>\rangle + (2T)^{1/2}|T_>\rangle) - \frac{1}{2}\langle C|T^2|C\rangle - \frac{1}{2}\langle p|t^2|p\rangle = -T/2 \qquad (10a)$$

$$\langle nC|\vec{t}\cdot\vec{T}|nC\rangle = \frac{1}{2}\langle T_>|T_t^2|T_>\rangle - \frac{1}{2}\langle C|T^2|C\rangle$$
$$- \frac{1}{2}\langle n|t^2|n\rangle = T/2 \qquad (10b)$$

$$\langle nA|\vec{t}\cdot\vec{T}|nA\rangle = \frac{1}{2}(2T+1)^{-1}((2T)^{1/2}\langle T_>| - \langle T_<|)T_t^2$$

$$((2T)^{1/2}|T_>\rangle - |T_<\rangle) - \frac{1}{2}\langle A|T^2|A\rangle - \frac{1}{2}\langle n|t^2|n\rangle$$
$$= (T-1)/2 \qquad (10c)$$

$$\langle nA|\vec{t}\cdot\vec{T}|pC\rangle = \frac{1}{2}((2T)^{1/2}\langle T_>| - \langle T_<|)T_t^2$$

$$(|T_>\rangle + (2T)^{1/2}|T_<\rangle) - \frac{1}{2}\langle A|T^2|C\rangle - \frac{1}{2}\langle n|t^2|p\rangle = (T/2)^{1/2} \qquad (10d)$$

Collecting the results of equations (8) or (10) and combining them with the trivial results for the $\langle U_0 \rangle$ matrix elements, the complete potentials become:

$$U_{pC} = U_0 - 2TU_1/A \tag{11a}$$

$$U_{nC} = U_0 + 2TU_1/A \tag{11b}$$

$$U_{nA} = U_0 + 2(T - 1)U_1/A \tag{11c}$$

$$U_{pn} = 2(2T)^{1/2}U_1/A \tag{11d}$$

It is important to remember that each of the above U's is complex, i.e., $U = V + iW$, implying two equations for each U: $V_{pC} = V_0 + 2TV_1/A$ and $W_{pC} = W_0 + 2TW_1/A$, etc.

Sometimes it is necessary to express the potentials in a form based on $U_< \equiv \langle T_< | U | T_< \rangle$ and $U_> \equiv \langle T_> | U | T_> \rangle$. Using equations (5) and $U = U_0 + 4(\vec{t} \cdot \vec{T})U_1/A$, these expressions can be transformed into the nucleon-nucleus form used above and evaluated in a straightforward fashion from the previous results. We obtain:

$$U_< = U_0 - 2U_1(T + 1)/A \tag{12a}$$

$$U_> = U_0 + 2U_1T/A \ . \tag{12b}$$

Schrödinger Equations

Our next step is to develop the Hamiltonian and Schrödinger equation into which these potentials are inserted. For the Hamiltonian, to our deliberately charge-independent potential $U = U_0 + 4(\vec{t} \cdot \vec{T})U_1/A$ we must add at least the obvious coulomb effects of the proton-nucleus

electrostatic potential $U_c = V_c$ and the target-analog state coulomb displacement energy $\Delta_c = -Q$. We include the electrostatic potential as $(\frac{1}{2} - t_3)U_c$, which is thus automatically zero for neutron projectiles. The coulomb energy is inserted by writing the internal nuclear Hamiltonian H_0 as either H_C or H_A for target or analog states; note that $H_A = H_C + \Delta_c$. We therefore write

$$H = H_0 + K + U + (\tfrac{1}{2} - t_3)U_c.$$

The Schrödinger equation is written $H\psi = E_{tot}\psi$, where E_{tot} is the total energy of the nucleon-nucleus system. Equivalent scattering processes are considered to be those which are described by the same total energy. Here ψ must describe the particular system involved. For the C(p,n)A and C(p,p)C reactions, the U_{pn} coupling term requires that the states involved be of the form

$$\psi = \chi_{pC}(r)|pC\rangle + \chi_{nA}(r)|nA\rangle,$$

since $|pC\rangle$ and $|nA\rangle$ states are mixed by $\vec{t} \cdot \vec{T}$. We explicitly separate out the isospin dependence into the kets. For the C(n,n)C reaction, no coupling exists to other processes, and we write only:

$$\psi = \chi_{nC}(r)|nC\rangle.$$

The equations for the distorted waves $\chi(r)$ are obtained by operating with $(H - E_{tot})$ on the above wavefunctions ψ, then summing over the isospin variables to project out the χ_{pC}, χ_{nA}, and χ_{nC} waves. For the (p,n) and (p,p) reactions, projecting out the $\langle pC|$ and $\langle nA|$ equations in turn gives:

$$(E_C + K + U_c + U_{pC})\chi_{pC}(r) + U_{pn}\chi_{nA}(r) = E_{tot}\chi_{pC}(r)$$

$$(E_A + K \quad + U_{nA})\chi_{nA}(r) + U_{pn}\chi_{pC}(r) = E_{tot}\chi_{nC}(r)$$

For the C(n,n)C reaction we obtain:

$$(E_C + K \quad + U_{nC})\chi_{nC}(r) = E_{tot}\chi_{nC}(r)$$

Remember that the total energy may be written as $E_{tot} = E_0 + E_{rel}$, where E_{rel} describes the relative nucleon-nucleus motion (E_{pC}, E_{nA}, or E_{nC}) and $H_0\psi = E_0\psi$ defines E_0 as the internal nuclear energy E_C or E_A. Then $E_C - E_{tot} = -E_{pC}$ and $E_A - E_{tot} = -E_{nA}$, so our equations become:

$$(K + U_c + U_{pC} - E_{pC})\chi_{pC}(r) = -U_{pn}\chi_{nA}(r)$$

$$(K \quad + U_{nA} - E_{nA})\chi_{nA}(r) = -U_{pn}\chi_{pC}(r)$$

$$(K \quad + U_{nC} - E_{nC})\chi_{nC}(r) = 0.$$

The relation between the bombarding energies for the same total energy can be obtained as follows. In the reaction C(p,n)A, we clearly have $E_{nA} = E_{pC} + Q = E_{pC} - \Delta_c$ by time reversal or by straightforward energy conservation. As the incident proton approaches the nucleus, kinetic energy is transformed to coulomb potential energy. In the (p,n) reaction, the proton has lost exactly the coulomb energy needed to provide the difference in coulomb displacement energies between the target and its analog, plus the neutron-proton mass difference. It is thus required that the outgoing neutron energy be $E_n = E_p + Q = E_p - \Delta_c$,

since this gives exactly the energy needed to form the (n + A) final state from the (p + C) initial state.

To understand the connection between E_{nC} and the energies E_{pC} and E_{nA}, we first look at the (n+C) and (n+A) scattering systems. We are concerned with scattering from nuclear states whose energies differ by Δ_c, implying $E_{nC} = E_{nA} + \Delta_c$ in order to scatter from the same states. However, for C(p,p)C and C(n,n)C we must have the same E_p and E_n to scatter from the same target nuclear states, so $E_{pC} = E_{nC}$. We therefore obtain equivalent scattering for the bombarding energies:

$$E_{pC},$$
$$E_{nA} = E_{pC} - \Delta_c, \text{ and}$$
$$E_{nC} = E_{pC}.$$

We thus write the final form of the optical model equations as:

$$(U_c + K + U_0 - 2TU_1/A - E_{pC})\chi_{pC}(r) = -2(2T)^{1/2}U_1/A\chi_{nA}(r)$$

$$(\quad K + U_0 + 2(T-1)U_1/A + \Delta_c - E_{pC})\chi_{nA}(r) = -2(2T)^{1/2}U_1/A\chi_{pC}(r)$$

$$(\quad K + U_0 + 2TU_1/A - E_{pC})\chi_{nC}(r) = 0.$$

Coulomb Corrections

The above discussion of coulomb effects deals with reasonably straightforward energy conservation. However, there is a more subtle effect which the coulomb interaction has on our model of the reaction. To understand why, first picture the nuclear force with the coulomb interaction turned off. The specifically nuclear optical model is

believed to be non-local, or at least, the formal justification of the model involves a summation of two-body forces, the result being a non-local potential. One of the consequences of converting this "true" non-local potential to its local equivalent is the introduction of a momentum or energy dependence. This result can be viewed as a statement that the model behaves differently at different bombarding energies, even apart from the simple kinematic effects expected from scattering theory. In the absence of the coulomb interaction, the initial and final kinetic energies are the same, so the additional momentum dependence does not further complicate the incoming and outgoing potentials. However, if we include the effects of the coulomb interaction, it is no longer sufficient to simply add in a coulomb potential and coulomb displacement energies--these are only the first-order effects. As we have seen, the coulomb displacement energies result in different kinetic energies for the incoming and outgoing particles, therefore changing the behavior of the scattering because of the momentum dependence. A simple viewpoint is to say that the incoming proton is slowed down, and thus it experiences the optical potential for a lower energy nucleon.

This argument suggests that here we have yet another coulomb effect in proton scattering, one which is intimately connected with the coulomb repulsion of the proton and the energy dependence of the optical potential. This effect is the basis of the optical model coulomb correction term ΔV_c (not to be confused with the coulomb displacement energy Δ_c).

We must now estimate the magnitude of such a correction and discuss how it is to be made. One of the earliest attempts to deal with this pro-

blem is the coulomb correction term in the global proton optical model of Perey (1963). Basically, if the nuclear optical potential is non-local and hence momentum-dependent, we may write the specifically nuclear potential V_m as

$$V_m = -V_{mo} + \alpha K.$$

We have separated the potential into momentum-independent (V_{mo}) and -dependent (αK) parts, where the dependence is assumed proportional to K, the kinetic energy of the projectile. Inside the nucleus, K is related to the bombarding energy E by $E = K + V_m + V_c$, where V_c is the coulomb potential. Combining these two equations, we obtain

$$V_m = -\frac{V_{om}}{(1+\alpha)} + \left(\frac{\alpha}{1+\alpha}\right)(E - V_c)$$

$$= -\frac{V_{om}}{(1+\alpha)} + \left(\frac{\alpha}{1+\alpha}\right)E - \left(\frac{\alpha}{1+\alpha}\right)V_c$$

We have written the equation for V_m in these two ways to emphasize that the coulomb correction may be made either by substituting $E' = E - V_c$ for E in the local optical model, or by adding to the potential another term with the same coefficient as the energy-dependent term.

This latter approach, the potential correction term, can be further expanded. Since the radial dependence of the coulomb potential is small over the nuclear volume, we may replace V_c with its average value $\overline{V}_c = 1.73Z/R_c$, where $R_c = r_c A^{1/3}$. Further, if we assume an energy dependence of 0.3E and $r_c = 1.25$ fm, as is typical in global analyses, we obtain $\alpha/(1 + \alpha) = 0.3$ and $(\alpha/(1 + \alpha)\overline{V}_c \cong 0.4Z/A^{1/3}$, the usual form of ΔV_c. We emphasize that momentum dependence of the optical potential

implies both an energy-dependent term and a related coulomb correction. This coulomb correction is then viewed as another consequence of converting the "true" non-local optical potential into a local form. Further, we may include the correction either by shifting the neutron and proton kinetic energies by $\overline{V}_c$, the average coulomb potential, or by adding a term of the order of $0.4Z/A^{1/3}$ to the proton potential. An attempt was made to evaluate these two approaches by Ferrer, Carlson, and Rapaport (1976) in the fitting of (n,n) and (p,p) data for five nuclei at E_n = 11.0 MeV. Their conclusions were that the methods were visually indistinguishable and somewhat insensitive to the size of the $Z/A^{1/3}$ term. Accordingly, we chose to correct the proton potential U_{pC} relative to both neutron potentials U_{nC} and U_{nA} simultaneously. We therefore write:

$$U_{pC} = U_0 - 2TU_1/A + U_c - \Delta V_c$$
$$U_{nC} = U_0 + 2TU_1/A.$$

This formulation emphasizes that the coulomb correction is explicitly added when employing the isospin potential framework; it is not to be included in the U_0 or U_1 terms.

2. LITERATURE SURVEY

Introduction

We now summarize the approach described above. Our basic concept was the division of the nucleon-nucleus potential into isospin-conserving strong interactions and nonconserving coulomb interactions. We then dealt with the coulomb effects as corrections to a strictly isospin-conserving Lane potential formalism. With the outline of our approach laid out, this viewpoint can be used to organize and evaluate other analyses. Generally, little can be learned from areas of agreement; it is the disagreements and difficulties that are most interesting. After considerable distillation and rearrangement of concepts in some fifty articles, the following half-dozen interrelated issues emerge.

DWBA versus Coupled Channels Approaches

Some early analyses calculated the (p,n) cross section using optical model potentials from previous analyses of proton and neutron elastic scattering. The usual approach, as by Drisko, Bassel, and Satchler (1962), involved use of the DWBA with distorted waves generated from the proton and neutron potentials, with the coupling term U_{pn} treated as a perturbation. A detailed discussion of the method is given by Satchler, Drisko, and Bassel (1964). For the DWBA to be successful, there are three criteria (Schery et al., 1974): (1) the reaction must be direct; (2) the spatial and spin coordinates of the target and analog states must be the

the same; and (3) the charge-exchange (p,n) reaction must be weak enough to be treated as a perturbation.

For the first point, Erramuspe (1967) pointed out that compound elastic scattering should be no problem at several MeV above the threshold for the (p,n) reaction to the analog state, a preferred channel for compound nucleus de-excitation. This point was discussed more recently by Hoffman and Coker (1974). Further, the prominence of the isobasic analog state neutron group in (p,n) spectra gives a measure of the relative weakness of "quasi-inelastic" (p,n') scattering from odd-mass targets (Satchler, Drisko, and Bassel, 1964). In summary, although the contribution of compound nuclear effects should be considered in individual cases, it does not seem to be a general problem.

The second point, the validity of the target-analog state isospin description, goes straight to the heart of the Lane model, which a priori assumes that these states are different only in isospin coordinates $T_3 = T$ and $T_3 = T_0 - 1$. The weakness of this assumption is simply that isospin may not be a good quantum number, since different states are mixed by the symmetry-breaking coulomb interaction. Anderson et al. (1964) estimated that this treatment should be valid for $E_p > 2\Delta_c$, and Lane and Soper (1962) stated that isospin purity should be good to less than a few percent below $A = 40$.

Finally, we come to the third criticism, one which concerns the convergence of DWBA. Using typical values of $(N-Z) \cong 0.006A^{5/3}$ (Evans, 1955) and $U_1/U_0 \cong 0.5$, the ratio R of the $(2\sqrt{N-Z}\, U_1/A)$ coupling term to the $(U_0 \pm (N-Z)U_1/A)$ distorted wave potential is given by the expression

$R \cong 0.077A^{-1/6}(1 \pm 0.003A^{2/3}) \cong 0.077A^{-1/6}$, so the DWBA approach should be reasonable for $A > 40$ ($R < 4\%$), although Wong et al. (1973) report some problems for $A = 51$.

Because of the growing importance of the Lane optical model, Schwarcz (1966) developed a method for exact solution of the coupled equations. He reported that for $A = 51$ the proportionality of the magnitude of $\sigma_{pn}(\theta)$ to U_1^2 in DWBA was valid to within 6-8% and that the angular distribution shapes were quite similar, especially for a surface-peaked U_1 form factor. Our conclusion is that the DWBA approach seems adequate for all but light nuclei unless a very precise analysis is desired.

A more subtle problem in using the DWBA for the coupling between the (p,n) and (p,p) reactions involves self-consistency of the potentials, as mentioned by Carlson, Zafiratos, and Lind (1975) and Patterson, Doering, and Galonsky (1976). This problem results from using elastic scattering potentials from (p,p) models without an explicit outgoing neutron channel. Their use in a model which includes such a channel may lead to some irregularities, especially in the absorptive potential. This situation is similar to the relationship between a spherical optical model and a deformed optical model using a coupled channel approach.

Lane Model Consistency

A second difficulty with the use of proton and neutron elastic scattering potentials is that many are not written in a form which allows easy separation of isospin-independent U_0 and isospin-dependent U_1

parts. Improper separation often leads to a different lack of self-consistency, a contradiction of the isospin conservation of the Lane model. An excellent example of this problem is given in an analysis by Wong et al. (1972) which attempted to describe (p,n) data using the proton and neutron elastic scattering potentials of Becchetti and Greenlees (1969), listed in Table 2. Since U_{pC} ($=U_p$) and U_{nC} ($=U_n$) can be separated as $U_0 \pm (N-Z)U_1/(4A)$ (+ for protons, - for neutrons), it is tempting to identify V_1 = 24.0 MeV and W_1 = 12.0 MeV from Table 2, as done by Wong et al. Close examination, however, reveals several ambiguities, particularly in the different geometrical factors. The usual solution, which was used by Wong et al., has been to average the geometry over both potentials despite the objection that such differences would not have been included unnecessarily in the original analysis. This approach was strongly critized by Cotanch and Robson (1973) and Hoffman (1973), the former suggesting a completely different representation, the latter recommending a forced isospin symmetry of the potentials for neutrons and protons (minus coulomb corrections). Although this approach seems reasonable, it is possible that the symmetry potential and the coulomb correction, which vary in the same manner across the periodic table (Sood, 1966), were not separated properly. This problem led Hoffman and Coker (1974) to put the entire neutron and proton potentials, including the coulomb correction, into the Lane model transformations, their only separation being into real and imaginary parts. We again emphasize these two problems, the inconsistent geometry of the Becchetti-Greenlees potentials and the difficulty of separating out the U_0, U_1, and coulomb parts. These difficulties introduce an important problem in most of the Lane model analyses:

TABLE 2

BECCHETTI-GREENLEES OPTICAL POTENTIAL

$U = V + iW$; V has a volume (Woods-Saxon) shape

W^V has a volume (Woods-Saxon) shape

W^S has a surface (Woods-Saxon derivative) shape

E is bombarding energy (lab) in MeV

Incident Protons	Incident Neutrons
$U_p = V_p + iW_p$	$U_n = V_n + iW_n$
$V_p = 54.0 - 0.32E + 24.0(N-Z)/A + 0.4Z/A^{1/3}$ MeV	$V_n = 56.3 - 0.32E - 24.0(N-Z)/A$ MeV

$$r_p = r_n = 1.17 \text{ fm}$$

$$a_p = a_n = 0.75 \text{ fm}$$

$W_p^V = -2.7 + 0.22E$ MeV	$W_n^V = -1.56 + 0.22E$ MeV
$W_p^S = 11.8 - 0.25E + 12.0(N-Z)/A$ MeV	$W_n^S = 13.0 - 0.25E - 12.0(N-Z)/A$ MeV
$r_p^i = 1.32$ fm	$r_n^i = 1.26$ fm
$a_p^i = 0.51 + 0.7(N-Z)/A$ fm	$a_n^i = 0.58$ fm

$$V_p^{so} = V_n^{so} = 6.2 \text{ MeV}$$

$$r_p^{so} = r_n^{so} = 1.0. \text{ fm}$$

$$a_p^{so} = a_n^{so} = 0.75 \text{ fm}$$

the interconnection between the type of data, the potential representation, and the isospin-conserving transformation equations. We now discuss these problems in some detail.

As we have explained, the reaction representation of the isospin states allows us to describe (p,p), (p,n), and (n,n) reactions with any of several potential forms which are connected by the Lane formalism and our systematic coulomb corrections. It is assumed that these representations may in principle be equivalent, although they are certainly not equally convenient. There is marked preference for a representation that connects directly to the data being analyzed, e.g., (U_p,U_n) for (p,p) and (n,n) elastic scattering or (U_p, U_1) for (p,p) and (p,n) reactions. By reducing the coupling between sets of parameters, this approach not only makes interpretation more straightforward, but also helps to reduce the number of simultaneous variables needed in search routines. For example, in analyzing (p,p) and (n,n) scattering data, the proton parameters affect the neutron predictions only indirectly, and vice versa. In the (U_0,U_1) representation, however, all parameters have essentially the same effects on both elastic scattering distributions.

Form Factors

When trying to describe the three different reactions (p,p), (p,n), and (n,n), the data and representation are not so closely linked, leading to consideration of other reasons for choosing a particular representation. Returning to the inconsistent geometries in the Becchetti-Greenlees potential, it is possible that there are physical reasons to prefer one representation over another. To understand such preferences, one must appreci-

ate that the transformations are linear combinations of form factors, i.e., both strengths and shapes. For example, if the original Becchetti-Greenlees imaginary Woods-Saxon derivative potentials W_p and W_n are transformed into the "equivalent" W_0 and W_1, the results will generally have very complicated shapes, as shown by Hoffman (1973). As suggested by Becchetti and Greenlees, the different neutron and proton geometries may be the result of using inappropriate form factors which are then forced to mock up the difference between the potential geometries seen by incoming protons and neutrons caused by differences between the average density distributions for protons and neutrons in nuclear matter. If so, use of a simple form factor in one representation may prevent the potential from describing a physically meaningful shape, and it is important to explore the arguments for the expected shapes of the U_0 and U_1 form factors.

The two extremes of V_1 shapes have been volume V_1^v and surface-peaked V_1^s. In principal, the same scattering can be obtained from equivalent surface and volume form factors. A possible guide to such a relationship uses the connection between a Woods-Saxon distribution $f(r_1,a_1)$ and its derivative, combined with assumed $V_1^v(r_1A^{1/3})^n$ ambiguities for a volume potential. The result, discussed by Satchler, Drisko, and Bassel (1964) is $V_1^s = V_1^v r_1 A^{1/3}/(na)$.

In their global analysis of neutron data, Becchetti and Greenlees obtained better agreement using a surface-peaked symmetry potential V_1. In fact, in every case where a comparison has been made of surface and volume form factors for V_1, the preference has been for either surface or surface-plus-volume; therefore, considerable evidence supports the

surface-peaked interaction. The most compelling reasons, however, are found in an article by Terasawa and Satchler (1963) and in the microscopic calculations of Anderson et al. (1969) and Hoffman and Coker (1974). For neutron-rich targets, the first article showed that only if the neutron and proton radial density distributions were the same could there be no surface peaking; at the other extreme, if the core densities for neutrons and protons were the same, then pure surface peaking resulted. Their conclusions supported an intermediate case. Anderson et al. obtained a direct reaction form factor which was closely described by a combined surface and volume optical model potential, and the results of Hoffman and Coker also generally suggested similar admixtures. Since the formal basis of the optical model rests on such microscopic approaches, it is clear that whatever representation is used for a Lane potential, the resulting V_{pn} should be somewhat surface-peaked.

This result then gives us a reason to select one representation over another. In the (U_0,U_1) representation, this surface-peaking can be parameterized directly by using a Woods-Saxon derivative form for V_1. The other approach, the (U_p,U_n) form, requires more complicated adjustments of both strengths and geometries for both V_p and V_n. Further, since the (p,n) distributions are generally more sensitive than the elastic ones (Hodgson and Rook, 1962), especially to the surface region (Satchler, Drisko, and Bassel, 1964), any calculation attempting to describe (p,n) data should be more successful using the (U_0,U_1) representation, which effectively divides the potential into elastic and charge-exchange parts. Since the majority of the (U_p,U_n) analyses use equal geometries, we see

that their control of the crucial surface behavior is only through the strengths of the imaginary potentials.

Coulomb Corrections

We have tried to present the coulomb effects in a fashion as logical and self-consistent as possible. Let us review our position up to here. We emphasize that the coulomb displacement energy Δ_c and the proton coulomb correction ΔV_c are different effects. Simple energy conservation for C(p,n)A reactions requires $E_{tot} = E_C + E_{pC} = E_A + E_{nA}$, and the coulomb displacement energy requires $E_C = E_A - \Delta_c$. Combining these two requirements demands $E_{nA} = E_{pC} - \Delta_c = E_{pC} + Q$. On the other hand, ΔV_c results from an interplay between optical model non-locality and the different kinetic energies for incoming neutrons and protons. We have also shown that E_{nA} and E_{nC} are not to be confused and have attempted to give some idea of the relationship between them.

We now compare our approach to those in the literature. It is standard to compare neutron and proton elastic scattering at the energies $E_{nC} = E_{pC} - \Delta_c$, and several cases (Carlson, Zafiratos, and Lind (1975), Lovas (1976), and Bangert et al. (1977), to name a few) also leave $\Delta V_c \cong 0.4Z/A^{1/3}$ in the proton potential, thereby "correcting" twice.

It is thus important to again delineate the formal connection between the energies E_{nC} and E_{pC}. Consider again scattering from an "uncharged" momentum-dependent nuclear potential $V_m(E_m)$. To obtain the same scattering when we turn on repulsive coulomb effects, we showed that this resulting "charged" V_q must be evaluated at a higher energy, i.e.,

$$V_m(E_m) \sim V_q(E_m + \overline{V}_c).$$

Defining this energy as $E_q \equiv E_m + \overline{V}_c$, we now rewrite our relation above as

$$V_m(E_q - \overline{V}_c) \sim V_q(E_q).$$

There are two different approximations which can be made next. Since $\overline{V}_c$, the average coulomb potential energy per charge, is approximately equal to Δ_c, the coulomb displacement energy between target and analog states, we may write

$$V_m(E_q - \overline{V}_c) \sim V_m(E_q - \Delta_c),$$

which explains the energy-shift method of applying the coulomb correction, since we now have

$$V_q(E_q) \sim V_m(E_q - \Delta_c).$$

However, we may also expand $V_m(E_q - \overline{V}_c)$ as

$$V_m(E_q - \overline{V}_c) \cong V_m(E_q) - (\partial V_q / \partial E_q)\overline{V}_c = V_m(E_q) + \Delta V_c,$$

thus obtaining the proton potential correction method, since

$$V_q(E_q) \sim V_m(E_q) + \Delta V_c .$$

Clearly, however, it is incorrect to include the coulomb correction term in the proton potential and to then also apply an energy shift between the E_{nC} and E_{pC} comparisons. It is also important to keep in mind the assumptions and approximations involved and to remember that values of ΔV_c

are quite uncertain and probably not constant from nucleus to nucleus (Satchler, 1969). Becchetti and Greenlees give two estimates of ΔV_c, either $\Delta V_c = 0.27Z/A^{1/3}$ or $0.4Z/A^{1/3}$. Further, one of their parameterizations used an effective proton energy $E_p' = E_p + 0.84Z/A^{1/3}$, possibly implying a relation $V_p(E) - 0.4Z/A^{1/3} \approx V_p(E + 0.84Z/A^{1/3})$. A recent article by Rapaport (1977) reports values for ΔV_c ranging from 0.4 to 0.8 times $Z/A^{1/3}$. Although the preliminary results of that article support the approach used in this work, it appears that there may be some unresolved questions about the ability of any simple coulomb correction to handle all effects.

Data Correlation

The next area of discussion involves the correlation by the Lane model of the three usual types of data: (p,p), (n,n), and (p,n) cross sections. The assumption is that all three may be described by the same two-part potential, although only recently has this test actually been made. The first attempts, e.g., those of Satchler (1967) or Erramuspe (1967), sought only to correlate (n,n) and (p,p) data and met with fair success. Such studies were not sensitive tests, however, since the U_1 part of the potential, as discussed above, is only a very small correction to the U_p or U_n potentials in the mass region ($A > 40$) of such tests. Several DWBA studies, notably Satchler, Drisko, and Bassel (1964), were made using modified Becchetti-Greenlees proton potentials as the starting point in (p,n) calculations; these established that reasonable descriptions of both (p,p) and (p,n) data could be obtained. The precision of these tests was limited,

however, by the factors we have previously noted for DWBA.

The first attempt to fit two of the three types of data and then predict the third was made by Schery et al. (1974), and further studies were made by Carlson, Zafiratos, and Lind (1975) and Patterson, Doering, and Galonsky (1976). In the latter two cases, (p,n) data were analyzed in models which included modified Becchetti-Greenlees proton parameters instead of proton data. Unfortunately, in all three cases reliance on the B-G potentials led the authors to assume volume V_1 form factors. Nevertheless, the latter two analyses obtained reasonable (n,n) scattering predictions, considering the precision allowed in using the B-G proton predictions instead of actual proton data. Surprisingly, when Schery et al. attempted to improve their (n,n) prediction by including proton data and searching on the proton potential, their neutron predictions deteriorated. Their conclusion was thus that a good description of (p,p) and (p,n) data did not uniquely determine the Lane potential and would not guarantee a good prediction of (n,n) data.

This behavior was further investigated by Lovas (1976), who used simultaneous searches on both the (p,p) - (p,n) and (p,p) - (n,n) data sets in attempts to predict the third. In both cases, refining the fit to the two data sets that were included worsened the prediction of the omitted one. The conclusion made was that the potentials were mutually exclusive and a self-consistent Lane model could not be found--a strong statement which would require the support of an unquestionable analysis.

We see above that several analyses have been unable to describe all three sets of data simultaneously. It is important to determine if this

failure is a problem in the Lane model or a problem in its application.

There are several deficiencies in the above analyses. First, no analysis allowed a surface-peaked (p,n) interaction. Second, all three analyses appear to have mishandled the coulomb correction to some degree, which could be a serious problem for high-Z targets. These two criticisms alone preclude a conclusion that the Lane approach itself is at fault.

However, there is a problem which might have further limited the success of the above analyses. Note that in no case has a thorough attempt been made to simultaneously describe all three reactions. This problem may be aggravated by the heavy reliance on the B-G potential, which may involve more subtle problems than simply eliminating a surface form factor for V_1. In obtaining such global parameters, extensive use is made of constant-volume-integral ambiguities to obtain smooth behavior. It is possible that such freedom does not exist when including (p,n) constraints, and hence an analysis based on the B-G parameters may not be able to describe the more sensitive charge-exchange data. If so, a more complete parameter search may be needed with greater freedon for form factor geometries. Further, if such an extensive search is to succeed in properly trading off between the twenty-three or so parameters in the Lane potential, we may need simultaneous fitting of all three types of cross-section data and any available polarization data.

Optical Model Limitations

Finally, there are some common difficulties with any optical model which are expected to be more severe because of the higher sensitivity and lower magnitude of the (p,n) reaction, especially for the very light nuclei used in this study. We expect compound and resonance effects to become evident at lower energies, approximately <10 MeV. As pointed out by Watson, Singh, and Segel (1969), the assumption that nuclear radii scale as $A^{1/3}$ may be poor when there are so few nucleons that their discrete nature becomes apparent and affects the energy and A-dependence of geometries. The level density at low A is usually such that the imaginary potentials may behave erratically with energy as particular exit channels open. Finally, quadrupole deformation may become apparent and $\ell \neq 0$ transfer may seriously limit the applicability of the spherical optical model, as suggested in Carlson's analysis.

Summary

We conclude this section with a summary of the problems observed in the literature. First, results of analyses using DWBA should be carefully evaluated, since only general features are accurate, and then only for medium to heavy nuclei. Second, many analyses are flawed in their handling of isospin conservation. Although strict isospin conservation is probably unnecessary, the analysis should not be so inconsistent that the character of the symmetry potential cannot be extracted from the results. Third, analyses which do not allow enough flexibility in the form factors, whatever their representation, to produce some degree of surface peaking are in

conflict with basic physical reasoning and considerable previous experience. Fourth, attempts to determine the potential with search procedures which are careless about parameter restrictions or include limited data are likely to produce only good agreement between theory and data. Such analyses may not provide the sensitivity needed to answer detailed questions. Finally, carelessness with the distinction between the coulomb displacement energy Δ_c of target and analog states and the coulomb correction ΔV_c for the momentum dependence of the optical model may also prevent detailed investigation of the results.

B. APPLICATION OF THE LANE OPTICAL MODEL

1. TWAVE3 COMPUTER PROGRAM

Overview

The computer code TWAVE3 is a modification of the code TWAVE written by S. Cotanch (Cotanch, 1973) and initially modified for TUNL by S. Datta. The basic calculation is a solution of the coupled equations obtained by introduction of the Lane model constraints into the optical potential. Particular attention has been given to the issues discussed in the sections above on form factors, potential representations, and coulomb corrections.

The format of the calculation can be chosen as either excitation function or angular distribution, over any specified range of energies or angles in either lab or center-of-mass coordinates. Input is formatted so that the operation of the code is flexible without requiring extensive rearrangement or modification of data decks. Output is provided in both tabular and graphical form to allow rapid evaluation of sensitivities and results. In short, the operation of the code is now both powerful and flexible without being unnecessarily inconvenient.

Potential

Since considerable effort was made to investigate the assumptions outlined in the potential and equation derivations above, the features of

the code which concern the potential and search will be discussed in some detail here. We first present the options for the optical potential; we will handle the search in a later section.

Specification of the potential involves several special features. First, a unique subroutine converts from any of the representations discussed above into the (U_{pC}, U_{nA}, U_{pn}) form in which the equations are actually solved. Specifically, the potential representations available are (U_{pC}, U_{nA}), (U_{pC}, U_{nC}), (U_{pC}, U_1), (U_0,U_1), ($U_<$, $U_>$), and (V_0,V_1,$W_<$,$W_>$). This conversion is not simply a recalculation of the strengths, but a point-by-point transformation as the radial form of the potential is evaluated, thus including all the implications of the different form factors. Second, the effects of different form factor parameterizations can be investigated, since options are available for Woods-Saxon surface derivative or gaussian W, Woods-Saxon volume or surface V_1, and either standard or Watson (see Watson, Singh, and Segel, 1969) surface derivative V_{so}. Third, the coulomb correction can be applied either as an additional term in the proton potential or as an energy shift $E_n = E_p - Q$ in the incident beam, or both. Finally, any term p in the potential strength or geometry may be entered in the explicitly energy-dependent parameterized form $p = a + bE + c(N-Z)/A + dZ/A^{1/3}$, where E is either the lab or center-of-mass energy. This feature, i.e. the bE term, is useful in evaluating energy dependences of various parameters.

Observables

The observables calculated by the program are cross sections and polarizations for the reactions C(p,p)C, C(p,n)A, and C(n,n)C. These

calculations are slightly different in our case than for normal elastic scattering, because the coupled equations will give both scattered proton and neutron waves for incident protons. We must therefore rewrite the normal optical model equation for ψ_{scat} in terms of two scattering amplitudes $f_n(\theta)$ and $f_p(\theta)$:

$$f_n(\theta) = A_n(\theta) + B_n(\theta)\vec{\sigma} \cdot \hat{n}$$
$$f_p(\theta) = A_p(\theta) + B_p(\theta)\vec{\sigma} \cdot \hat{n}$$

where $\vec{\sigma}$ is the usual Pauli spin operator and $\hat{n}$ is the unit normal to the scattering plane, defined in accordance with the Madison convention.

The cross section is written in the usual way (McCarthy, 1968) as

$$\sigma(\theta) = [\, f_N(\theta)\chi_{inc}]^{\dagger}[\, f_N(\theta)\chi_{inc}] = |A_N|^2 + |B_N|^2 + (A_N^* B_N + A_N B_N^*)\hat{n} \cdot \vec{P}_b ,$$

where N may be either p (proton) for elastic scattering or n (neutron) for charge-exchange scattering, and $\vec{P}_b$ is the incident beam polarization.

Similarly, the quantity $\vec{P}(\theta)$ observed in our polarization measurements would be

$$\vec{P}_N(\theta) = P_N(\theta)\hat{n} = [\, (A_N^* B_N + A_N B_N^*)/\sigma_N(\theta)]\hat{n} ,$$

where $\sigma_N(\theta) = |A_N|^2 + |B_N|^2$ since $\vec{P}_b = 0$ for measurements of $\vec{P}_N(\theta)$.

From the full equation for $\sigma_N(\theta)$ we may also calculate an analyzing power $A(\theta)$ from the difference between $\sigma_N(\theta)$ for $\vec{P}_b$ parallel and antiparellel to $\hat{n}$:

$$A_N(\theta) = (A_N^* B_N + A_N B_N^*)/\sigma_N(\theta),$$

which is identical to the magnitude of $P_N(\theta)$. We therefore cannot

explain differences between $P_N(\theta)$ and $A_N(\theta)$ with this type of model.

Data Sets

With the program TWAVE3 we are able to calculate each of the quantities $\sigma_{pp}(\theta)$, $\sigma_{nn}(\theta)$, $\sigma_{pn}(\theta)$, $A_{pp}(\theta)$, and $A_{pn}(\theta)$ (among others), all simultaneously predicted by a single potential. The code is written to display the results of these calculations along with data for each.

We are now in position to discuss the search options associated with TWAVE3. Data sets of any of the above types are entered along with an error for each, either percentage or absolute. If desired, any set can also be marked for renormalization in the chi-square (χ^2) calculation. The search calculation is basically a reiterative χ^2 minimization, with the figure of merit χ^2_{tot} defined as

$$\chi^2_{tot} = \sum_k (1/N_k) \sum_n (t_{ik} - x_{ik})^2/\Delta x^2_{ik},$$

where the sums are over the i^{th} data point and the k^{th} observable. Note that the χ^2 is a sum of the χ^2 per point values of all distributions included.

This type of weighting introduces some complexities into the fitting procedure, as discussed by Becchetti and Greenlees. For example, the (p,p) data is usually of much higher statistical quality than the (p,n) or (n,n) data, giving the χ^2 for the proton elastic data much higher statistical weight. Often the objective χ^2 and subjective visual evaluation of a search can be quite different. It is thus frequently necessary to adjust the size of errors assigned to the various distributions to

insure that the optimization is aimed at the desired features. This behavior was taken into account by making it convenient to adjust the relative weights of the various distributions.

ROCORD Search Routine

To explain further the results of the search we must look in some detail at the behavior of the search program itself. Rocord is a non-linear search routine based on the Rosenbrock (1960) rotating-coordinate search method. The basic input parameters are an n-dimensional parameter vector P, the corresponding range vector R, and a percentage accuracy (grid or step size) s. The search is organized into sets of trials, called stages, along each dimension, each determining the displacement d_i of the minimum along each axis. The set of n stages along all axes is then called an iteration.

The search pattern of a stage involves increasingly larger steps in powers of s in order to encounter either the boundary specified by R or an increase in chi-square. In the case of a boundary, the range vector R is shifted by a multiple of s and the stage is terminated. If chi-square has increased, the search direction is reversed with the step size reset to s. When the minimum has been bracketed by three trials, a parabola is calculated and the minimum chi-square, best displacement, and steepness of descent are estimated. If the estimated minimum offers substantial improvement or the steepness is great enough to make the location of the minimum uncertain, another trial is made with the estimated displacement; the final result d_i will be the better of this result and

the previous one. On the other hand, if such a trial is not crucial, the final displacement d_i is taken to be the estimated value. The search then proceeds to the next stage.

After all n stages, an iteration is complete and a set of n displacements has been obtained. From the previous P vector and rotation matrix A, the d vector is used to calculate a new matrix A. If any stage of the iteration located the minimum outside of an accuracy s of the previous iteration's best value, another iteration is begun. If all stages required displacements less than s, the search is terminated as successful and a number of random coordinate rotations are generated to confirm the minimum.

It was felt that the expense of each optical model calculation was such that every effort should be made to obtain the best estimates possible. In general, if the shape of the fit was essentially similar to that of the data, reductions in chi-square to within 50% of the final value were obtained in two iterations. On the other hand, the complexity of the surface involved (up to 17 parameters) favored a generally conservative code. The boundary constraints usually guaranteed that no one parameter would be greatly altered until its correlations to the others had been established. Very rarely would the routine "blow up" and produce a completely worthless fit.

Considerable effort was made to give as much diagnostic information as possible about the behavior of the surface being investigated. In particular, the parabola-fitting routine provides estimates for each parameter of range and sharpness, which are very useful in selecting

parameters requiring further optimization and the ranges over which they should be varied.

2. ^{9}Be LANE MODEL ANALYSIS

Reasons for Limitation to ^{9}Be

With our theoretical approach determined and the resulting code written, there were several reasons to restrict the analysis to the ^{9}Be target reactions. Most obviously, the resonance structure observed in the $^{15}N(p,n_0)^{15}O$ excitation function invalidated the direct nature of the optical model analysis. Furthermore, for reasons explained below, a meaningful Lane model analysis required the inclusion of both (p,p) and (n,n) elastic scattering data, neither of which were available for ^{15}N.

On the other hand, several aspects of the $^{9}Be(p,n_0)^{9}B$ analysis were appealing. First, our 0° excitation function was quite well-behaved at energies above approximately 11 MeV, and the angular distributions possess a distinct direct reaction diffraction signature. Second, other data in the energy region of our (p,n_0) data were plentiful and of high quality. Notably, many of the (n,n) and (p,p) data sets were obtained at this laboratory. Further, several traditional proton and neutron elastic scattering optical model analyses already existed, particularly those of Werby, Edwards, and Thompson (1971), Loyd and Haeberli (1970), Votava et al. (1973), and Hogue (1977). The comparison of the results of our Lane model approach to these analyses should give some information about the possible relative superiority of the Lane approach.

Data Sets

The data in this analysis were taken from several sources, with a preference for results obtained at this laboratory in the last five years. For the (p,p) reaction, the TUNL cross-section and polarization results of Votava et al. (1973) were supplemented by cross-section data of Bingham, Brussel, and Steben (1964) and polarization data of Loyd and Haeberli (1970) and Rosen (1965). Overlapping data sets were generally consistent, with the exception of that of the older $\sigma_{pp}(\theta)$ data. Although these latter data were untabulated and had to be extracted graphically, the disagreement could not be due to such extraction. The (p,n) cross-section data were those reported in the first portion of this work, and the (p,n) analyzing power data are from an experiment conducted at TUNL (to be discussed in Part Two). Finally, the (n,n) data were recently measured by the TUNL neutron time-of-flight group (Hogue, 1977). A detailed summary of the data set is given in Table 3.

Failure of Volume V_1 Form Factor

The initial stage of analysis concentrated on the 13-MeV data near the middle of our energy range. It was immediately found that no volume V_1 form factor could reproduce the locations of the minima in the (p,n) cross section. In fact, the results obtained from standard parameter sets, such as that of Watson, Singh, and Segel (1969), exhibited essentially no dips in region of the first minimum in the data. At several stages in the analysis attempts were made to obtain a volume solution for V_1, yet the best such distributions either had a severe forward-angle dip or required renormalizing the data by 50%, which was not permitted with our

TABLE 3

DATA FOR ^{9}Be LANE MODEL ANALYSIS

Reaction	Distribution	Beam Energy(MeV)	Assigned Absolute Error	Reference
$^{9}Be(p,p)^{9}B$	$\sigma_{pp}(\theta)$	11,12	10.0%	Bingham et al., 1964
		13,14,15	7.0%	Votava et al., 1973
	$A_{pp}(\theta)$	11,12	0.02	Loyd and Haeberli,1970
		13,15	0.03	Votava et al., 1973
		14.5	0.05	Rosen et al., 1965
$^{9}Be(n,n)^{9}Be$	$\sigma_{nn}(\theta)$	10.95, 12.04, 12.94,13.94	6.0%	
		14.94	8.0%	Hogue, 1977
$^{9}Be(p,n_0)^{9}Be$	$\sigma_{pn}(\theta)$	11.0,12.0.13.5, 15.0	10.0%	Present Results
	$A_{pn}(\theta)$	11.1,12.0,13.5, 15.0	0.04	Present Results

assigned uncertainties. There appeared to be a definite connection between the prediction of this minimum and the use of a surface form factor. More discussion of these solutions will be presented in the comparison of our results to those of other analyses.

Parameter Sensitivity Tests

In contrast to the volume V_1 potential, relatively minor adjustments to standard parameters produced promising results using a surface-peaked form factor. In order to catalog the behavior of individual parameters, systematic variations were made of each of the fifteen Lane potential parameters to show their effect on each of the four predicted distributions σ_{pp}, σ_{pn}, σ_{nn}, and P_{pp}. These parameters were the strength, radius, and diffuseness for five potentials: volume $V_0(r_0,a_0)$, surface $W_0(r_0^i,a_0^i)$, spin-orbit $V_{so}(r_{so},a_{so})$, surface $V_1(r_1,a_1)$, and surface $W_1(r_1^i,a_1^i)$. Imaginary volume potentials were omitted from the study on the basis of the optical model for light nuclei developed by Watson, Singh, and Segel (1969).

The variations were obtained from an approximate optimization of all parameters to basis values p_i describing data near the middle of our energy region. Estimates were then made of the change Δp_i needed for a chi-square increase in the total basis chi-square value for all included data sets, and calculations were made at the values $p = p_i \pm \Delta p_i$. The results of these calculations are shown in Figures 13. It is important to remember that the primary intent of these studies was to compare the effects of different parameters on all four distributions, not to show

Figure 13. Effects of Variation of Individual Lane Potential Parameters

a) Variation of $V_0(r)$ Parameters V_0, r_0, a_0

b) Variation of $W_0(r)$ Parameters W_0, r_0^i, a_0^i

c) Variation of $V_{so}(r)$ Parameters V_{so}, r_{so}, a_{so}

d) Variation of $V_1(r)$ Parameters V_1, r_1, s_1

e) Variation of $W_1(r)$ Parameters W_1, r_1^i, s_1^i

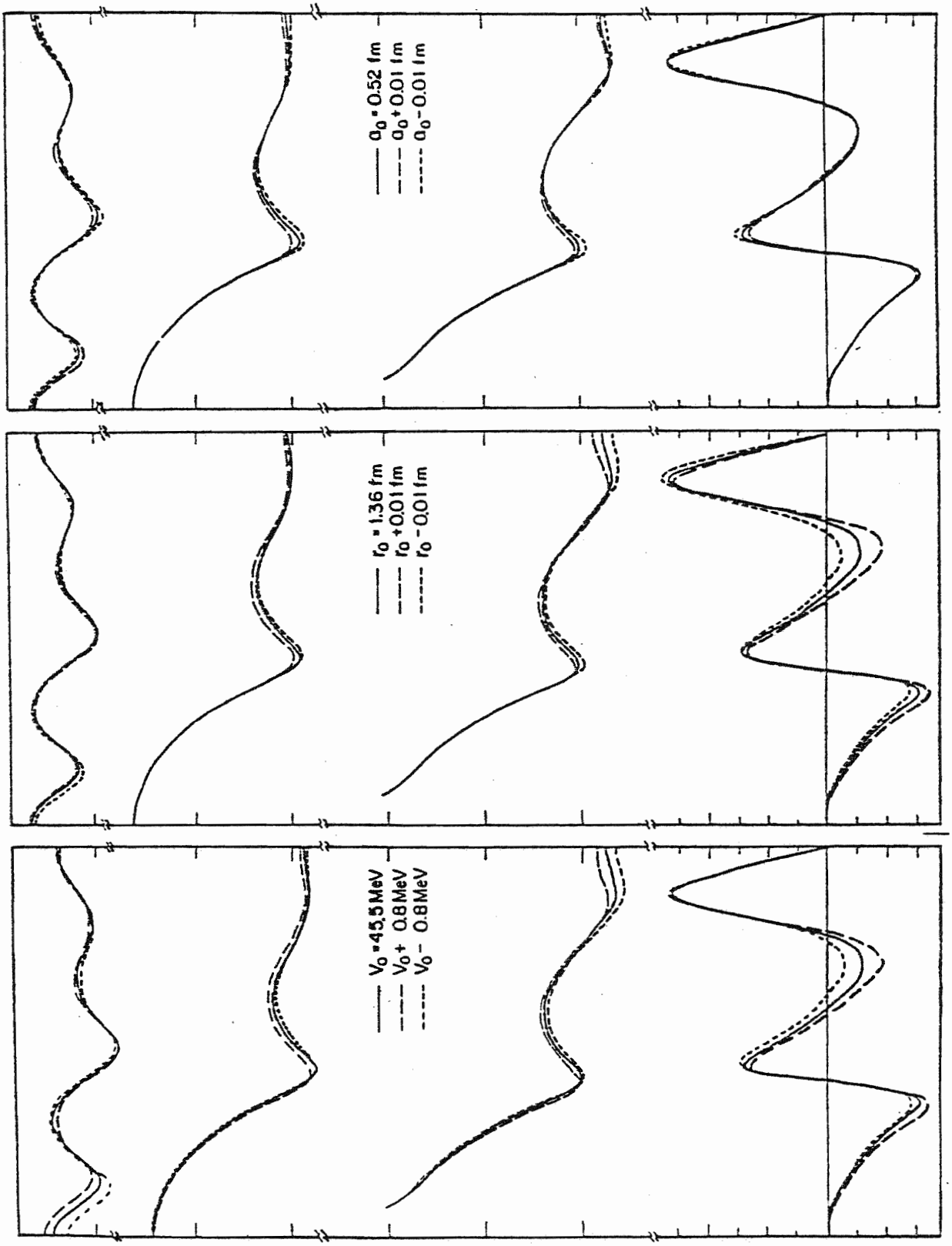
V_0 = 45.5 MeV
V_0 + 0.8 MeV
V_0 − 0.8 MeV
r_0 = 1.36 fm
r_0 + 0.01 fm
r_0 − 0.01 fm
a_0 = 0.52 fm
a_0 + 0.01 fm
a_0 − 0.01 fm

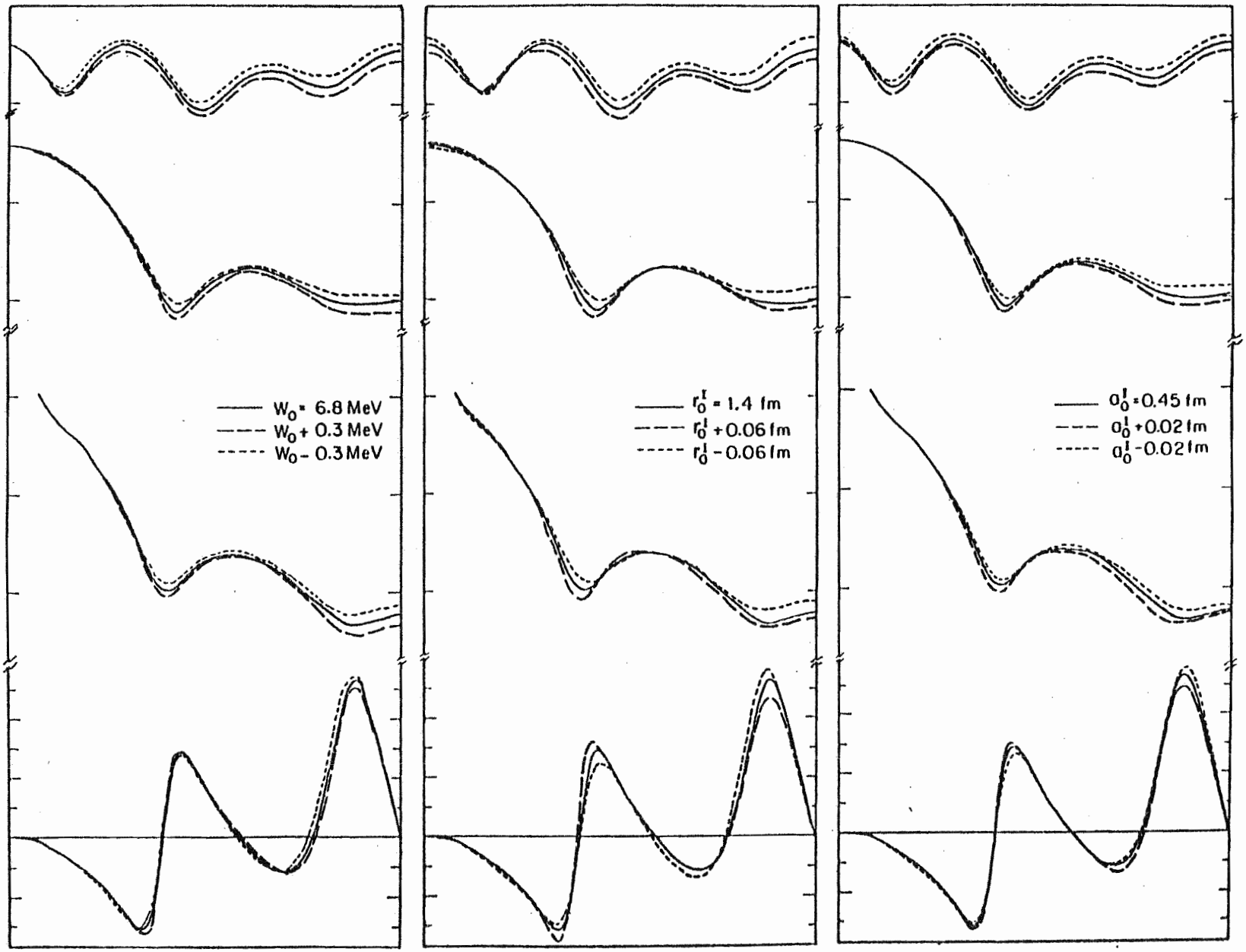
W0 = 6.8 MeV
W0 + 0.3 MeV
W0 - 0.3 MeV
r0I = 1.4 fm
r0I + 0.06 fm
r0I - 0.06 fm
a0I = 0.45 fm
a0I + 0.02 fm
a0I - 0.02 fm

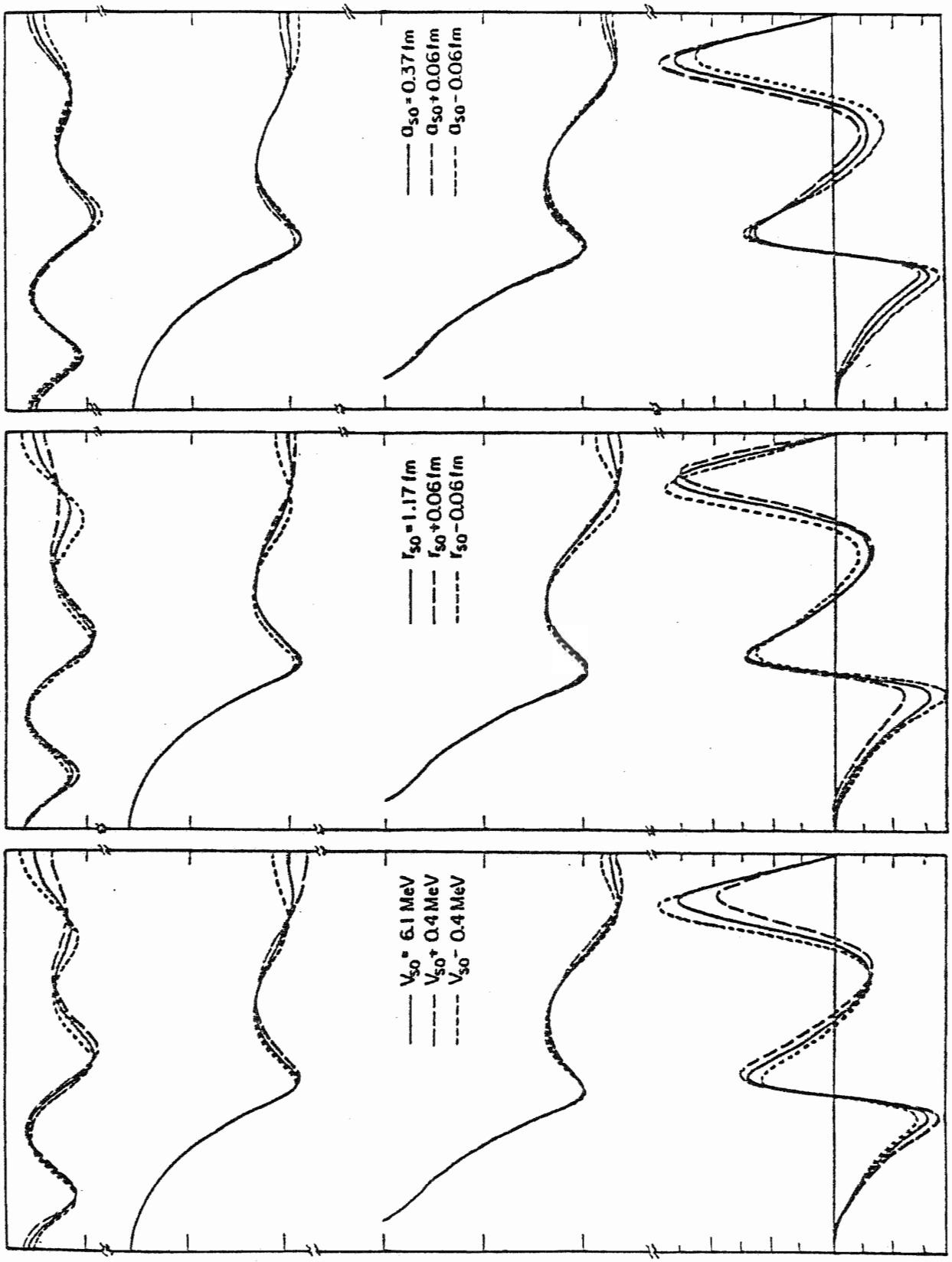
V_{so} = 6.1 MeV
V_{so} + 0.4 MeV
V_{so} - 0.4 MeV
r_{so} = 1.17 fm
r_{so} + 0.06 fm
r_{so} - 0.06 fm
a_{so} = 0.37 fm
a_{so} + 0.06 fm
a_{so} - 0.06 fm

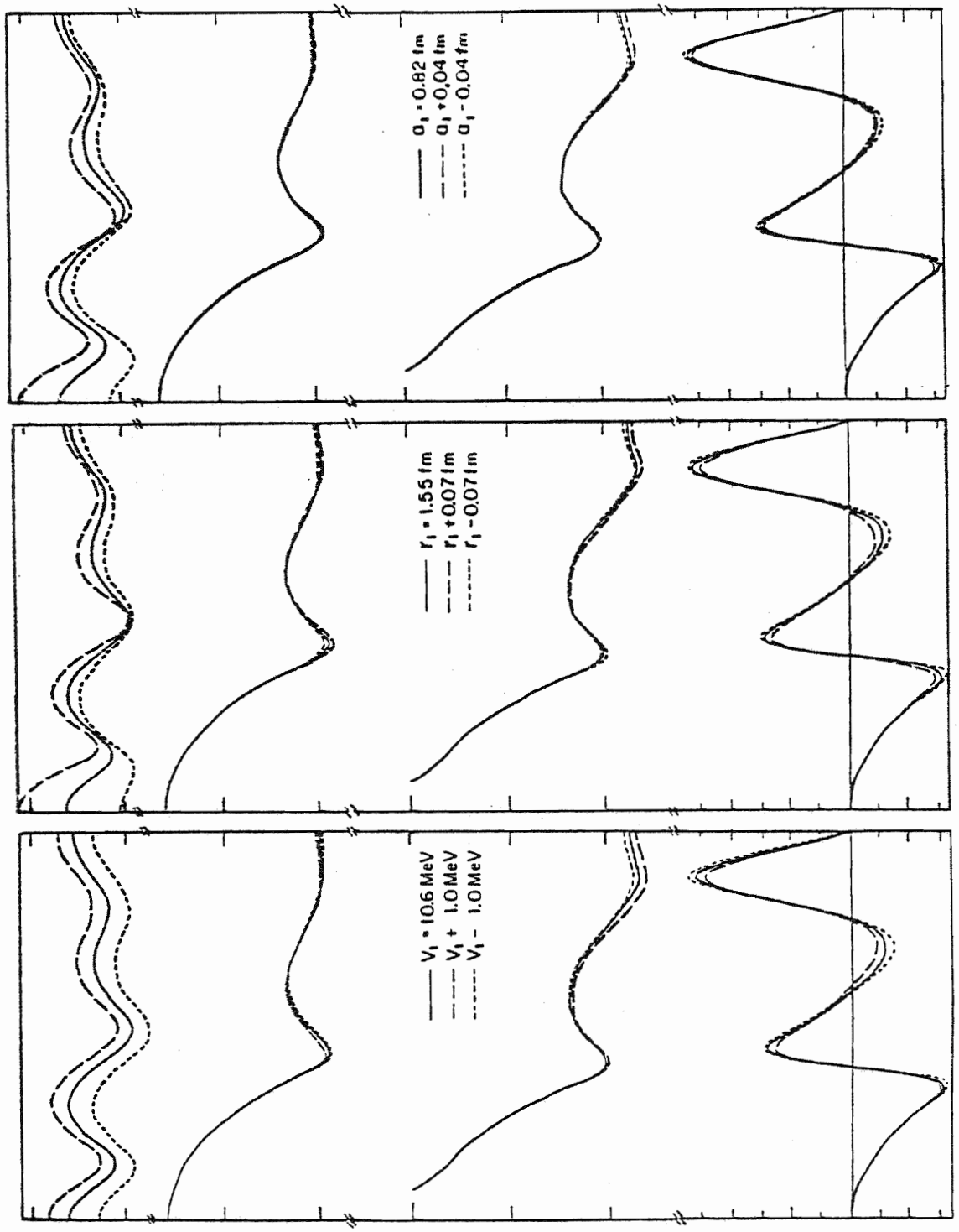
V_1 = 10.6 MeV
V_1 + 1.0 MeV
V_1 − 1.0 MeV
r_1 = 1.55 fm
r_1 + 0.07 fm
r_1 − 0.07 fm
a_1 = 0.82 fm
a_1 + 0.04 fm
a_1 − 0.04 fm

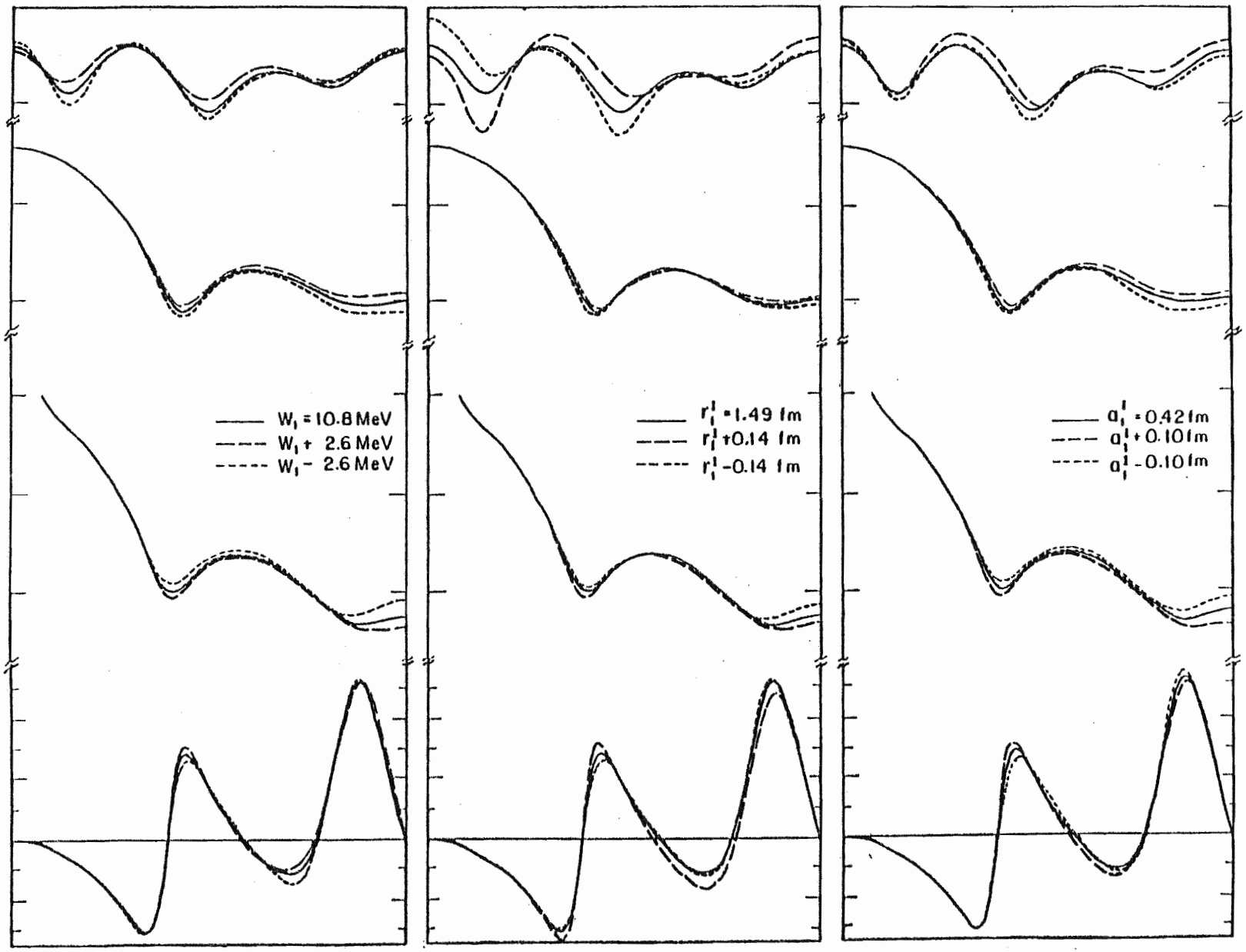
W_I = 10.8 MeV
W_I + 2.6 MeV
W_I - 2.6 MeV
r_I' = 1.49 fm
r_I' + 0.14 fm
r_I' - 0.14 fm
a_I' = 0.42 fm
a_I' + 0.10 fm
a_I' - 0.10 fm

which parameters cause the greatest increase in chi-square. This limitation is due to the different weighting of each type of data; for these variations the errors were: $\Delta\sigma_{pp} = 10.0\%$, $\Delta P_{pp} = 0.05$, $\Delta\sigma_{pn} = 20.0\%$, and $\Delta\sigma_{nn} = 6.0\%$. Since a certain parameter affects some distributions much more than others, the sensitivities of individual parameters are strongly influenced by such relative weighting. It is therefore invalid to conclude from the figures that "p_i is more critical than p_j," but it is perfectly valid to conclude that "p_i has a greater effect on distribution x than on distribution y."

To provide some feel for the overall sensitivities of different parameters, we show in Table 4 the basis value, the estimated change required for a 50% chi-square increase, and the ratio of these two quantities (a relative sensitivity). With the assigned errors in mind, this table may be used to estimate the relative weighting of each parameter in the total chi-square. For example, with the errors used, W_1 must be varied by 53% and V_0 by only 4% to produce the same change in the fitting quality.

Turning now to the figures themselves, we note several features. In general, the $\sigma_{pn}(\theta)$ and $P_{pn}(\theta)$ distributions appear to be most sensitive, although sometimes, as in the case of the W_0 parameters, all distributions are affected about equally. There is some connection of the effects of the isospin-independent and dependent parameters to the elastic and quasielastic distributions, respectively, and the spin-orbit parameters are principally determined by the polarization data. Interestingly, the isospin parameters do not always affect neutron and proton scattering in

TABLE 4

PARAMETER SENSITIVITIES (13.0 MeV)

Parameter	Base Value	Required Change	Sensitivity
V_0	45.530	1.830	25.0
r_0	1.347	0.025	55.6
a_0	0.515	0.027	19.2
W_0	6.805	0.720	9.4
r_0^i	1.400	0.127	11.0
a_0^i	0.445	0.049	9.0
V_{so}	6.094	0.993	6.1
r_{so}	1.169	0.141	8.3
a_{so}	0.374	0.139	2.7
V_1	10.613	2.300	4.6
r_1	1.547	0.163	9.4
a_1	0.819	0.094	8.7
W_1	10.750	5.770	1.9
r_1^i	1.488	0.318	4.7
a_1^i	0.424	0.233	1.8

opposite ways; note the effect of r_1 in particular. It appears that the usual VR^n and Wa ambiguities are present, except that the surface V_1 cannot be simply traded off against either r_1 or a_1. Finally, in discussing the final results we will refer to these observations: (1) no parameter significantly affects the forward-angle $\sigma_{nn}(\theta)$ prediction; (2) $\sigma_{pn}(\theta)$ is only approximately proportional to V_1^2; and (3) the depth of the first minimum of the $\sigma_{pn}(\theta)$ prediction is heavily determined by r_1^i.

Fitting Approach

The above forty-five distributions emphasized the interdependence of the quantities involved and suggested an analysis approach which combined manual adjustment with automatic searching. Our procedure was to deliberately introduce desired changes in shape; a subsequent search with selected parameters and weighting of data sets then allowed the user to investigate the ambiguities of the various parameter combinations.

Starting from the "best-fit" 13-MeV results, attempts were made to extend the analysis upward to 15 MeV and downward as far as possible. Although the upward extension was straightforward, the decreasing depth of the first minimum in $\sigma_{pn}(\theta)$ at the lower energies forced a strong energy dependence on the W_1 strength and geometry; this in turn caused other parameters to vary. It was impossible to obtain reasonable fits for the energies below 11 MeV, so it was decided to stop the analysis at the lowest energy of our $\sigma_{pn}(\theta)$ data, 11.0 MeV.

Coulomb Corrections

We had originally planned to evaluate both the energy-drop and the potential-correction methods of applying the coulomb correction. However, our inability to obtain (n,n) fits below 11 MeV restricted the energy range of the first method, and our only conclusion is that both approaches seem reasonable for the range 13-15 MeV. We thus concentrated on an attempt to determine the proton potential correction ΔV_c. To give a better idea of the significance of this correction, Figure 14 shows the potential obtained for proton scattering, separating the nuclear V_p, coulomb V_c, and coulomb correction ΔV_c terms.

Our approach to obtaining ΔV_c was to search on each data set over the 4-MeV energy interval, obtaining results which ranged from 0.9 to 1.5 MeV, with a final value chosen as 1.375 MeV. We emphasize that our method depends on the correct normalization of all three sets of cross-section data. The magnitude of the $\sigma_{pn}(\theta)$ data almost fixes the value of V_1, leaving the ΔV_c determination to a comparison of $\sigma_{pp}(\theta)$ and $\sigma_{nn}(\theta)$.

An attractive alternate approach would be a simultaneous analysis of neutron and proton scattering from a $T = 0$ target, since then $U_{pn} = 0$ and the coulomb terms are the only difference between proton and neutron potentials (Rapaport, 1977). For comparison to our experiment, the target ^{10}B would be ideal, and such neutron cross-section measurements are set up for our laboratory in the future.

Fitting Results

Once a set of reasonable fits had been obtained over the entire energy range, attempts were made to remove the energy dependences or at least to

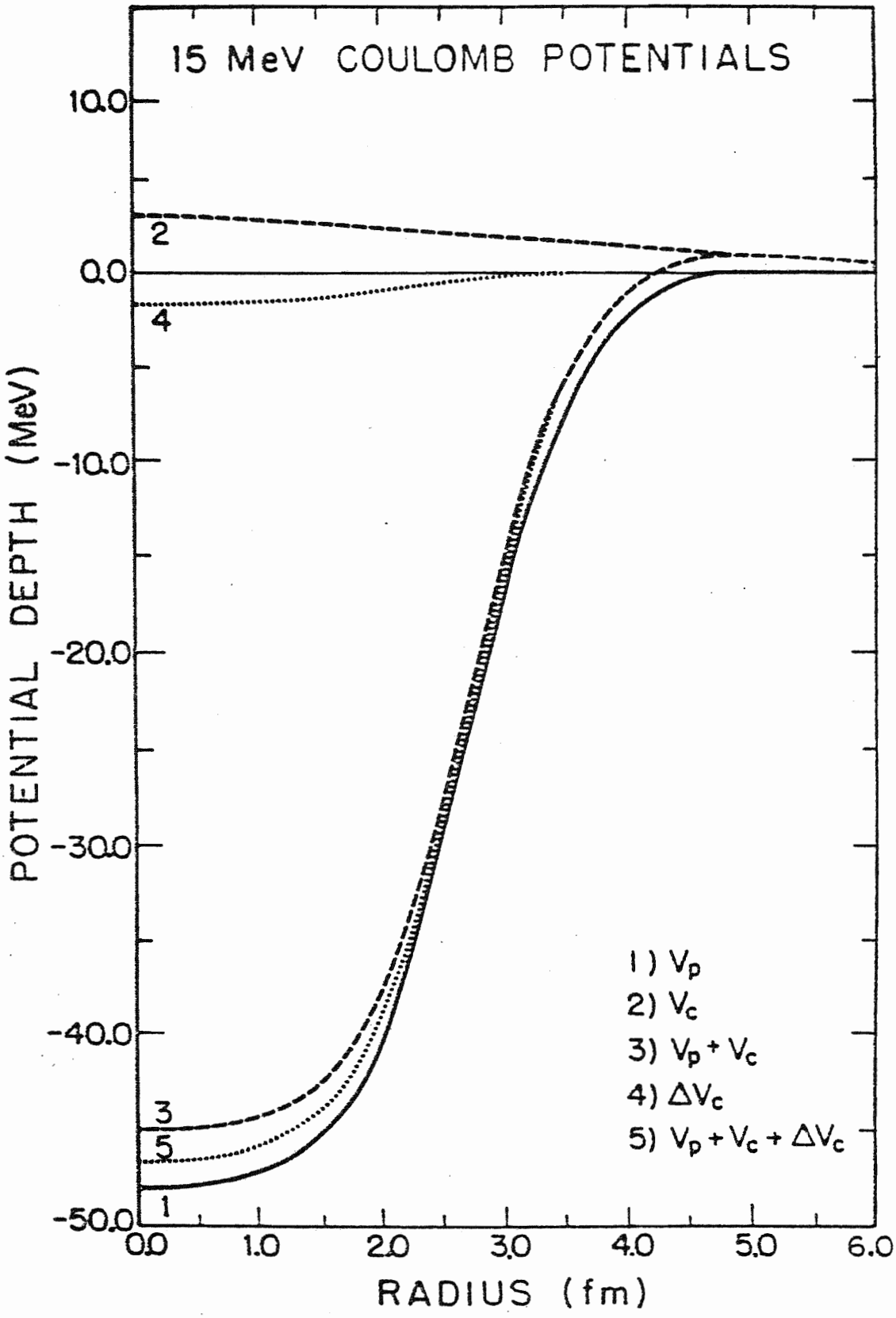

Figure 14. Optical Model Coulomb Potential

reduce them to linear order. The only parameter for which this could not be done was the spin-orbit strength. In some cases, the linearization of the parameters actually produced better fits without an additional search. In fact, all of the geometry parameters can be set to their values at 13 MeV, and the only resulting deterioration of the fits is in the description of the first minimum of the (p,n) cross section. A future analysis is planned as an attempt to further delineate the energy dependence of the parameter set and to possibly improve the predictions.

The angular distributions resulting from this parameter set are shown in Figures 15, and the values for the parameters at 11, 13, and 15 MeV are given in Table 5. The only systematic difficulties appear to be in the prediction of the changing shape of the first minimum in the (p,n) cross section and the magnitude of the forward angle (n,n) data. As mentioned previously, this first problem results in an energy dependence in r_1^i, and the second cannot be solved by adjustment of any potential parameter.

Comparison to Previous Analyses

For comparison to previous analyses of ^{9}Be, the linearized parameter set was converted to proton and neutron potentials using the transformation equations. We emphasize that this conversion is only approximate, since there are differences in the geometrical shapes of the different wells. To understand the implications of this conversion and illustrate our previous discussion of form factors and transformations, in Figure 16 we show the potential wells for U_{pC}, U_{nC}, and U_{pn} which result from the (U_0,U_1) form factors obtained in this study for 11.0 and 15.0 MeV. Note that the

Figure 15. Predicted Angular Distributions of Lane Analysis

a) Charge-Exchange Cross Section

b) Neutron Elastic Cross Section

c) Proton Elastic Cross Section

d) Proton Elastic Polarization

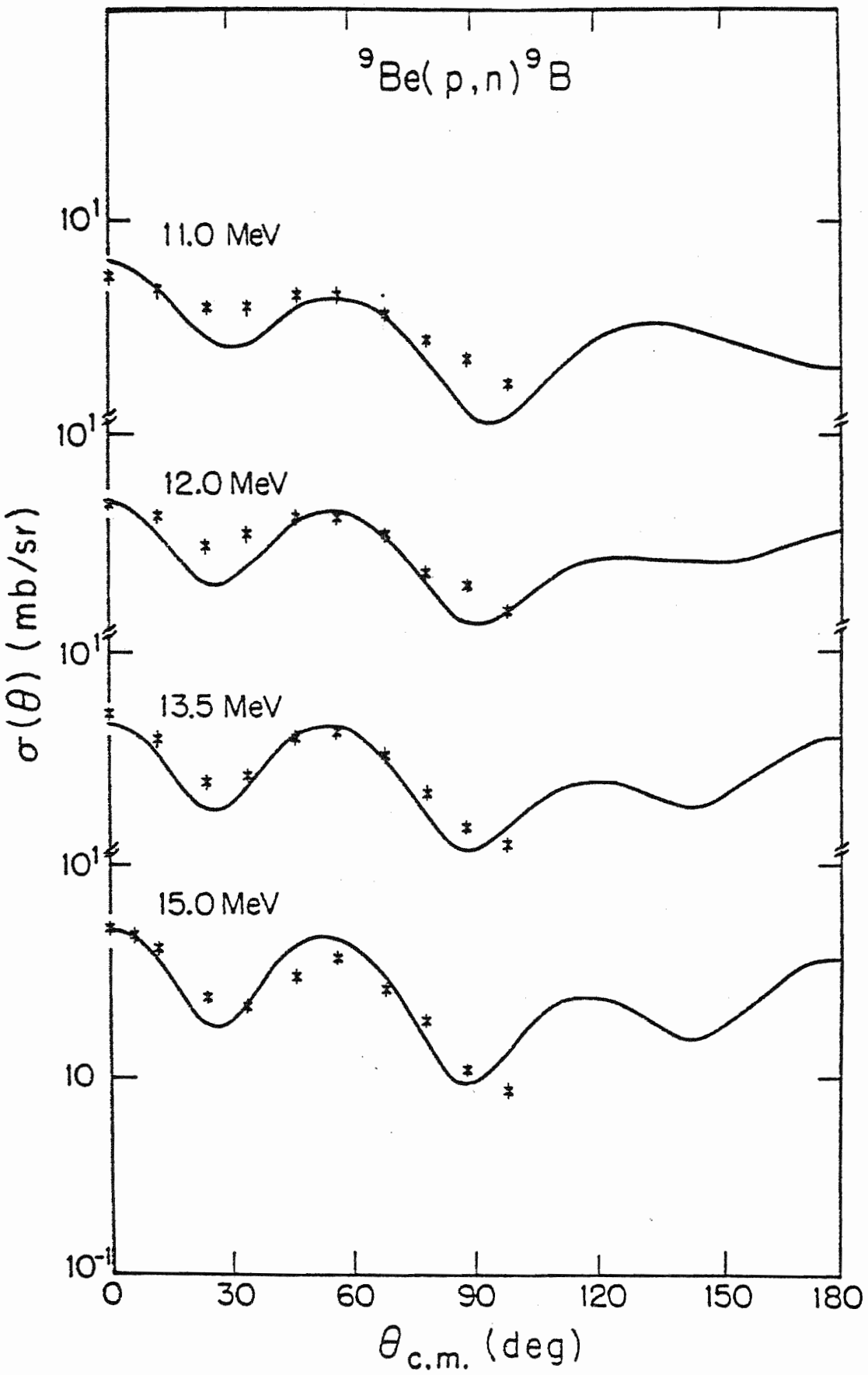
$^{9}Be(p,n)^{9}B$
11.0 MeV
12.0 MeV
13.5 MeV
15.0 MeV
10^{1}
10^{1}
10^{1}
10^{1}
10
10^{-1}
$\sigma(\theta)$ (mb/sr)
0
30
60
90
120
150
180
$\theta_{c.m.}$ (deg)

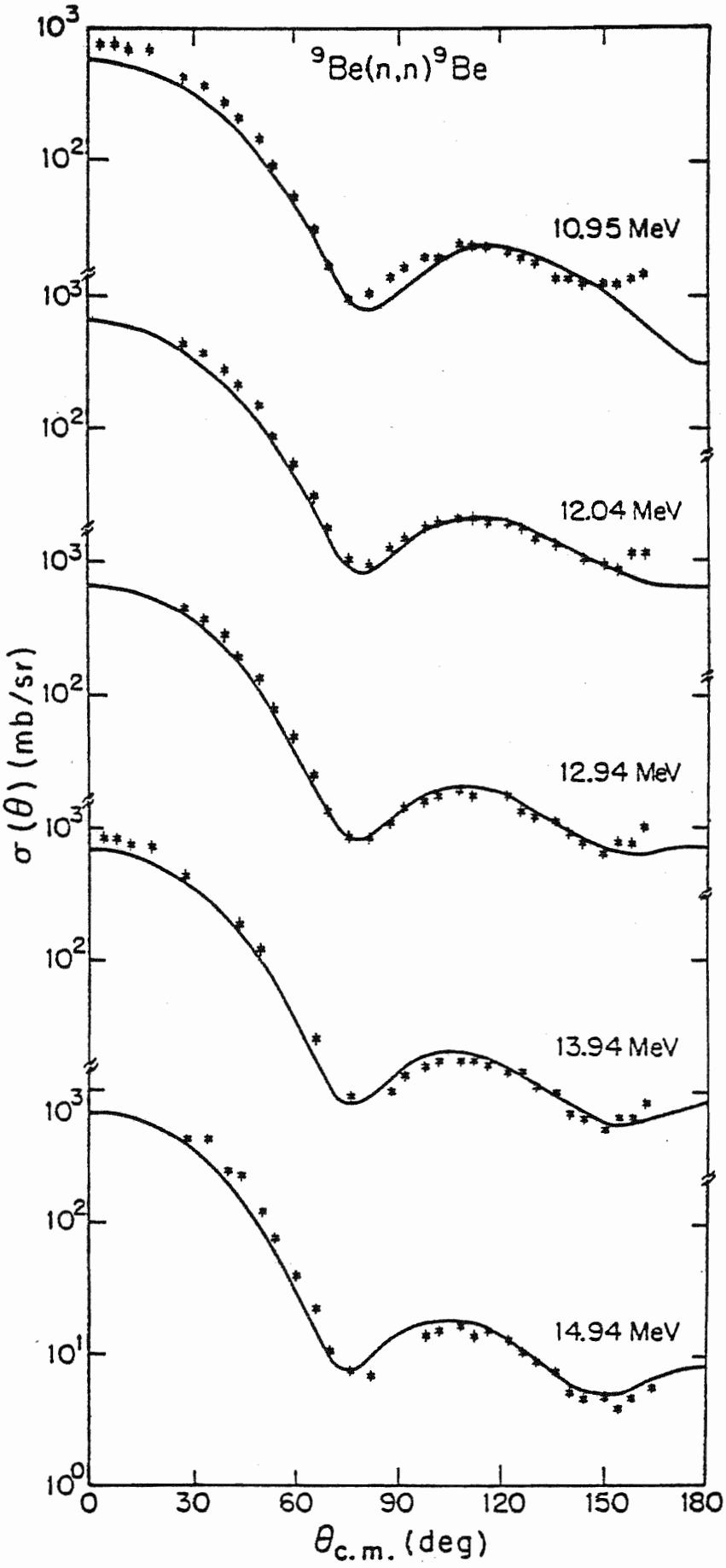
^{9}Be(n,n)^{9}Be
10.95 MeV
12.04 MeV
12.94 MeV
13.94 MeV
14.94 MeV
$\sigma(\theta)$ (mb/sr)
$\theta_{c.m.}$ (deg)
10^3
10^2
10^1
10^0
0
30
60
90
120
150
180

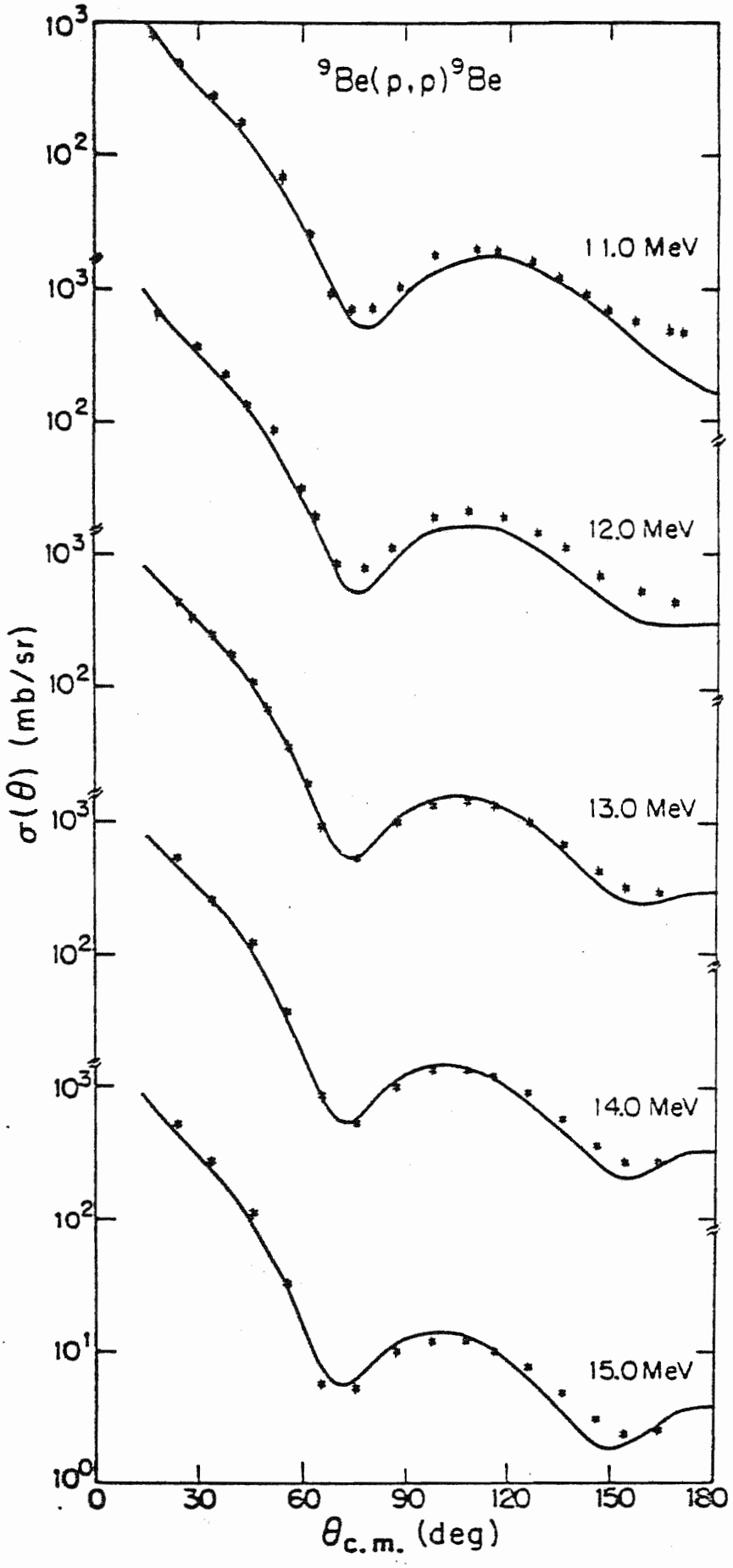
^{9}Be(p,p)^{9}Be
11.0 MeV
12.0 MeV
13.0 MeV
14.0 MeV
15.0 MeV
$\sigma(\theta)$ (mb/sr)
$\theta_{c.m.}$ (deg)
10^3
10^2
10^1
10^0
0
30
60
90
120
150
180

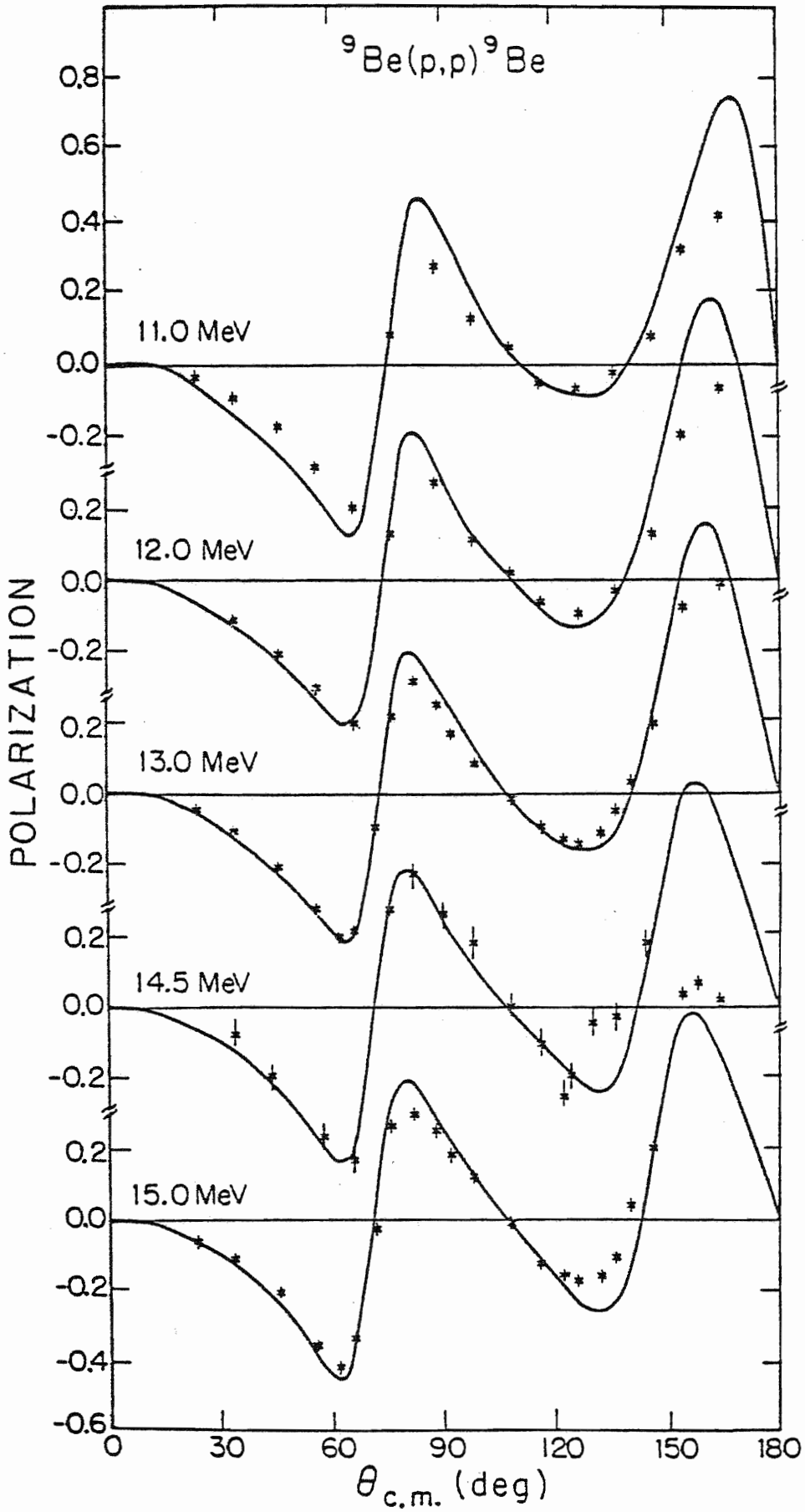
$^{9}Be(p,p)^{9}Be$
11.0 MeV
12.0 MeV
13.0 MeV
14.5 MeV
15.0 MeV
POLARIZATION
$\theta_{c.m.}$ (deg)
0.8
0.6
0.4
0.2
0.0
-0.2
-0.4
-0.6
0
30
60
90
120
150
180

TABLE 5

ENERGY DEPENDENCE OF LANE POTENTIAL

Parameter	Constant	Variable with Beam Energy (MeV) 11.0	13.0	15.0
V_0 (MeV)	---	43.5	44.25	45.00
r_0 (fm)	1.345	---	---	---
a_0 (fm)	---	0.54	0.50	0.46
W_0	---	6.8	7.20	7.60
r_0^i	1.35	---	---	---
a_0^i	0.45	---	---	---
V_{so}	---	8.0	6.00	5.70
r_{so}	---	1.275	1.1875	1.1025
a_{so}	0.36	---	---	---
V_1	---	10.20	11.00	11.80
r_1	---	1.4975	1.5225	1.5475
a_1	---	0.87	0.81	0.75
W_1	---	7.60	9.50	11.40
r_1^i	---	1.69	1.47	1.25
a_1^i	---	0.32	0.40	0.48

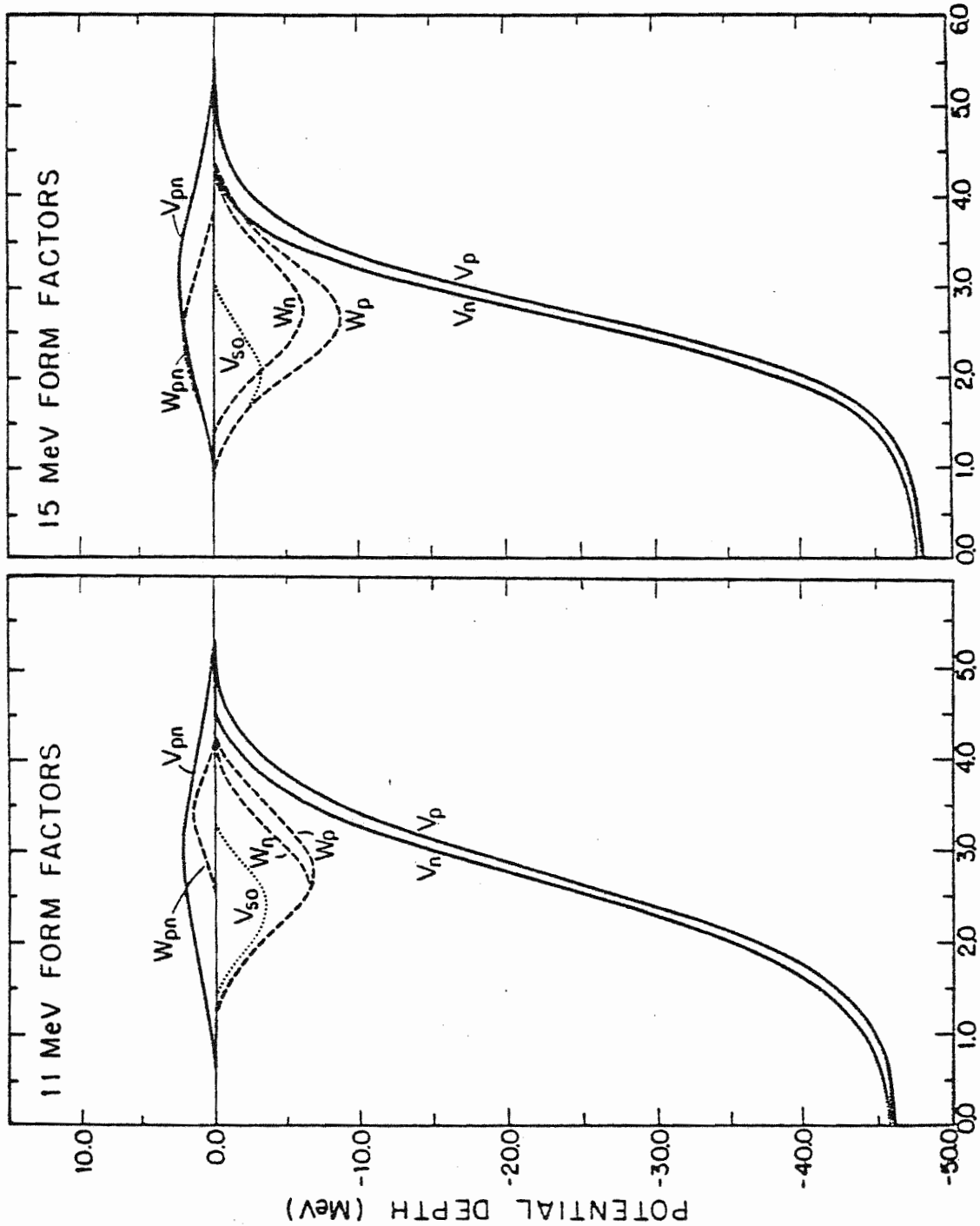

Figure 16. Radial Form Factors of Various Potential Wells

U_{nA} potential is identical to that for U_{nC}, since for a $T = \frac{1}{2}$ target the quantities [+2T/A] and [-2(T-1)/A] are both equal to [+1/A]. For this figure, our notation is $U_{pC} = V_p + iW_p$, $U_{nC} = V_n + iW_n$, $U_{pn} = V_{pn} + iW_{pn}$. The important features are the basic similarity of the overall potential to traditional Woods-Saxon shapes and the change with energy in the shape of the imaginary potentials for neutrons and protons. This figure emphasizes that the form factors resulting from the (U_0,U_1) representation can be obtained in the usual (U_p,U_n) representation only by introducing isospin-dependent radii for the potentials. The greater radius in the proton scattering potential is a reflection of the greater radial probability for excess neutrons to exist in the surface region, i.e., the neutron skin effect. Since (n-p) forces are stronger than (p-p) or (n-n) interactions, incoming protons should therefore be affected at a greater radial separation than neutrons.

The energy dependence of our solutions as converted into the (U_p,U_n) representation are shown in Figures 17, along with estimates of the results of previous analyses. Attempts have been made to re-express the energy dependences shown in these figures by converting the results of each analysis to constant-volume integrals, but little additional understanding was obtained. It therefore seems that either the coupled-channels potentials and elastic scattering potentials are not comparable or that the (U_0,U_1) to (U_p,U_n) conversion is not accurate enough.

The comparisons above can also be approached from the opposite point of view. Any analysis which has simultaneously fit neutron and proton data has produced potentials which now may be entered into TWAVE3 to

Figure 17. Energy Dependence of Equivalent Proton Potentials

a) Strength Parameters V_p, W_p, V_{so}

b) Radius Parameters r_0, r_0^i, r_{so}

c) Diffuseness Parameters a_0, a_0^i, a_{so}

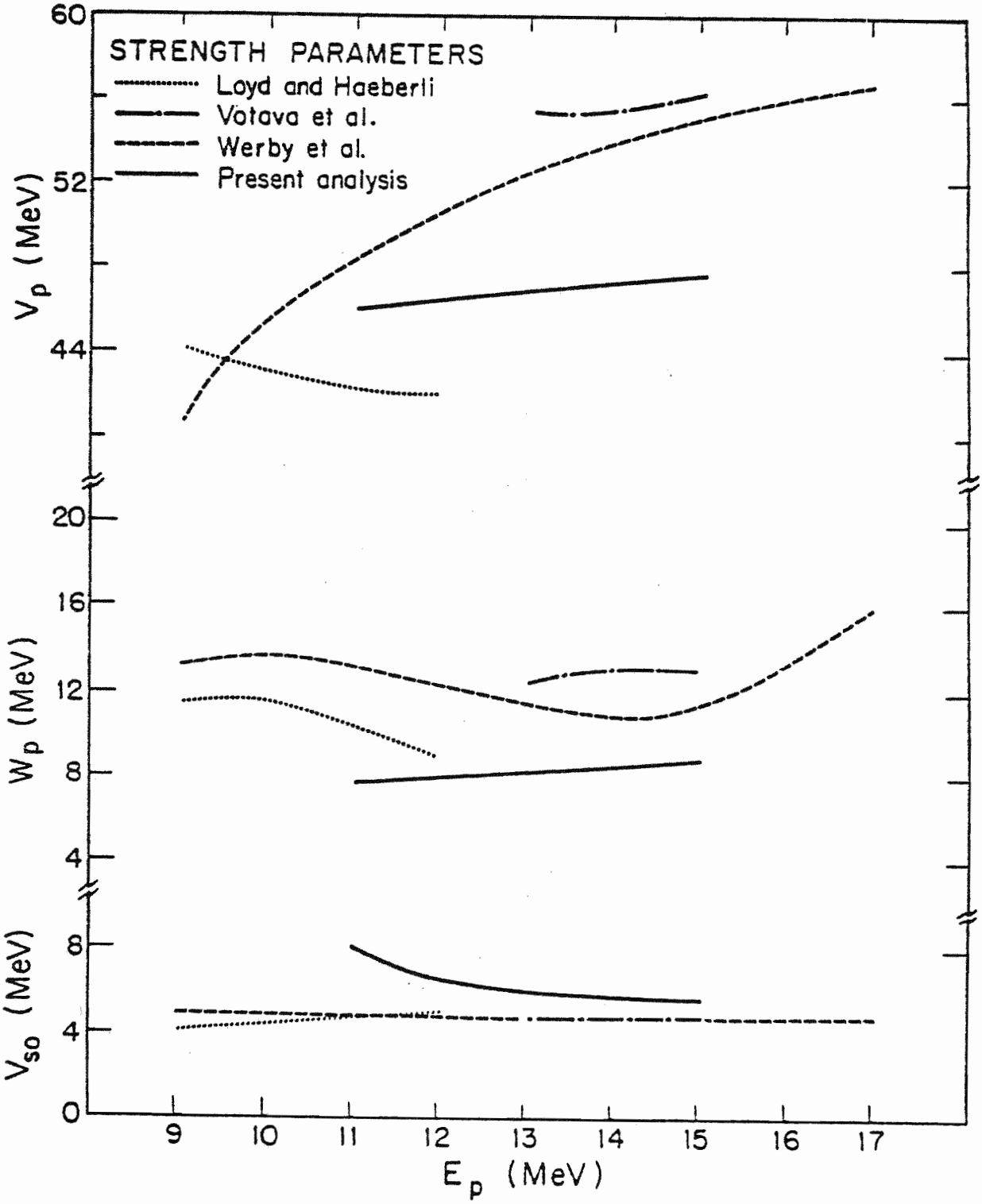
STRENGTH PARAMETERS
Loyd and Haeberli
Votava et al.
Werby et al.
Present analysis
V_p (MeV)
W_p (MeV)
V_{so} (MeV)
E_p (MeV)
60
52
44
20
16
12
8
4
8
4
0
9
10
11
12
13
14
15
16
17

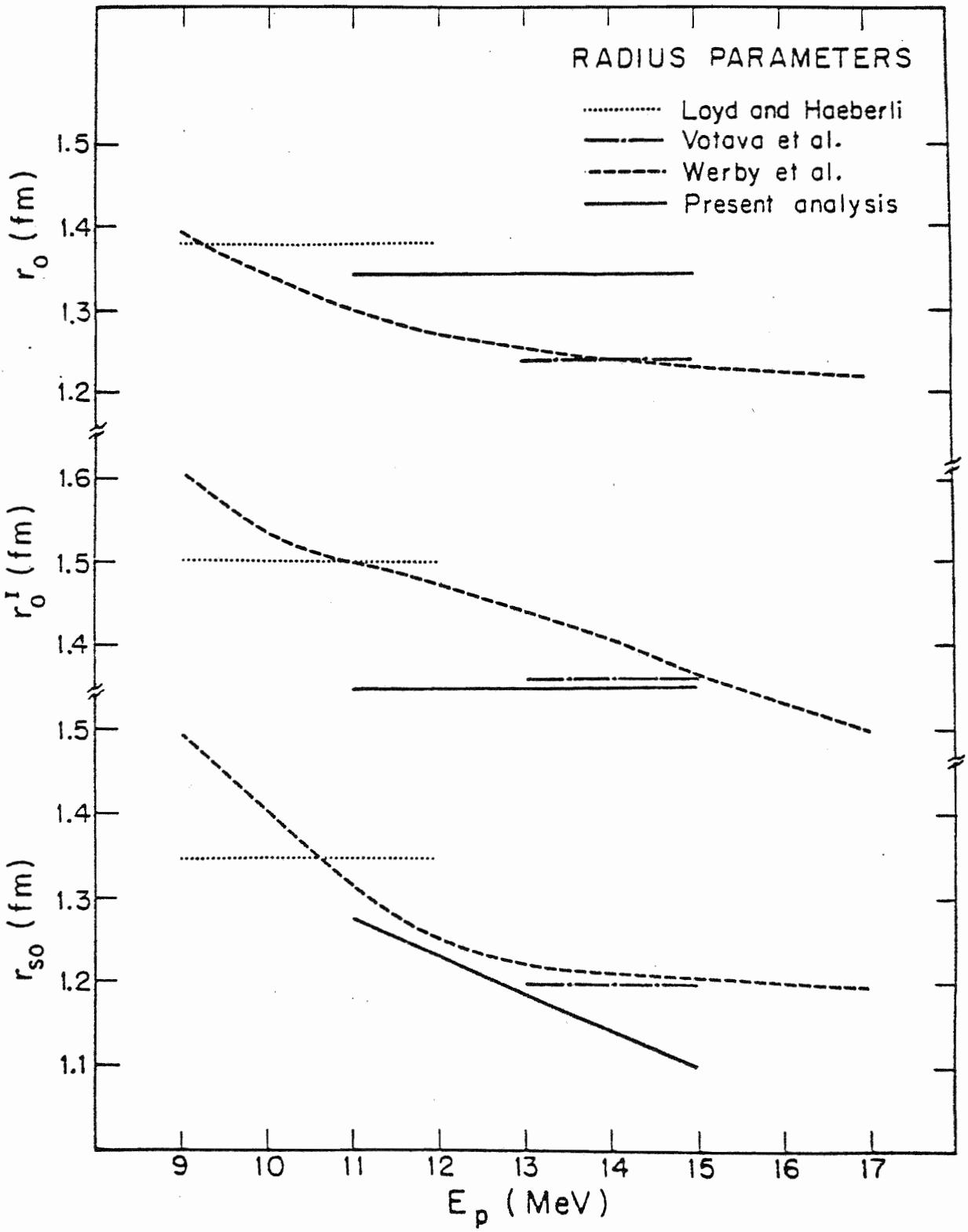
RADIUS PARAMETERS
Loyd and Haeberli
Votava et al.
Werby et al.
Present analysis
r_o (fm)
r_o' (fm)
r_{so} (fm)
E_p (MeV)

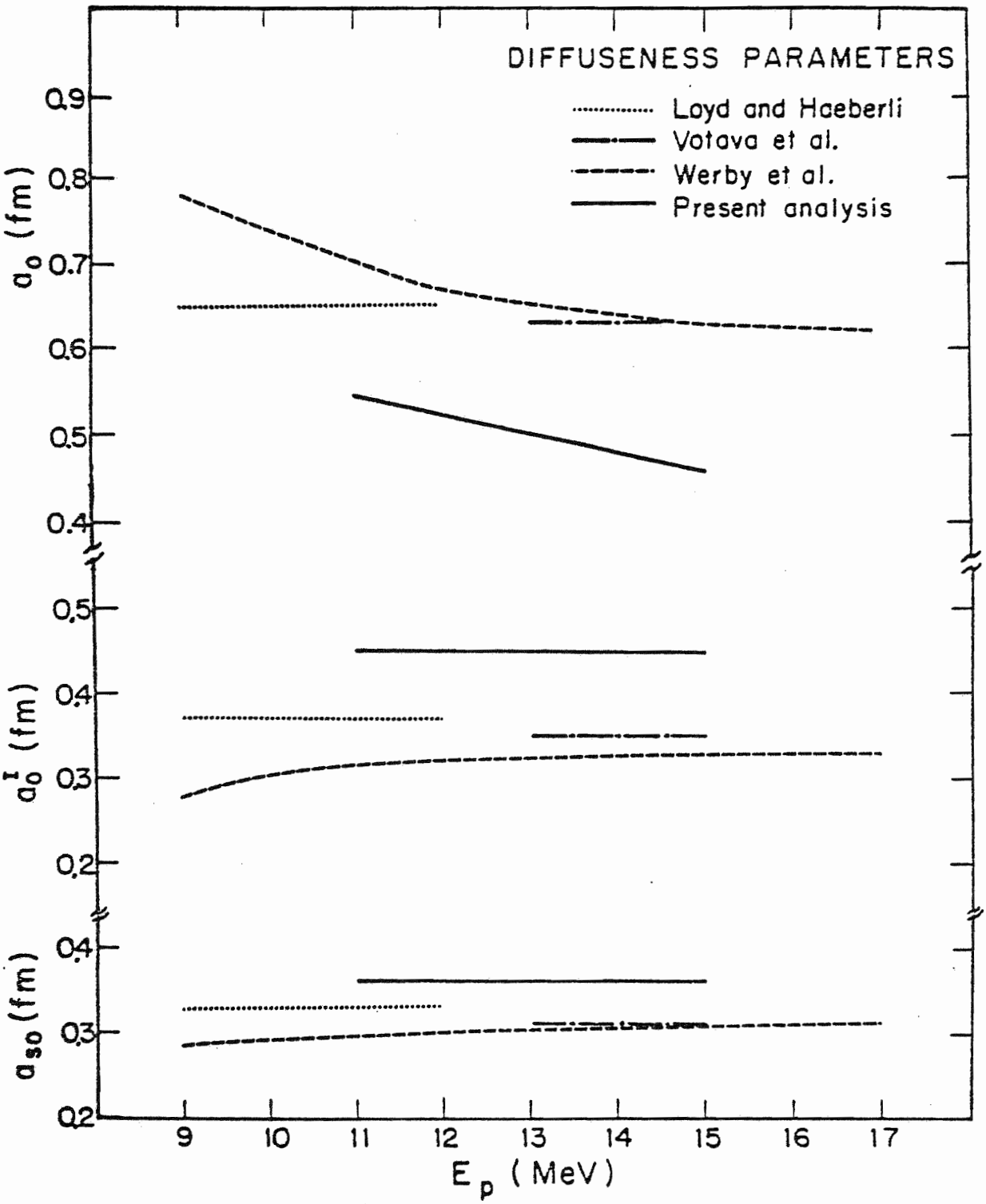
DIFFUSENESS PARAMETERS
Loyd and Haeberli
Votava et al.
Werby et al.
Present analysis
a_o (fm)
a_o^I (fm)
a_{so} (fm)
E_p (MeV)

calculate both a (p,n) cross section and the effect of the open neutron channel on the (p,p) cross section. Two such analyses are the global potential of Watson, Singh, and Segel (1969) and the ^{9}Be analysis of Hogue (1977). Sample predictions are shown in Figure 18. The potential prediction of Hogue is clearly at odds with the magnitude of the (p,n) data; the results of the potential of Watson et al., though of the correct magnitude, illustrate the typical failure of a volume V_1 term to predict the correct shape for $\sigma_{pn}(\theta)$.

Carlson, Zafiratos, and Lind (1975) measured $\sigma_{pn}(\theta)$ at 22.8 MeV for several targets including ^{9}Be; they also developed a global (U_p,U_1) potential based on the Becchetti-Greenlees model. Their Lane model underestimated by a factor of about 15 the $^{9}Be(p,n_0)^{9}B$ cross section, but it did predict the correct shape. These results were verified with our code and led to an interesting study. We increased V_1 from their value to predict the correct magnitude for $\sigma_{pn}(\theta)$ and then searched to improve the resulting poor fit to the (p,p) data. In the process, the good shape of their original prediction for $\sigma_{pn}(\theta)$ changed to one similar to that just shown for Watson's potential, which is generally characteristic of the volume form factor results in our analysis. This result emphasizes our own conclusions about the inadequacy of the volume form factor.

Charge-Exchange Analyzing Power

The documentation of the failure of our Lane model approach to fit the analyzing power for the $^{9}Be(p,n_0)^{9}B$ reaction is given in Figure 19. The solid curves represent the distribution predicted by the solution discussed above; this solution gave a good description to all but $A_{pn}(\theta)$

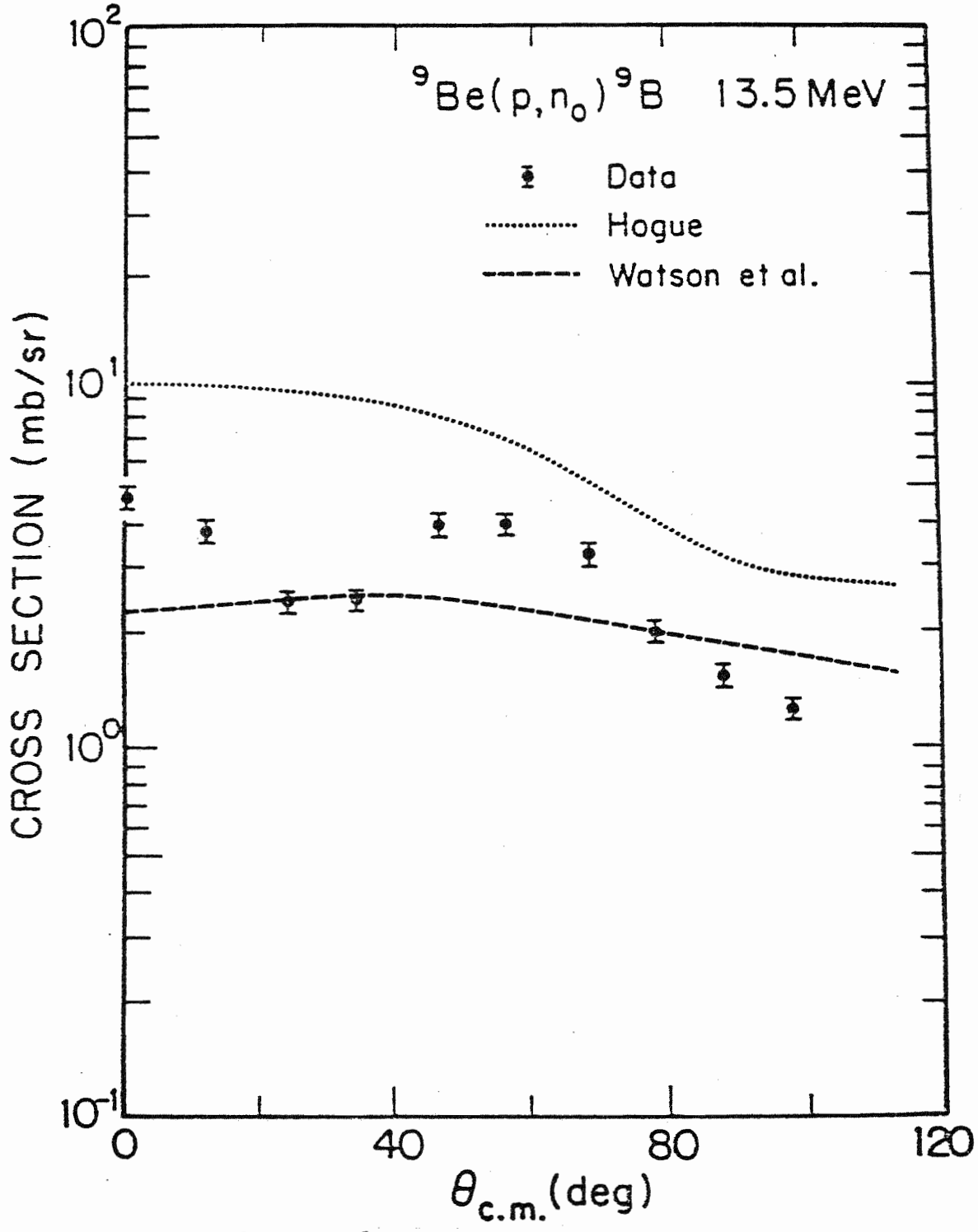

Figure 18. ^{9}Be(p,n$_0$)^{9}B Cross Section Predictions by Other Analyses

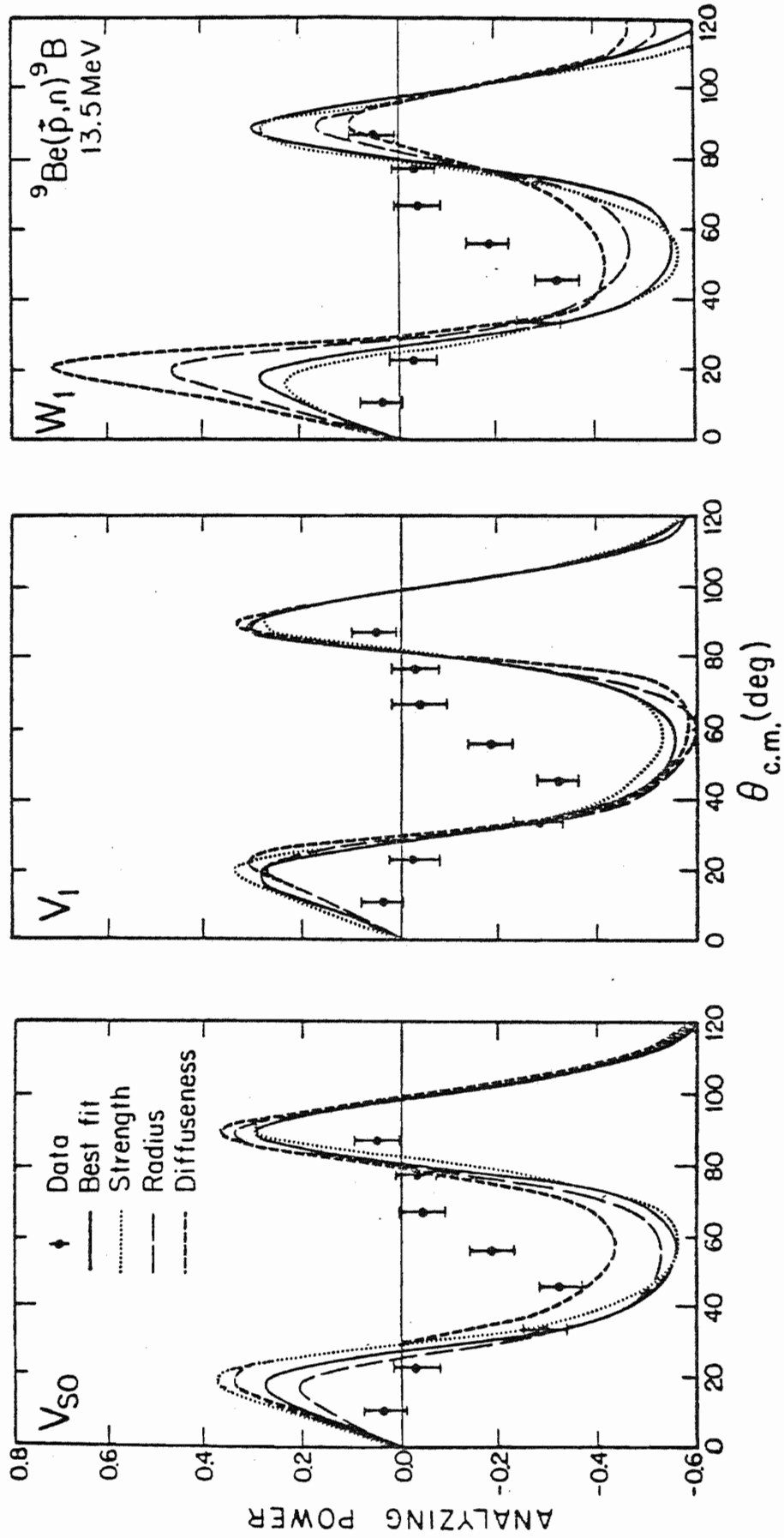

Figure 19. Sensitivity of Charge-Exchange Analyzing Power Prediction to Various Parameters

measurements. The other curves show the results obtained by increasing each of the most sensitive parameters by amounts which resulted in a clearly unacceptable fit to the other data. Obviously, no single parameter can be found which would substantially improve the agreement. In fact, it appears that the area under the curve remains essentially constant; as each parameter change improves the fit at the positive maximum in the analyzing power, the fit worsens in the region of the following negative excursion. We therefore conclude that no solution can be found using our current solution as a starting set.

At this point we call attention to two approaches which suggest solutions which would not be obtained from the analysis we have used. First, the volume form factor predicts an analyzing power which is usually smaller, less rapidly oscillating, and of opposite phase when compared to the surface result. It may be that a more general surface-plus-volume form factor would be successful in describing both $\sigma_{pn}(\theta)$ and $A_{pn}(\theta)$ distributions. Further, the extreme low energy behavior of both distributions is generally better described by a volume form factor, and such an admixture may allow the description to extend successfully to lower energies. Second, previous authors (Moss et al., 1972 and Gosset, Mayer, and Escudié , 1975) have examined the case for an isospin-dependent spin-orbit term in the Lane model potential, and their analyses of (p,n) analyzing power data have indicated support for such a term. This addition might help in the description of the (p,n) cross section and the back-angle neutron and proton elastic scattering cross sections, as well as in giving the freedom needed to obtain a good analyzing power descrip-

tion. In one view, the model we have used includes only the second-order effects in which the incoming proton must first flip spin, then flip isospin (or flip isospin, then spin) through the separate mechanisms of the $\vec{t} \cdot \vec{T}$ and $\vec{\ell} \cdot \vec{s}$ terms. However, an isospin spin-orbit term would be of the form $(\vec{t} \cdot \vec{T})(\vec{\ell} \cdot \vec{s})$ and is capable thereby of directly changing a spin-up proton into a spin-down neutron, i.e., a more direct or first-order process. There are plans to expand the algebra in TWAVE3 to allow the investigation of such a term in the near future.

Summary

A summary of the results of the Lane model analysis of the $^{9}Be(p,p)^{9}Be$, $^{9}Be(p,n)^{9}B$, and $^{9}Be(n,n)^{9}Be$ reactions will be given to conclude our application discussion. In the energy region of our (p,n) data, 11.0 to 15.0 MeV, we obtained good fits simultaneously to cross-section data for all three reactions and to polarization results for proton elastic scattering, while no simultaneous description could be found of the charge-exchange analyzing power. The shape of the (p,n) differential cross section unambiguously favored selection of a surface V_1 form factor, and a tentative coulomb correction value Δ_c of 1.375 MeV was obtained. The apparent intrusion of non-direct processes at lower energies precluded analysis below 11.0 MeV and may be responsible for strong energy dependences in the parameters even at higher energies.

Finally, we restate some of the deficiencies mentioned above and anticipate some criticisms which may be forthcoming. As discussed, errors in normalizing the data not only jeopardize the simultaneous pre-

diction of all three data sets but seriously hamper our efforts to estimate a coulomb correction factor. Also, the necessity for energy dependence in the parameter set needs to be further studied to remove or clarify existing trends. Finally, the direct-reaction nature of the model makes the presence of compound nuclear effects particularly troublesome, since these effects may be even larger in (p,n) reactions than in elastic scattering (Richter and Parish, 1968). Therefore, in our analysis we may have been more sensitive to such contributions than were Votava et al. (1973), who stated that their proton optical model was likely to be valid above 10 MeV, or Werby et al. (1971), who showed that the compound nuclear contribution to the elastic scattering was unimportant at 8 MeV.

Further, Carlson, Zafiratos, and Lind (1975) assumed that the failure of their model to describe light nuclei was related to the existence of $\ell \neq 0$ transfers, which are indeed well documented for ^{9}Be + n (Hogue, 1977) and ^{9}Be + p (Votava et al., 1973). This contribution may indeed be present, but the spherical optical model is capable of mocking up such mechanisms. We prefer to believe that the failure of the analysis of Carlson et al. lies in their use of Becchetti-Greenlees optical parameters for light nuclei, a region where their failure is well known.

LANE MODEL CONCLUSIONS

The ability of the Lane potential to correlate the various data sets is very impressive, since no previous analysis has attempted to simultaneously fit all three cross sections, nor have the elastic and charge-exchange polarization distributions ever before been included. We are confident that additional investigation of the energy dependence will produce fits which describe all data except that contaminated by non-direct processes and data for the charge-exchange analyzing power. We also believe that we have made a strong case for the inclusion of an isospin-dependent spin-orbit term in the Lane potential, having established that no solution using the present potential can produce a good fit to the charge-exchange analyzing power data. Finally, in pushing the model to the limit we have shown that careful inclusion of charge effects may allow the first direct evaluation of the optical model coulomb correction for any target system.

PART TWO

COMPARISONS OF POLARIZATION AND ANALYZING POWER

I. INTRODUCTION

A. Definitions of Polarization Observables P and A

In order to understand the sections to follow, we must be very sure of the relation between the outgoing beam polarization P produced by a reaction with an incident unpolarized beam and the analyzing power A of that reaction for an incident beam of polarized particles. Since these two quantities and the experiments which measure them are similar, our discussion will be organized to emphasize their relationships.

We begin with definitions which relate our two observables P and A to the familiar nuclear cross-section measurement $\sigma(\theta)$ for the reaction X(a,b)Y. Here we have incident particles a, target X, outgoing beam b, and residual nucleus Y. The cross section $\sigma(\theta)$ is simply the probability that an incident particle a will result in an outgoing particle b at an angle θ. This measurement ignores the spin orientations of particles and nuclei, i.e., the experiment observables are unpolarized because the spin degrees of freedom have been averaged.

Instead of averaging, we may select particular spin directions for one or more of the types of particles; spin-dependent effects are then possible, and we must define new observables, i.e., polarization observables. In this work we are primarily concerned with the presence of polarization in either the incident beam $\vec{a}$ or the outgoing beam $\vec{b}$. The resulting reac-

tions are denoted by $X(\vec{a},b)Y$ or $X(a,\vec{b})Y$ and the observables are the analyzing power $A(\theta)$ or the polarization $P(\theta)$. We will also refer to the polarization transfer $K(\theta)$ obtained by measuring the correlation between incoming and outgoing polarizations in the reaction $C(\vec{a},\vec{b})A$.

Note that for convenience we are not following the usual convention of labelling the observables $A(\theta)$, $P(\theta)$, and $K(\theta)$ as $A_y(\theta)$, $P^y(\theta)$ and $K_y^{y'}(\theta)$, since the measurements in this work involve only spin $\frac{1}{2}$ incoming and outgoing beams, and the y-axis is by definition along the y'-axis, where $\hat{y}$ and $\hat{y}'$ are along the normal to the reaction plane.

Our development up to this point has relied on a generalization of the familiar arrangement of a cross-section measurement, which averages over spin in both incoming and outgoing beams. Simply stated, polarization observables result from <u>not</u> averaging: the analyzing power $A(\theta)$ is associated with the spin orientation of the incident beam, the polarization $P(\theta)$ with the spin orientation of the outgoing beam. We must now supplant these vague associations with more specific definitions in terms of measurable quantities. To do so, we draw on the familiar concepts of the polarizing and analyzing of beams in optics.

The outgoing beam of intensity I_0 in a cross-section experiment is actually polarized, i.e., for spin-½ the beam has both spin-up and spin-down components I_U and I_D which are averaged by the polarization-insensitive detector: $I_0 = (I_U + I_D)/2$. If we can instead obtain a measurement of only the component I_U, then we can define the outgoing beam polarization $P(\theta)$ produced by the reaction $X(a,\vec{b})Y$ as

$$P(\theta) = \left(\frac{I_U}{I_0} - 1\right) = \frac{(I_U - I_D)}{(I_U + I_D)} ,$$

where all intensities are obtained at the angle θ. This expression takes the values +1 (or -1) for a fully-polarized spin-up (or spin-down) outgoing beam, and the value zero for an unpolarized ($I_U = I_D$) beam.

Again returning to our basic cross-section experiment, we express the analyzing power $A(\theta)$ as a measure of the effect on the reaction cross section of polarization in the incident beam. To do this, we measure the difference in outgoing intensities $(I_0 - I_P)$ obtained with incoming unpolarized (I_0) and polarized (I_P) beams. In analogy to our definition of $P(\theta)$, we define the analyzing power $A(\theta)$ of the reaction $X(\vec{a},b)Y$ for a fully polarized incident spin-up beam as

$$A(\theta) \equiv (I_P - I_0)/I_0 = (I_P/I_0 - 1),$$

where all intensities are obtained at the angle θ. Maximum and minimum values of $A(\theta)$ are +1 and -1; if there is no change in intensity, $A(\theta) = 0$.

The operational definitions of P and A above appear quite straightforward, but their application uncovers two crucial problems. First, our polarization measurement requires a polarization-sensitive detector of some sort; second, our analyzing power experiment demands a source of incident polarized beam. Neither of these technologies is readily apparent from our simple $\sigma(\theta)$ scattering experiment. Before returning to their development, however, we will first examine the theoretical implications of a comparison of the two observables $A(\theta)$ and $P(\theta)$ for the same reaction. Our definitions thus far are sufficient for a basic understanding, and a look at the significance of the measurements will motivate our discussion of further experimental details.

B. Theoretical Relationships between P and A
Spin Observable Constraints

Following a presentation made by Arnold (1977), we can develop some relationships between the three observables P, A, and K. We will write the general transition probabilities between initial and final spin states as T_{fi}. To illustrate, for measurement of a cross section $\sigma(\theta)$ we sum over all spin directions in the incident and exit channels and normalize to unity:

$$\sigma(\theta) = T_{+-} + T_{++} + T_{-+} + T_{--} \equiv 1.$$

In a polarization measurement, incident spins are summed to give an unpolarized beam, and $P(\theta)$ is calculated as the difference of probabilities for outgoing spin up and down:

$$P(\theta) = (T_{+-} + T_{++}) - (T_{--} + T_{-+}).$$

If the incident beam is polarized, we measure the analyzing power $A(\theta)$ as the difference in sums over outgoing polarizations and the polarization transfer as the difference between correlated and anti-correlated incident and exit spin probabilities:

$$A(\theta) = (T_{++} + T_{-+}) - (T_{+-} + T_{--})$$
$$K(\theta) = (T_{++} + T_{--}) - (T_{-+} + T_{+-})$$

The comparison between P and A may now be expressed as a difference in transition probabilities, i.e.,

$$P - A = 2(T_{+-} - T_{-+})$$

The last result suggests an important role for spin-flip probabilities. Note also that $K(\theta)$ is the difference between flip and non-flip probabilities. We focus on this spin-flip aspect by defining the spin-flip probability $S(\theta)$ as

$$S(\theta) = T_{+-} + T_{-+} = (1 - K(\theta))/2$$

and the spin-flip asymmetry $\Delta S(\theta)$ as

$$\Delta S(\theta) = T_{+-} - T_{-+} = (A - P)/2. \qquad (1)$$

As probabilities, T_{+-} and T_{-+} are both positive, so algebraically their sum and difference are related by:

$$|T_{-+} - T_{+-}| \leq T_{+-} + T_{-+}$$

$$|\Delta S| \leq S \qquad (2)$$

$$|A - P| \leq 2S \qquad (3)$$

Equations (1) thru (3) above allow us to draw some significant conclusions about differences between A and P. First, from (2), $\Delta S \neq 0$ obtains only with a non-zero spin-flip probability $S \neq 0$. Since spin flip is forbidden for spin-zero targets by parity conservation, we obtain the trivial result that $P \equiv A$ for their case. This result suggests that target spin may be a necessary consideration in understanding cases of $P \neq A$. Further, to obtain $P \neq A$, the $\Delta S \neq 0$ condition (3) states that

spin flip alone is insufficient; one must have an asymmetric spin flip, i.e., unequal probabilities for T_{+-} and T_{-+}. In other words, the (incident spin down) → (exit spin up) and (incident spin up) → (exit spin down) reaction rates must be somehow different.

We summarize the results up to this point: an asymmetric spin-flip mechanism is a necessary condition for $P \neq A$. Arnold proceeds to discuss possible $\Delta S \neq 0$ mechanisms, and we will pick up his argument in a later discussion.

Symmetry Constraints: Conzett's Theorem

We now turn to an approach with a somewhat different viewpoint, the one which historically suggested the measurements made here. Let us compare P and A for the reaction X(a,b)Y. We use the notation $X(\vec{a},b)Y$ to denote either the reaction, the A experiment, or the observable A for the reaction, and likewise for $X(a,\vec{b})Y$ and the parameter P.

In order to study differences in A and P, we must compare the reactions $X(\vec{a},b)Y$ and $X(a,\vec{b})Y$. In the simplest view, the crucial difference is polarized <u>incident</u> versus polarized <u>exit</u> beams. This distinction can be emphasized by specializing to $\underline{a} = \underline{b}$, hence $\underline{X} = \underline{Y}$, which gives elastic scattering. For the resulting comparison of $X(\vec{a},a)X$ with $X(a,\vec{a})X$, the incident versus exit beam polarizations are now the only differences. The identity of P and A for such cases was discussed by Blin-Stoyle (1952), who showed that equality was obtained for spin-½ projectiles, provided the Hamiltonian was invariant under time reversal and rotation or reflection of the coordinate system. Although its primary application was

to elastic scattering processes, the theorem was more general and applied to "inverse reactions" for which $a + X \rightarrow Y + b$ and $b + Y \rightarrow X + a$.

Before this extension of the theorem can be useful, we must look more carefully at its conditions. In 1958, an article appeared which dropped the requirement for spatial symmetry and generalized the result to spin moments greater than $\frac{1}{2}$ (Satchler, 1958); this paper is commonly referenced as the "polarization-analyzing power equality." Although not crucial to our analysis, it was Satchler's theorem that prompted Biedenharn (1958) to point out the significance of "inverse reactions." The previous articles implicitly required that two reactions be defined as inverses if they were interchanges under time reversal-which is not true in processes which involve inelastic as well as elastic processes. Biedenharn showed that reversibility was not required, but that simpler reciprocity was sufficient. The only requirement for insuring this reciprocity of the $X(a,\vec{b})Y$ and $X(\vec{a},b)Y$ experiments is that the momenta involved be reversed appropriately.

Biedenharn's theorem then gives exactly the condition needed to generalize the polarization-analyzing power equality for elastic scattering to our P and A measurements for reciprocal reactions, i.e.,

$$(A) = X(\vec{a},b)Y = Y(b,\vec{a})X = (P_R).$$

To proceed further, we restrict our discussion to the quasi-elastic (p,n) reactions as involved in this study. Rewriting the above equation, we obtain

$$(A) = C(\vec{p},n)A = A(n,\vec{p})C = (P_R).$$

For example, this result would give A for the $^{9}Be(\vec{p},n)^{9}B$ reaction equal to P_R for its reciprocal $^{9}B(n,\vec{p})^{9}Be$.

However, we need P, not P_R; to compare these two quantities, we must examine

$$(P_R) = A(n,\vec{p})C \quad \text{versus} \quad C(p,\vec{n})A = (P)$$

By our definition of a quasielastic (p,n) reaction, A and C are simply related by isospin reflection, as are p and n. Specifically, in our previous discussion we showed that the matrix element for the (p,n) transition was $\langle t_+ T_- \rangle = 2\sqrt{2T}\, U_1/A$. Similarly, the (n,p) transition is produced by the $t_- T_+$ term of the $\vec{t} \cdot \vec{T}$ operator and is $\langle t_- T_+ \rangle = 2\sqrt{2T}\, U_1/A$ also. In the limit of exact charge symmetry, we thus obtain $P_R = P$ by rotation of C into A and p into n, thereby emphasizing the importance of the (p,n) mirror transition. In summary, from reciprocity ($A = P_R$) and charge symmetry ($P_R = P$) together we obtain $A = P$.

This $A = P$ result was first obtained by Conzett (1974) and is now known as Conzett's Theorem. Since the reciprocity step is on firm ground, we are led to connect differences between P and A with breaking of exact isospin symmetry. We reiterate: a breaking of isospin symmetry is necessary for $P \neq A$.

The results of the two above discussions can be combined to obtain the following two minimum requirements for observation of $P \neq A$ in (p,n) mirror reactions:

(1) asymmetric spin-flip transition, and

(2) isospin symmetry breaking.

This concludes our introductory comments on the theoretical implications of P and A comparisons. After presenting the empirical results of several cases, we will use these two requirements as a basis for more interpretation.

C. Comparison of Experimental Techniques for P and A Double-Scattering Experiments

To review, we began our comparison of the measurements of P and A by introducing polarization degrees of freedom into a cross-section experiment X(a,b)Y. Basically, for $A(\theta)$ we polarize the incident beam and measure the change in the cross section for the reaction $X(\vec{a},b)Y$. For $P(\theta)$, we measure the outgoing beam polarization produced with an incident unpolarized beam in the reaction $X(\vec{a},b)Y$. We now pick up our experimental discussion and solve the problems encountered previously, i.e., the development of polarization detectors and sources of polarized beams. This discussion is largely historical, but it provides a crucial insight into the relationship between the P and A experimental techniques.

Remember that our $\sigma(\theta)$ measurement involves the reaction X(a,b)Y. Basically, to make a P measurement, i.e., $X(a,\vec{b})Y$, we have the incident unpolarized beam a, but our cross-section experiment detectors are not sensitive to the polarization of the outgoing beam $\vec{b}$. Conversely, for the A measurement, $X(\vec{a},b)Y$, we have no polarized beam source for $\vec{a}$, although we can basically use cross-section detection techniques for b.

An obvious solution to the above dilemma is to couple the two A and P experiments, first using an $X(a,\vec{b})Y$ reaction to provide the beam $\vec{b}$ of polarization P_1 needed for a second $Q(\vec{b},c)R$ reaction with analyzing

power A_2. As discussed below, the cross section $\sigma(\theta_1,\theta_2)$ for this two-step, or double-scattering, experiment is related to the separate cross sections $\sigma_1(\theta_1)$ and $\sigma_2(\theta_2)$ by

$$\sigma_{12}(\theta_1,\theta_2) = \sigma_1(\theta_1)\sigma_2(\theta_2)[1 + P_1(\theta_1) \cdot A_2(\theta_2)].$$

In general, using this technique allows the effects of polarizations to be observed but not completely measured, since the two unknowns P_1 and A_2 are inseparable.

The solution to this problem comes from using the polarization-analyzing power theorem for reciprocal reactions discussed above. Applying reciprocity to a polarization measurement $P(\theta_1)$ in $X(a,\vec{b})Y$ gives equality with the inverse analyzing power $A_I(\theta_2)$ in $Y(\vec{b},a)X$. Applying this result to our double-scattering experiment, we see that the selection of a pair of reactions for which our theorem is valid can give us a relation $\sigma_{12} = \sigma_1\sigma_2(1 + A^2)$, which can be solved for the observable A in closed for unambiguously. The classic example of reactions which assure such validity is, of course, elastic scattering, for which $A(\vec{a},a)A$ and $A(a,\vec{a})A$ are completely equivalent. Once we have performed one experiment in this way, we have calibrated a reaction both as a source <u>of</u> or as an analyzer <u>for</u> polarized beams, allowing us to bootstrap our way through other reactions. For an incident beam polarization P_b and reaction analyzing power $A(\theta)$, we may thus write the reaction cross section $\sigma_P(\theta)$ as $\sigma_P(\theta) = \sigma_0(\theta)[1 + P_bA(\theta)]$, where $\sigma_0(\theta)$ is the unpolarized cross section.

We now see that the polarized beam "sources" and polarization "detectors" which we originally needed are reactions themselves, essentially

experiments in their own right. With the advent of atomic beam polarized ion sources in the late 1960's, polarized beams of $\vec{p}$, $\vec{d}$, and $\vec{t}$ particles became available directly and largely replaced the first step of double-scattering experiments, the beam polarizing step. Such sources have since made analyzing power measurements much easier. However, the double-scattering technique is still necessary in polarization measurements, with the second scattering from a calibrated analyzer giving the polarization of the outgoing target beam. Therefore, both P and A measurements include the analyzing of polarized beams; in both cases we measure the difference between polarized and unpolarized cross sections in terms of the same quantity, $\varepsilon = PA$. This relationship is the end result of this section, and it provides the basic viewpoint for our individual A and P experiment discussions. For an analyzing power experiment, $A(\theta) = \varepsilon(\theta)/p_b$, where p_b is the known ion source beam polarization. In a polarization experiment, $P(\theta) = \varepsilon(\theta)/\overline{A}$, and $\overline{A}$ is the calibrated scatterer's analyzing power.

Measurement of the Scattering Asymmetry $\varepsilon(\theta)$

Since in both P and A experiments the observed quantity is the scattering asymmetry $\varepsilon(\theta)$ of a polarized beam, we can initially discuss the techniques for this measurement from a point of view unrestricted to either the A or P experiments. In developing these techniques it is helpful to remember that we must determine the effect polarization of the incoming beam has on the scattering cross section. That is, we can measure a number of counts $N_p(\theta)$ at an exit angle θ with an incident polarized beam and normalize to the number $N_0(\theta)$ obtained with the beam unpolarized.

Since this ratio is unity in the absence of any polarization effect, we conveniently indicate the amount of effect by defining

$$\varepsilon(\theta) = \frac{N_p(\theta)}{N_0(\theta)} - 1 \ . \tag{1}$$

To agree with our previous discussion, this expression can be rewritten as $N_p(\theta) = N_0(\theta)(1 + \varepsilon(\theta))$. For a spin-dependent observable such as $\varepsilon(\theta)$, spatial symmetries are often important. By integrating over 2π and requiring that $\int N_p(\theta)d\theta = \int N_0(\theta)d\theta$, we observe that $\varepsilon(\theta)$ is odd under left-right reflection, i.e.,

$$\varepsilon(-\theta) = -\varepsilon(\theta). \tag{2}$$

Substituting our definition (1) into this equation gives the relation $N(\theta) + N(-\theta) = 2N_0(\theta)$. If we denote $N(\theta)$ as N_+, $N(-\theta)$ as N_-, and $N_0(\theta)$ as N_0, we can rewrite this as

$$N_+ + N_- = 2N_0 \ . \tag{3}$$

Substituting (3) into (1), we finally obtain

$$\varepsilon(\theta) = \frac{(N_+ - N_-)}{(N_+ + N_-)} \ . \tag{4}$$

This last relation explains the reference to $\varepsilon(\theta)$ as the left-right asymmetry produced in the scattering process and suggests the notation $N_+ = N_L$ and $N_- = N_R$ for scattering to the left and right detectors. The discussion of spatial reflection also suggests that equivalent measurements could be made either by reversing the incident beam quantization axis (spin-flip) and obtaining $N_U = N_+$ and $N_0 = N_-$, or by moving the

detector from left to right sides of the beam. By studying the special features of these two approaches we can then appreciate the advantages of a third, more general method.

The primary difficulty with an asymmetry measurement conducted with a single detector is the requirement that the only change in the left-right or up-down configurations be the detector position or the spin direction, since any other changes, such as in beam integration or alignment, will produce instrumental errors. This suggests placing detectors on both the left and right sides of the beam and measuring N_L and N_R simultaneously, so that no re-alignment is needed and beam integration will affect both counting rates symmetrically.

In eliminating the beam integration problem, however, we have introduced instrumental asymmetries due to generally different detector efficiencies or positions. However, the one-detector spin-flip experiment suggests that the two detectors may be effectively interchanged by reversing the incident spin direction. When the measurement is done as described below, the method of using two detectors and alternately reversing the spin direction will allow cancellation of first-order instrumental asymmetries. This technique has been the basis of most polarization experiments at this laboratory for several years, and we have acquired considerable confidence in its reliability.

Correction for Instrumental Asymmetries

To make these points clearer, we must write down expressions for the detector asymmetries which are experimentally measured in each of these

cases, adapting the discussion of Ohlsen and Keaton (1973). Starting from our relation $N_p = N_0(1 + \varepsilon)$, we make explicit the various factors determining N by writing $N = fqt(1 + \varepsilon)$, where f is the detector efficiency (including solid angle), q is the number of incident particles, t is the target thickness in nuclei per unit area, and ε is the desired true scattering asymmetry. In a one-detector, spin-flip experiment we obtain $N_U = fq_U t(1 + \varepsilon)$, $N_D = fq_D(1 - \varepsilon)$, with an obvious notation. We now define an observable $\alpha = (1 + \varepsilon)/(1 - \varepsilon)$ and easily obtain $\alpha = (\frac{N_U}{N_D})\ (q_D/q_U) = (q_D/q_U)\alpha'$, where α' is the measured ratio of spin-up to spin-down counts. The presence of the q_D/q_U term means that we are clearly dependent on good beam current integration in using this method.

In the two-detector, non-flip experiment, the corresponding quantities are $N_L = f_L qt(1 + \varepsilon)$, $N_R = f_R qt(1 - \varepsilon)$, and $\alpha = (f_R/f_L)\alpha'$, where α' is now the observed ratio of left to right detector counting rates. Since f includes both efficiency and solid angle, we must here use identical detectors at exactly the same distances or else attempt to correct for their differences.

In the two-detector, spin-flip experiment, we obtain four N's for combinations of down spin with left or right detector. These four quantities are:

$$N_{LU} = f_L q_U(1 + \varepsilon)$$
$$N_{LD} = f_L q_D(1 - \varepsilon)$$
$$N_{RU} = f_R q_U(1 - \varepsilon)$$
$$N_{RD} = f_R q_D(1 + \varepsilon).$$

We then observe that we may form $\alpha = (1 + \varepsilon)/(1 - \varepsilon)$ as either

$$\alpha_L = \frac{N_{LU}}{N_{LD}} \frac{f_L q_D}{f_L q_U} \equiv \alpha_L' \frac{q_D}{q_U}$$

or as

$$\alpha_R = \frac{N_{RD}}{N_{RU}} \frac{f_R q_U}{f_R q_D} \equiv \alpha_R' \frac{q_U}{q_D} ,$$

with α_L' and α_R' the up-down counting ratios defined as in the previous arrangements. If we take α to be the geometric mean of these two quantities, we obtain

$$\alpha \equiv (\alpha_L \alpha_R)^{\frac{1}{2}} = (\alpha_L' \alpha_R')^{\frac{1}{2}} = [(N_{LU}/N_{RU})(N_{RD}/N_{LD})]^{\frac{1}{2}},$$

$$\varepsilon = (\alpha - 1)/(\alpha + 1)$$

with no corrections needed. We further note that we may define a corrected detector pair $L = (N_{LU}N_{RD})^{\frac{1}{2}}$ and $R = (N_{LD}N_{RU})^{\frac{1}{2}}$, thus interpreting our α as L/R, an effective left-right ratio.

We have shown above that the "two-detector spin-flip" experimental arrangement allows complete cancellation of the instrumental asymmetries in the one detector or non-flip arrangements discussed previously. The only crucial assumptions made are that f_L and f_R are the same for spin up and spin down, and that q_U and q_D are not correlated to left or right detectors. The first assumption requires that there be no count rate losses, the second that the spin flip be a "proper flip," as discussed by Ohlsen and Keaton (1973).

We have now presented the general method of calculating $\varepsilon(\theta)$ for either a polarization or analyzing power experiment. To further explain the actual measurements we must discuss the different characteristics of

polarization and analyzing power measurements. After we have discussed the determination of the various N's above, we will return to our $\varepsilon = (\alpha - 1)/(\alpha + 1)$, $\alpha = [\,(N_{LU}N_{RD})/(N_{RU}N_{LD})\,]^{\frac{1}{2}}$ results above for detailed analysis.

II. ANALYZING POWER EXPERIMENT TECHNIQUES

A. Beam Polarization Measurement

This discussion of measurement of $A(\theta) = \varepsilon(\theta)/p_b$ separates naturally into the problems of measuring p_b and those involved in obtaining $\varepsilon(\theta)$. Turning first to the beam polarization measurement, we remark that the advantage of a polarized ion source over a double-scattering experiment is not only its higher beam intensity, but also its facility for accurate measurement of beam polarization without a separate scattering experiment. Since this accuracy is crucial to our P and A comparison, we will discuss the technique in some detail. On the other hand, we leave the description of the ion source itself to the literature (Clegg, Bissinger, and Trainor, 1974).

The method used at this laboratory to determine the polarization of the beam from the ion source is known as the quench ratio technique, which is briefly discussed elsewhere (Lisowski, 1973). We simply state that the quench ratio is an atomic beam measurement used to determine the ratio $Q = I_t/(I_t - I_p)$. Here I_t is the total beam current, with an unpolarized component $(I_t - I_p)$, where I_p is the fully polarized beam current. The beam polarization I_p/I_t is then obtained from $p_b = (1 - 1/Q)$.

The problem discussed here involves the more general case where the beam I_t at the polarized source spin filter consists of three components:

uncharged, 100% polarized metastable atoms (I_p); uncharged, unpolarized beam (I_b), and charged unpolarized beam (I_c). The idealized quench ratio technique measures the ratio $I_t/(I_t - I_p)$ by applying a DC electric field to the spin filter to quench the metastable beam; hence, a DC quench ratio (DCQR). The difficulty is that the electric field also deflects the charged beam, measuring instead $Q_{DC} = I_t/(I_t - I_p - I_c)$. Since the beam polarization is calculated as $p_b = (1 - 1/Q)$, obtaining p_c with Q_{DC} for Q over-estimates p_b.

To prevent the above error, we use a method which separates the components I_c and I_b. By tuning the magnetic field of the spin filter off-resonance, all I_p component is removed. Measuring a DCQR in this condition gives $Q_{DB} = (I_C + I_B)/I_B$. We then calculate the proper $Q = Q_{DC}/Q_{DB}$. For worst-case values, one might have $Q_{DC} = 5.0$ and $Q_{DB} = 1.5$, which gives:

$$p_c = 1 - 1/Q_{DC} = 0.80 \quad \text{(observed polarization)}$$
$$Q = Q_C/Q_{DB} = 3.333$$
$$p_b = 1 - 1/Q = 0.70 \quad \text{(true polarization)}$$

and

$$I_B = I_T/Q_{DC} = 0.20\ I_T$$
$$I_C = I_T(Q_{DB} - 1)/Q_{DC} = 0.10\ I_T$$
$$I_p = I_T(Q_{DC} - Q_{DB})/Q_{DC} = 0.70\ I_T$$

In situations where it was necessary to run with charged backgrounds, the performance of the ion source was carefully monitored and corrections were made as necessary.

B. Asymmetry Measurement

We now begin the discussion of the experimental techniques used to obtain the intensities $N(\theta)$ needed for the $\varepsilon(\theta)$ expressions above. We emphasize that these numbers must include only those events due to the reaction of interest; all others must be either suppressed or corrected for. This extraction is essentially the basic problem in all neutron spectroscopy.

Background Characteristics. Competing events can be classified in different ways. One approach divides them according to their source, either direct from the target assembly or indirect from the laboratory walls, floor, etc., in other words, room-scattered backgrounds. Another useful division is into particle type, i.e., neutron or gamma-induced events. Finally, even particles of the same type from the same source can often be separated by their energies, as in the case of different neutron groups from the same reaction. In summary, we can separate events into neutrons and gammas of different energies, each either target or room-scattered.

It is thus necessary in designing experiments to take advantage of the different characteristics above in separating out the particular neutron group of interest. For example, contributions from the target assembly can usually be estimated by a separate measurement with the target removed, i.e., target-out runs, although this procedure is time-consuming.

The most powerful techniques, however, can be loosely grouped into the two categories of recoil energy analysis and time correlation of events from different locations. This information, in turn, must be extracted from the actual experimental data, which is in the form of recoil

energy pulses from various detectors. This extraction often requires a considerable amount of processing and interpretation in order to reach conclusions about the nature of any particular event. An excellent basic reference for these topics is Fast Neutron Physics (Marion and Fowler, 1960).

Recoil energy analysis. The energy pulse is usually analyzed according to both its pulse height and pulse shape. The pulse height gives the total energy deposited in the detector by the event, while the shape gives decay time information which varies with the type of particle. There is thus a straightforward connection between recoil energy and the energy of a certain type of particle, and between the type of particle and the decay time of its recoil pulse. Further, recoil energies and the resulting pulse heights differ for different particles of the same energy, so pulse height analysis is also capable of separating different types of events. For example, gamma pulses are usually lower in energy than neutron pulses; in fact, in our helium gas scintillators the gamma pulse heights are so low that these detectors are virtually gamma-insensitive.

Our basic neutron energy measurement uses the recoil-energy pulse-height distribution from either hydrogen or helium scattering. The problems with this approach are poor energy resolution (less than 10%) and spectra which are difficult to unfold, as explained below. Both problems are aggravated by continuous energy distributions, as in $^{9}Be(p,n)^{9}B$, by large amounts of gamma radiation, as in $^{15}N(p,n)^{15}O$, or by very low neutron energies, as in all experiments here.

Event correlation techniques. The limitations of the energy analysis lead to a discussion of the second important class of spectroscopy techniques, the event-correlation approach. This device usually takes one of two forms, time-of-flight measurement or detector shielding. The simpler is shielding, where absorbers are placed between sources and detectors to reduce fluxes. Although most of these experiments were shielded as little as possible to minimize scattering into the detector, in the $^{15}N(p,n)^{15}O$ measurement lead plates were used to attenuate the target gamma flux and copper shadow bars were positioned to reduce background from the gas target beam stop.

The time-of-flight techniques to be discussed now were developed especially for these experiments. The advantages were particularly important, since both the gamma and low energy neutron backgrounds are particularly easy to handle in time-of-flight spectra. The continuum contribution, although not eliminated, can at least be approached with a different perspective. Further, as mentioned above, the time-of-flight requirement provides a coincidence condition between target and detector, very effectively distinguishing the time-uncorrelated room background neutrons.

The development and use of the polarized beam time-of-flight setup has been discussed in a separate paper (Lisowski et al., 1977), so only the basic difficulty and its solution will be given here. The low beam intensities of pulsed polarized beams are not sufficient for the capactive beam pick-offs normally used to generate the timing pulse. Therefore, a specially-designed scintillator was placed in the beam pipe before the target to intercept a portion of the pulsed incident beam. The resulting

photomultiplier signal was used to give reliable beam-pulse detection and timing with polarized beam currents in the nanoampere range. With the pickoff method, the chopping and bunching characteristics of the TUNL accelerator for polarized beams could be studied and optimized.

C. Experimental Arrangement

Targets and Detectors

The target-detector arrangements used in the experiments have resulted from various attempts to use the available techniques to obtain the information described above. The earliest experiment used a single NE213 liquid scintillator with pulse-shape discrimination applied against gammas. Later versions used two such detector systems or two high-pressure-helium gas scintillators, which are relatively gamma-insensitive. The last runs added the improvement of pulsed beam time-of-flight techniques. Details concerning each experiment are given in accompanying Table 6.

Electronics

As explained above, all information about the experiment must be extracted from raw data which are simply electronic signals. In even the most complex case, these signals are only (1) timing (anode or fast) pulses and linear (dynode or slow) pulses from each neutron detector, plus (2) a timing pulse from the beam pick-off. These raw signals are then processed for computer access, which may require only simple shaping or include complex combinations of discrimination, timing, and coincidence circuits.

The simplest case used two helium scintillators as neutron detectors. The only information available in this case is linear pulses which corre-

TABLE 6

PARAMETERS FOR ANALYZING POWER EXPERIMENTS

Date	Target	Thickness (mg/cm^2)	Detectors	Distance (cm)	Electronics
11-73	^{9}Be	8.5	NE 213 (single)	140	PSD
1-75	^{9}Be	8.5	NE 213	68	PSD
6-75	^{9}Be	8.5	He cell	46	
6-75	^{15}N	4.4	He cell	46	
5-76	^{15}N	4.4	NE 213	28	PSD
6-76	^{15}N	4.4	NE 213	46	PSD
8-76	^{9}Be	8.5	NE 213	64	PSD
8-76	^{15}N	3.3	NE 213	64	PSD, TOF

spond to the helium recoil energy. This recoil information must then be used to separate the events described above. The electronics for this measurement are shown schematically in Figure 20a. In this and all following figures, linear and logic pulses are indicated by bold and thin lines, respectively. The linear signal from each detector (LDET, RDET) is simply passed to a shaping amplifier (SA). For pulses above an adjustable threshold, a zero-crossing discriminator (ZCD) produces a logic pulse which is used both to gate the integrated recoil energy pulse and provide a routing signal for the interface. Again, the only information provided here is the recoil energy pulse height distribution, and the only requirement imposed is a minimum energy condition.

This energy condition proved insufficient to handle several experimental difficulties. In particular, the breakup continuum in the $^{9}Be(p,n)^{9}B$ reaction was a severe problem. Also, the gamma yield from the (^{15}N + p) reaction was high enough that one of the helium gas scintillators yielded considerable gamma background. Although such detectors are normally gamma-insensitive, in this case the normal Xenon component was exceeded and poor performance resulted. Even so, the pulse height from most gammas (i.e. high energy Compton electron pulses) was no greater than that from excited-state and room-scattered neutrons (i.e. helium recoils), so energy discrimination was generally adequate in the ^{15}N experiment. Spectra obtained with these detectors, when carefully analyzed off-line to extract remaining backgrounds, yielded data which was in very good agreement with similar results obtained using other techniques.

The next version of the experiment used liquid scintillators, and electronics are shown in Figure 20b. In this arrangement, the constant-

fraction discriminator (CFD) provides the fixed timing reference to which the varying zero-crossing time of the double-differentiated energy pulse is compared. Inspection of the time difference by the time-to-amplitude converter (TAC) provides pulse shape discrimination (PSD). Lower level energy discrimination is also provided by the CFD unit, which is therefore set to a higher bias than the ZCD and used as the TAC start pulse. For events whose pulse shapes and heights meet minimum conditions, gating and routing signals are generated as in the previous arrangement. Note, however, that now two pulse height spectra are obtained, one for recoil energy pulse height and another for pulse-shape timing. Two conditions are thus required: sufficient energy and proper pulse shape.

Although some leak-through of gamms from the PSD circuitry was observed, the n-γ discrimination time could be used as an independent spectrum. This flexibility allowed evaluation of the effect of different PSD windows on the recoil energy spectrum and resulting asymmetry values. Much of this data needed little further analysis.

The final system, shown in Figure 20c, included both pulse-shape and time-of-flight conditions. To the previous arrangement we added a lower level discriminator (LLD), which provides good time resolution, and a CFD unit triggered by the pick-off (PO) timing signal. These outputs are then timed with a TAC to provide a time-of-flight (TOF) measurement. As in the PSD circuit, the lower counting rate signal is used as the TAC start signal. The pulse-shape discrimination (PSD) window is now set by a hardware single-channel analyzer (SCA). The CFD unit in the PSD circuit again provides energy discrimination, so its SCA gate provides us with

Figure 20. Electronics for Analyzing Power Experiments

a) Helium Scintillator

b) PSD Arrangement

c) PSD and TOF Arrangement

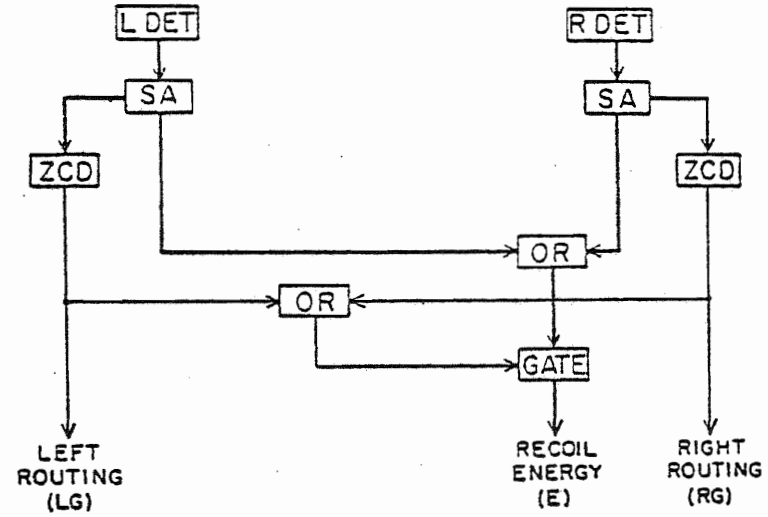
L DET
R DET
SA
SA
ZCD
ZCD
OR
OR
GATE
LEFT ROUTING (LG)
RECOIL ENERGY (E)
RIGHT ROUTING (RG)

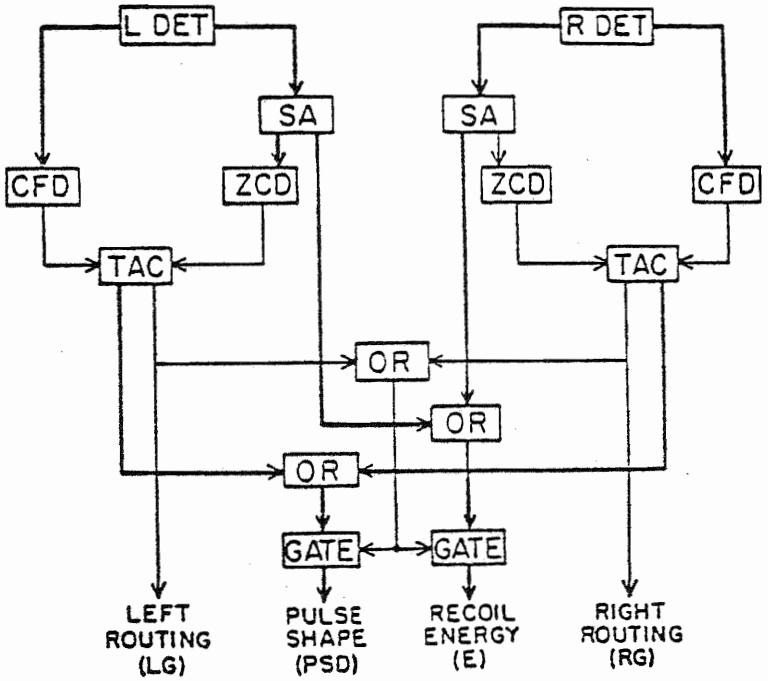
L DET
R DET
SA
SA
CFD
ZCD
ZCD
CFD
TAC
TAC
OR
OR
OR
GATE
GATE
LEFT ROUTING (LG)
PULSE SHAPE (PSD)
RECOIL ENERGY (E)
RIGHT ROUTING (RG)

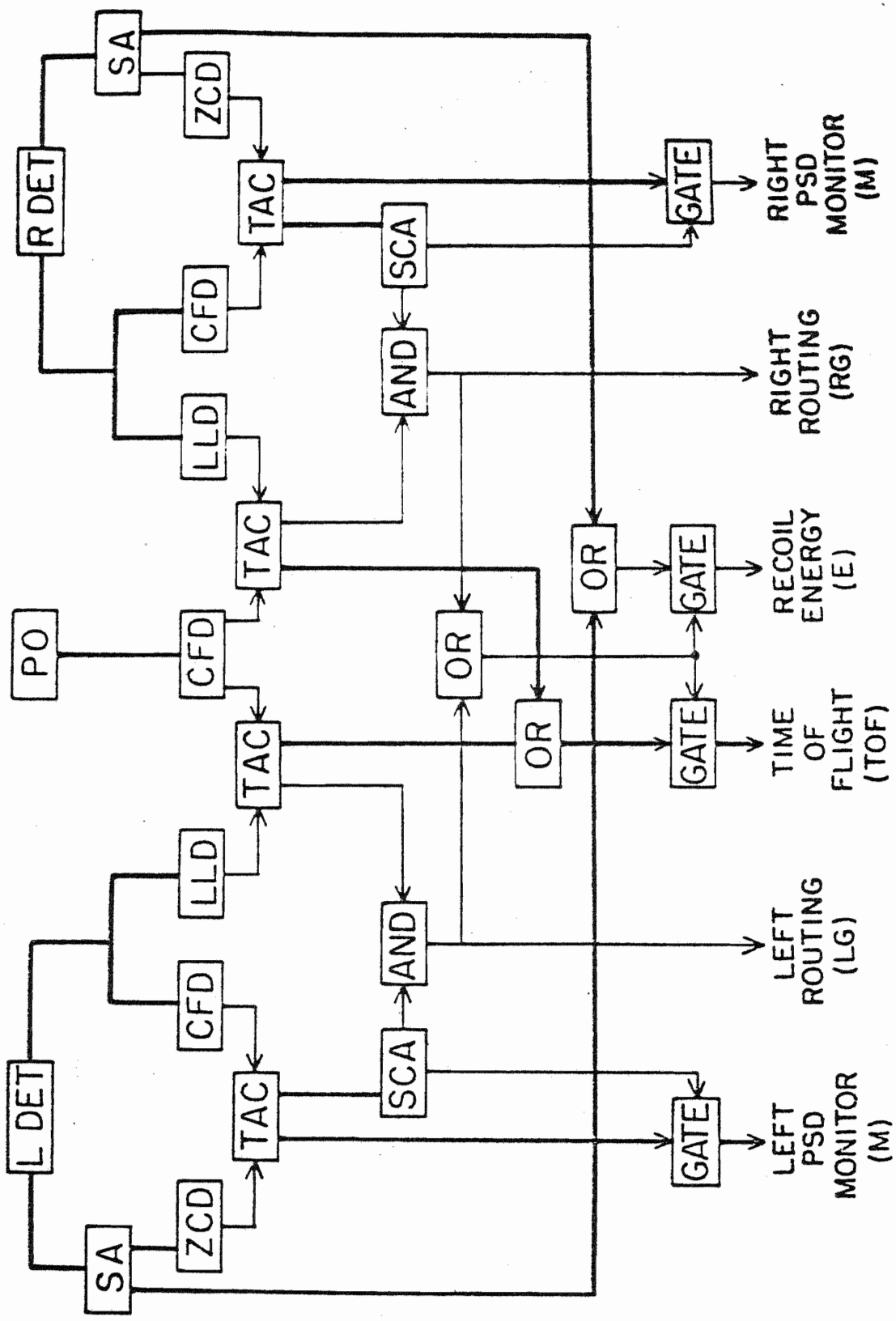
SA
ZCD
R DET
TAC
SCA
GATE
RIGHT PSD MONITOR (M)
CFD
AND
RIGHT ROUTING (RG)
LLD
TAC
OR
GATE
RECOIL ENERGY (E)
PO
CFD
OR
TAC
OR
GATE
TIME OF FLIGHT (TOF)
LLD
AND
LEFT ROUTING (LG)
CFD
L DET
SCA
TAC
GATE
LEFT PSD MONITOR (M)
ZCD
SA

both pulse-shape and energy requirements. A coincidence requirement between this signal and the TOF signal then provides not only energy, PSD, and TOF requirements, but demands a correlation between detector and target (pick-off) events which is very effective in reducing counting rates from unwanted pulses at the computer interface. This coincidence output is then used to gate and route signals as before.

Three pulse height spectra are now provided: recoil energy, pulse-shape timing (as a monitor only), and time of flight. This combination was essential in the $^{15}N(p,n)^{15}O$ experiment at energies where the PSD was unable to adequately resolve the neutrons and gammas. Also, the TOF information helped to evaluate the contribution of breakup background in the $^{9}Be(p,n)^{9}B$ experiment. At this point we have described in detail the experimental arrangements and the information they provide, but all in reference to analyzing power measurements only. The end result has been a standardized set of pulses which are presented to a computer interface and processed by a computer code to obtain the desired $N(\theta)$, $\varepsilon(\theta)$, and finally $A(\theta)$ values. We now retrace our steps and bring our discussion of the polarization experiment up to the point we have reached with the analyzing power experiment.

III. POLARIZATION EXPERIMENT TECHNIQUES

Introduction

We emphasize that in any $P(\theta)$ determination, a double-scattering process is involved; thus a convenient division is into a target reaction and an analyzing reaction. The portion of the experiment relating to the first reaction is straightforward nuclear bombardment and is largely concerned with producing as intense an outgoing flux as is usable, while the second scattering is a carefully controlled and calibrated analyzing power experiment similar to those just described. We therefore split our discussion between the first reaction, i.e., target arrangements, and the analyzer scattering, or polarimeter design.

A. Target Arrangements

The target arrangement discussion separates into a description of the target geometries used and the background problems expected. Target geometries are summarized in Table 7, and the only further explanation will be of counting rate considerations. To increase the efficiency of a double-scattering experiment, it is necessary to optimize the first reaction yield by making beam intensities and target thicknesses as large as possible within the following constraints. The limitation on beam current is heat dissipation in the ^{3}H or ^{9}Be targets themselves or in the foil window of the ^{15}N target. Maximum currents in these experiments were 1 to 2 μA.

TABLE 7

PARAMETERS FOR POLARIZATION EXPERIMENTS

Date	Target	Target Thickness (keV at E_p)	Analyzer-to-Side Detector Distance (cm)	Analyzing Angles	Data Summary: Angles (lab)	Data Summary: Energies (MeV)
5-75	^{15}N	110(10.3)	19.1	120°	10°-100°	10.3,11.3
6-75	^{9}Be	390(8.1)	24.1	"	10°-90°	8.1
9-75	^{9}Be	"	21.6	"	10°-100°	8.1,9.1,10.0
					70°	7.9-10.0
	^{15}N	160(10.3)	"	"	40°	10.2-11.3
5-76	^{15}N	"	19.1		40°-70°	11.3
					50°	11.0-11.5
6-76	^{15}N	220(6.5)	"	100°	10°-155°	5.65
			"	"	20°-140°	6.28
			"	100°,120°	20°,50°,100°	5.45-6.50
6-76	^{9}Be	120(3.0)	"	70	30°,50°,70°	3.5-8.2
		60(3.0)	"	80	20°-80°	2.9
		"	"	90	20°-50°	2.7
				100		
7-76	^{15}N	220(6.5)	"	115	20°,40°	5.65
				120	20°,50°,100°	4.55-9.2

Maximum target thickness is set by the desired energy spread in the beam, which depends on the expected resonance structure. For comparisons of P and A values, we chose target thicknesses large enough to eliminate errors due to small energy shifts but thin enough to show some of the broader resonance behavior in the reaction. The compromise was typically on the order of 200 keV.

The backgrounds are largely determined by the reactions involved and have thus already been discussed in the A experiments. We remark that the experimental situation is must the same in any neutron detection experiment, A or P, and we thus expect to use similar energy discrimination and target-detector coincidence techniques, i.e., recoil-energy detection and time-of-flight measurements.

B. Polarimeter Design

We now take up the second part of the double scattering, the analyzing reaction. Again, we emphasize that the underlying principles are the same as in our A experiment. In the P measurement, however, there are differences in the choice of analyzing reaction and the details required for efficiency and accuracy. After first describing the basic form of the polarimeter, we will briefly discuss its special features and calibration, finally explaining its use as in our previous development of asymmetry measurements in analyzing power experiments.

As shown in Figure 21, the polarimeter consists of three parts: a collimator-solenoid, a central analyzing scatterer, and a symmetric pair of side detectors. The entire assembly is mounted on a carriage which can be rotated horizontally through an angle θ_1 about the incident beam

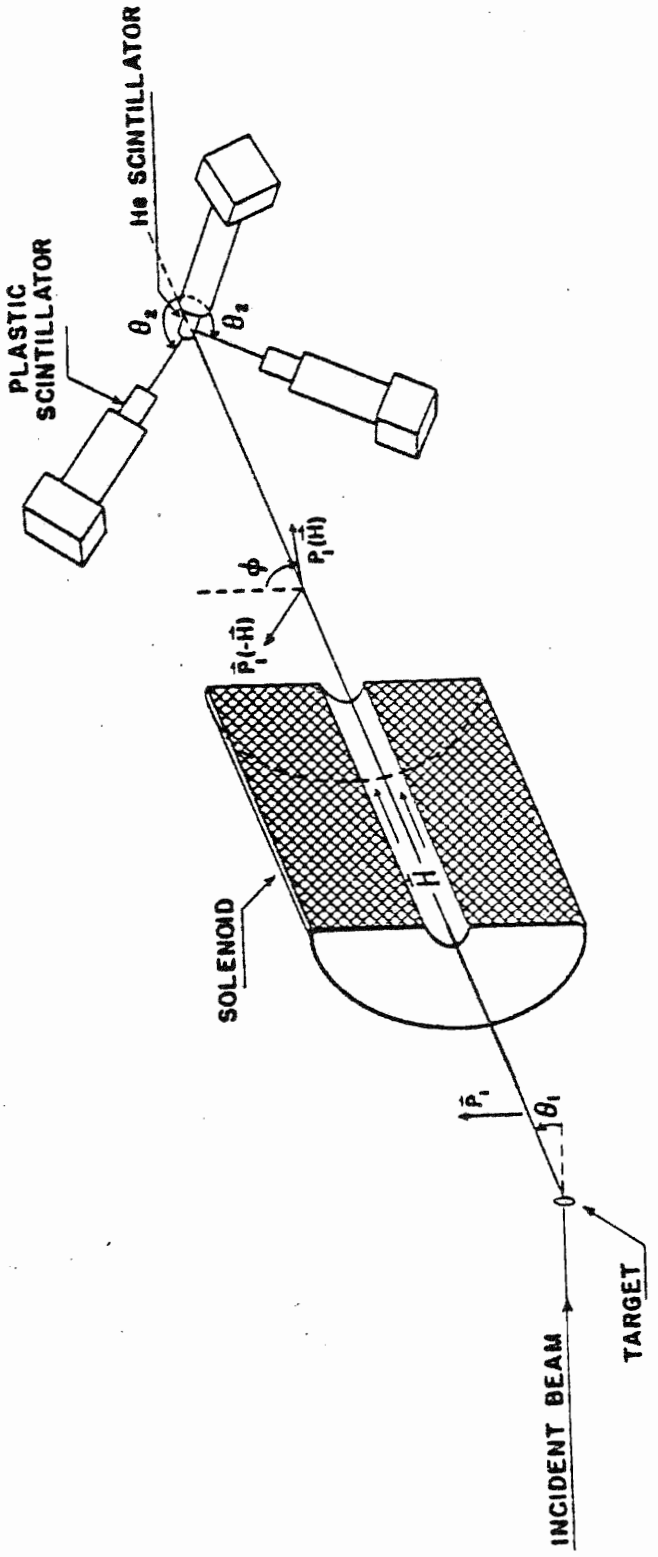

Figure 21. Neutron Polarimeter Arrangement

axis and can be moved radially to place the helium cell a distance r_1 from the target. Similarly, side detectors can be rotated in a vertical plane through an angle θ_2 from the horizontal target-scatterer axis and positioned at radial distances r_2 from the central scatterer.

The basic operation of the polarimeter is illustrated in Figures 21 and 22. Polarized neutrons from the target $(p,\vec{n})$ reaction pass through a double-truncated conical collimator, their spins precessing in a solenoidal magnetic field. Because the reaction plane is horizontal, the polarization axis of the collimated neutron beam is vertical before precession in the solenoid. Thus, by rotating clockwise or counter-clockwise through an angle ϕ (normally $\pi/2$), we may introduce a spin "flip" relative to the vertical second scattering plane. Then the collimated and precessed neutron beam is analyzed by scattering from ^{4}He up and down through θ_2 to the vertical side detectors. The ^{4}He(n,n)^{4}He elastic scattering is chosen because of its high analyzing power, i.e., greater than 90% above 0.5 MeV, because the analyzing power varies slowly with neutron energy (Walter, 1974), and because there are instrumental advantages to be presented below. Note carefully the three angles involved: θ_1 is the (p,n) reaction angle, ϕ is the precession angle, and θ_2 is the analyzing angle. We will therefore measure $P^y(\theta_1)$ by using the average analyzing power $\overline{A}_y(\theta_2)$ in the relation $P^y = \varepsilon(\theta_1,\theta_2)/\overline{A_y}(\theta_2)$. The distance r_1 between the target and scatterer is as short as possible, and the scatterer-to-side detector distance r_2 is usually a compromise, since increasing time-of-flight separation and average analyzing power comes at the expense of counting rate.

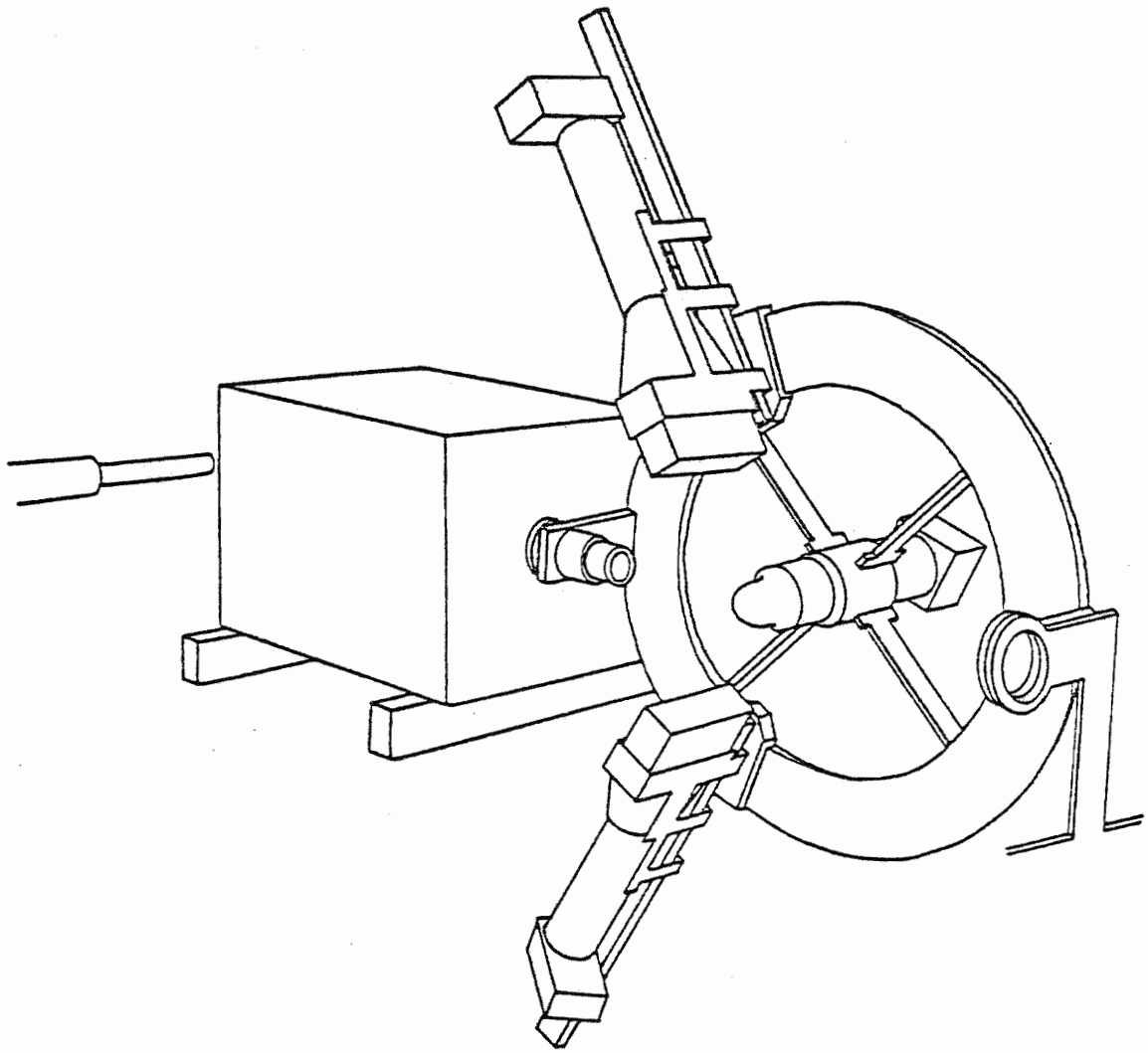

Figure 22. Detail of Neutron Polarimeter

With this physical arrangement in mind, we now discuss the calculation of the required asymmetry $\varepsilon(\theta)$ and analyzing power $\overline{A}$ in $P(\theta) = \varepsilon(\theta)/\overline{A}$. We first explain the determination of $\overline{A}$ for our polarimeter, then we discuss the measurement of $\varepsilon(\theta)$ in analogy to the approach used in the previous analyzing power experiment.

Because of count rate limitations, it is usually necessary to use tight geometries and large scatterers and detectors. The point-geometry n - ^{4}He analyzing power must then be corrected for two effects. First, the geometry must be expanded to include the variation of analyzing power over the large solid angles involved. Further, the sizable central scatterer now requires the multiple scattering corrections common in many (n,n) experiments. Both of these effects are calculated by our general Monte Carlo simulation program MOCASSINS, described in detail elsewhere (Lisowski, 1973). The adjustable parameters needed for such calculations are given in Table 7. In all cases for this work, the ^{4}He scintillator was pressurized to 200 atmospheres (6% Xe, 94% He) and NE102 plastic scintillators (5.1 × 7.6 × 15.2 cm^3) were used as side detectors. At the lowest neutron energies, it was necessary to move the side detectors toward forward angles to follow the maximum in the n - ^{4}He analyzing power, as shown in Figure 23. This figure gives the fully-corrected average analyzing power $\overline{A}$ for our polarimeter with the scatterer and side detectors separated by r_2 = 19.0 cm. In this work the lowest energy was about 0.6 MeV, and the analyzing power there reached its lowest value for all the P^y measurements, about 0.5.

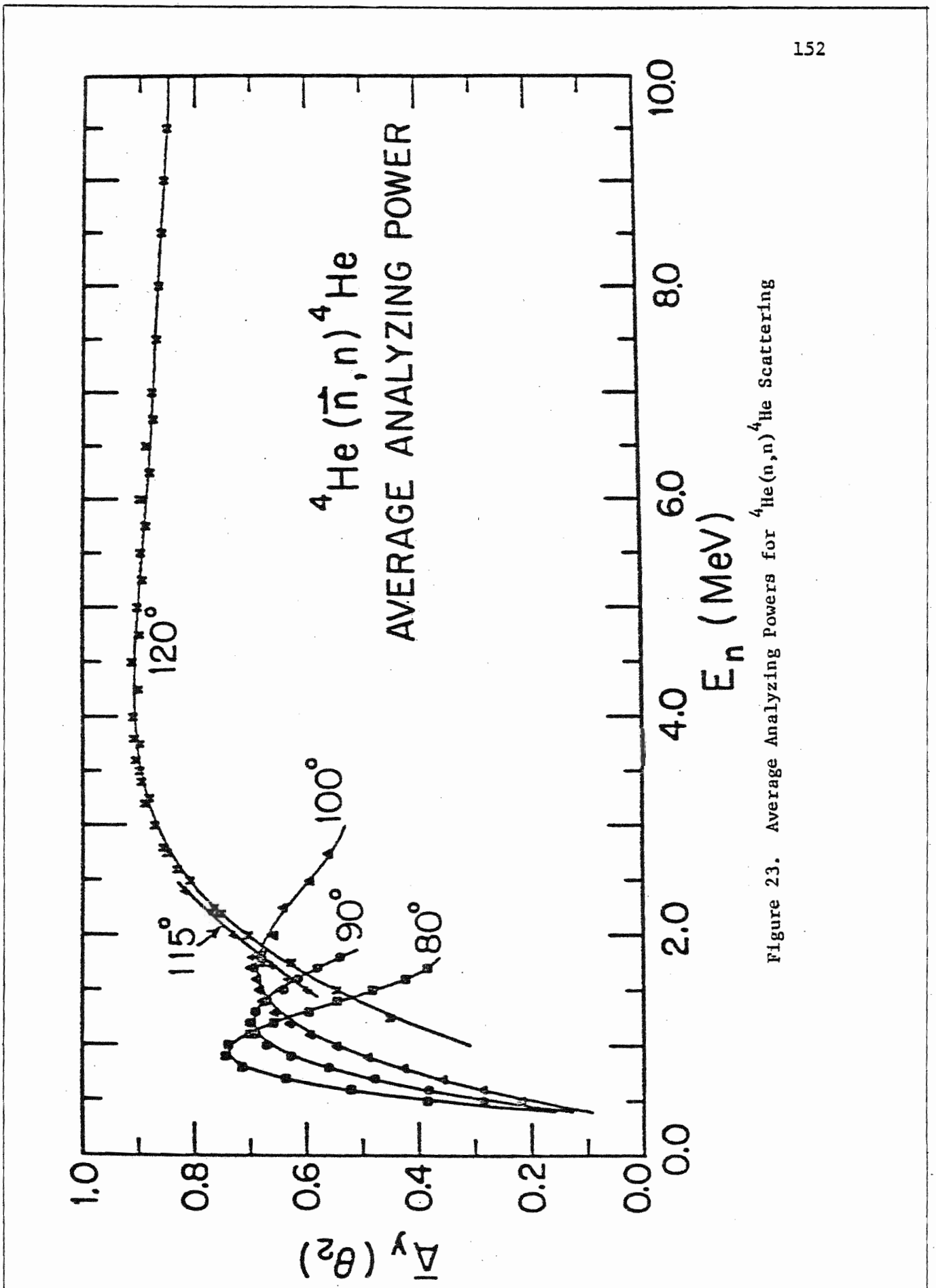

Figure 23. Average Analyzing Powers for ^{4}He(n,n)^{4}He Scattering

C. Asymmetry Measurement

Two-Detector Spin-Flip Arrangement

The remaining discussion is arranged for direct comparison and contrast with the previous analyzing power discussion. Recall that the superior experimental technique required use of a two-detector, spin-flip arrangement with gamma rejection, good energy resolution, and time-of-flight capability. All of these features can be incorporated into our polarimeter, and we now show how to collect and arrange the information needed for the equivalent $\varepsilon(\theta) = (L - R)/(L + R)$ expression.

The "spin flip" in this case is more properly a magnetic precession of the spin axis of the polarized neutron beam before the scattering from ^{4}He. To simplify the notation in this section, we point out here that our convention is to continue to refer to detectors as left and right, even though they are now physically "up" and "down." Similarly, spin directions are still called up and down, even though the actual situation is in terms of forward or reversed solenoid current, causing spin rotation either to the left or right.

The high-current spin-precession solenoid (270 A maximum) was calibrated previously using the $^{12}C(d,n)^{13}N$ reaction, and this calibration was re-checked using the reaction $T(p,n)^3He$ in the course of this work. For most of the neutron energies involved, i.e., $E_n < 7$ MeV, sufficiently high fields were available to precess the spin by $\phi = \pm 90°$, thereby allowing a complete 180° reversal of spin direction. For the very highest neutron energies, however, there was insufficient current for complete precession. The correction to the observed asymmetry $\varepsilon_{obs}(\theta)$ is then given by

$\varepsilon(\theta) = \varepsilon_{obs}(\theta)/R(\phi)$, with

$$R(\phi) = \sin \frac{\pi}{2} \frac{I(\phi)}{I(\frac{\pi}{2})} \quad ,$$

where $I(\phi)$ is the current used and $I(\pi/2)$ is that required for full $\pi/2$ precession. The worst precession corrections were only 2.5%, and generally errors were negligible because of the slow sinusoidal variation of $R(\phi)$ for $I(\phi) \approx I(\pi/2)$. With this correction we were able to take advantage of the full "proper rotation" formalism for two detectors.

Electronics

We now turn to an examination of the spectroscopy techniques used in our polarization measurements. Recall that our principal means of background elimination were shielding, gamma suppression, target-detector coincidence requirements, and energy discrimination. Our use of the massive solenoid as a collimator is an example of shielding technique, but only the direct target-side detector flux is attenuated in this way. The majority of background suppression results from the choice of ^{4}He as an analyzer, since proper design allows the scatterer to double as a scintillator with several excellent characteristics. First, this detector can be made inherently gamma-insensitive since γ - ^{4}He events yield low light output. Second, careful fabrication of the ^{4}He cell allows energy discrimination with resolutions approaching 8% (Morgan and Walter, 1968). Most important, however, pulses from the ^{4}He scatterer and side detector allow a powerful combination of recoil energy pulse height analysis and time-of-flight (TOF) energy and coincidence techniques.

To examine this capability in detail, we turn to a discussion of the polarimeter electronics. Referring to Figure 24, we first explain the separate TOF measurements for scattering to the left and right. We will use the same abbreviations as for the A experiment electronics. The TAC's are started with the low count-rate side detectors and provide the important detector-scatterer coincidence requirement. The linear signal from the ^{4}He scatterer is used for pulse height discrimination (SCA) to eliminate the events due to low-energy neutrons and many of the gamma rays, which also have low pulse heights because of the detector characteristics. A slow coincidence between the valid TOF and valid recoil energy signals provides left and right routing signals and low count rate gating of the TOF and ^{4}He recoil spectra at the computer interface.

Before proceeding further, we close our discussion of P^y experimental techniques by mentioning two further background suppression methods. In one case, a timing pick-off was inserted in the beam line before the target, and the pulsed beam system was turned on to study measurements of the time of flight between the target and scatterer. Since adequate time separation already existed in the scatterer-detector path, this improvement did not gain us much, and so this development was not carried further; however, we expect that it will be useful in later experiments requiring closer geometries or involving less separation between neutron groups. A second improvement has been the installation of $n - \gamma$ discriminating scintillators as side detectors, allowing a reduction of gamma-induced accidental backgrounds in the time spectrum.

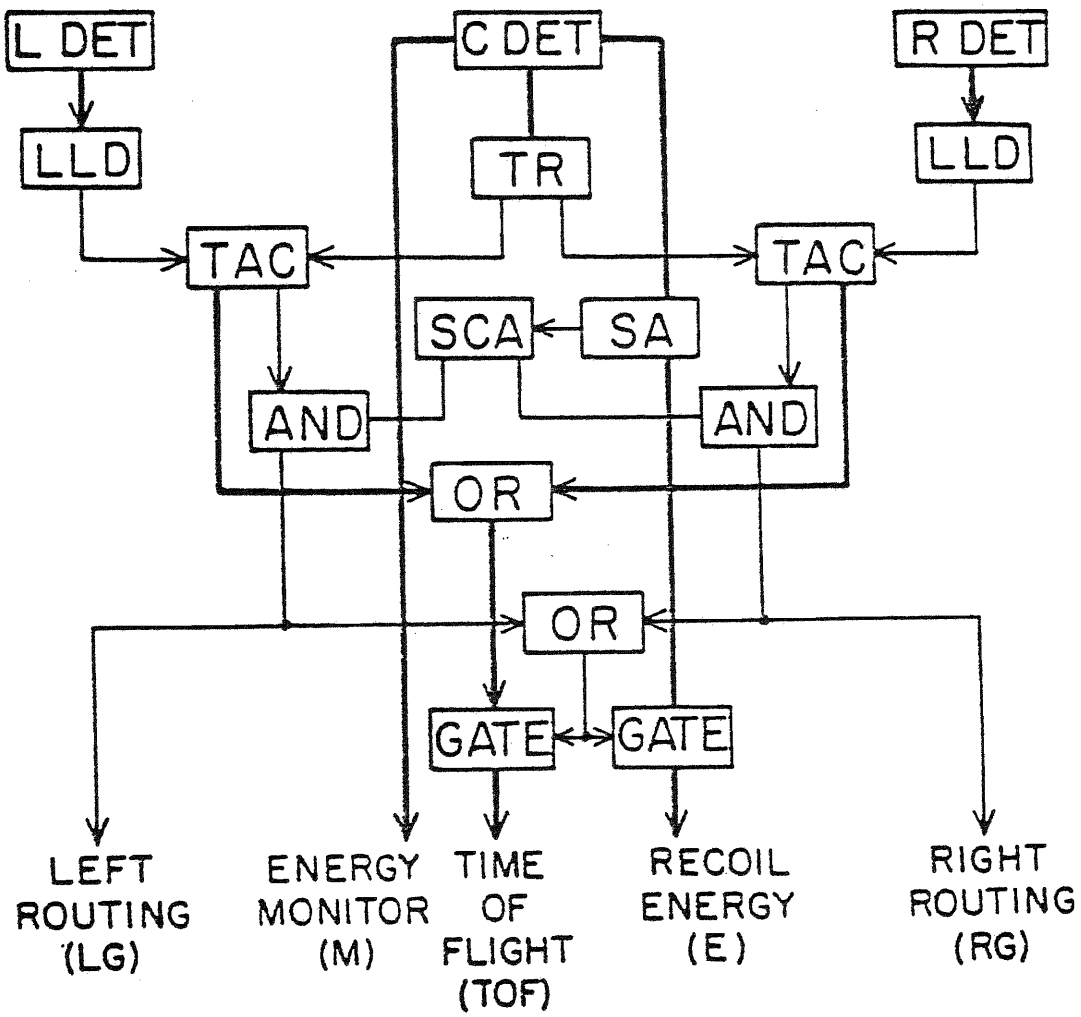

Figure 24. Electronics for Polarization Experiments

IV. DATA COLLECTION AND ANALYSIS FOR P AND A EXPERIMENTS

A. On-Line Data Manipulation

Interface

With discussions of both polarization and analyzing power experiments through the electronics stage, we again combine P and A approaches for explanation of the data-taking procedures. The interface and data processing for the $A(\theta)$ determinations are almost identical to those for $P(\theta)$. This was done in order to minimize complexity without compromising flexibility. Our discussion will lead to the extraction of the various N_{LU}, N_{RU}, etc. and to final calculations of $\varepsilon(\theta)$ for both on-line and off-line analyses. Note that the explanation generally applies to both experiments, although the shapes of spectra obtained will be different; also, some points will not concern both experiments, e.g., quench ratio measurements.

The information available from the experiment has been arranged into a standard form which allows the generalized set of computer interfacing for both P and A shown in Figure 25. In this general experiment, the electronics provides three pulse height distributions: (1) recoil energy (E), (2) pulse-shape discrimination (PSD) or time-of-flight (TOF), and (3) monitor (M). Detector routing is also obtained from left or right gating signals (LG, RG). Other devices provide target beam current integration (BCI) and spin-up or spin-down indication (SPIN). This information provides

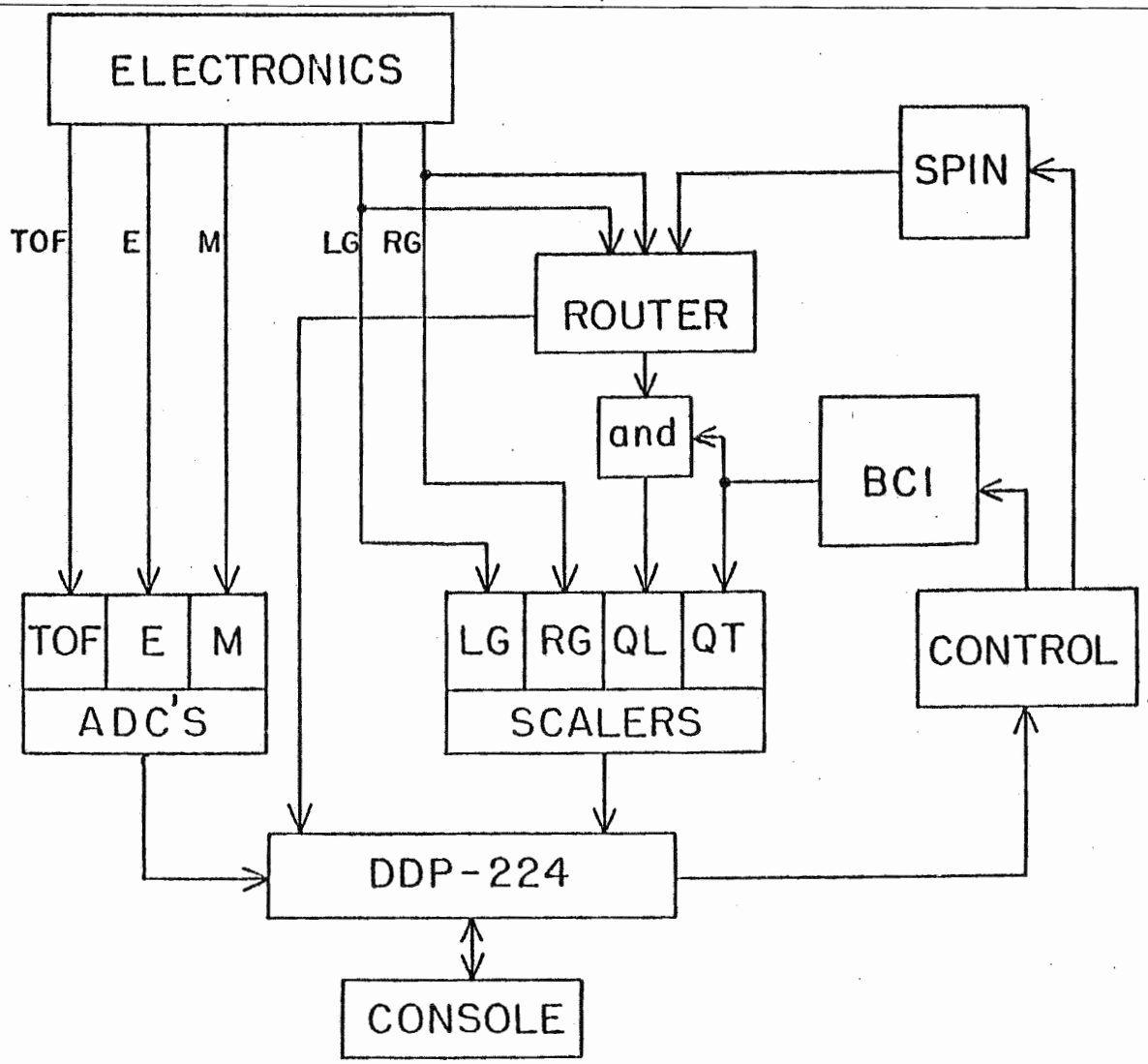

Figure 25. Computer Interfacing for A or P Experiments

a full description of the experiment and is accessed and stored by the on-line computer (DDP-224) through its interface, which converts all signals into computer-compatible form. The pulse heights are processed by analog-to-digital converters (ADC's), and the routing information is arranged and coincidenced with the ADC's. The scalars provide monitors for left and right counting rates and for both total collected charge (QT) and "live charge" (QL), i.e., collected charge gated by the router to correct for dead time. The computer also provides automatic control of appropriate devices such as the spin-rotation solenoid, beam stops, and the polarized ion source, as well as intercommunication with the experimenter through a console.

Data-Taking Sequence and Data Storage

To extract our detector sums N_{LU}, N_{RU}, etc., the above information must first be organized in some fashion. The computer automatically sequences the data collection to give a proper spin flip and thus provides error cancellation in two-detector experiments. Data for a particular measurement (energy or angle) is collected as the cumulative average of a set of independent runs, each organized as a group of quench ratio measurements Q (in the A experiments) and spin-up or spin-down counting segments N, all for the same collected charge. This entire group is sequenced symmetrically in spin directions down-up-up-down as $Q_D N_D N_U Q_U N_U N_D Q_D$ to better avoid possible correlations between detection efficiency and beam polarization changes.

Each run therefore gives four sets (two detectors for each of two spin directions) of correlated time-of-flight and recoil energy events.

These are best thought of as two-dimensional time-energy arrays which must be examined to extract the neutron group of interest from competing events. We illustrate the technique for the polarization measurement in Figure 26. For the A measurement, the procedures are similar although spectra have different shapes. First we project each of the four arrays onto the time axis, obtaining the usual neutron time-of-flight spectra for scattering to the left or right side detector. Our example shows a gamma-ray peak with n_0 and n_1 groups on a time-independent background. We then choose "true" and "accidental" windows for further inspection and re-sort each event having these flight times according to the recoil energy deposited in the central scatterer. Aside from the usefulness the true TOF window has for neutron energy discrimination, it also provides a two-body kinematics constraint as a coincidence between ^{4}He and side detector recoil pulses for scattering at the analyzing angle. This resulting spectrum is a resolution-broadened slice from the full ungated recoil spectrum. Neutron groups thus appear as peaks when projected onto the energy axis, superimposed on a smoothly decreasing background of accidental and time-correlated background. The recoil energy spectra from the accidental windows provides a direct determination of the energy dependence of the time-uncorrelated background; these spectra can thus be averaged up and down and then subtracted event-for-event from the true spectra. The resulting four energy spectra then show the recoil energy distributions for events which have passed all the experimental criteria discussed in the previous sections: recoil energy discrimination, gamma suppression, scatterer-detector coincidence, and time-of-flight. A window is placed on only the n_0 energy peak; from the sums of events in the four spectra we

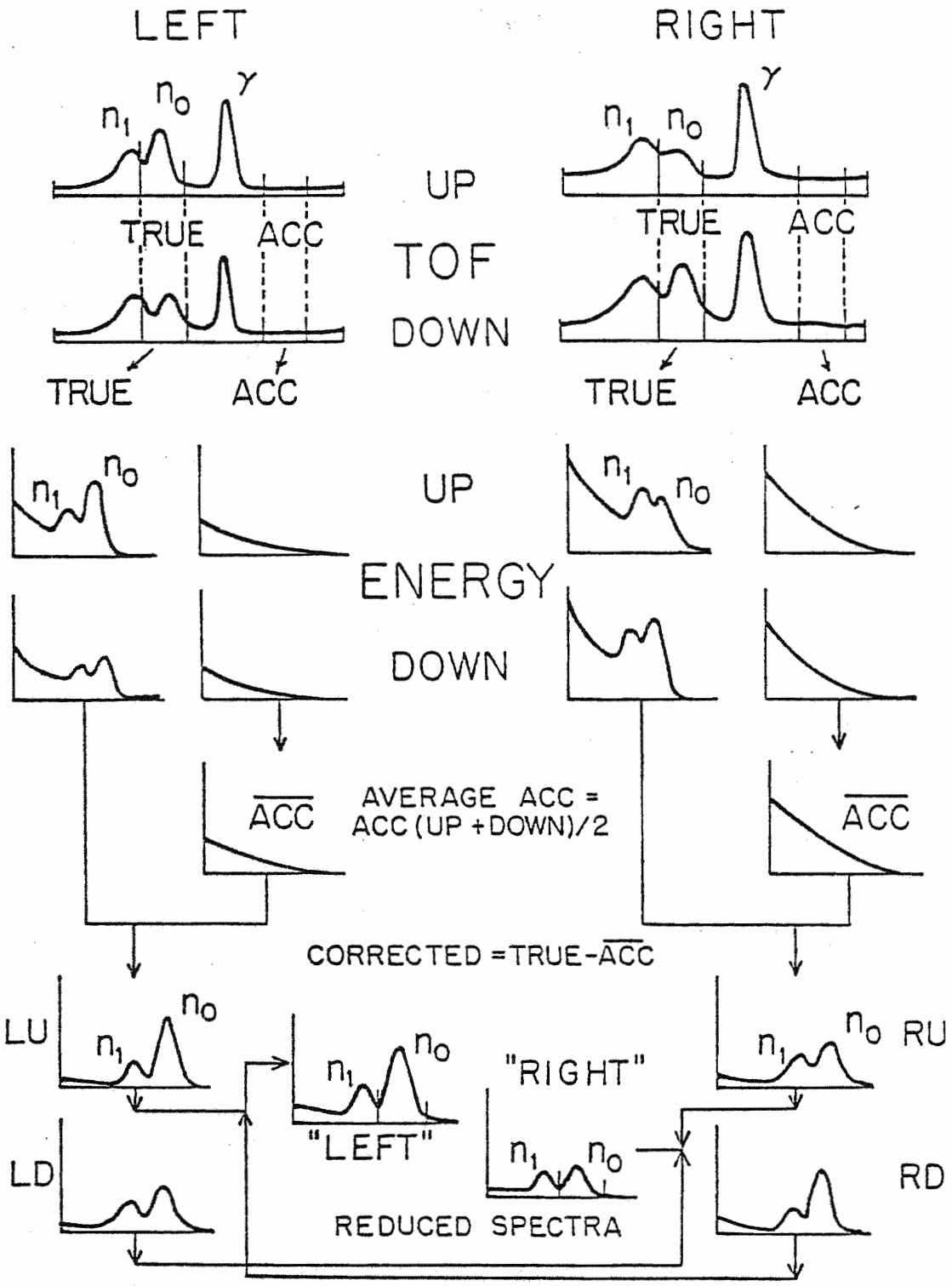

Figure 26. Arrangement and Manipulation of Time-of-Flight and Recoil Energy Spectra

finally obtain the N_{LU}, N_{LD}, N_{RU}, and N_{RD} used to calculate $\varepsilon(\theta)$ as

$$\varepsilon(\theta) = \frac{(N_{LU}N_{RD})^{\frac{1}{2}} - (N_{RU}N_{LD})^{\frac{1}{2}}}{(N_{LU}N_{RD})^{\frac{1}{2}} + (N_{LU}N_{RD})^{\frac{1}{2}}}$$

This is usually the best estimate we can obtain on-line.

B. Off-Line Data Reduction

Despite all the care taken in the design of our experiments, the on-line spectra still include varying amounts of background contamination. Clearly, time-correlated sources such as neutrons produced in the target but for neighboring states in the residual nucleus are difficult to resolve with either the TOF requirement or the recoil energy analysis. Target-out subtractions are useful for estimating such contributions, but the amount of time required to perform such measurements at every energy and angle is prohibitive. As a result, all spectra have contributions which could not be eliminated instrumentally at the time of the measurement, and their effect on the observed asymmetry must be estimated by off-line analysis. Two very powerful computer codes were developed in the course of this work, NPOLA by Dr. P. W. Lisowski for the coincidence-gated recoil spectra of polarization measurements, and RECOIL by the author for the ungated spectra of analyzing power experiments.

Polarization Analysis

The types of spectra involved have resulted in two very different spectrum stripping approaches. For NPOLA the spectrum usually consists of separate peaks superimposed on a background continuum which may be reliably interpolated across the region of interest with a suitable

parameterization. Unresolved peaks may also be approximated as gaussian shapes and described by least-squares fitting procedures. In short, in NPOLA the background shape is assumed, calculated, and extracted from the actual data. Examples of this method are shown for three different cases in Figure 27. Asymmetries and errors are then calculated using Poisson statistics and standard error propagation expressions.

An even more powerful investigation of background effects was made in the P measurement for the $T(p,n_0)^3He$ reaction, as illustrated in Figure 28. The individual time-energy events were stored on tape during the experiment so that effects of different time slices could be investigated off-line. The re-sorted energy spectra corresponding to each time slice are shown in the second row. The block asymmetry plots at the bottom result from calculating the asymmetry region-by-region across each spectrum and supplement the background shape information with background asymmetry information. This last approach is important since the background correction to be applied depends on the background asymmetry, e.g., a contribution with the same polarization as the group of interest would require <u>zero</u> correction. In the $T(p,n_0)^3He$ case shown, we see that the results justify the full correction for an unpolarized background.

Analyzing Power Analysis

The approach used in RECOIL to correct the spectra from the analyzing power measurements was somewhat the opposite of that used in NPOLA. Since the full proton (or ^4He) recoil spectrum is all that is available, there is obviously no coincidence peak. Rather, as shown in Figure 29, a continuous distribution of pulse heights is obtained with a high-energy cut-off

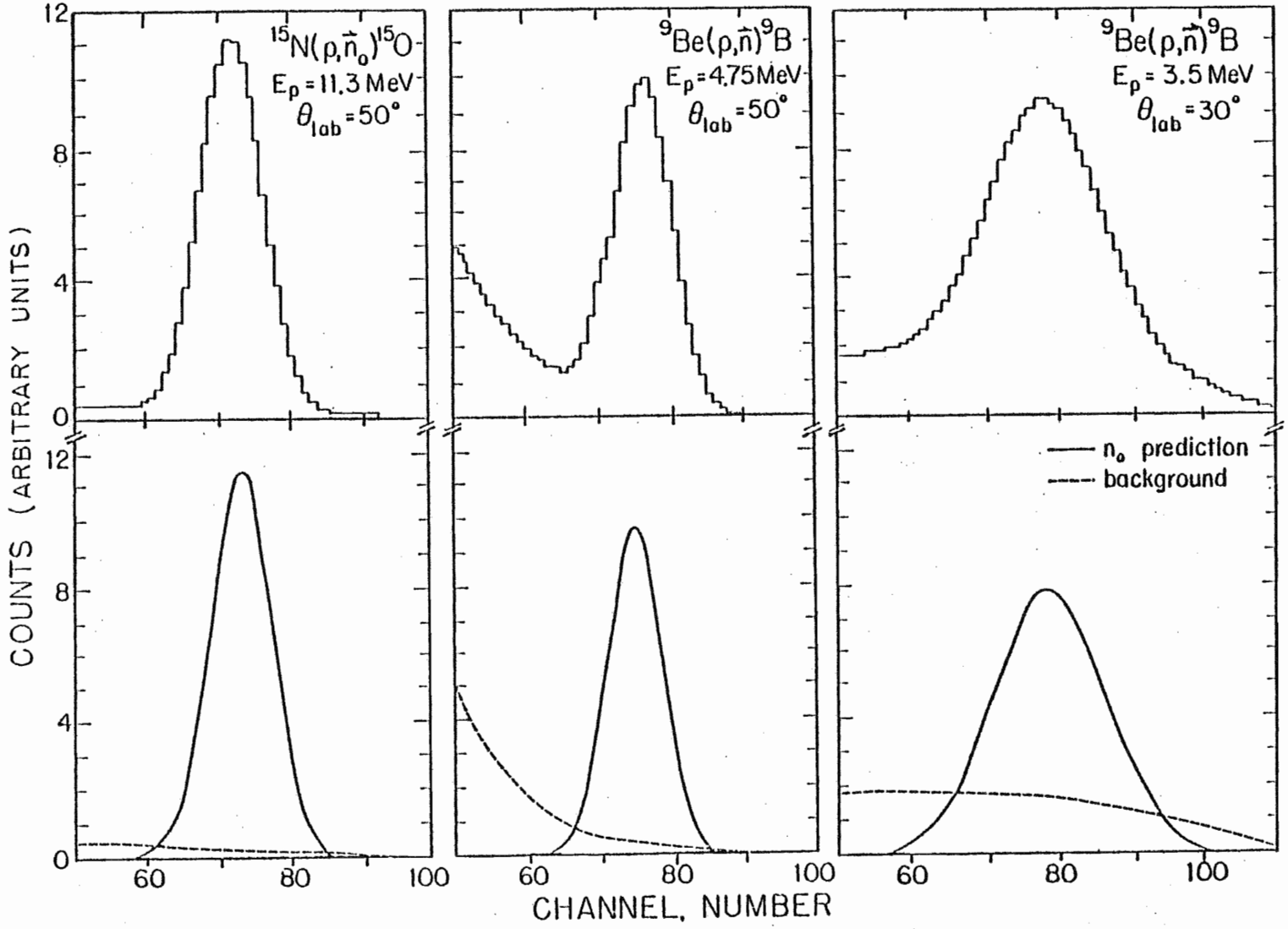

Figure 27. Typical Coincidence-Gated Recoil Energy Spectra from Neutron Polarization Experiments

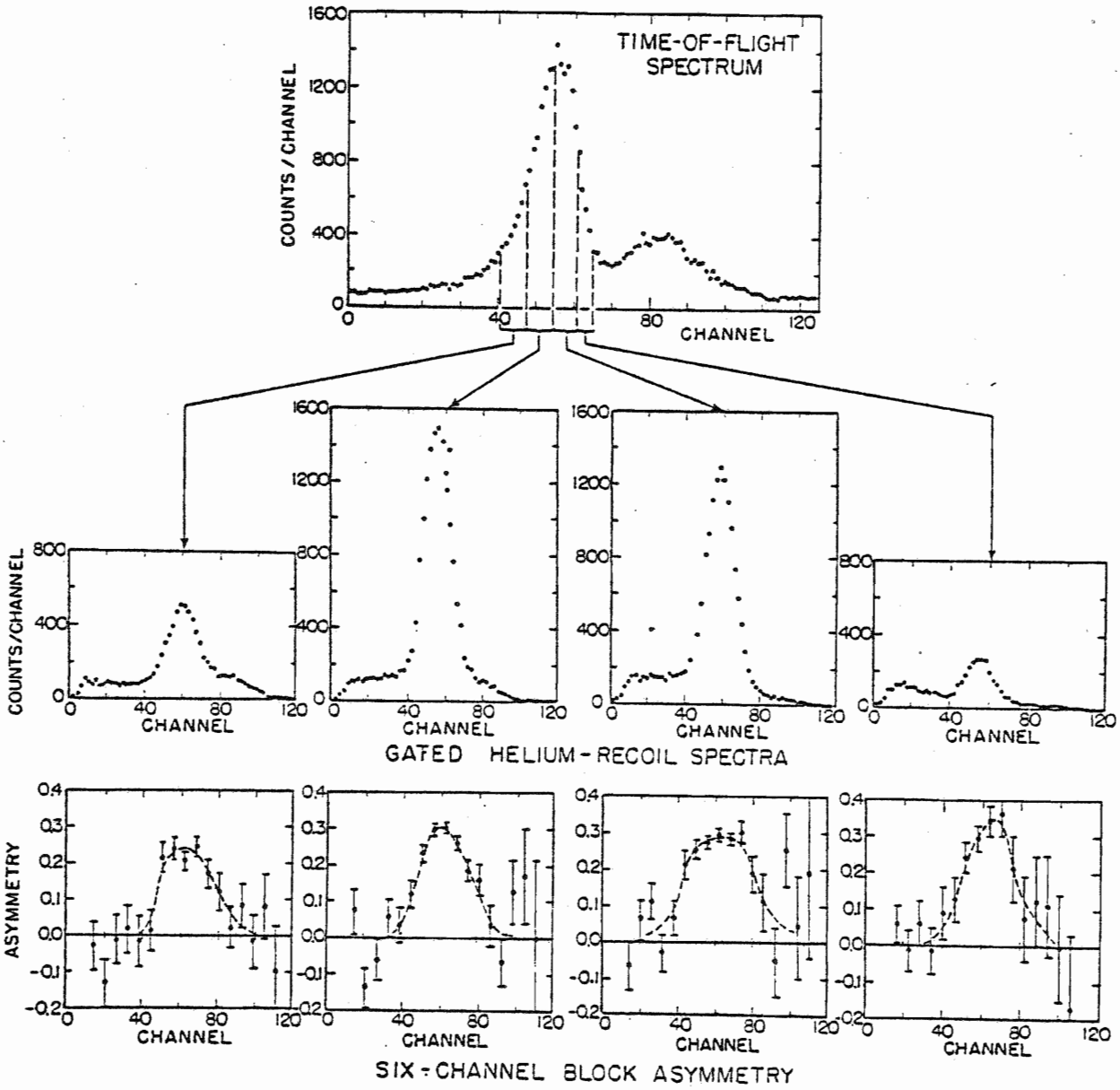

Figure 28. Detailed Analysis of Time and Energy Relationships in Neutron Polarization Spectra

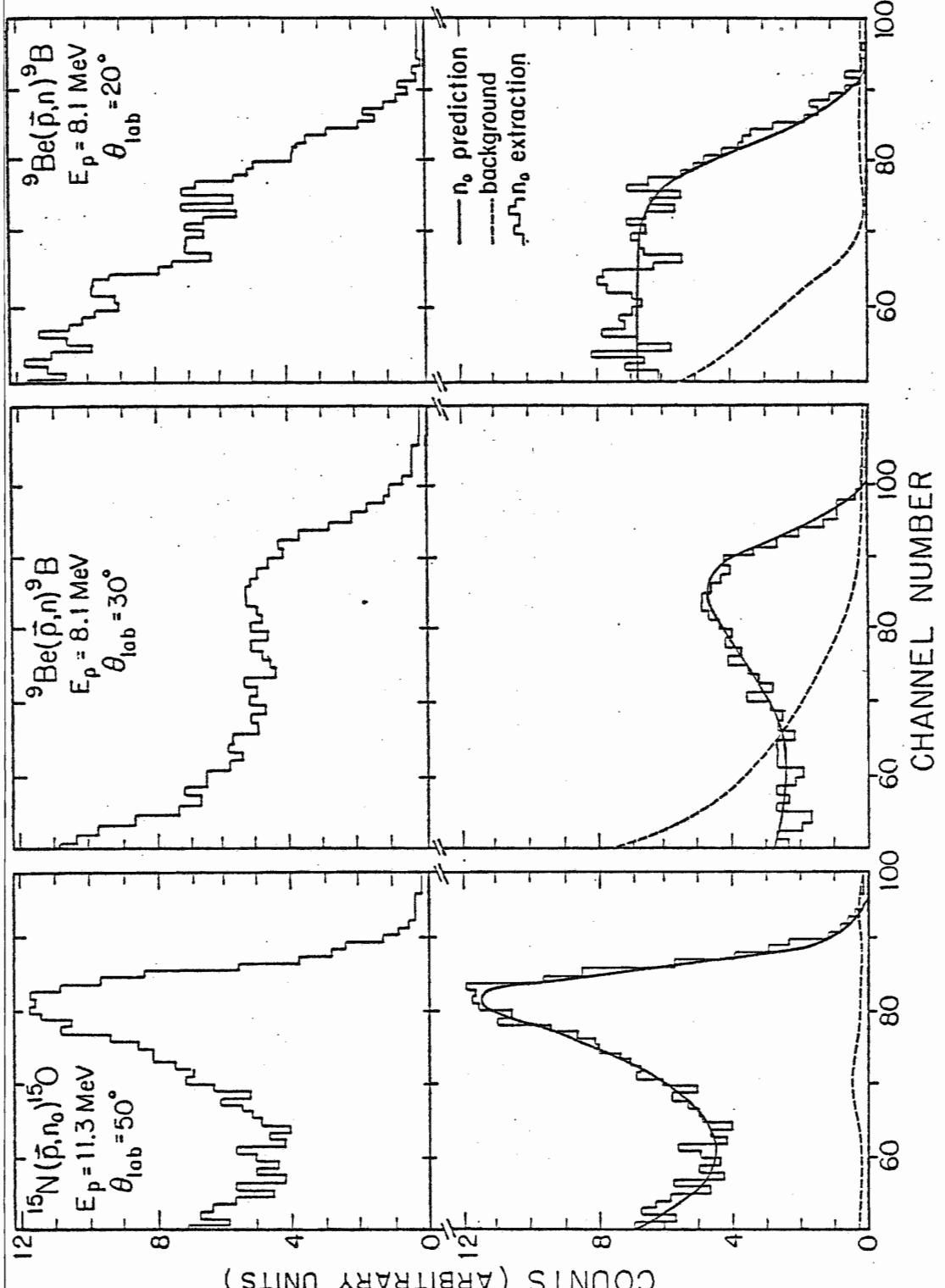

Figure 29. Typical Analyzing Power Experiment Recoil Energy Spectra

corresponding to 180° proton (or ^{4}He) recoil. This pulse height distribution is calculable using cross sections obtained from phase shifts along with response functions for each scintillator. Further details about the basic calculation are found in Morgan and Walter (1968).

Considerable discussion of RECOIL is included here since the spectrum stripping procedure is somewhat unusual and its design, programming, and operation formed a large part of this thesis research. We divide the discussion into these sections: (1) spectra available, (2) generation of line shapes, background estimation from (3) shape analysis and (4) asymmetry analysis, and (5) asymmetry calculation and error propagation.

Spectra available. The spectra are recorded by the experiment in sets of four (two detectors for two spins each) and may include a background set from either target-out or time-of-flight uncorrelated measurements. Either of these backgrounds is assumed to be unpolarized and averaged up and down to improve the statistics for determining the background shape. Often a target-out run was made, although for less collected charge to save time; such cases must be renormalized before subtraction.

Line shape generation. The shape generation procedure was described above, and its basic program was originally written by Dr. G. L. Morgan. A modification was made by the author to incorporate a correction for target thickness by dividing the target into several sections and then calculating separate neutron energies and recoil energy distributions from each. The summed energy distribution is then converted to a light output pulse height spectrum.

For the proton scintillator, the center-of-mass cross section is approximately isotropic and the energy-light conversion is proportional to $E^{3/2}$ (Finckh, 1974). Since the range of recoil energies is small over the region of interest near the maximum recoil energy, this conversion is simply taken as linear. The resulting proton recoil energy pulse height spectrum is a step function. For $n - {}^4He$, the cross section is angle-dependent but the response is linear; the resulting distribution has a characteristic "knee" at the high-energy cut-off. For both cases, the resolution function $R(E_{rec})$ was of the form determined by Morgan and Walter (1968), i.e., to be $R(E_{rec}) = (R_A^2 + R_B^2/E_{rec})^{\frac{1}{2}}$, where E_{rec} is the pulse height and R_A and R_B are resolution parameters. Since the responses of the two side scintillators are usually not identical, different parameters are allowed for each and the resulting resolution-broadened line shapes are stored in separate left and right arrays. These line shapes are the sources of the predicted distributions for the fitting step.

Background estimation from shape analysis. These shapes must then be adjusted to match the observed spectra, the only free parameters being detector gain and, of course, the individual yields. For a first shape estimate, we temporarily average up and down spectra for each side, then adjust the gain and amplitude of the left and right n_0 reference spectra to provide a smoothly varying difference spectrum between the data and the n_0 prediction. This difference spectrum then becomes our first estimate of the unpolarized background shape.

From this point we iteratively adjust gains and amplitudes for the four spectra (up or down, left or right) in an attempt to find left and right gains and amplitudes that give difference spectra which have reasonable shapes and allow good prediction of the total observed spectrum. Examples of such extraction are shown in Figure 29. If the line shape is seriously in error or the background appreciably polarized, good agreement will be impossible to find and adjustments must be made.

Background estimation from asymmetry analysis. Once the four shapes for the ground-state neutrons and the two shapes for the left and right backgrounds have been optimized, asymmetry constraints are investigated. First, the up-down asymmetries of ground-state counts for the two detectors should be related by a sign change, assuming good beam current integration. Second, the assumed fully-polarized ground-state contribution and unpolarized background shapes may be used to calculate a channel-by-channel asymmetry which, to be self-consistent, must agree with that actually observed.

Asymmetry calculation and error propagation. From our fitting, the reliability of the background determination extending through the spectrum toward lower energies can be evaluated. For regions in each detector which appear reasonably well determined, asymmetries are calculated by correcting the observed numbers of counts by subtracting the estimated background contribution.

We now present the full two-detector spin-flip asymmetry calculation and error analysis results used by the code RECOIL. To simplify, we use the subscripts $p = L, R$ to denote detector position and $s = U,D$ to

denote spin direction. The input from the experiment are then target-out spectra G_{ps}, total spectra T_{ps}, and the ratio f of total charge to target-out charge. We first average the up and down target-out spectra to obtain

$$G_p = \sum_s G_{ps}/2$$

and then subtract G_p from the T_{ps} spectra to obtain target-out corrected spectra N_{ps}:

$$N_{ps} = T_{ps} - f\, G_p.$$

We then obtain left and right background estimates B_p by fitting.

In some cases, beam current integration was unstable enough to cause markedly different up and down detector sums. Although the spin-flip technique cancels any effect in the measured spectra, our summation must weight the background subtraction by the ratio of up-to down-integrated charge. To do this, we estimate the up-down charge ratio δ and its uncertainty $\Delta\delta$:

$$\delta = \left(\prod_p N_{pU} / \prod_p N_{pD}\right)^{\frac{1}{2}}$$

$$\Delta\delta = (\delta/2)\left[\Sigma\left(\frac{1}{N_{ps}}\right)\right]^{\frac{1}{2}}$$

It is useful to calculate asymmetries for each stage of data correction, i.e., for the raw data, the target-out corrected data, and the background-corrected data. For each calculation, the error expression can be written to involve four detector sums D_{ps} and two error terms E_p. For the raw spectra we obtain:

$$D_{ps} = N_{ps} + G_p$$
$$E_p = 0$$

For the target-out correction we obtain:

$$D_{ps} = N_{ps}$$
$$E_p = (1 + f/2)G_p$$

And for the full background correction we obtain:

$$D_{pU} = N_{pU} - \delta^{\frac{1}{2}}B_p$$

$$D_{pD} = N_{pD} - \delta^{-\frac{1}{2}} B_p$$

$$E_p = (1 + f/2)G_p + 2B_p + (B_p \Delta\delta/(2\delta))^2$$

In terms of these expressions, we may then write the corrected left-right ratio α, the asymmetry ε, and its uncertainty $\Delta\varepsilon$ as:

$$\alpha = (D_{LU}/D_{LD})^{\frac{1}{2}}(D_{RD}/D_{RU})^{\frac{1}{2}}$$
$$\varepsilon = (\alpha - 1)/(\alpha + 1)$$
$$\Delta\varepsilon = \alpha/(\alpha + 1)^2 \beta^{\frac{1}{2}}$$

where $\beta = \Sigma[\frac{1}{D_{ps}} + (\frac{E_p}{\delta})(\frac{1}{D_{ps}^2})]$.

V. COMPARISONS OF DATA FOR POLARIZATION AND ANALYZING POWER

A. Introduction

Complexity of Comparisons

Before turning to the presentation of our results, a few comments are in order. First, comparison of the observables P and A basically requires comparison of different experimental techniques, each with its own systematic errors. In particular, the backgrounds and their corrections depend heavily on the different types of spectra obtained, and we have emphasized repeatedly the techniques and analysis for handling these effects. Since there exist previous P data from various sources for all three reactions studied, we have been able to compare our corrected data with those of others. In general, results have shown systematic deviations outside of assigned errors, a problem we feel is associated with background problems. The usual previous measurements considered time-of-flight but not recoil energy information; from our combination of both requirements, we feel that the recoil energy constraint is sometimes necessary. For example, neutrons which scatter from the ^{4}He containment vessel either before or after the ^{4}He analyzing scattering may yet reach side detectors within the time window required for elastic scattering. In this case, however, their scattering angle is not the specified analyzing angle, so their asymmetry should not be averaged in with that of the direct-scattered neutrons. In the time

spectrum, this background is time-correlated and sometimes difficult to extract. However, neutrons which scatter at these incorrect angles yield incorrect recoil energies, and our examination of the shape and asymmetry of the energy spectrum reveals their effect. Considerable experience at understanding this two-parameter approach for inspection of backgrounds in coincidence-gated recoil spectra has been obtained by our group over the last few years, particularly for n-d and n-p scattering. In a later discussion we will show that proper background subtraction has altered a number of conclusions reported by others regarding P versus A comparisons.

Second, the amount of related data reported here is itself formidable, both in type and in sheer quantity. Included are angular distributions and excitation functions of three quantities for three reactions: $\sigma(\theta)$, $P^y(\theta)$, and $A_y(\theta)$ data for $^3H(p,n_0)^3He$, $^9Be(p,n_0)^9B$, and $^{15}N(p,n_0)^{15}O$. For each measured data point, up to sixteen separate spectra had to be combined; off-line processing often generated further background spectra based on complicated iterations comparing the shapes and magnitudes of different distribution assumptions. For analyzing power $A(\theta)$ determinations, each measured asymmetry then had to be corrected by averaging a large number of beam polarization results. The polarization measurements required interpolation in tables of energy- , angle- , bias- , and pressure-dependent ^4He analyzing powers and energy-dependent solenoid currents. For both P and A, measurements were often repeated as consistency checks, sometimes using different techniques, and error-weighted averages of the different measurements were required to obtain the final values. Lastly, polynomial

fitting of angular distributions for $P(\theta)$ or $A(\theta)$ was made with supplemental $\sigma(\theta)$ results obtained from either the literature or from associated TUNL experiments. It is worthwhile to keep these complexities in mind for the presentation which follows.

Arrangement of Results

When these experiments were performed, the only guidance was Conzett's Theorem, which suggested that differences between P and A would depend on isospin symmetry violation by coulomb forces and hence inequality might be more likely at low energies. In discussing the first comparisons for $T(p,n_0)^3He$ in 1972, Haight et al. made the statement: "Thus, if charge-dependent effects are ignored, one might expect the neutron polarization P, with the incident beam unpolarized, to equal to the analyzing power A, when the reaction is initiated with a polarized beam." On the other hand, in 1973 Rohrer and Brown concluded from their study of P and A in $^7Li(p,n_0)^7Be$: "The near equivalence of the anlyzing power of $^7Li(p,n)^7Be$ and the neutron polarization produced with unpolarized neutrons is somewhat surprising...." Such variety of opinion has existed throughout this study, with some researchers who would "expect" equality, some seeing it as "surprising," and no one with many clear suggestions as to which experiments would provide most insight. In short, experimental results have been far ahead of theoretical explanations, and thus it is difficult to present the data of this thesis in a deliberate fashion. We further illustrate the odd directions taken by these studies by pointing out that in May of 1976 the experimental results on A and P for $^3H(p,n_0)^3He$ showed a substantial difference, while those for $^{15}N(p,n_0)^{15}O$ indicated excellent agreement.

One month later the situation was reversed, with new P data for ^{3}H that superceded the old giving full agreement between P and A, while further ^{15}N measurements at lower energies produced radical disagreement between the two. We therefore simply present our measurements in order of increasing atomic number $T(p,n_0)^{3}He$, $^{9}Be(p,n_0)^{9}B$, and $^{15}N(p,n_0)^{15}O$. Where possible, our procedure will be to present A results along with a smooth curve describing the data and then to compare the P data to this curve.

B. Presentation of Results

The $^{3}H(p,n_0)^{3}He$ Reaction

We open with our results for $T(p,n_0)^{3}He$. Although this data was among the last taken of that presented here, its early discussion is fitting since our P^y results resolved a conflict between P and A which originated with the first such comparison some five years previously. As explained in the preface, the A_y data published in 1972 by Haight et al. was greater by about 17% than the existing sets of P^y data obtained at four different laboratories. This difference was particularly surprising since the R-matrix calculations of Werntz and Meyerhof predicted near equality. Further measurements of A_y, culminating with the careful and extensive data by Doyle et al. (1976) of Ohio State University, all verified the difference. In discussions with the OSU group, the situation in May 1976 was summarized as a self-consistent set of P^y measurements of indisputably lower magnitude than a self-consistent set of A_y values. The OSU group had just verified the A_y set with techniques which were unquestionable, therefore focusing criticism on the P^y data set. On the experimental side, we had already begun to suspect that background effects in ^{4}He cells had caused underestimated polarizations; this problem

might be corrected by our additional recoil energy constraint. From a theoretical viewpoint, however, the difference was not entirely unexpected, since it only appeared near threshold, where coulomb symmetry-breaking effects should be strongest. We therefore decided to remeasure selected P^y data to resolve nagging uncertainties about Conzett's theorem and the existing P^y data sets.

We first summarize the A_y data set by showing in Figure 30a an excitation function $A_y(E)$ for 45° c.m. obtained by Haight et al. (1972) and Doyle et al. (1976). We also show in Figure 30b previous $A_y(\theta)$ angular distributions from Doyle et al. and Brown and Rohrer (1974) at 2.26 and 2.48 MeV. Note that all data sets are in mutual agreement and may be represented by the curves shown. These curves are then replotted for comparison to our P^y results. First we show in Figure 30a our excitation function of $P^y(E)$ at 45°(c.m.) along with the results of previous groups (Cramer and Cranberg, 1971; Kelsey, Hoop, and Van der Maat, 1964; Walter et al., 1962; and Smith and Thornton, 1972). In Figure 30b we compare our $P^y(\theta)$ angular distribution data to both the A_y curves and the P^y data of Smith and Thornton (1972). In all cases, the agreement between the A_y curve and our new P^y data is very good, while the previous P^y data all appear to be too low in magnitude. Possible reasons for this problem were discussed in the previous polarization analysis section, and it seems that the separate time-of-flight and recoil energy criteria used in our P^y measurement may have eliminated some background contributions that had not been properly accounted in the earlier data.

Figure 30. Polarization and Analyzing Power Comparison for the $^{3}H(p,n_0)^{3}He$ Reaction

a) Excitation Function Comparison

b) Angular Distribution Comparison

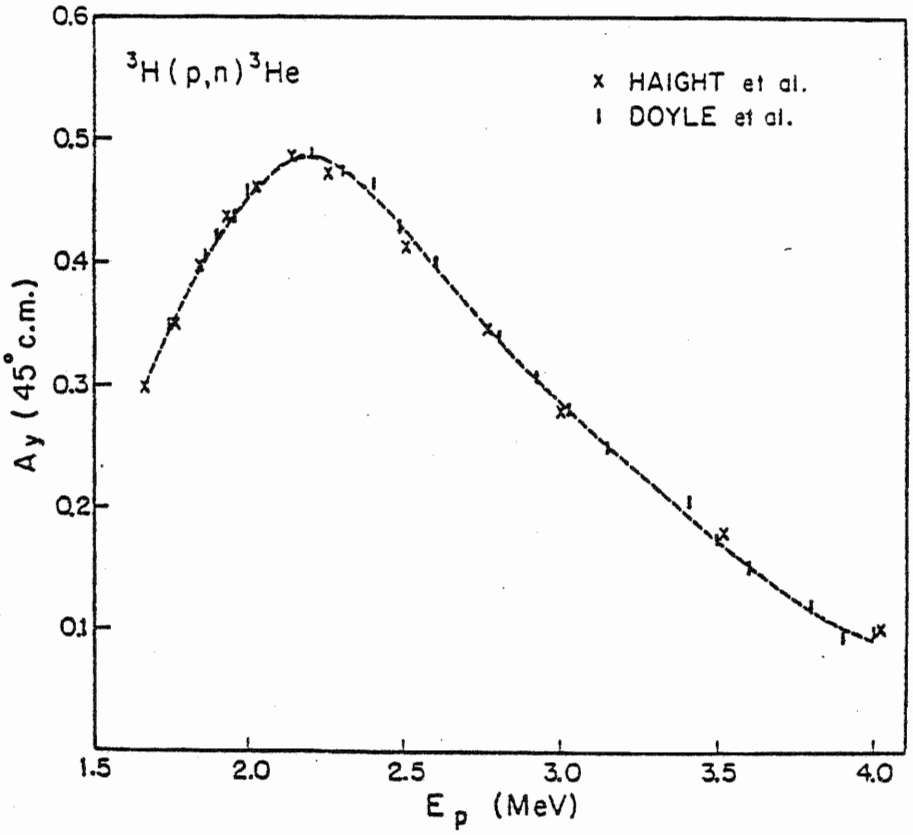
$^3H(p,n)^3He$
x HAIGHT et al.
| DOYLE et al.
A_y (45° c.m.)
E_p (MeV)
0.6
0.5
0.4
0.3
0.2
0.1
1.5
2.0
2.5
3.0
3.5
4.0

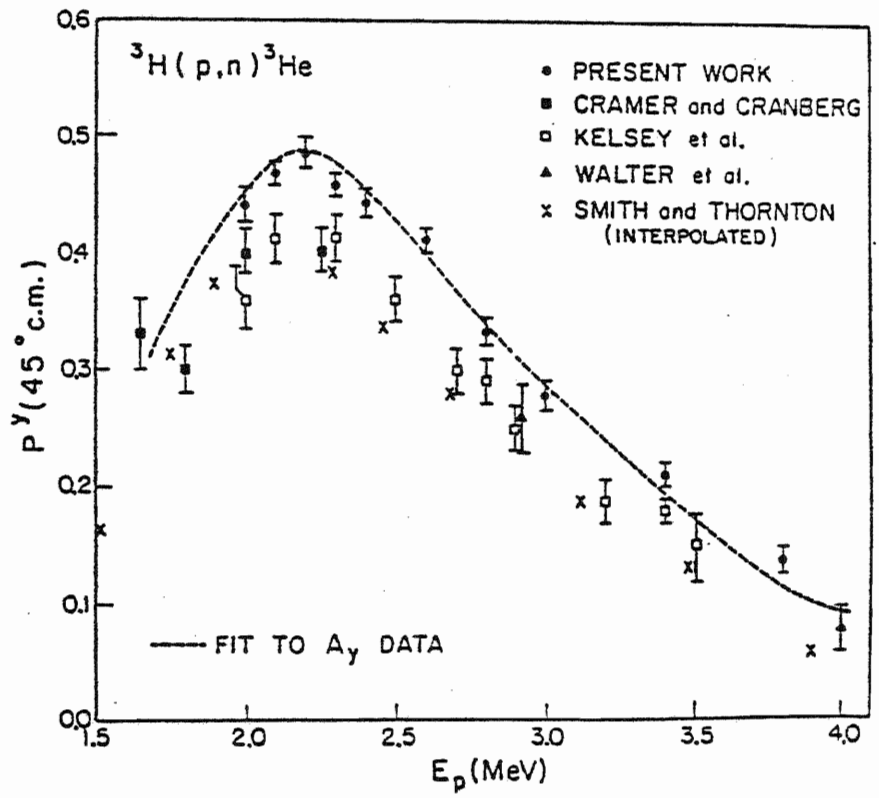
$^3H(p,n)^3He$
• PRESENT WORK
■ CRAMER and CRANBERG
□ KELSEY et al.
▲ WALTER et al.
× SMITH and THORNTON (INTERPOLATED)
—— FIT TO A_y DATA
P^y(45° c.m.)
E_p(MeV)
0.6
0.5
0.4
0.3
0.2
0.1
0.0
1.5
2.0
2.5
3.0
3.5
4.0

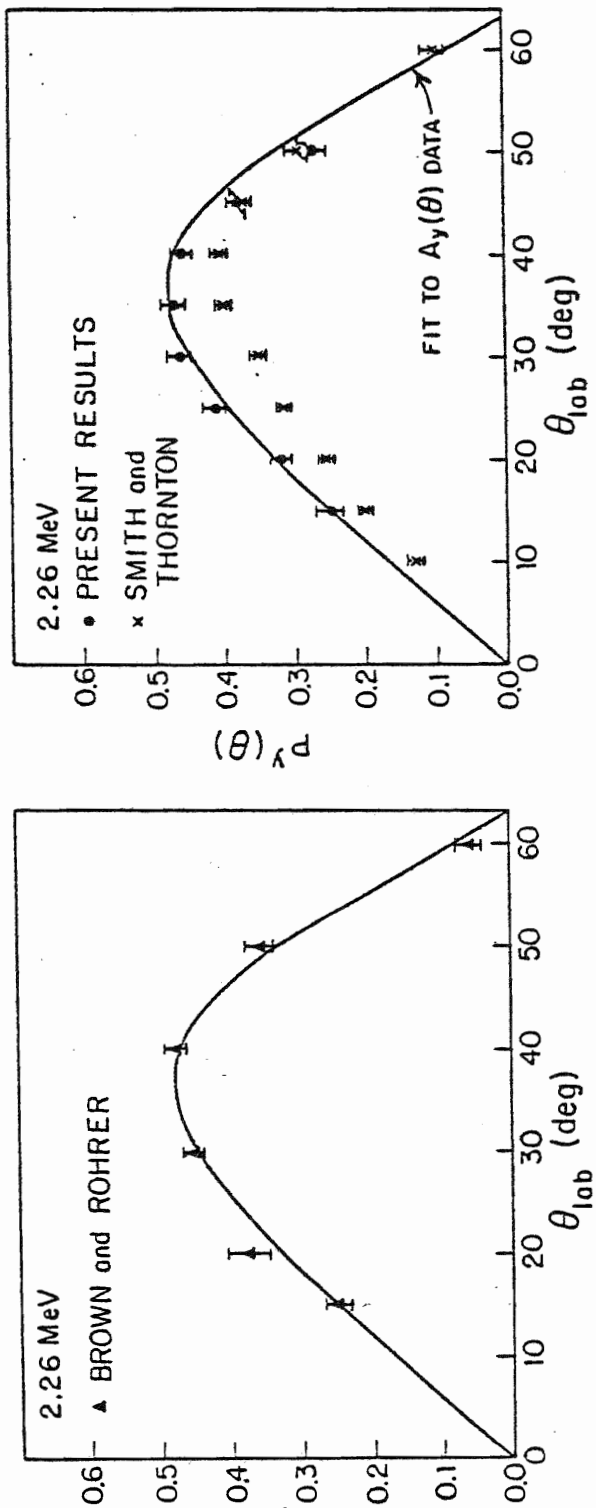
2.26 MeV
▲ BROWN and ROHRER
$A_y(\theta)$
θ_{lab} (deg)

2.26 MeV
• PRESENT RESULTS
× SMITH and THORNTON
FIT TO $A_y(\theta)$ DATA
$P^y(\theta)$
θ_{lab} (deg)

2.48 MeV
I DOYLE et al.
▲ BROWN and ROHRER
$A_y(\theta)$
θ_{lab} (deg)

2.46 MeV
• PRESENT RESULTS
× SMITH and THORNTON
FIT TO $A_y(\theta)$ DATA
$P^y(\theta)$
θ_{lab} (deg)

The $^{9}Be(p,n_0)^{9}B$ Reaction

Prior to the measurements reported here, P^y data had been obtained for $^{9}Be(p,n_0)^{9}B$ by various authors: Kelsey et al. (1963) and Kelsey (1963) from threshold to 8.5 MeV at 30°, 50°, 70°, and 90° (lab), and Walker et al. (1965b) at seven energies from 7.1 to 11.1 MeV. Rohrer and Brown (1976) measured $A_y(\theta)$ distributions at six energies from 2.4 to 2.9 MeV and obtained agreement with the low energy $P^y(\theta)$ data, although errors in the P results were generally large enough to allow only a coarse comparison.

We initially intended to obtain $A_y(\theta)$ data for comparison to the $P^y(\theta)$ data of Walker et al. at 8.1, 9.1, 10.0, and 11.1 MeV, but we extended our measurements to 12.0 to 15.0 MeV to go along with the cross-section measurements previously described. In view of the large breakup yield, we decided that the background corrections applied by Walker et al. might have been overestimated since only time-of-flight information was used. We therefore made our own $P^y(\theta)$ measurements at 8.1, 9.1, and 10.0 MeV and also obtained an excitation function of $P^y(E)$ at 70° (lab) in roughly 200 keV steps from 7.8 to 10.0 MeV to investigate energy trends. As shown in Figure 31, our results indicated that the $P^y(\theta)$ data obtained by Walker et al. were too large in magnitude by factors of up to 30%. The difference in magnitude but not shape between the two data sets seems to confirm over-correction for the large, partially polarized breakup background.

Figure 32 shows our final $A_y(\theta)$ and $P^y(\theta)$ results at 8.1, 9.1, and 10.0 MeV. The A_y data is from both single-detector and twin helium

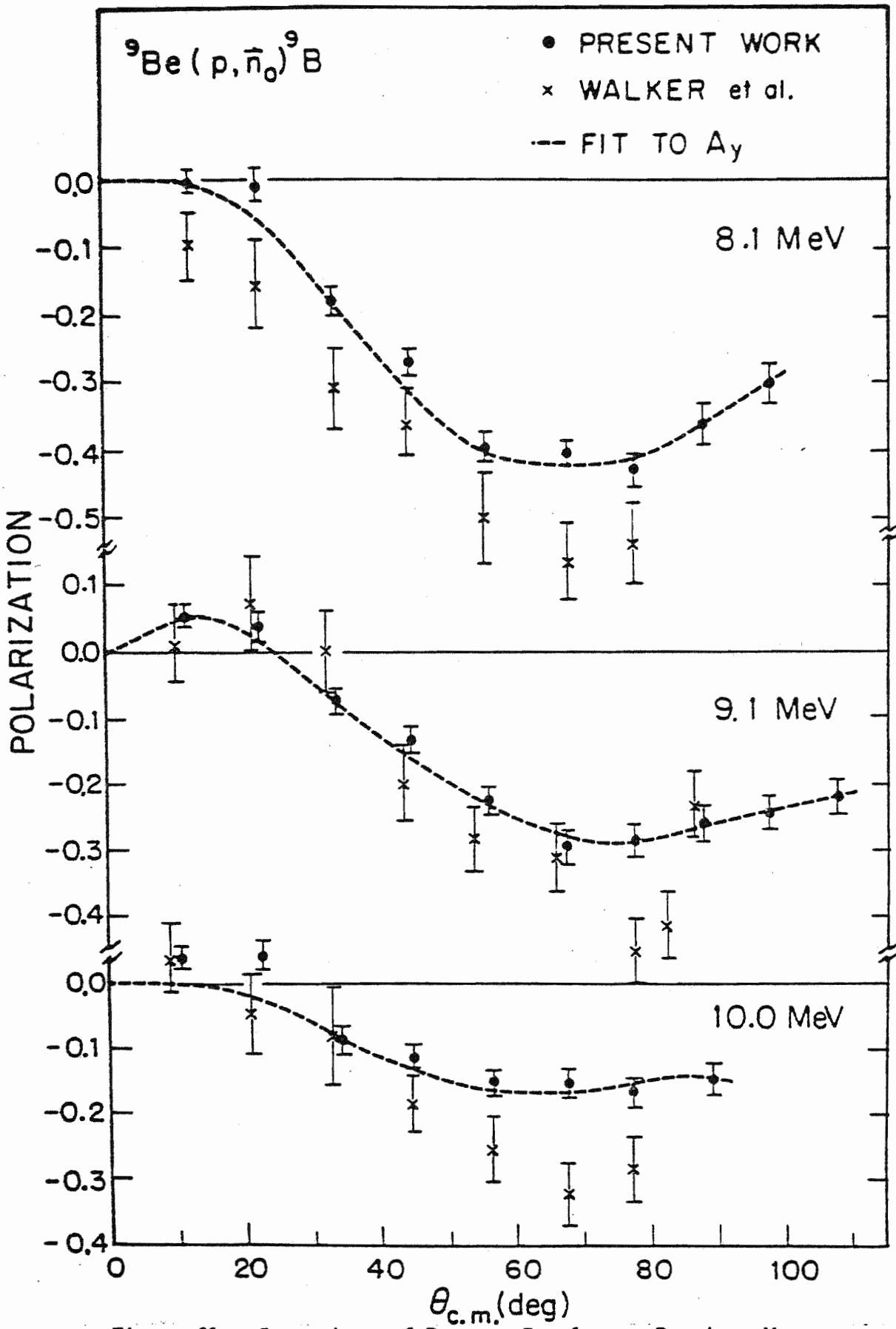

Figure 31. Comparison of Present Results to Previous Measurements for the $^9Be(p,n_0)^9B$ Reaction

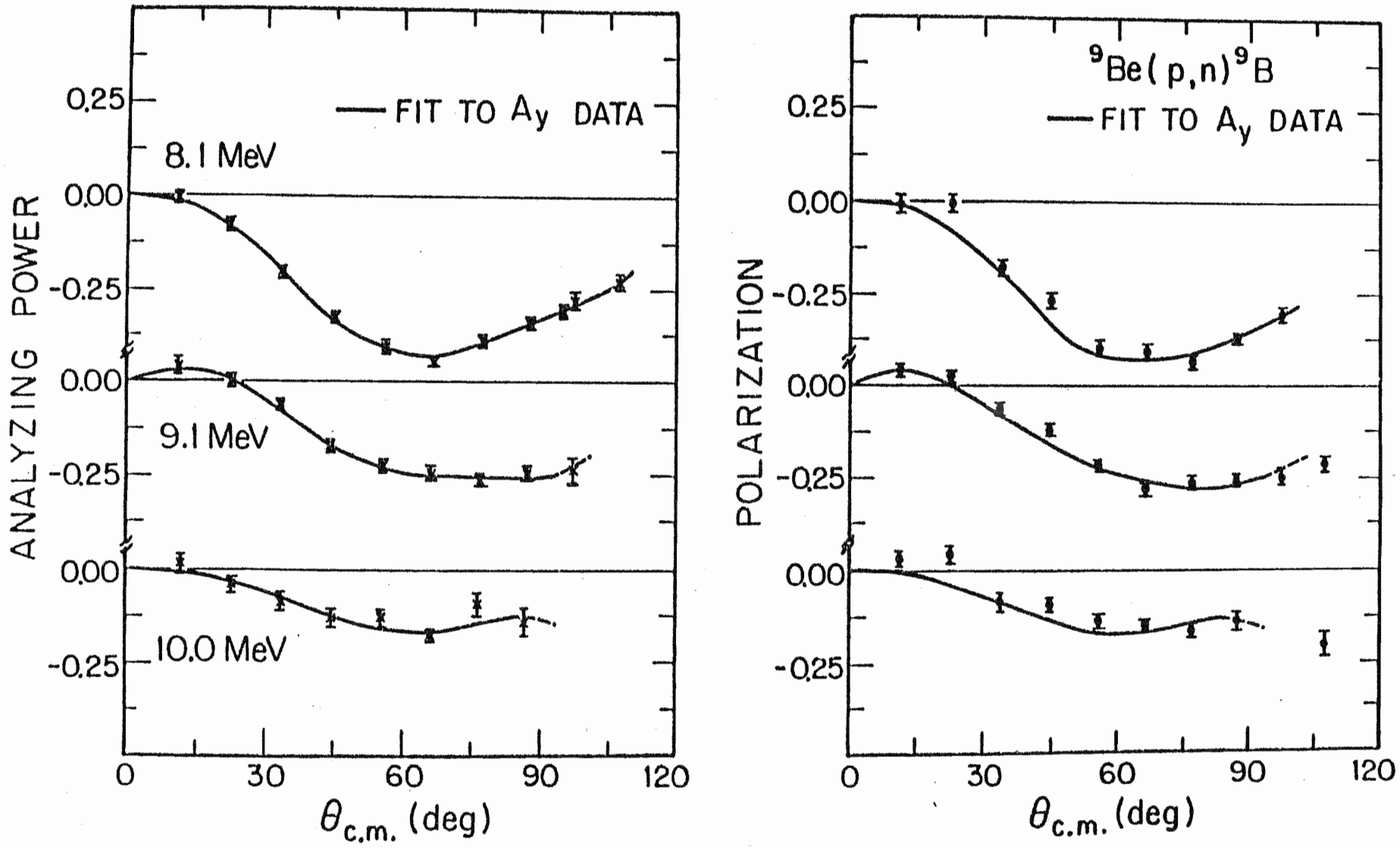

Figure 32. Comparison of $P^y(\theta)$ and $A_y(\theta)$ for the $^9Be(p,n_0)^9B$ Reaction at 8.1, 9.1, and 10.0 MeV

scintillator experiments; the two sets were consistent and have been combined statistically. Especially considering the experimental difficulties with breakup background extraction, the consistent agreement between the A_y data was satisfying. In fact, considering the magnitude of the background in both the P^y and A_y experiments, the differences between P^y and A_y which are seen in Figure 32 are possibly due to remaining systematic errors in our analyses. We conclude from our data that it is likely that any difference between P^y and A_y in this energy range is indeed small.

Figure 33 shows the TUNL $\sigma(\theta)$ and $A_y(\theta)$ results in the energy range 11.0 to 15.0 MeV. Errors in the $\sigma(\theta)$ data are estimated relative uncertainties and do not include the 5% absolute uncertainty discussed previously, since here we are mainly interested in the shape of the $\sigma(\theta)$ distributions. The $\sigma(\theta)$ curves shown are Legendre polynomial fits to our $\sigma(\theta)$ data and the $A_y(\theta)$ curves are extracted from the $\sigma(\theta)$ fits and associated Legendre polynomial fits to the product $\sigma(\theta)\ A_y(\theta)$, i.e.,

$$\sigma(\theta)\ A_y(\theta) = \sum_{n=1}^{N} a_n\ P_n^1(\cos\ \theta).$$

Dashed lines indicate regions where the fitting results were judged to be unphysical.

Our next comparison was prompted by the implications of Conzett's Theorem, which suggested that differences between P and A might be most likely near threshold. We therefore verified the low energy $A_y(\theta)$ data of Rohrer and Brown at three angles for 2.9 MeV and obtained partial angular distributions of $P^y(\theta)$ at 2.7 and 2.9 MeV. These results are shown

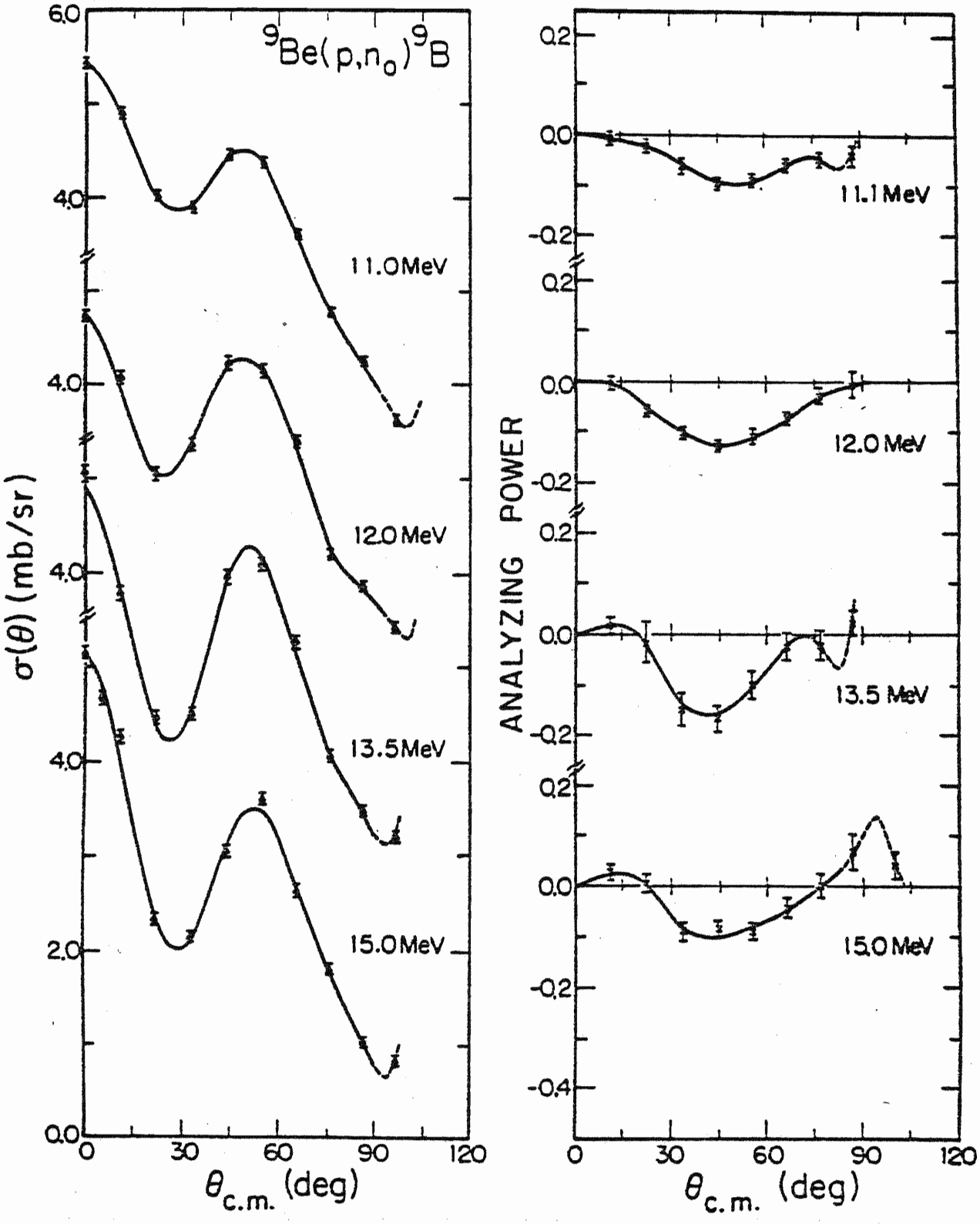

Figure 33. Distributions of $\sigma(\theta)$ and $A_y(\theta)$ for the $^9Be(p,n_0)^9B$ Reaction from 11.1 to 15.0 MeV

in Figure 34 and indicate excellent agreement between P and A. These data are especially remarkable since we anticipate severe tests at low energies for both the quench ratio beam polarization measurements needed to determine A_y (Haight et al., 1972) and the polarimeter analyzing power corrections for calculating P^y. On the other hand, these low energy values of $P^y(\theta)$ are felt to be more accurate than the data at higher energies because the background contribution due to ^{9}Be breakup neutrons is very low here.

Finally, a three-angle (30°, 50°, and 70° lab) excitation function of P^y and A_y was obtained to connect these low energy measurements with the previous 8-MeV results. As shown in Figure 35, good agreement was obtained despite considerable resonance structure at lower energies and increasing backgrounds at higher energies. Our P^y results are generally 20-30% greater than those of Kelsey and Kelsey et al., and background corrections of up to 10-15% were made to both our data sets. Since backgrounds in both measurements were assumed to be unpolarized, we expect that these corrections may in some cases be too large, especially for the P^y data. Keeping this in mind, we feel that all results for ^{9}Be are consistent with the conclusion $P^y = A_y$.

The $^{15}N(p,n_0)^{15}O$ Reaction

We now turn to the heaviest of our targets, ^{15}N. Previous polarization data was obtained by Walker et al. (1965a) in six angular distributions from 7.9 to 12.3 MeV. Although that data was originally intended to be the reference for our $A_y(\theta)$ measurements, we again found that our $P^y(\theta)$ results do not confirm the earlier measurements of other groups.

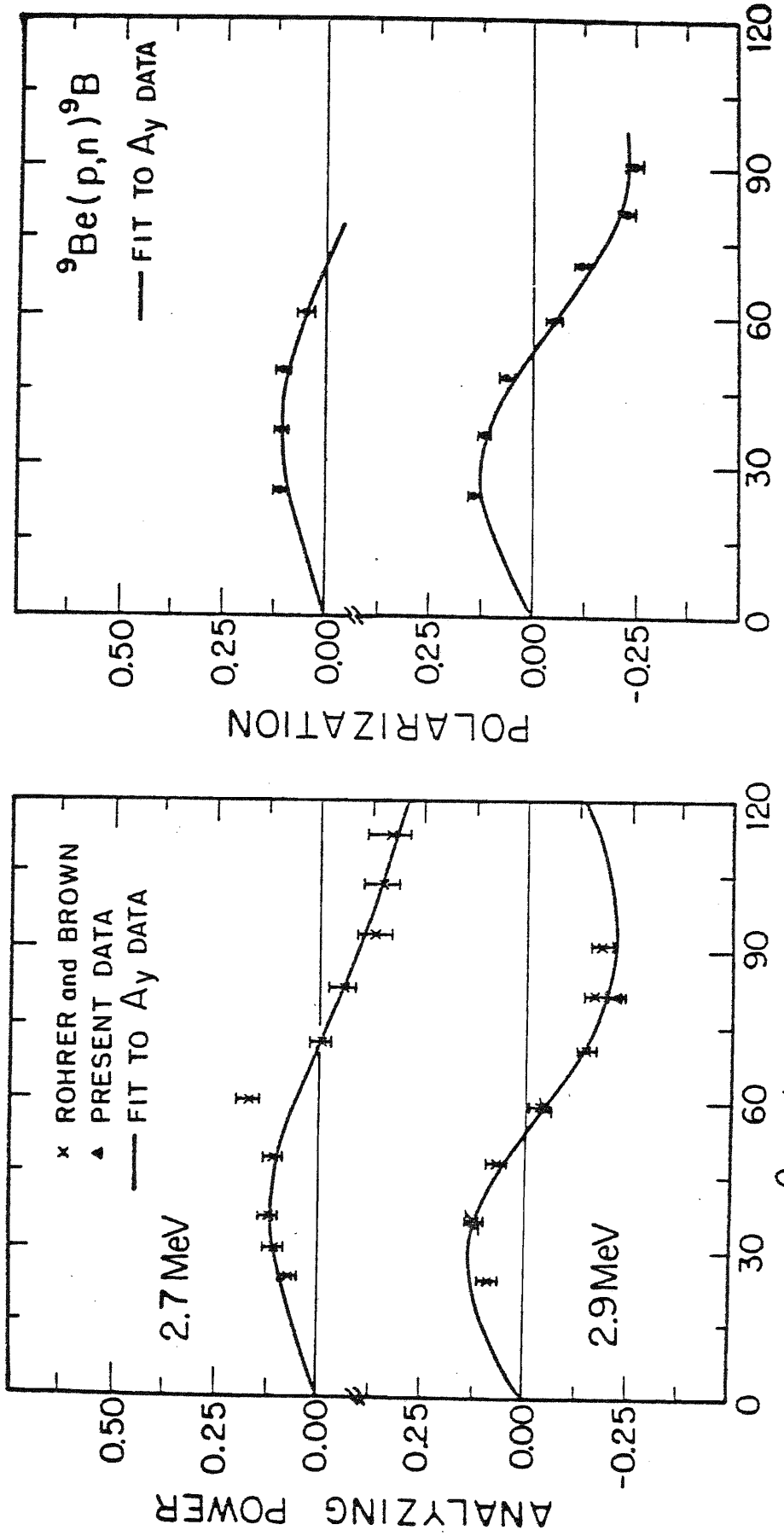

Figure 34. Comparison of $P^y(\theta)$ and $A_y(\theta)$ Results for the ^{9}Be(p,n_0)^{9}B Reaction at 2.7 and 2.9 MeV

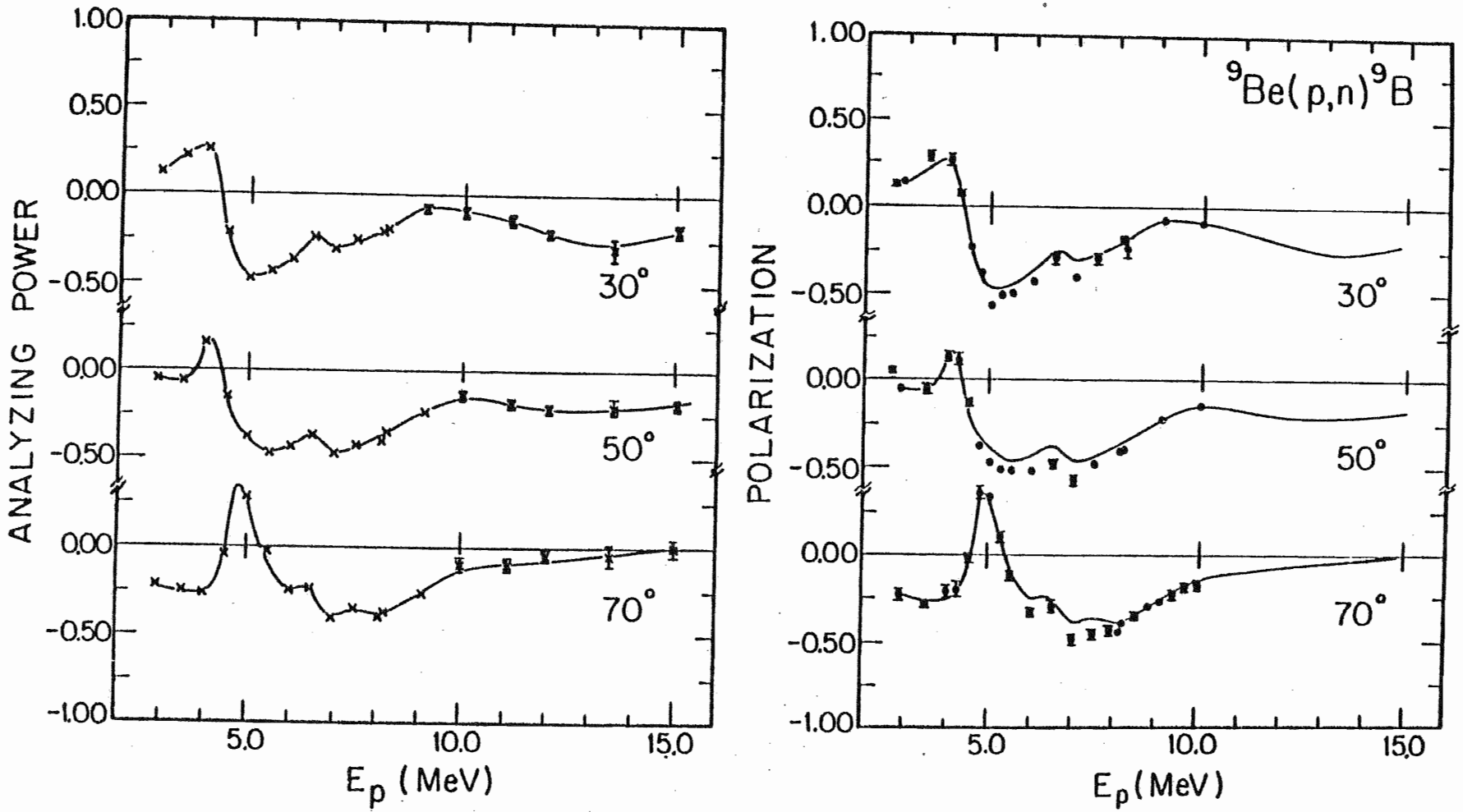

Figure 35. Comparison of $P^y(E)$ and $A_y(E)$ Results for the $^{9}Be(p,n_0)^{9}B$ Reaction from 2.7 to 15.0 MeV

Walker's measurements are therefore used only where we have no P^y data, and we expect such comparisons to be of limited value.

We begin by presenting in Figure 36 our earliest results, comparisons of $P^y(\theta)$ and $A_y(\theta)$ at 10.3 and 11.3 MeV. These results were verified in successive experiments and provide evidence for close agreement between P^y and A_y at these energies. Next, in Figure 37 we show our angular distributions of $A_y(\theta)$ at 5.17, 7.9, 8.5, and 9.2 MeV in comparison to both the Walker et al. $P^y(\theta)$ data and scattered $P^y(\theta)$ points from our own three-angle P^y excitation function to be presented shortly. As cautioned above, this comparison is inconclusive. Then, in Figure 38, we present our first definite evidence of $P \neq A$ with angular distributions of $P^y(\theta)$ and $A_y(\theta)$ at 5.65 and 6.28 MeV. The disagreement at 5.65 MeV is decisive, and $A_y(\theta)$ and $P^y(\theta)$ values have been checked by as several times to be positively certain of the strong differences. Since cross-section measurements (Jones, Lidofsky, and Weil, 1958) show that this region has many resonances with widths less than 100 keV, we were prompted to extend these measurements to both lower and higher energies using thick targets ($\Delta E_p \cong 200$ keV) to provide some averaging over the resonances. Excitation functions of P^y and A_y at 20°, 50°, and 100° (lab) were obtained for energies from 4.5 to 9.3 MeV, and results are shown in Figure 39 along with a more careful study of a resonance near 10.7 MeV. Uncertainties given here, especially in the A_y data, are largely statistical; the gross differences between A_y and P^y made a detailed error analysis unnecessary. Furthermore, the spectra, which were obtained using time-of-flight requirements, were unusually clean and the increase in the errors due to background subtraction difficulties would not have affected our conclusions.

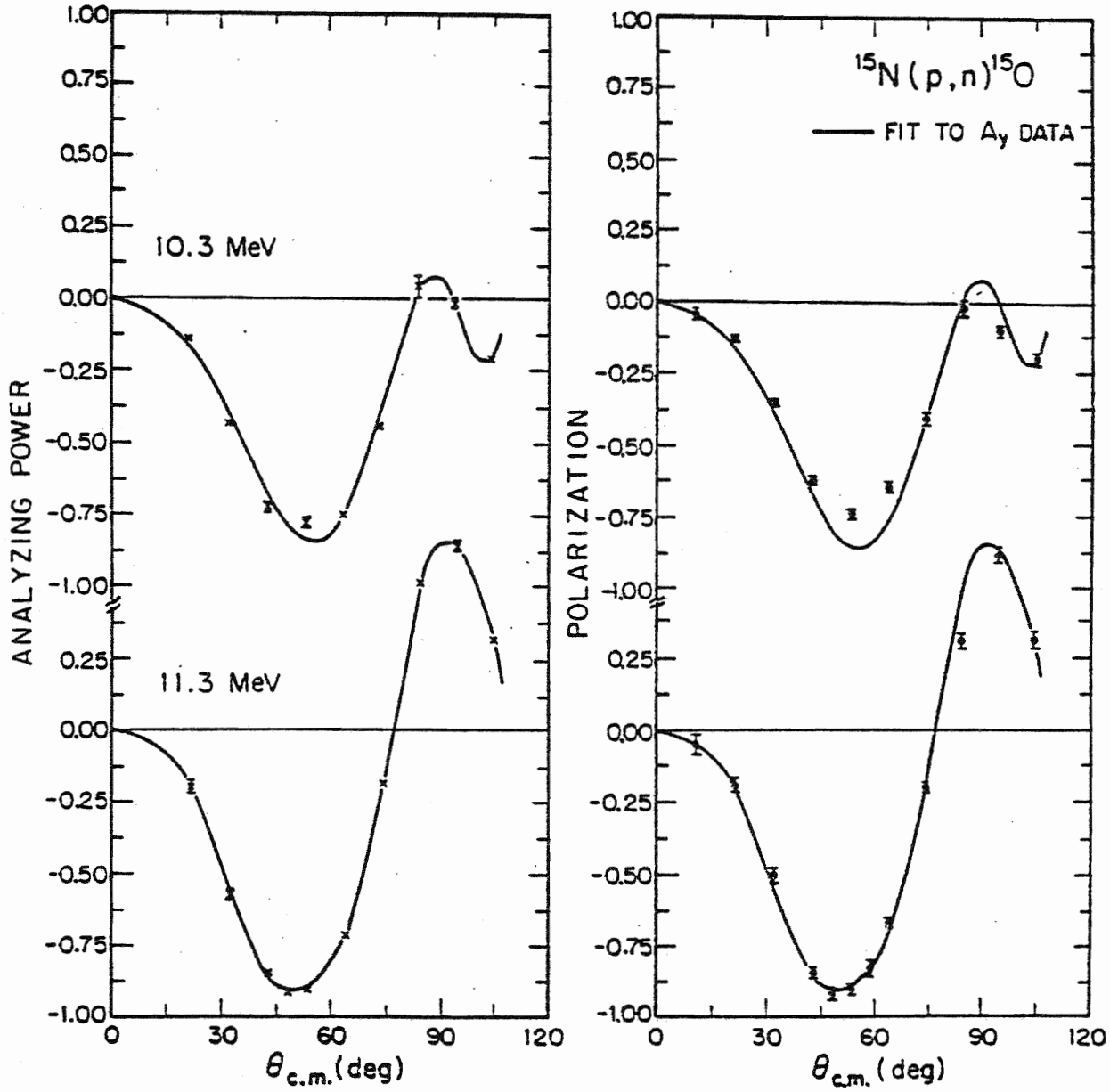

Figure 36. Comparison of $P^y(\theta)$ and $A_y(\theta)$ Results for the $^{15}N(p,n_0)^{15}O$ Reaction at 10.3 and 11.3 Mev

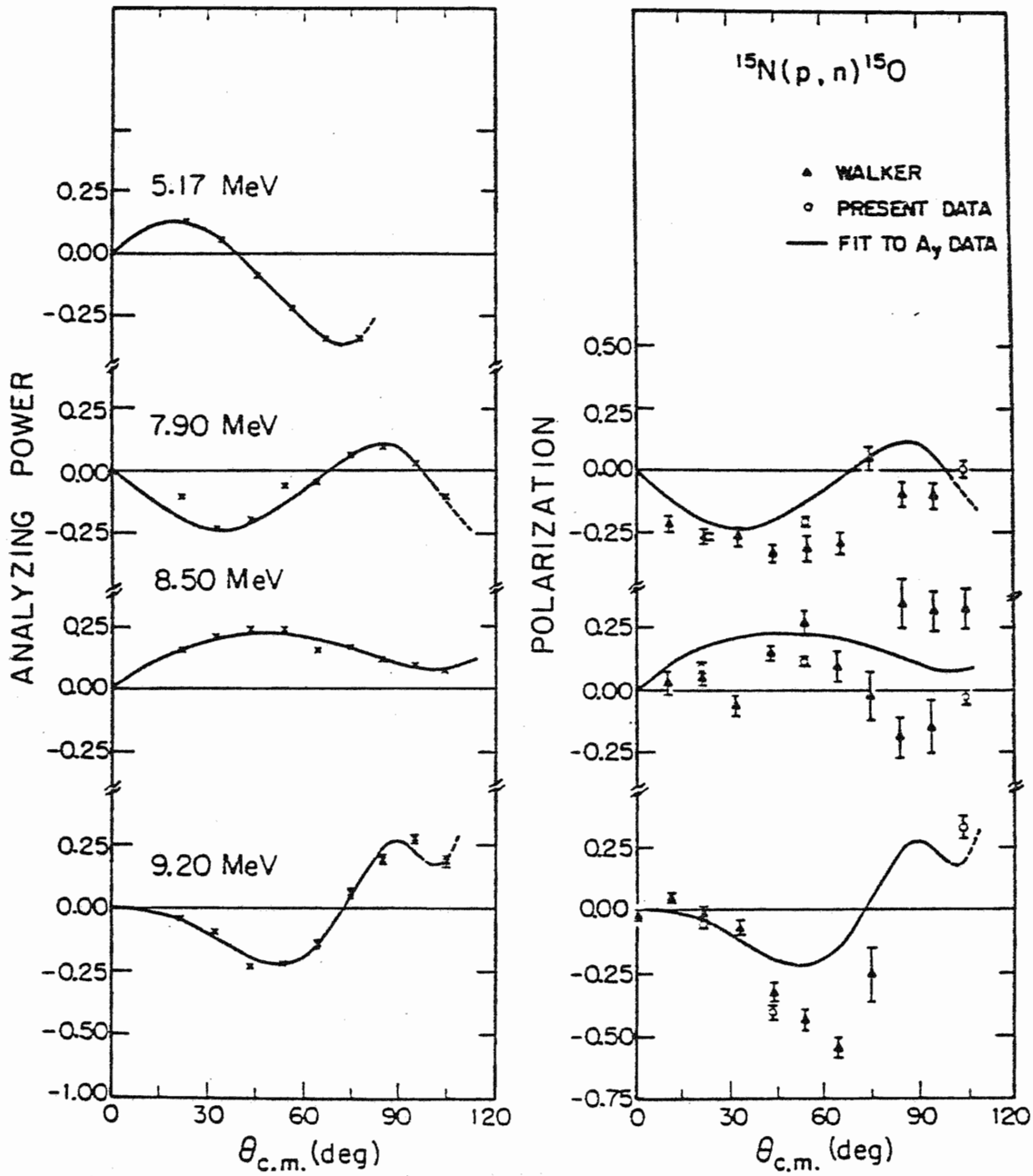

Figure 37. Comparison of $P^y(\theta)$ and $A_y(\theta)$ Results for the $^{15}N(p,n_0)^{15}O$ Reaction at 5.17 to 9.2 MeV

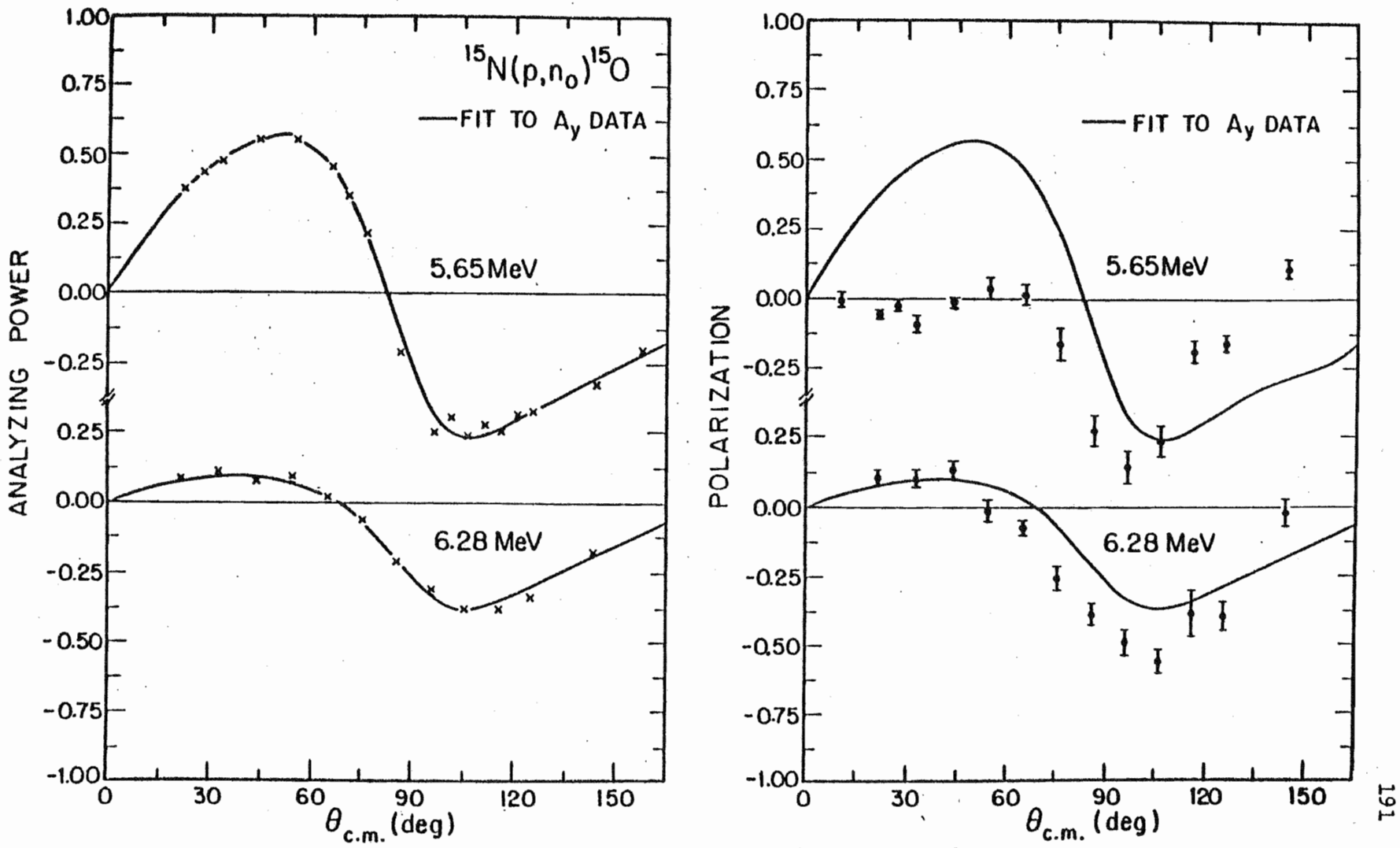

Figure 38. Comparison of $P^y(\theta)$ and $A_y(\theta)$ Results for the $^{15}N(p,n_0)^{15}O$ Reaction at 5.65 and 6.28 MeV

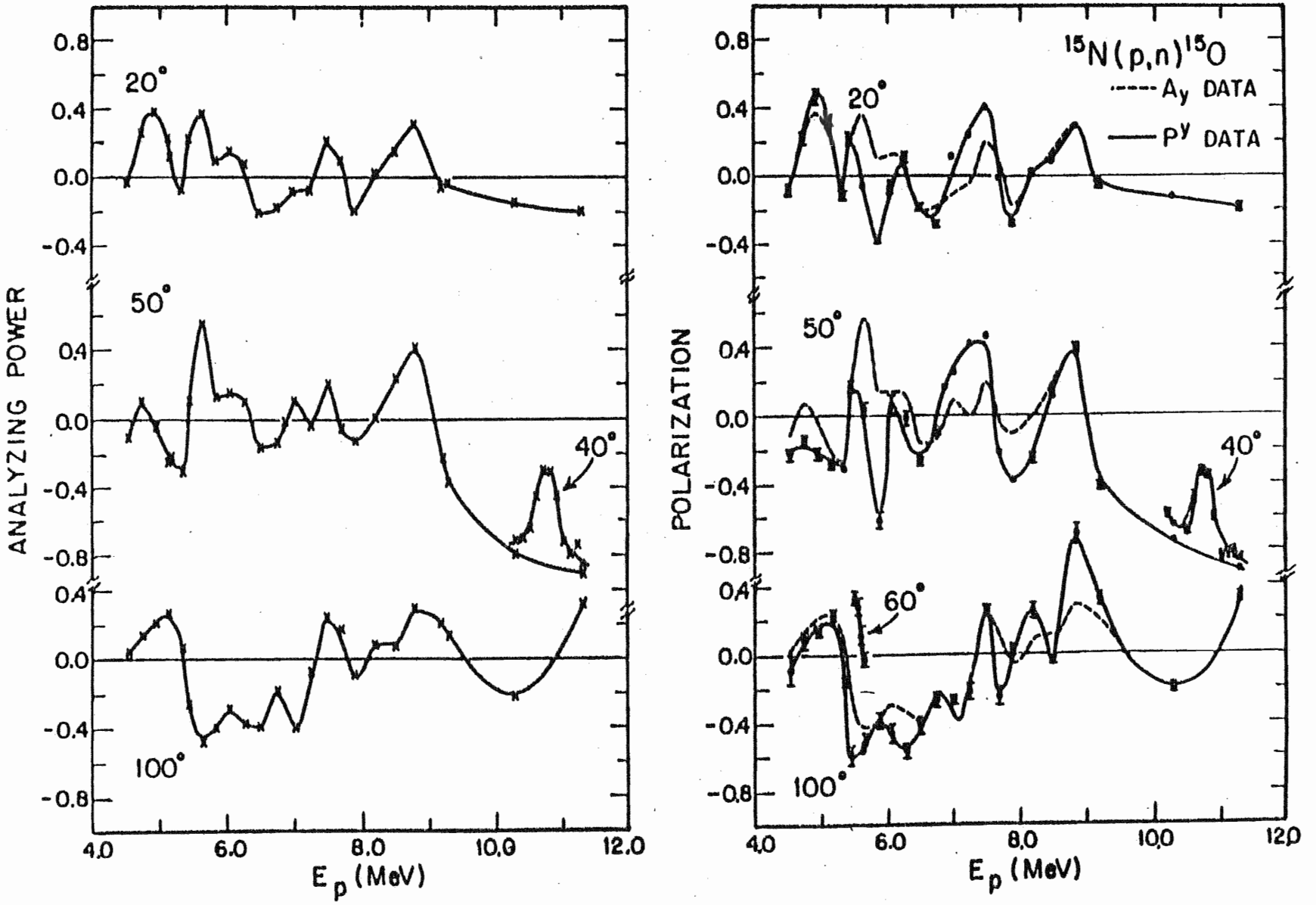

Figure 39. Comparison of $P^y(E)$ and $A_y(E)$ Results for the $^{15}N(p,n_0)^{15}O$ Reaction from 4.5 to 11.5 MeV at 20°, 50°, and 100° (lab)

Summary

In summary, for $^{3}H(p,n_0)^{3}He$ we see no evidence for any difference between P^y and A_y, either in the excitation functions or in the angular distributions. The $^{9}Be(p,n_0)^{9}B$ data is a bit harder to evaluate because of the severe background problems. However, at low energies, the verification of the Rohrer and Brown A_y data and the excellent agreement between the A_y values and our P^y results is conclusive. At higher energies, the breakup contribution makes absolute comparisons more difficult--it is likely that the observed differences in the excitation function are not truly associated with a difference between the quantities. This conclusion is supported by the good agreement of the more intensively investigated and analyzed region between 8.1 and 10.0 MeV. For ^{9}Be, therefore, we can only place an upper limit on the difference and point out two features which support $P = A$: (1) the functions exhibit very similar behavior, and (2) better accuracy has always led to better agreement.

For ^{15}N, however, the situation is one of marked disagreement at lower energies and convincing agreement above 10 MeV. The disagreements have been tested in several ways. First, several data points were repeated, often in experiments months apart using different detection systems. The data always repeated with good agreement. Analyses of the spectra were made independently with on-line and off-line programs, thus eliminating the possibility of gross errors in computer codes. Energy repeatibility in a resonance region was of great concern, so target thicknesses and energy differences between points were arranged so that intermediate values could be reliably interpolated. Target assemblies and energy spreads were

identical for both P^y and A_y measurements. In fact, much data was taken using exactly the same target in experiments which alternated between measuring each type of data, i.e., A_y or P^y. Systematic errors in background subtraction, beam polarization, analyzing power, or solenoid current correction are effectively ruled out as causes for $P \neq A$ for two reasons: (1) such problems would have prevented the good agreement between P and A observed in other cases (presuming such good agreement is not capricious), and (2) such difficulties can only produce different magnitudes, not different signs, for the observables. For all of these reasons we are convinced of our results.

Ironically, much effort went into the high accuracy of the earlier data at 10.3 and 11.3 MeV, for we faced the problem of verifying what appeared to be at most small differences; the more precisely we measured the values, the better the agreement became. The first differences appeared in taking the forward-angle $A_y(\theta)$ data to compare to a previous 5.65 MeV $P^y(\theta)$ angular distribution. The differences were so astounding that we even questioned the operation of the polarized source. Only by remeasuring one of the high-asymmetry points in the previous 11.3 MeV data were we convinced of the difference.

VI. INTERPRETATION OF RESULTS

Introduction

We open the discussion of results by summarizing the measurements in all available P^y and A_y comparisons. For $^3H(p,n_0)^3He$, all results (Donoghue et al., 1976, and references therein) give good agreement for energies at least up to 13.55 MeV. For the next case, $^7Li(p,n_0)^7Be$, Rohrer and Brown (1973) and Doyle et al. (1976) report some differences. The latter data is not yet published, but the implication of the errors uncovered by us in older P^y data for ^3H, ^9Be, and ^{15}N is that the magnitude of the effect shown by Rohrer and Brown may not be significant. Finally, our evidence discussed above for ^9Be generally supports equality, while ^{15}N exhibits both regions of complete disagreement and at best only fair agreement below 10 MeV; above this energy the agreement is excellent over most of the angular range.

In view of the above results we must attempt to explain at least the following two obvious conclusions. First, the differences occur only in $^{15}N(p,n_0)^{15}O$, the heaviest of the mirror reactions. Second, the differences appear to exist only at lower energies in this reaction. Our explanation must be based on the two conditions we discussed at the beginning of Part Two. First, a breaking of isospin symmetry is necessary, but not sufficient, for $P \neq A$. Second, a transverse spin-flip mechanism is sufficient in itself. The mechanisms providing these conditions may or may not be related.

A. Macroscopic Interpretation

We first examine the implications of our previous Lane model analysis for the P and A comparisons available and the two conditions above. The Lane approach was designed for symmetry-breaking perturbations on a charge-independent basis, and we may indeed use its results to predict the size of macroscopic coulomb corrections. However, this approach is sharply limited for the problem at hand. First, the macroscopic approach can only calculate one observable, because in this method $P \equiv A$; it therefore cannot explain any difference. Significantly, an attempt to calculate "P" from $^{9}Be(p,n_0)^{9}B$ and "A" from the reciprocal reaction $^{9}B(n,p_0)^{9}B$ at $E_n = E_p - Q$ produced the self-consistent $P \equiv A$, even with a coulomb correction to the proton potential. This result suggests that model's disregard of target spin may be crucial, as implied by the $P \equiv A$ identity for spin 0 targets. Second, we failed to predict the observed A data for ^{9}Be and suggested that a $(\vec{t} \cdot \vec{T})(\vec{\ell} \cdot \vec{s})$ term might be required. Such an expansion may indeed provide the required p to n spin and isospin flip, but the effect is spatially symmetric; Arnold (1976) suggested that a $(\vec{t} \times \vec{T})$ term would be necessary to provide $P \neq A$. From these two limitations we conclude that the previous macroscopic approach appears quite incapable of explaining the differences in the ^{15}N reaction, suggesting a shift to a more microsccpic viewpoint.

B. Microscopic Interpretation

Isospin Mixing

The remaining discussion given here is basically an expansion of the last part of the unpublished paper by Arnold (1977) which suggested the above

spin-flip asymmetry requirement. We first address the problem of isospin symmetry-breaking, drawing on discussions by Bohr and Mottelson (1969) and Wilkinson (1956). Although the isospin violation is likely to be coulomb in nature, evaluation of the size of the effect may be difficult. A case in point is the proven validity of isospin quantum numbers in describing (p,n) IAS reactions, even for heavy nuclei where the coulomb energies are comparable to the binding energy per nucleon. Further, the isospin impurity of the initial and final states ^{15}N and ^{15}O is estimated to be less than 0.1% (Bohr and Mottelson, 1969). These results underline the power of isospin symmetry and, at the same time, point the way toward a possible explanation. If symmetries are strong in the direct IAS reaction and between the initial and final states, we should focus on isospin in the compound or resonance reaction viewpoint of the intermediate ^{16}O state. This is exactly the subject of a paper by Wilkinson (1956), who argued that in direct reactions the intermediate state was too short-lived to be mixed appreciably by the coulomb interaction. By examining evidence for the effective isospin impurity α obtained from the observed transition rates α^2 for isospin-forbidden reactions, Wilkinson showed that isospin symmetry would be strong for low-lying states, would then pass through a higher-energy region of almost complete breakdown, and finally would improve at the highest energies to again yield a good isospin quantum number. For light ($A \leq 20$) nuclei below E_{ex} = 14 to 20 MeV, states which differ only in isospin quantum numbers are well separated, so the mixing parameter $\alpha \sim E_c/D(E)$ should be small for Wilkinson's coulomb mixing potential $E_c \approx 0.1$ MeV. At the highest energies (22-30 MeV), the symmetry effects

are obtained not from single states, but from the overall arrangement of many overlapping levels. The effective mixing parameter is therefore $\alpha' \sim E_c/\Gamma(E)$ and falls off at higher energies. As a guide, Barnett (1968) stated that for ^{16}O resonances which were observed in the $^{15}N(p,n_0)^{15}O$ reaction, the average width $\langle\Gamma\rangle$ and spacing $\langle D\rangle$ for $T = 0$ were comparable for $E_{ex} = 15 - 25$ MeV. For $T = 1$ states at lower energies (about 16 MeV), resonances were well separated with $\langle\Gamma\rangle \ll \langle D\rangle$; by about 23 MeV, $\langle\Gamma\rangle$ was approximately equal to $\langle D\rangle$.

Wilkinson thus divided the ^{16}O spectrum into three energy regions in order of increasing energy: well-separated $T = 1$ states on a $T = 0$ background; partially overlapping $T = 0$ and $T = 1$ states; and broad, completely-overlapping states of all isospins. In the intermediate energy region, isospin mixing should be at a maximum. From the transition rates available, Wilkinson's estimates of effective impurity peaked at approximately 0.5 for energies $E_{ex} = 12$ to 22 MeV, or E_p = threshold to 10.5 MeV in $^{15}N(p,n)$.

We further substantiate Wilkinson's observations by referring to Barnett's $^{15}N(p,n)^{15}O$ total cross-section measurement, shown in Figure 40, and his tabulation of resonance parameters in the 16-22 MeV energy range of ^{16}O. Certain reactions are isospin-constrained into the $T = 0$ or $T = 1$ channels, and the appearance of the same resonance in both channels is clear evidence for isospin mixing. Of fourteen resonances from $^{15}N(p,n_0)^{15}O$ in this region, five appeared clearly in both channels. This approach was also followed by Arnold (1977), who discussed (p,n) reactions, which may have both $T = 0$ and $T = 1$ components, in terms of isospin-conserving

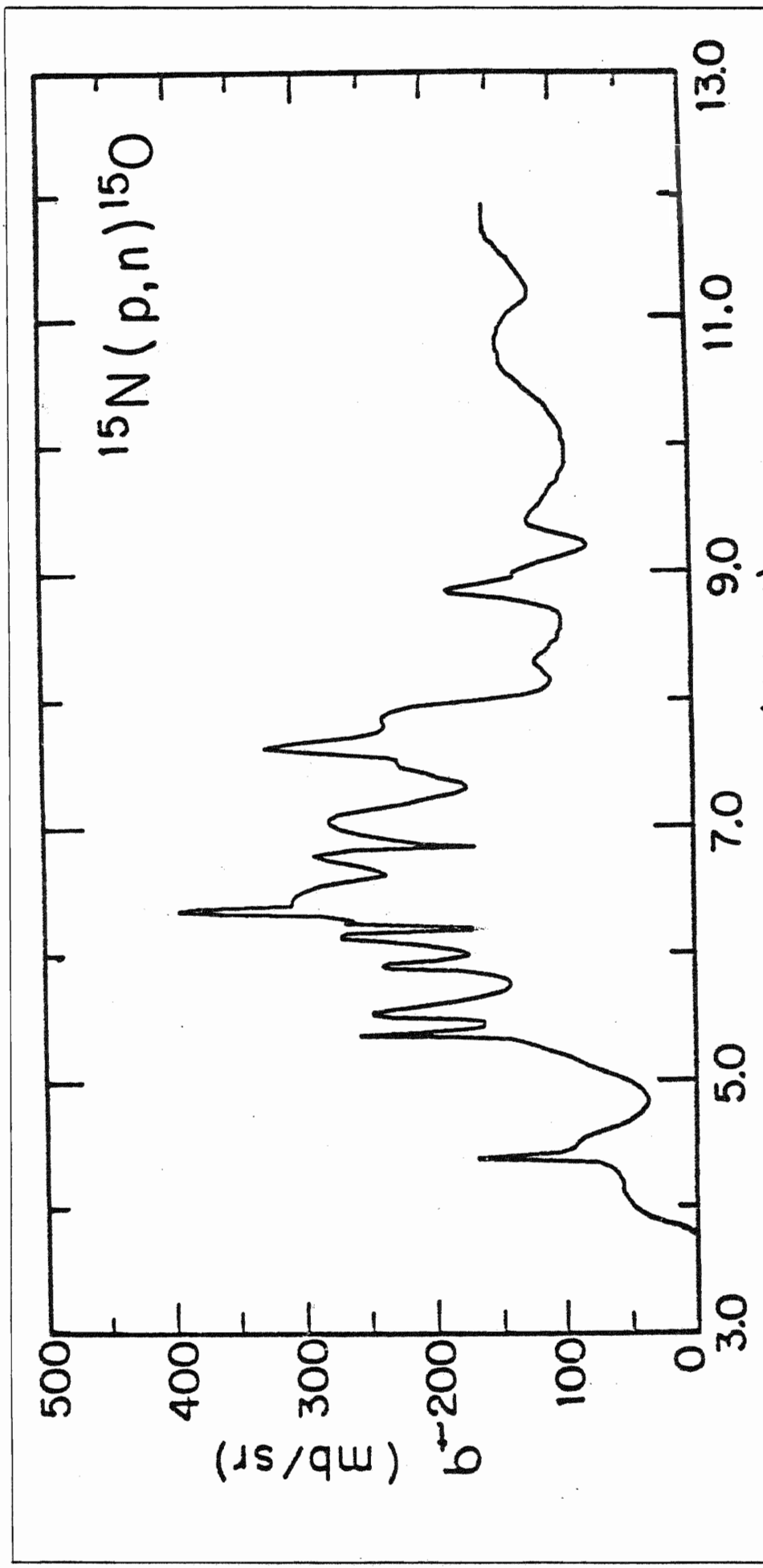

Figure 40. Total Cross Section for the $^{15}N(p,n)^{15}O$ Reaction

and nonconserving amplitudes. The conserving amplitudes are confined to either the $T = 0$ or $T = 1$ channels, the non-conserving ones "cross over" between channels.

In summary, our conclusions are that the resonant nature of the $^{15}N(p,n_0)^{15}O$ reaction is well suited to the isospin symmetry arguments given above, particularly in that the energy at which isospin symmetry is expected to re-emerge agrees well with the disappearance of our differences between P and A.

Asymmetric Spin Flip

We now turn to the spin-flip asymmetry requirement, again expanding on the paper by Arnold (1977). Continuing to focus on the role of single-particle resonances, we associate spin-flip with the spin-orbit $\vec{\ell} \cdot \vec{s}$ interaction and examine the orbital angular moments involved in the $(p + {}^{15}N)$ single-particle view of ^{16}O. Gillet and Mau (1962) report a calculation of states which result from coupling a (2s) or (1d) particle onto a ^{15}N core. They calculate nine resonances in the region of Barnett's data, five of which appear to correspond to observed levels. All of the identified states are $T = 1$ with appreciable $2s_{1/2}$ and $1d_{3/2}$ amplitudes, and three appear clearly in both the $T = 0$ and $T = 1$ channels. Since the average spacing is less than 1.0 MeV and level widths are about 0.1 to 0.65 MeV, it appears that the case for mixing is quite good. The lowest of these three most promising states is at $E_{ex} = 18.1$ MeV ($E_p = 6.3$ MeV), the highest is at 20.1 MeV (8.5 MeV). Further, Hansen and Stelts (1963) tentatively identified overlapping ($T = 0$, $2s_{1/2}$) and

and ($T = 1$, $1d_{3/2}$) resonances at around 17.3 to 17.5 MeV (5.5 to 5.8 MeV). It is thus clear that examples of (s - d) configuration mixing are entirely plausible in $^{15}N + p$ at our energies. Arnold (1977) suggests that this orbital mixing may be the mechanism for the required asymmetric spin flip, as compared to the predominantly ($1p_{1/2}$) - ($1p_{3/2}$) spin mixing in lighter p-shell nuclei such as ^{9}Be.

This microscopic configuration-mixing viewpoint again supports the case for $P \neq A$ for $^{15}N(p,n_0)^{15}O$ and $P = A$ for lighter target reactions. Further, the level density and direct reaction arguments suggest that in the lighter nuclei the conditions for $P = A$ should improve. Certainly, the excitation functions for $^{3}H(p,n_0)^{3}He$, and $^{9}Be(p,n_0)^{9}B$ do not exhibit the partially-overlapped level characteristics of the $^{15}N(p,n_0)^{15}O$ reaction below $E_p = 12$ MeV.

CONCLUSION

We close with some appropriately philosophical observations on the results of these studies. In Part One we simply imposed isospin symmetry on a macroscopic optical potential reaction model, obtaining considerable success at relating the cross sections for (p,p), (p,n) and (n,n) reactions. The success of the approach perhaps derives from the exploitation of a strong symmetry which must underlie whatever complicated microscopic processes are involved. In the failure to describe the charge-exchange spin effects, we may be encountering a reminder of either the power or the weakness of the symmetry approach. That is, at this point we cannot say whether the failure is due to our not extending the symmetry fully to the spin-orbit interaction, or to our having pushed the model to describe a too-delicate spin-isospin flip mechanism whose symmetry has finally succumbed to symmetry-breaking effects. Ironically, at this last point in the Lane optical model, we are dealing with an approach which apparently can contribute little to understanding the problem of Part Two, the comparison of P and A. In the macroscopic optical model view this comparison is academic, since the quantities are identical. We have therefore been forced into a reorientation in order to understand our polarization-analyzing power results, shifting from the implications of isospin symmetry for microscopic rather than macroscopic approaches. On the microscopic level, the equality of P and A would appear extremely complex and

fortuitous, while isospin symmetry again provides an overall constraint which tends to arrange this complexity in patterns which provide the equality. Through the development of this work, we have thus seen an interesting interplay between pervasive isospin symmetries and the fragile details at the limits of specific reaction models.

APPENDIX

9BE(P,N)9B
CROSS-SECTION DATA

11.0 MEV

0.00	5.327	0.057
0.00	5.518	0.057
11.24	4.904	0.055
22.45	4.020	0.054
33.58	3.887	0.051
44.61	4.452	0.052
55.50	4.375	0.049
66.21	3.617	0.044
76.74	2.778	0.037
87.07	2.260	0.035
97.18	1.647	0.029

12.0 MEV

0.00	4.686	0.055
0.00	4.805	0.077
11.23	4.075	0.075
22.43	3.046	0.070
33.56	3.359	0.068
44.57	4.232	0.071
55.45	4.147	0.070
66.16	3.384	0.063
76.69	2.208	0.054
87.01	1.802	0.049
87.01	1.913	0.036
97.12	1.407	0.031
97.12	1.479	0.032

13.5 MEV

0.00	5.039	0.083
11.22	3.785	0.076
22.41	2.463	0.066
33.52	2.506	0.065
44.53	3.963	0.071
55.40	4.092	0.073
66.10	3.272	0.070
76.62	2.057	0.056
86.94	1.445	0.049
86.94	1.496	0.051
97.05	1.204	0.044
97.05	1.192	0.046

15.0 MEV

0.00	5.144	0.034
5.61	4.677	0.071
11.21	4.263	0.071
22.39	2.336	0.058
33.49	2.154	0.053
44.49	3.045	0.058
55.36	3.602	0.058
66.06	2.630	0.058
76.57	1.806	0.046
86.89	1.037	0.040
96.99	0.831	0.035

0 DEGREE YIELD

10.00	6.152	0.314
10.50	5.942	0.304
11.00	5.423	0.278
11.50	5.026	0.259
12.00	4.805	0.257
12.50	4.459	0.231
13.00	4.496	0.240
13.50	5.039	0.267
14.00	4.777	0.255
14.50	4.870	0.252
15.00	5.188	0.279

ENERGIES IN MEV
CROSS SECTIONS IN MB/SR (C.M.)
ANGLES IN DEGREES (C.M.)
RELATIVE STATISTICAL UNCERTAINTIES

15N(P,N)15O

CROSS-SECTION DATA

9.05 MEV

0.00	25.170	0.484
10.87	23.744	0.791
32.52	14.012	0.468
53.86	7.629	0.257
64.36	6.151	0.208
74.74	4.994	0.170
84.96	4.041	0.138
95.04	3.149	0.109
104.96	2.806	0.068
114.73	3.167	0.109
124.36	3.977	0.136
133.86	6.263	0.212
143.24	9.543	0.321
152.52	12.886	0.432
161.72	15.696	0.525

10.3 MEV

0.00	16.365	0.331
10.84	14.938	0.521
21.65	13.305	0.464
32.42	9.826	0.344
43.11	7.806	0.274
53.71	6.356	0.224
64.19	4.370	0.155
74.55	2.437	0.088
84.77	1.336	0.050
94.84	1.513	0.056
104.76	2.272	0.082
114.55	2.687	0.097
124.19	2.475	0.090
133.70	2.274	0.083
143.11	3.036	0.110
152.42	5.545	0.197
161.65	7.799	0.275

11.0 MEV

0.00	4.549	0.155
21.63	3.800	0.130
43.06	4.418	0.150
64.12	4.651	0.158
84.68	3.074	0.075
94.76	3.093	0.107
104.68	3.536	0.122
114.47	3.650	0.126
124.12	3.027	0.105
133.64	2.573	0.090
143.05	2.956	0.103
152.37	5.234	0.179
161.62	7.889	0.267

11.3 MEV

0.00	5.542	0.116
10.82	5.002	0.170
21.61	3.729	0.091
32.36	2.715	0.094
43.04	2.746	0.068
53.62	2.854	0.098
64.09	2.679	0.067
74.44	2.456	0.085
84.65	2.394	0.078
94.72	2.849	0.099
104.65	2.994	0.104
114.44	2.686	0.094
124.09	2.259	0.080
133.62	2.041	0.072
143.03	2.900	0.102
152.36	5.067	0.174
161.61	7.759	0.263

0 DEGREE YIELD

8.45	21.435	0.681
8.65	7.678	0.246
8.85	22.928	0.728
9.05	25.844	0.821
9.25	22.991	0.730
9.45	22.659	0.720
9.65	15.678	0.499
9.85	14.360	0.458
10.05	19.303	0.614
10.25	16.707	0.532
10.45	14.549	0.463
10.65	12.731	0.287
10.85	13.206	0.421
11.05	5.385	0.171
11.25	5.672	0.183
11.45	6.121	0.197
11.65	9.011	0.288

ANGLES IN DEGREES (C.M.)
ENERGIES IN MEV
CROSS SECTIONS IN MB/SR (C.M.)
RELATIVE STATISTICAL UNCERTAINTIES

9BE(P,N)9B

ANALYZING POWER DATA

2.9 MEV

36.00	0.125	0.004
59.20	-0.048	0.009
81.20	-0.220	0.013

8.1 MEV

11.30	-0.005	0.011
22.56	-0.081	0.013
33.74	-0.207	0.011
44.81	-0.324	0.012
55.73	-0.401	0.015
66.48	-0.448	0.010
77.03	-0.390	0.013
87.37	-0.341	0.013
94.80	-0.313	0.019
97.40	-0.287	0.021
107.40	-0.239	0.019

9.1 MEV

11.27	0.037	0.025
22.81	-0.000	0.013
33.67	-0.067	0.015
44.22	-0.178	0.016
55.63	-0.228	0.012
66.37	-0.248	0.018
76.91	-0.265	0.016
87.24	-0.252	0.022
97.30	-0.245	0.037

10.0 MEV

11.26	0.013	0.026
22.48	-0.043	0.023
33.63	-0.099	0.026
44.67	-0.136	0.024
55.56	-0.135	0.024
66.28	-0.184	0.010
76.78	-0.098	0.031
87.10	-0.144	0.040

POLARIZATION DATA

2.7 MEV

24.50	0.114	0.016
36.60	0.111	0.017
48.50	0.110	0.018
60.10	0.056	0.022

2.9 MEV

24.10	0.149	0.014
36.00	0.123	0.011
47.70	0.071	0.019
59.20	-0.042	0.021
70.40	-0.109	0.015
81.20	-0.221	0.022
91.00	-0.239	0.019

8.1 MEV

11.30	-0.008	0.021
22.50	-0.009	0.024
33.70	-0.180	0.021
44.80	-0.272	0.021
55.70	-0.399	0.023
66.40	-0.409	0.018
77.00	-0.438	0.015
87.30	-0.369	0.015
97.40	-0.308	0.018

9.1 MEV

11.30	0.045	0.014
22.50	-0.037	0.016
33.60	-0.068	0.010
44.70	-0.123	0.016
55.60	-0.216	0.017
66.30	-0.282	0.016
75.90	-0.268	0.018
87.20	-0.251	0.015
97.30	-0.251	0.024
107.20	-0.215	0.023

10.0 MEV

11.30	0.030	0.022
22.50	0.042	0.023
33.60	-0.089	0.023
44.60	-0.096	0.015
55.50	-0.140	0.021
66.20	-0.153	0.016
76.80	-0.168	0.025
87.10	-0.144	0.026
107.10	-0.207	0.034

ANGLES IN DEGREES (C.M.)

9BE(P,N)9B

ANALYZING POWER DATA

11.1 MEV

11.24	-0.017	0.025
22.45	-0.045	0.028
33.59	-0.125	0.033
44.61	-0.197	0.025
55.50	-0.181	0.027
66.22	-0.120	0.027
76.75	-0.101	0.030
87.07	-0.083	0.040

12.0 MEV

11.24	-0.005	0.024
22.43	-0.113	0.020
33.56	-0.202	0.023
44.56	-0.256	0.017
55.45	-0.211	0.030
66.17	-0.138	0.025
76.69	-0.047	0.031
87.05	-0.003	0.052

13.5 MEV

11.22	0.037	0.031
22.41	-0.029	0.080
33.52	-0.293	0.066
44.53	-0.329	0.049
55.40	-0.198	0.056
66.11	-0.043	0.056
76.63	-0.039	0.060
86.93	0.052	0.050

15.0 MEV

11.21	0.053	0.029
22.39	0.008	0.035
33.50	-0.180	0.036
44.50	-0.169	0.031
55.36	-0.178	0.031
66.06	-0.085	0.039
76.58	0.001	0.049
86.89	0.137	0.071
99.98	0.081	0.052

ANGLES IN DEGREES (C.M.)

9BE(P,N)9B

ANALYZING POWER DATA

30 DEGREES (LAB)

2.90	0.125	0.004
3.50	0.221	0.006
4.00	0.258	0.013
4.50	-0.220	0.008
5.00	-0.472	0.005
5.50	-0.432	0.005
6.00	-0.364	0.007
6.50	-0.242	0.007
7.00	-0.304	0.006
7.50	-0.254	0.007
8.10	-0.207	0.011
8.20	-0.188	0.009
9.10	-0.067	0.015
10.00	-0.089	0.026
11.10	-0.125	0.033
12.00	-0.202	0.023
13.50	-0.292	0.066
15.00	-0.180	0.036

50 DEGREES (LAB)

2.90	-0.048	0.009
3.50	-0.059	0.005
4.00	0.142	0.013
4.50	-0.155	0.014
5.00	-0.373	0.007
5.50	-0.465	0.009
6.00	-0.434	0.006
6.50	-0.365	0.007
7.00	-0.468	0.008
7.50	-0.426	0.007
8.10	-0.401	0.015
8.20	-0.345	0.008
9.10	-0.228	0.012
10.00	-0.136	0.024
11.10	-0.181	0.027
12.00	-0.211	0.030
13.50	-0.198	0.056
15.00	-0.178	0.031

70 DEGREES (LAB)

2.90	-0.220	0.013
3.50	-0.249	0.008
4.00	-0.265	0.016
4.50	-0.043	0.016
5.00	0.287	0.013
5.50	-0.026	0.012
6.00	-0.244	0.008
6.50	-0.233	0.006
7.00	-0.397	0.008
7.50	-0.349	0.007
8.10	-0.390	0.013
8.20	-0.364	0.013
9.10	-0.265	0.016
10.00	-0.098	0.031
11.10	-0.101	0.030
12.00	-0.047	0.031
13.50	-0.039	0.060
15.00	0.001	0.049

POLARIZATION DATA

30 DEGREES (LAB)

2.70	0.125	0.020
2.90	0.139	0.016
3.50	0.285	0.025
4.00	0.266	0.025
4.25	0.073	0.018
4.50	-0.232	0.015
4.75	-0.378	0.017
5.00	-0.569	0.014
5.25	-0.512	0.016
5.50	-0.502	0.011
6.00	-0.430	0.020
6.50	-0.300	0.028
7.00	-0.401	0.021
7.50	-0.294	0.031
8.10	-0.180	0.021
8.20	-0.233	0.066
9.10	-0.068	0.010
10.00	-0.089	0.023

50 DEGREES (LAB)

2.70	0.063	0.024
2.90	-0.048	0.023
3.50	-0.050	0.028
4.00	0.134	0.032
4.25	0.116	0.038
4.50	-0.127	0.023
4.75	-0.374	0.021
5.00	-0.468	0.012
5.25	-0.508	0.020
5.50	-0.511	0.015
6.00	-0.516	0.019
6.50	-0.476	0.025
7.00	-0.574	0.028
7.50	-0.475	0.025
8.10	-0.399	0.023
8.20	-0.395	0.020
9.10	-0.216	0.017
10.00	-0.140	0.021

70 DEGREES (LAB)

2.90	-0.235	0.023
3.50	-0.283	0.019
4.00	-0.211	0.030
4.25	-0.201	0.042
4.50	-0.021	0.022
4.75	0.359	0.031
5.00	0.333	0.017
5.25	0.103	0.030
5.50	-0.124	0.022
6.00	-0.331	0.020
6.50	-0.295	0.034
7.00	-0.488	0.028
7.50	-0.453	0.024
7.90	-0.434	0.023
8.10	-0.438	0.015
8.20	-0.391	0.016
8.50	-0.349	0.020
8.80	-0.294	0.018
9.10	-0.268	0.018
9.40	-0.225	0.021
9.70	-0.185	0.025
10.00	-0.168	0.025

ENERGIES IN MEV

$^{15}N(P,N)^{15}O$

ANALYZING POWER DATA

5.17 MEV

22.70	0.130	0.020
33.90	0.050	0.012
45.00	-0.093	0.009
56.00	-0.218	0.010
66.80	-0.346	0.011
77.40	-0.343	0.014

7.9 MEV

21.80	-0.108	0.007
32.70	-0.230	0.009
43.40	-0.191	0.010
54.10	-0.055	0.009
64.60	-0.040	0.012
75.00	0.073	0.013
85.30	0.102	0.014
95.30	0.029	0.016
105.30	-0.092	0.013

8.5 MEV

21.80	0.154	0.009
32.60	0.205	0.012
43.30	0.240	0.014
54.00	0.237	0.014
64.50	0.153	0.020
74.90	0.167	0.023
85.10	0.124	0.020
95.20	0.095	0.018
105.10	0.075	0.020

9.2 MEV

21.70	-0.046	0.011
32.50	-0.096	0.010
43.30	-0.239	0.012
53.90	-0.222	0.011
64.40	-0.148	0.014
74.80	0.057	0.017
85.00	0.190	0.018
95.10	0.275	0.018
105.00	0.184	0.020

ANGLES IN DEGREES (C.M.)

15N(P,N)15O

ANALYZING POWER DATA

5.65 MEV

22.40	0.379	0.004
27.90	0.437	0.004
33.50	0.479	0.005
44.40	0.554	0.004
55.30	0.557	0.006
66.00	0.464	0.010
71.30	0.353	0.009
76.50	0.226	0.014
86.80	-0.205	0.015
96.90	-0.494	0.014
101.90	-0.441	0.007
106.80	-0.506	0.011
111.70	-0.468	0.011
116.50	-0.492	0.011
121.30	-0.432	0.008
125.60	-0.424	0.008
144.40	-0.326	0.006
157.90	-0.204	0.006

6.28 MEV

22.00	0.088	0.006
33.00	0.116	0.015
43.80	0.081	0.005
54.60	0.098	0.011
65.20	0.024	0.008
75.60	-0.060	0.017
85.90	-0.209	0.008
96.00	-0.307	0.007
105.90	-0.376	0.009
115.60	-0.380	0.008
125.20	-0.337	0.008
143.80	-0.173	0.007

10.3 MEV

21.67	-0.141	0.009
32.44	-0.435	0.014
43.14	-0.725	0.014
53.74	-0.781	0.014
64.23	-0.751	0.007
74.32	-0.443	0.013
84.81	0.038	0.037
94.88	-0.020	0.026
104.81	-0.214	0.005

11.3 MEV

21.70	-0.193	0.020
32.38	-0.575	0.015
43.06	-0.843	0.007
48.34	-0.908	0.004
53.65	-0.902	0.008
64.13	-0.706	0.007
74.48	-0.186	0.009
84.69	0.513	0.008
94.76	0.639	0.020
104.69	0.319	0.014

POLARIZATION DATA

5.65 MEV

11.20	-0.010	0.030
22.30	-0.060	0.009
27.80	-0.031	0.023
33.33	-0.100	0.032
44.30	-0.021	0.014
55.10	0.035	0.043
65.80	0.005	0.036
76.30	-0.170	0.060
86.60	-0.483	0.057
96.70	-0.615	0.062
106.60	-0.521	0.060
116.30	-0.198	0.040
125.80	-0.169	0.030
144.30	0.098	0.037

6.28 MEV

22.08	0.103	0.030
33.04	0.099	0.030
43.91	0.132	0.033
54.66	-0.016	0.039
65.27	-0.079	0.027
75.72	-0.259	0.042
85.99	-0.392	0.040
96.08	-0.493	0.045
105.99	-0.564	0.043
115.77	-0.589	0.055
125.27	-0.599	0.052
143.91	-0.025	0.050

10.3 MEV

10.85	-0.043	0.018
21.67	-0.125	0.009
32.44	-0.354	0.013
43.14	-0.622	0.013
53.74	-0.738	0.014
64.23	-0.645	0.018
74.59	-0.406	0.024
84.81	-0.022	0.031
94.88	-0.101	0.020
104.81	-0.200	0.024

11.3 MEV

10.83	-0.048	0.034
21.63	-0.189	0.023
32.38	-0.503	0.026
43.04	-0.844	0.017
48.34	-0.917	0.020
53.62	-0.902	0.012
58.87	-0.828	0.028
64.09	-0.666	0.019
74.48	-0.198	0.014
84.69	0.319	0.031
94.76	0.618	0.028
104.69	0.325	0.030

ANGLES IN DEGREES (C.M.)

15N(P,N)15O

ANALYZING POWER DATA

20 DEGREES (LAB)

4.54	-0.030	0.009
4.75	0.264	0.012
4.95	0.388	0.007
5.15	0.243	0.006
5.17	0.128	0.006
5.35	-0.057	0.006
5.45	0.229	0.005
5.65	0.379	0.004
5.85	0.113	0.003
6.05	0.156	0.008
6.28	0.088	0.006
6.50	-0.200	0.010
6.75	-0.171	0.003
7.00	-0.070	0.003
7.25	-0.068	0.011
7.50	0.220	0.006
7.70	0.108	0.007
7.90	-0.189	0.008
8.20	0.030	0.006
8.50	0.154	0.009
8.80	0.309	0.007
9.20	-0.046	0.010
9.30	-0.024	0.007
10.30	-0.141	0.009
11.30	-0.193	0.020

40 DEGREES (LAB)

10.32	-0.708	0.010
10.42	-0.689	0.014
10.53	-0.641	0.013
10.63	-0.454	0.011
10.73	-0.302	0.016
10.83	-0.308	0.015
10.93	-0.439	0.016
11.03	-0.711	0.020
11.13	-0.786	0.021
11.23	-0.732	0.023
11.30	-0.843	0.007

50 DEGREES (LAB)

4.54	-0.099	0.012
4.75	0.104	0.013
4.95	-0.043	0.010
5.15	-0.247	0.006
5.27	-0.218	0.010
5.35	-0.302	0.005
5.45	0.111	0.005
5.65	0.557	0.006
5.85	0.130	0.008
6.05	0.157	0.006
6.28	0.098	0.011
6.50	-0.168	0.015
6.75	-0.141	0.004
7.00	0.102	0.003
7.25	-0.043	0.011
7.50	0.203	0.007
7.70	-0.055	0.009
7.90	-0.127	0.010
8.20	0.011	0.016
8.50	0.237	0.014
8.80	0.410	0.010
9.20	-0.222	0.011
9.30	-0.356	0.011
10.30	-0.781	0.014
11.30	-0.902	0.008

POLARIZATION DATA

20 DEGREES (LAB)

4.54	-0.085	0.025
4.75	0.218	0.030
4.95	0.461	0.042
5.15	0.321	0.028
5.35	-0.117	0.022
5.45	0.217	0.033
5.65	-0.060	0.009
5.87	-0.373	0.025
6.06	-0.071	0.033
6.28	0.103	0.030
6.50	-0.184	0.020
6.75	-0.281	0.019
7.00	0.114	0.017
7.25	0.234	0.020
7.50	0.404	0.011
7.70	-0.009	0.014
7.90	-0.279	0.015
8.20	0.023	0.015
8.50	0.086	0.017
8.85	0.291	0.015
9.20	-0.054	0.018
10.30	-0.125	0.009
11.30	-0.189	0.023

40 DEGREES (LAB)

10.22	-0.058	0.027
10.32	-0.647	0.011
10.52	-0.682	0.025
10.62	-0.490	0.037
10.72	-0.338	0.024
10.82	-0.358	0.023
10.92	-0.601	0.025
11.03	-0.831	0.026
11.13	-0.815	0.037
11.23	-0.817	0.035
11.30	-0.844	0.017

50 DEGREES (LAB)

4.54	-0.224	0.030
4.75	-0.144	0.031
4.95	-0.223	0.034
5.15	-0.278	0.027
5.35	-0.307	0.017
5.45	0.172	0.031
5.65	0.035	0.043
5.87	-0.610	0.048
6.06	0.065	0.053
6.28	-0.016	0.039
6.50	-0.271	0.022
6.75	-0.090	0.023
6.87	0.172	0.020
7.00	0.255	0.010
7.25	0.421	0.022
7.50	0.467	0.014
7.70	-0.210	0.014
7.90	-0.377	0.020
8.20	-0.252	0.028
8.50	0.110	0.019
8.85	0.391	0.024
9.20	-0.415	0.023
10.30	-0.738	0.014
11.30	-0.902	0.012

ENERGIES IN MEV

15N(P,N)15O

ANALYZING POWER DATA

100 DEGREES (LAB)

4.54	0.049	0.015
4.75	0.143	0.012
4.95	0.214	0.009
5.15	0.269	0.008
5.35	0.068	0.006
5.45	-0.255	0.007
5.65	-0.481	0.005
5.85	-0.397	0.008
6.05	-0.289	0.008
6.28	-0.379	0.009
6.50	-0.387	0.012
6.75	-0.177	0.003
7.00	-0.393	0.011
7.25	-0.072	0.012
7.50	0.240	0.010
7.70	0.171	0.013
7.90	-0.090	0.013
8.20	0.089	0.013
8.50	0.075	0.020
8.80	0.288	0.008
9.20	0.204	0.011
9.30	0.138	0.013
10.30	-0.214	0.005
11.30	0.319	0.014

POLARIZATION DATA

60 DEGREES (LAB)

5.50	0.328	0.041
5.55	0.288	0.053
5.60	0.116	0.055
5.65	-0.023	0.042

100 DEGREES (LAB)

4.54	-0.086	0.085
4.75	0.088	0.048
4.95	0.141	0.029
5.15	0.231	0.034
5.35	-0.153	0.029
5.45	-0.589	0.060
5.65	-0.521	0.060
5.87	-0.391	0.046
6.06	-0.462	0.054
6.28	-0.564	0.043
6.50	-0.418	0.048
6.75	-0.266	0.043
7.00	-0.266	0.019
7.25	-0.219	0.047
7.50	0.253	0.027
7.70	-0.248	0.052
7.90	0.024	0.028
8.20	0.248	0.046
8.50	-0.029	0.026
8.85	0.705	0.059
9.20	0.322	0.041
10.30	-0.200	0.024
11.30	0.325	0.030

ENERGIES IN MEV

LIST OF REFERENCES

REFERENCES

J. D. Anderson, S. D. Bloom, C. Wong, W. F. Hornyak, and V. A. Madsen, Phys. Rev. 177 (1969) 1416.

J. D. Anderson and C. Wong, Phys. Rev. Lett. 7 (1961) 250.

J. D. Anderson, C. Wong, J. W. McClure, and B. D. Walker, Phys. Rev. 136 (1964) B118.

L. G. Arnold, Bull. Am. Phys. Soc. 22 (1977) 588.

L. G. Arnold, Proc. Fourth Int. Symp. on Polarization Phenomena in Nuclear Physics, Zürich, 1975, ed. W. Grüebler and V. König (Birkhäuser Verlag, Basel, 1976) p. 503.

R. Bangert, B. Gonsoir, M. Roth, B. Steinmetz, A. Strömich, Nucl. Phys. A287 (1977) 280.

A. R. Barnett, Nucl. Phys. A120 (1968) 342.

R. W. Bauer, J. D. Anderson, C. Wong, Nucl. Phys. 56 (1964) 117.

F. D. Becchetti, Jr. and G. W. Greenlees, Phys. Rev. 182 (1969) 1190.

P. R. Bevington, Data Reduction and Error Analysis for the Physical Sciences (McGraw-Hill, New York, 1969).

L. C. Biedenharn, Nucl. Phys. 10 (1959) 620.

F. W. Bingham, M. K. Brussel, and J. D. Steben, Nucl. Phys. 55 (1964) 265.

R. J. Blin-Stoyle, Proc. Phys. Soc. A65 (1952) 452.

A. Bohr and B. Mottelson, Nuclear Structure: Single-Particle Motion, vol. 1 (W. A. Benjamin, New York, 1969) pp. 31-42, 171-76.

L. Brown and U. Rohrer, Nucl. Phys. A221 (1974) 325.

R. C. Byrd, P. W. Lisowski, G. Mack, S. E. Skubic, W. Tornow, R. L. Walter, and T. B. Clegg, Bull. Am. Phys. Soc. 21 (1976b) 637.

R. C. Byrd, P. W. Lisowski, W. Tornow, and R. L. Walter, Bull. Am. Phys. Soc. 22 (1977) 587.

R. C. Byrd, P. W. Lisowski, S. E. Skubic, W. Tornow, R. L. Walter, and T. B. Clegg, Proc. Fourth Int. Symp. on Polarization Phenomena in Nuclear Reactions, Zürich, 1975, ed. W. Grüebler and V. König (Birkhäuser Verlag, Basel, 1976a) p. 501.

J. D. Carlson, C. D. Zafiratos, and D. A. Lind, Nucl. Phys. A249 (1975) 29.

T. B. Clegg, G. A. Bissinger, and T. A. Trainor, Nucl. Instr. and Meth. 120 (1974) 445.

H. E. Conzett, Phys. Lett. 51B (1974) 445.

S. Cotanch, Florida State University Tandem Accelerator Laboratory Technical Report No. 4 (1973).

S. Cotanch and D. Robson, Phys. Rev. C7 (1973) 1714.

D. S. Cramer and L. Cranberg, Nucl. Phys. A171 (1971) 59.

T. R. Donoghue, Sr. M. S. Doyle, H. W. Clark, L. J. Dries, J. L. Regner, W. Tornow, R. C. Byrd, P. W. Lisowski, and R. L. Walter, Phys. Rev. Lett. 37 (1976) 981.

Sr. M. A. Doyle, H. W. Clark, K. R. Crosthwaite, L. J. Dries, J. L. Regner, and T. R. Donoghue, Bull. Am. Phys. Soc. 21 (1976).

R. M. Drisko, R. H. Bassel, and G. R. Satchler, Phys. Lett. 2 (1962) 318.

M. Drosg, Nucl. Instr. and Meth. 105 (1972) 573.

H. J. Erramuspe, Nucl. Phys. A105 (1967) 569.

R. D. Evans, The Atomic Nucleus, (McGraw-Hill, New York, 1955).

J. C. Ferrer, J. D. Carlson, and J. Rapaport, Phys. Lett. 62B (1976) 399.

E. Finckh, in Nuclear Spectroscopy and Reactions, Part B, ed. J. Cerny (Academic Press, New York, 1974) p. 573.

D. W. Glasgow, F. O. Purser, J. C. Clement, G. Mack, K. Stelzer, J. R. Boyce, D. H. Epperson, H. H. Hogue, E. G. Bilpuch, H. W. Newson, and C. R. Gould, in Nuclear Cross Sections and Technology, vol. 1, ed. R. A. Schrack and C. D. Bowman (National Bureau of Standards, 1975) p. 99.

J. Gosset, B. Mayer, and J. L. Escudié, Phys. Rev. C14 (1975) 878.

A. E. S. Green and P. C. Sood, Phys. Rev. 111 (1958) 1147.

R. C. Haight, J. J. Jarmer, J. E. Simmons, J. C. Martin, and T. R. Donoghue, Phys. Rev. Lett. 28 (1972) 1587.

L. F. Hansen and M. R. Stelts, Phys. Rev. 132 (1963) 1123.

P. E. Hodgson and J. R. Rook, Nucl. Phys. 37 (1962) 632.

G. W. Hoffman, Phys. Rev. C8 (1973) 761.

G. W. Hoffman and W. R. Coker, Z. Physik 269 (1974) 307.

H. H. Hogue (unpublished Ph.D. dissertation, Duke University, 1977).

J. J. Jarmer, R. C. Haight, J. E. Simmons, J. C. Martin, and T. R. Donoghue, Phys. Rev. C9 (1974) 1292.

K. W. Jones, L. J. Lidofsky, and J. L. Weil, Phys. Rev. 112 (1958) 1252.

C. A. Kelsey, Nucl. Phys. 45 (1963) 235.

C. A. Kelsey, B. Hoop, and P. Van der Maat, Nucl. Phys. 51 (1964) 395.

C. A. Kelsey, G. P. Lietz, S. F. Trevino, and S. E. Darden, Phys. Rev. 129 (1963) 759.

A. M. Lane, Nucl. Phys. 35 (1962) 676.

A. M. Lane and J. M. Soper, Nucl. Phys. 37 (1962) 506.

P. W. Lisowski (unpublished Ph.D. dissertation, Duke University, 1973).

P. W. Lisowski, R. L. Walter, S. A. Wender, and T. B. Clegg, Nucl. Instr. and Meth. 146 (1977) 477.

P. W. Lisowski, G. Mack, R. C. Byrd, W. Tornow, S. E. Skubic, R. L. Walter, and T. B. Clegg, Proc. Fourth Int. Symp. on Polarization Phenomena in Nuclear Reactions, Zürich, 1975, ed. Grüebler and V. König (Birkhäuser Verlag, Basel, 1976) p. 499.

R. G. Lovas, Nucl. Phys. A262 (1976) 356.

D. H. Loyd and W. Haeberli, Nucl. Phys. A148 (1970) 236.

I. E. McCarthy, Introduction to Nuclear Theory (John Wiley and Sons, New York, 1968) p. 163, 369.

J. B. Marion and J. L. Fowler (eds.) Fast Neutron Physics (Interscience Publishers, New York, 1963).

G. L. Morgan, private communication (1975).

G. L. Morgan and R. L. Walter, Phys. Rev. 168 (1968) 1114.

J. M. Moss, C. Brassard, R. Vyse, and J. Grosset, Phys. Rev. C6 (1972) 1698.

G. G. Ohlsen and P. W. Keaton, Jr., Nucl. Instr. and Meth. 109 (1973) 41.

D. M. Patterson, R. R. Doering, and A. Galonsky, Nucl. Phys. A263 (1976) 261.

F. G. Perey, Phys. Rev. 131 (1963) 745.

J. Rapaport, Phys. Lett. 70B (1977) 141.

A. Richter and S. J. Parish, Phys. Rev. Lett. 21 (1968) 1824.

U. Rohrer and L. Brown, Nucl. Phys. A217 (1973) 525.

U. Rohrer and L. Brown, Nucl. Phys. A261 (1976) 141.

L. Rosen, J. G. Beery, A. S. Goldhaber, and E. H. Auerbach, Ann. of Phys. 34 (1965) 96.

H. H. Rosenbrock, Comput. J. 3 (1960) 175.

G. R. Satchler, in Isospin in Nuclear Physics, ed. D. H. Wilkinson (North-Holland, Amsterdam, 1969) p. 389.

G. R. Satchler, Nucl. Phys. 8 (1958) 65.

G. R. Satchler, Nucl. Phys. A91 (1967) 75.

G. R. Satchler, R. M. Drisko, and R. H. Bassel, Phys. Rev. 136 (1964) B637.

S. D. Schery, D. A. Lind, H. W. Fielding, and C. D. Zafiratos, Nucl. Phys. A234 (1974) 109.

E. H. Schwarcz, Phys. Rev. 149 (1966) 752.

J. R. Smith and S. T. Thornton, Nucl. Phys. A186 (1972) 161.

P. C. Sood, Can. J. of Physics 44 (1966) 1203.

T. Terasawa and G. R. Satchler, Phys. Lett. 7 (1963) 265.

V. V. Verbinski, W. R. Burrus, T. A. Love, W. Zobel, and N. W. Hill, Nucl. Instr. and Meth. 65 (1968) 8.

H. J. Votava, T. B. Clegg, E. J. Ludwig and W. J. Thompson, Nucl. Phys. A204 (1973) 529.

B. D. Walker, C. Wong, J. D. Anderson, and J. W. McClure, Phys. Rev. 137 (1965b) 1504.

B. D. Walker, C. Wong, J. D. Anderson, J. W. McClure, and R. W. Bauer, Phys. Rev. 137 (1965a) 347.

R. L. Walter, in Nuclear Spectroscopy and Reactions, Part B, ed. J. Cerny (Academic Press, New York, 1974) p. 635.

R. L. Walter, W. Benenson, P. S. Dubbledam, and T. H. May, Nucl. Phys. 30 (1962) 292.

B. A. Watson, P. P. Singh, and R. E. Segel, Phys. Rev. 182 (1969) 977.

M. F. Werby, S. Edwards, and W. J. Thompson, Nucl. Phys. A169 (1971) 81.

D. H. Wilkinson, Phil. Mag. 1 (1956) 379.

C. Wong, J. D. Anderson, S. D. Bloom, J. W. McClure, and B. D. Walker, Phys. Rev. 123 (1961) 598.

C. Wong, J. D. Anderson, J. C. Davis, and S. M. Grimes, Phys. Rev. C7 (1973) 1895.

C. Wong, J. D. Anderson, J. W. McClure, B. A. Pohl, and J. J. Wesolowski, Phys. Rev. C5 (1972) 158.

BIOGRAPHY

Roger Carl Byrd

Born:	November 24, 1950 Rome, Georgia
Education:	North Carolina State University Georgia Institute of Technology, B.S. 1972
Positions:	Exchange Student, Kernforschungsanlage Jülich, Jülich, West Germany, Summer 1971 Student Trainee, Brookhaven National Laboratory, Summer 1972 James B. Duke Fellow, Duke University, 1972-75 Research Assistant, Duke University, 1975-78
Honorary Societies:	Phi Eta Sigma, Tau Beta Pi, Phi Kappa Phi, Sigma Xi

Publications:

IAESTE, R. C. Byrd, Ga. Prof. Eng., (Dec., 1970) 6.

Polarization Transfer in the D(p,n)pp Reaction at $\theta = 0°$ for Proton Bombarding Energies from 10.5 to 15 MeV,
T. B. Clegg, R. L. Walter, P. W. Lisowski and R. C. Byrd, in Proc. of Conference on Few Body Problems in Nuclear and Particle Physics, Laval, Quebec, Canada, Aug. 27-30, 1974.

Comparison of P_y and A_y for $^{9}Be(p,n)^{9}B$ at 8.1 and 9.1 MeV, P. W. Lisowski, G. Mack, R. C. Byrd, W. Tornow, S. E. Skubic, R. L. Walter, and T. B. Clegg, in Proc. of the 4th Int. Symposium on Polarization Phenomena in Nuclear Reactions, ed. W. Grüebler and V. König (Birkhäuser Verlag, Basel, 1976), p. 499.

Neutron Polarization and Analyzing Power in the $^{15}N(p,n)^{15}C$ Reaction, R. C. Byrd, P. W. Lisowski, S. E. Skubic, W. Tornow, R. L. Walter, and T. B. Clegg, ibid., p. 501.

Polarization Transfer Effects in $(\vec{p},\vec{n})$ Reactions on Light Nuclei at 0°, P. W. Lisowski, C. E. Busch, and T. B. Clegg, ibid., p. 638.

Polarization Transfer in the $D(\vec{p},\vec{n})p,p$ Reaction from 10 to 15 MeV, R. L. Walter, R. C. Byrd, P. W. Lisowski, and T. B. Clegg, ibid., p. 489.

Neutron-Proton Polarization Measurement at 14.2 MeV, W. Tornow, P. W. Lisowski, R. C. Byrd, S. E. Skubic, R. L. Walter, and T. B. Clegg, ibid., p. 439.

Publications: (continued)

Measurement of Polarization Transfer Coefficients for $(\vec{d},\vec{n})$ Reactions on ^{14}N, ^{16}O, and ^{28}Si, P. W. Lisowski, R. C. Byrd, W. Tornow, R. L. Walter, and T. B. Clegg, ibid., p. 653.

Measurement of $K_y^{y'}$ (0°) Over Resonance Region in $^{12}C(d,n)^{13}N$, R. L. Walter, R. C. Byrd, P. W. Lisowski, G. Mack, and T. B. Clegg, ibid., p. 649.

Determination of Polarization Transfer Coefficient $K_y^{y'}$ (0°) for the Breakup Reactions $^4He(\vec{d},\vec{n})^4He,p$ and $D(\vec{d},\vec{n})D,p$, P. W. Lisowski, R. C. Byrd, R. L. Walter, and T. B. Clegg, ibid., p. 573.

Polarization Transfer Effects in (p,n) Reactions on Light Nuclei at $\theta = 0°$, P. W. Lisowski, R. C. Byrd, R. L. Walter, and T. B. Clegg, Nucl. Phys. A259 (1976) 188.

Equality of Analyzing Power and Polarization in the Reaction $^3H(p,n)^3He$, T. R. Donoghue, Sr. M. A. Doyle, H. W. Clark, L. J. Dries, J. L. Regner, W. Tornow, R. C. Byrd, P. W. Lisowski, and R. L. Walter, Phys. Rev. Lett. 13 (1976) 809.

A Remeasurement of P_y for the $^2H(d,\vec{n})^3He$ Reaction and Its Implication to The f-wave Admixture of the 2^- State at 22 MeV in ^4He, W. Tornow, S. E. Skubic, R. C. Byrd, P. W. Lisowski and R. L. Walter, Phys. Rev. C. 13 (1976) 2080.

Discrepancies Between Global Nucleon-Nucleon Phase Shifts and New Data for n-p Scattering at 16.9 MeV, W. Tornow, P. W. Lisowski, R. C. Byrd and R. L. Walter, Phys. Rev. Letters 39 (1977) 915.

The Analyzing Power $A_y(\theta)$ for the Elastic Scattering of 12-MeV Neutrons from Deuterons, W. Tornow, P. W. Lisowski, R. C. Byrd and R. L. Walter, accepted for publication in Nuclear Physics.

Abstracts:

Polarization Transfer in $^{12}C(\vec{d},n)^{14}N$ and $^{28}Si(\vec{d},n)^{29}P$ at $\theta = 0°$, P. W. Lisowski, R. C. Byrd, G. Mack, R. L. Walter and T. B. Clegg, Bull. Am. Phys. Soc. 19 (1974) 1076.

Analyzing Power Measurements for $^9Be(\vec{p},n)^9B$, P. W. Lisowski, R. C. Byrd, S. Skubic, G. Mack, R. L. Walter and T. B. Clegg, Bull. Am. Phys. Soc. 20 (1975) 693.

Polarization Transfer in the $^{16}O(d,n)^{17}F$ Reaction at $\theta = 0°$, R. L. Walter, R. C. Byrd, P. W. Lisowski, S. Skubic and T. B. Clegg, ibid., 694.

Abstracts: (continued)

Comparison of the Polarization and Analyzing Power in (p,n) Mirror Reactions on ^{15}N and ^{9}Be, R. C. Byrd, P. W. Lisowski, G. Mack, S. E. Skubic, W. Tornow, R. L. Walter and T. B. Clegg, Bull. Am. Phys. Soc. 21 (1976) 637.

Polarization at 90° c.m. in n-p Scattering for E_n = 13.5 and 16.0 MeV, W. Tornow, P. W. Lisowski, R. C. Byrd, S. E. Skubic, and R. L. Walter, ibid., 636.

Remeasurement of P^y in the $T(p,n)^3He$ Reaction Below 4 MeV, W. Tornow, R. C. Byrd, P. W. Lisowski, R. L. Walter, and T. R. Donoghue, Bull. Am. Phys. Soc. 21 (1976) 977.

High Accuracy Measurements of n-p Analyzing Power $A_y(\theta)$ at 16.9 MeV, W. Tornow, R. C. Byrd, P. W. Lisowski, C. Floyd and R. L. Walter, Bull. Am. Phys. Soc. 22 (1977) 1017.

Elastic Scattering of Polarized Neutrons from Hydrogen and Deuterium, W. Tornow, P. W. Lisowski, R. C. Byrd and R. L. Walter, ibid., 531.

Comparison of the Polarization and Analyzing Power in (p,n) Reactions on ^{9}Be and ^{15}N, R. C. Byrd, P. W. Lisowski, W. Tornow and R. L. Walter, ibid., 587.